frontiers | Research Topics

Justified modeling frameworks and novel interpretations of ecological and epidemiological systems

Edited by
Bapan Ghosh, Salih Djilali and Asep K. Supriatna

Published in
Frontiers in Applied Mathematics and Statistics

ISSN 1664-8714
ISBN 978-2-8325-4014-5
DOI 10.3389/978-2-8325-4014-5

About Frontiers

Frontiers is more than just an open access publisher of scholarly articles: it is a pioneering approach to the world of academia, radically improving the way scholarly research is managed. The grand vision of Frontiers is a world where all people have an equal opportunity to seek, share and generate knowledge. Frontiers provides immediate and permanent online open access to all its publications, but this alone is not enough to realize our grand goals.

Frontiers journal series

The Frontiers journal series is a multi-tier and interdisciplinary set of open-access, online journals, promising a paradigm shift from the current review, selection and dissemination processes in academic publishing. All Frontiers journals are driven by researchers for researchers; therefore, they constitute a service to the scholarly community. At the same time, the *Frontiers journal series* operates on a revolutionary invention, the tiered publishing system, initially addressing specific communities of scholars, and gradually climbing up to broader public understanding, thus serving the interests of the lay society, too.

Dedication to quality

Each Frontiers article is a landmark of the highest quality, thanks to genuinely collaborative interactions between authors and review editors, who include some of the world's best academicians. Research must be certified by peers before entering a stream of knowledge that may eventually reach the public - and shape society; therefore, Frontiers only applies the most rigorous and unbiased reviews. Frontiers revolutionizes research publishing by freely delivering the most outstanding research, evaluated with no bias from both the academic and social point of view. By applying the most advanced information technologies, Frontiers is catapulting scholarly publishing into a new generation.

What are Frontiers Research Topics?

Frontiers Research Topics are very popular trademarks of the *Frontiers journals series*: they are collections of at least ten articles, all centered on a particular subject. With their unique mix of varied contributions from Original Research to Review Articles, Frontiers Research Topics unify the most influential researchers, the latest key findings and historical advances in a hot research area.

Find out more on how to host your own Frontiers Research Topic or contribute to one as an author by contacting the Frontiers editorial office: frontiersin.org/about/contact

Justified modeling frameworks and novel interpretations of ecological and epidemiological systems

Topic editors

Bapan Ghosh — Indian Institute of Technology Indore, India

Salih Djilali — University of Chlef, Algeria

Asep K. Supriatna — Padjadjaran University, Indonesia

Citation

Ghosh, B., Djilali, S., Supriatna, A. K., eds. (2024). *Justified modeling frameworks and novel interpretations of ecological and epidemiological systems*. Lausanne: Frontiers Media SA. doi: 10.3389/978-2-8325-4014-5

Table of contents

frontiers | Frontiers in Applied Mathematics and Statistics

TYPE Editorial
PUBLISHED 04 January 2024
DOI 10.3389/fams.2023.1346541

OPEN ACCESS

EDITED AND REVIEWED BY
Raluca Eftimie,
University of Franche-Comté, France

*CORRESPONDENCE
Bapan Ghosh
✉ keshab.bapan@iiti.ac.in

RECEIVED 29 November 2023
ACCEPTED 11 December 2023
PUBLISHED 04 January 2024

CITATION
Ghosh B, Djilali S and Supriatna AK (2024) Editorial: Justified modeling frameworks and novel interpretations of ecological and epidemiological systems.
Front. Appl. Math. Stat. 9:1346541.
doi: 10.3389/fams.2023.1346541

Editorial: Justified modeling frameworks and novel interpretations of ecological and epidemiological systems

Bapan Ghosh[1]*, Salih Djilali[2] and Asep K. Supriatna[3]

[1]Differential Equations, Modeling, and Simulation Group, Department of Mathematics, Indian Institute of Technology Indore, Indore, India, [2]Department of Mathematics, Faculty of Exact Sciences and Informatics, University of Chlef, Chlef, Algeria, [3]Department of Mathematics, Padjadjaran University, Bandung, West Java, Indonesia

KEYWORDS

fractional order differential equations, global stability, optimal control theory, fuzzy environment, stochastic environment, predator-prey dynamics, dengue dynamics, COVID-19 pandemic

Editorial on the Research Topic
Justified modeling frameworks and novel interpretations of ecological and epidemiological systems

Nowadays, researchers have paid significant attention to developing new modeling frameworks using differential equations combined with statistical tools and scientific computations. The present Research Topic has invited researchers to submit their high-quality and well-motivated contributions to modeling and analysis of ecological and epidemiological processes.

Upon a thorough review of all the submitted manuscripts based on the novelty of the contribution we present ten research articles in this article Research Topic. The accepted articles can be categorized into three important subtopics: predator-prey dynamics, disease modeling, and other biological processes. In particular, four articles focused on harvesting, cannibalism, refuge, and foraging behavior in the context of various ecological interactions. The remaining six articles explored dengue dynamics, controlling the spread of COVID-19, preventing illness exposure in susceptible children from pneumonia, and developing mechanisms for tissue repair. The main results of all these articles are discussed in more detail below.

In the first sub topic, Panigoro et al. have proposed a fractional order predator-prey system with two stages for predator species. The authors have assumed harvesting in the prey species. The model has shown that a lower prey harvesting rate could maintain the viability of the species. Moreover, an intermediate harvesting rate could either maintain coexistence or lead to extinction, while an excessive harvesting rate causes extinction of prey species following a saddle-node bifurcation. Meanwhile, Rayungsari et al. have considered a fractional order Rosenzweig-MacArthur type predator prey model incorporating cannibalism among predators. A consecutive Hopf bifurcation has appeared with respect to the cannibalism as well as refuge parameters, leading to a bubble structure in the bifurcation diagram.

The environment is uncertain. This fact makes the parameters in a model also so. With this consideration, Sukarsih et al. proposed the well celebrated Rosenzweig-MacArthur system using fuzzy theoretic framework for possibilistic uncertain parameters and initial conditions. The authors studied the qualitative behavior of the model using the fifth order Runge-Kutta method, which was modified for the fuzzy system using the Zadeh extension principle. This contribution uncovered that when the initial populations of prey and predators are uncertain, the behavior of the fuzzy model would be qualitatively the same as the crisp model. Prakash and Vamsi have implemented a time optimal control for a predator-prey system in continuous white noise and discontinuous Levy noise modeling framework to understand the trade-off between quality and quantity of additional food to predators.

In the second subtopic, Aldila et al. have used Quasi-Steady State Approximation (QSSA) method in a SIR-UV vector-borne disease model in order to make the complicated and coupled SIR-UV system into a simple IR-model. This investigation potentially revealed that dengue would periodically appear at least every year in Jakarta. Another vector-borne disease model (Coffield Jr. et al.), uncovers the dynamics of Chagas disease transmission in neighbouring villages. They reported that the effects of human travel and passive vector migration are unlikely to play a significant role in the overall dynamics and in the number of human infections. Hence, control strategies related to travel will also unlikely yield meaningful benefit.

We have witnessed the dramatic loss of human life and the collapse of the world economy due to COVID-19. The COVID-19 patients faced more challenges when they had other diseases prior to COVID-19 infection. Rois et al. proposed a COVID-19 model with comorbidity to estimate cumulative cases infected with COVID-19 from 1 November 2020 to 19 May 2021 in Indonesia. The number of COVID-19 infections can reduce significantly by means of two optimal controls, namely public education and increased medical care. In the same line, Teklu and Terefe developed a new COVID-19 and syphilis co-infection mathematical model with ten distinct classes of the human population. The model analyses showed that the COVID-19 and syphilis co-infection spread could be under control whenever the basic reproduction number is less than unity. They also demonstrated that the protections and treatments are the two fundamental control aspects. Legesse et al. developed a mathematical model to understand the impact of exclusive versus inclusive nursing on baby mortalities and morbidities from conception to 6 months. The main conclusion of this study is that limiting pneumonia transmission to prevention alone during an outbreak is the most cost-effective approach.

Finally, in the third sub section, Mulk et al. implemented inverse finite element (FE) techniques and optimized algorithms to examine the mechanical properties of PVA-C specimens. The mechanism in designing and characterizing soft tissue materials is a novel contribution in this research.

The Research Topic successfully presents genuine, recent, and important results in modeling and analysis of ecological and epidemiological processes. The results can be summarized as follows Panigoro et al. contribution leads to interesting guidelines in fishery management and biological conservation. The bubble formation in the context of fractional predator-prey systems (Rayungsari et al.) is also a new phenomenon. How biological-interaction and stochastic environmental processes affect the dynamics of predator-prey systems are nicely explained by Sukarsih et al. and Prakash and Vamsi. As proposed, the articles in this Research Topic accomplished either numerical simulation, case studies, experimental data, or field observations to illustrate and validate their theories, principles, and results (Aldila et al.; Rois et al.; Teklu and Terefe; Legesse et al.; Coffield Jr. et al.). For instance, combining mathematical models and real-data, Aldila et al. concluded that dengue in Jakarta will periodically appear at least every year. They suggested some action plans to control the disease. Rois et al. and Teklu and Terefe formulated COVID-19 models independently. They proposed some control tactics in reducing the COVID-19 cases. All the contributions, along with mathematical, statistical, and numerical tools, are able to explain new ecological dynamics and suggest prudent disease control strategies.

Author contributions

BG: Conceptualization, Project administration, Resources, Supervision, Visualization, Writing – original draft, Writing – review & editing. SD: Conceptualization, Supervision, Visualization, Writing – review & editing. AS: Conceptualization, Project administration, Resources, Visualization, Writing – original draft, Writing – review & editing.

Funding

The author(s) declare that no financial support was received for the research, authorship, and/or publication of this article.

Acknowledgments

We are grateful to all the eminent authors for publishing their valuable contributions to this Research Topic. We would like to thank the reviewers for their thoughtful comments and efforts towards improving the content for all the manuscripts. We sincerely appreciate all helps and suggestions received from Frontiers team over time.

Conflict of interest

The authors declare that the research was conducted in the absence of any commercial or financial relationships that could be construed as a potential conflict of interest.

Publisher's note

frontiers | Frontiers in Applied Mathematics and Statistics

TYPE Original Research
PUBLISHED 06 January 2023
DOI 10.3389/fams.2022.1096141

OPEN ACCESS

EDITED BY
Asep K. Supriatna,
Universitas Padjadjaran, Indonesia

REVIEWED BY
Ebenezer Bonyah,
University of Education, Winneba, Ghana
Pankaj Tiwari,
University of Kalyani, India

*CORRESPONDENCE
Fatmawati
✉ fatmawati@fst.unair.ac.id

SPECIALTY SECTION
This article was submitted to Mathematical Biology, a section of the journal Frontiers in Applied Mathematics and Statistics

RECEIVED 11 November 2022
ACCEPTED 07 December 2022
PUBLISHED 06 January 2023

CITATION
Rois MA, Fatmawati, Alfiniyah C and Chukwu CW (2023) Dynamic analysis and optimal control of COVID-19 with comorbidity: A modeling study of Indonesia.
Front. Appl. Math. Stat. 8:1096141.
doi: 10.3389/fams.2022.1096141

Dynamic analysis and optimal control of COVID-19 with comorbidity: A modeling study of Indonesia

Muhammad Abdurrahman Rois[1], Fatmawati[1]*, Cicik Alfiniyah[1] and Chidozie W. Chukwu[2]

[1]Department of Mathematics, Faculty of Science and Technology, Universitas Airlangga, Surabaya, Indonesia, [2]Department of Mathematics, Wake Forest University, Winston-Salem, NC, United States

Comorbidity is defined as the coexistence of two or more diseases in a person at the same time. The mathematical analysis of the COVID-19 model with comorbidities presented includes model validation of cumulative cases infected with COVID-19 from 1 November 2020 to 19 May 2021 in Indonesia, followed by positivity and boundedness solutions, equilibrium point, basic reproduction number (R0), and stability of the equilibrium point. A sensitivity analysis was carried out to determine how the parameters affect the spread. Disease-free equilibrium points are asymptotically stable locally and globally if $R_0 < 1$ and endemic equilibrium points exist, locally and globally asymptotically stable if $R_0 > 1$. In addition, this disease is endemic in Indonesia, with $R_0 = 1.47$. Furthermore, two optimal controls, namely public education and increased medical care, are included in the model to determine the best strategy to reduce the spread of the disease. Overall, the two control measures were equally effective in suppressing the spread of the disease as the number of COVID-19 infections was significantly reduced. Thus, it was concluded that more attention should be paid to patients with COVID-19 with underlying comorbid conditions because the probability of being infected with COVID-19 is higher and mortality in this population is much higher. Finally, the combined control strategy is an optimal strategy that provides an effective guarantee to protect the public from the COVID-19 infection based on numerical simulations and cost evaluations.

KEYWORDS

COVID-19, comorbidity, stability, sensitivity analysis, optimal control, cost evaluation

1. Introduction

The COVID-19 virus was reported in the Wuhan-Hubei Province of China in December 2019 and was spread rapidly to various parts of the world [1–6]. Symptoms are usually mild and appear gradually. In general, the symptoms of COVID-19 are fever, dry cough, and tiredness. In addition, there are other symptoms such as chest pain and tenderness, nasal congestion, headache, conjunctivitis, diarrhea, loss of sense of taste or smell, skin rash, or discoloration of the fingers or toes [6]. The symptoms experienced are usually mild and appear gradually. Furthermore, moderate and severe infection symptoms can occur in

humans and appear gradually, such as having fever and cough accompanied by difficulty in breathing or shortness of breath, chest pain, and others [1, 6]. Individuals with previous comorbidity (such as diabetes, lung, and heart disease) are more likely to develop severe disease with stronger COVID-19 symptoms than individuals who do not have a comorbidity [7, 8]. In the case of COVID-19 comorbidity in Indonesia, 12 different diseases have been recorded, which range from the most at risk to the least at risk, namely hypertension, diabetes mellitus, heart, pregnancy, lung, kidney, immune disorders, cancer, other respiratory disorders, asthma, tuberculosis, and liver [9].

The first case in Indonesia was reported directly by President Jokowi Widodo on 2 March 2020 and there were as many as two people infected, namely a mother and child suspected of contracting it from a Japanese citizen [10]. Data from web [11], on 2 October 2020, to be precise, indicate that Indonesia was ranked 23 out of 215 countries reported being infected with 295,499 confirmed cases, 10,972 reported deaths, and 221,340 reported recoveries. Meanwhile, according to data on 14 June 2021, Indonesia was ranked 18 out of 222 countries reported being infected, with 1,919,547 confirmed cases, 53,116 reported deaths, and 1,751,234 reported recoveries.

The increasing number of COVID-19 cases requires a control strategy to control the COVID-19 outbreak. Control technique isolation and individual quarantine are the most efficient measures whenever a new outbreak occurs in a region without a vaccine or therapy [12, 13]. Several appeals or mitigations from WHO to control COVID-19 are social distancing, use of masks in public places, and intensive contact tracing (tracing) followed by quarantine of individuals who have the potential to contract the disease, and isolation of infected individuals in hospitals or independently [14]. Therefore, public education plays an important role in controlling the outbreak because it can convey information regarding how to prevent and reduce the transmission of COVID-19.

Furthermore, it is necessary to use mathematical modeling to determine the spread of COVID-19 infection and whether the control measures are effective. WHO also acknowledges that mathematical modeling can help health decision-makers (doctors or health professionals) and policymakers make decisions or find solutions (governments) [15]. The Susceptible-Infected-Removed (SIR) model is a mathematical representation of how diseases spread. The SIR model was first developed in 1927 by Kermack and McKendrick, who established it as a reference work and contributed significantly to the development of the mathematical theory of disease transmission [16, 17]. Several studies are related to the spread of disease, for example, research on the Coronavirus that caused SARS [18] and MERS [19, 20].

Soewono [21] applied the SEIR model, which has four subpopulations: susceptible (S), exposed (E), infected (I), and recovered (R), to simulate the spread of COVID-19. This model is an improvement on the SIR COVID-19 model. Furthermore, Das et al. [22] add a subpopulation of C (infected with comorbidity), so that the population is divided into five subpopulations, namely S, E, I, C, and R. The comorbidity referred to in this study is a general congenital disease, while research from Omame et al. [23] also proposed a comorbidity COVID-19 model, Omame et al. model coinfection with comorbidities (especially diabetes mellitus). So, Omame et al. built a model by dividing the population into eight subpopulations, namely susceptible (S), susceptible to comorbidity (S_c), individuals infected with COVID-19 without comorbidities (I), isolation and hospitalization for individuals infected with COVID-19 without comorbidity (H), recovered from COVID-19 but without comorbidity (R), infected with COVID-19 and comorbidity (I_c), isolation and hospitalization for those infected with COVID-19 and comorbidity (H_c), and recovered from COVID-19 but with comorbidity (R_c). In another study, Jia et al. [24] by incorporating subpopulations of isolation (H) and quarantine (Q), the model provided divides the population into seven subpopulations, namely S, E, I, A, Q, H, and R. The model is also based on the most recent data from the WHO, indicating that susceptible individuals must first be quarantined to stop the further spread. Research on COVID-19 was also conducted by Prathumwan et al. [25] by adding quarantine subpopulations (Q) and isolation (H) as well so that the model constructed has six subpopulations, namely S, E, I, Q, H, and R. The mathematical model that has been formed needs control to reduce the number of COVID-19 infections. Researchers discussing control issues include Deressa and Duress [26], Olaniyi et al. [27], and Das et al. [22]. Deressa and Duressa provide three controls, namely public education, protecting yourself from COVID-19 infection (such as wearing masks, washing hands, and maintaining distance), and treating individuals infected with COVID-19 in hospitals. In comparison, Olaniyi et al. provide two controls, public education and individual care management in hospitals. Other researchers, Das et al. [22], provide two controls to reduce the number of infected with comorbidity and without comorbidity, namely the control other than using drugs and the vaccination process. There are many studies related to COVID-19 besides those mentioned above, see for example the following literature studies [28–54].

By combining the research of Das et al. [22], Jia et al. [24], and Prathumwan et al. [25], the COVID-19 model will be constructed in this study. The discussion is divided into the following sections: The model formulation is presented in Section 2 followed by model validation and mathematical analysis in Section 3. A numerical simulation of the model without control is given in Section 4. Section 5 presents the model with controls and its simulation is given in Section 6. The last discussion on cost evaluation is presented in Section 7. The study is concluded with some key points in Section 8.

2. Model formulation

We consider the new COVID-19 model with eight subpopulations, as shown in the compartment diagram in Figure 1.

Based on the compartmental diagram in Figure 1 and the model assumptions, we have the following system of differential equations:

$$\begin{aligned}
\frac{dS}{dt} &= \pi - \frac{\beta_1 SI}{N} - \frac{\beta_2 SC}{N} - q_1 S - \mu S,\\
\frac{dE}{dt} &= \frac{\beta_1 SI}{N} + \frac{\beta_2 SC}{N} - \alpha E - \mu E,\\
\frac{dI}{dt} &= \xi\alpha E - h_1 I - r_1 I - d_1 I - \mu I,\\
\frac{dC}{dt} &= (1-\xi)\,\alpha E - h_2 C - r_2 C - d_2 C - \mu C,\\
\frac{dQ}{dt} &= q_1 S - \frac{\rho_1\beta_1 QI}{N} - \frac{\rho_2\beta_2 QC}{N} - r_3 Q - \mu Q,\\
\frac{dH}{dt} &= \theta h_1 I + \delta h_2 C + \frac{p\rho_1\beta_1 QI}{N} + \frac{q\rho_2\beta_2 QC}{N}\\
&\quad - r_4 H - d_3 H - \mu H,\\
\frac{dJ}{dt} &= (1-\theta)\,h_1 I + (1-\delta)\,h_2 C\\
&\quad + \frac{(1-p)\rho_1\beta_1 QI}{N} + \frac{(1-q)\rho_2\beta_2 QC}{N} - r_5 J - d_4 J - \mu J,\\
\frac{dR}{dt} &= r_1 I + r_2 C + r_3 Q + r_4 H + r_5 J - \mu R.
\end{aligned} \tag{1}$$

In this model, the COVID-19 model is divided into susceptible (S), exposed (E), infected without comorbidity (I), infected with comorbidity (C), isolated (Q), treatment isolated (H), isolated without treatment (J), and recovered (R). Susceptible subpopulation increases with the recruitment or birth rate denoted by π and can be infected due to contact with infected individuals without comorbidity and with comorbidity denoted by β_1 and β_2, respectively. Susceptible individuals who are quarantined are denoted by q_1 and cannot be returned to being susceptible due to the effects of public anxiety, which make some assumptions or opinions that susceptible individuals need to be quarantined, so that if quarantine is successful, then recovery is denoted by r_3 and if not successful due to contact with infected individuals without comorbidity and with comorbidity, showing symptoms of being infected, then isolation is denoted by ρ_1 and ρ_2, respectively. Furthermore, p and q are the proportion of changes from quarantine to isolation. The progression from exposed to infection is denoted α, and ξ is the proportion of change from exposed to infection without comorbidity. From the infected subpopulation without comorbidity and with comorbidity, isolation is denoted by h_1 and h_2. The parameters r_1, r_2, r_3, and r_4 indicate the recovery rate of the subpopulations infected without comorbidity, infected with comorbidity, quarantine, isolated with treatment, and isolated without treatment. Furthermore, deaths from each subpopulation are denoted by μ and deaths from COVID-19 in subpopulations I, C, H, and J are denoted by d_1, d_2, d_3, and d_4.

3. Mathematical analysis

3.1. Model validation

We calibrate our model (Equation 1) using cumulatively confirmed COVID-19 cases for Indonesia. We have retrieved COVID-19 case data from the Republic of Indonesia Task Force (SATGAS) situation report for the period 1 November 2020 to 19 May 2021 [9]. The parameter fitting uses the *lsqcurvefit* command, and the value of $MAPE = 0.026022$ is obtained. The results of the fitting parameters seem to match the infection case data as shown in Figure 2, and new parameter values are obtained according to conditions in Indonesia as follows in Table 1.

3.2. Positivity and boundedness of solutions

The change in the total population is given by

$$\begin{aligned}
\frac{dN}{dt} &= \frac{dS}{dt} + \frac{dE}{dt} + \frac{dI}{dt} + \frac{dC}{dt} + \frac{dQ}{dt} + \frac{dH}{dt} + \frac{dJ}{dt} + \frac{dR}{dt},\\
&= \pi - \mu N - d_1 I - d_2 C - d_3 H - d_4 J,\\
&\leq \pi - \mu N,
\end{aligned}$$

whose solutions give

$$N(t) \leq \frac{\pi}{\mu} + \left(N(0) - \frac{\pi}{\mu}\right) e^{-\mu t}.$$

Consequently as $t \to \infty$, then $\lim_{t\to\infty} N(t) \leq \frac{\pi}{\mu}$. So, we can conclude that N is boundedness to $N(t) \leq \frac{\pi}{\mu}$.

Considering the above solutions, we have that the model has a boundedness solution which is contained in a feasible region Ω, where

$$\Omega = \left\{(S,\, E,\, I,\, C,\, Q,\, H,\, J,\, R) \mid N(t) \leq \frac{\pi}{\mu}\right\}.$$

Next, we show the positivity of solving the Equation (1) system by following Riyapan et al. [42] and Rois et al. [46], as follows:

Theorem 1. Let S, E, I, C, Q, H, J, and R be the system solutions (Equation 1). If $S(0) \geq 0$, $E(0) \geq 0$, $I(0) \geq 0$, $C(0) \geq 0$, $Q(0) \geq 0$, $H(0) \geq 0$, $J(0) \geq 0$, and $R(0) \geq 0$, then all solutions are positive for every $t \geq 0$.

Proof. 1. Take the first equation of the system (Equation 1) as follows:

$$\frac{dS}{dt} = \pi - \frac{\beta_1 SI}{N} - \frac{\beta_2 SC}{N} - q_1 S - \mu S.$$

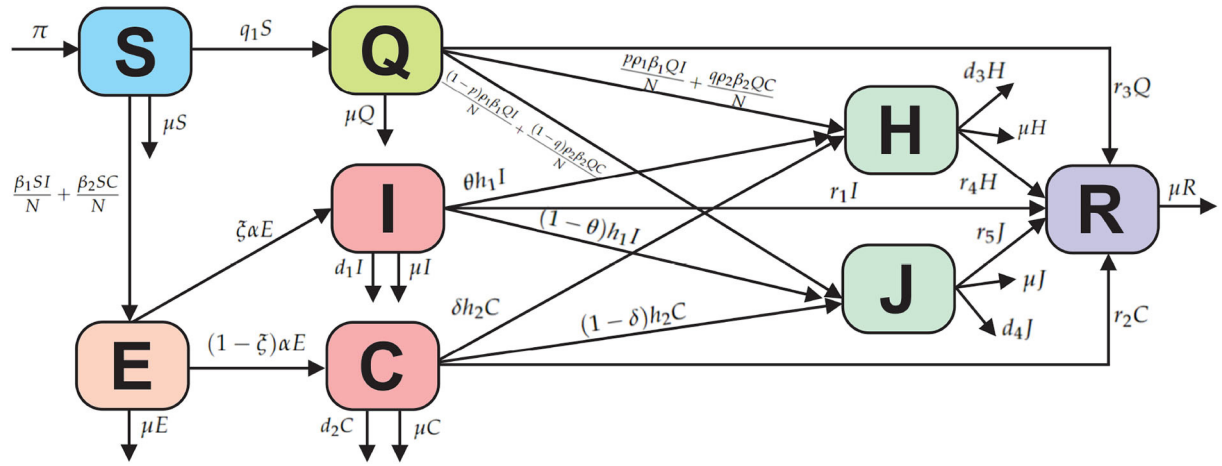

FIGURE 1
Compartmental diagram of the COVID-19 model with comorbidity.

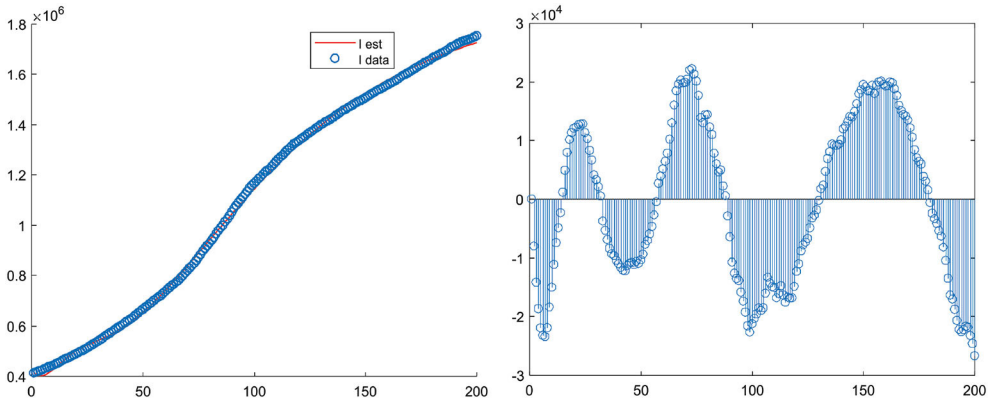

FIGURE 2
Parameter fitting results from the COVID-19 model.

TABLE 1 Parameter values according to the fitting of the infected cases of COVID-19 in Indonesia.

Parameter	Value	Parameter	Value	Parameter	Value
π	3783175.865	r_5	0.088554	δ	0.00059843
β_1	0.65799	h_1	0.007884	p	0.090862
β_2	0.79664	h_2	0.00034162	q	0.28312
q_1	0.16574	ρ_1	0.99779	d_1	0.00086579
r_1	0.0068295	ρ_2	0.9533	d_2	0.022871
r_2	0.0025349	α	0.25098	d_3	0.36203
r_3	0.030397	ξ	0.022219	d_4	0.76233
r_4	0.31851	θ	5.812×10^{-5}	μ	0.0138

Let $\eta = \frac{\beta_1 I}{N} + \frac{\beta_2 C}{N}$.

$$\begin{aligned} \frac{dS}{dt} &= \pi - S\left(\eta + q_1 + \mu\right), \\ \frac{dS}{dt} + S\left(\eta + q_1 + \mu\right) &= \pi, \\ \frac{d\left(e^{(q_1+\mu)t+\int_0^t \eta ds} S(t)\right)}{dt} &= \pi e^{(q_1+\mu)t+\int_0^t \eta ds}, \end{aligned} \tag{2}$$

then a homogeneous solution is obtained

$$\begin{aligned} \frac{d\left(e^{(q_1+\mu)t+\int_0^t \eta ds} S(t)\right)}{dt} &= 0, \\ S(t) &= k e^{-(q_1+\mu)t-\int_0^t \eta ds}. \end{aligned}$$

Thus, let us assume that the solution is non-homogeneous

$$S(t) = k e^{-(q_1+\mu)t-\int_0^t \eta ds}. \tag{3}$$

Next, substituting the Equation (3) into the Equation (2) to get

$$\begin{aligned} \frac{dk(t)}{dt} &= \pi e^{(q_1+\mu)t+\int_0^t \eta ds}, \\ k(t) &= \int_0^t \pi e^{(q_1+\mu)y+\int_0^y \eta dx} dy + K. \end{aligned} \tag{4}$$

The Equation (4) is substituted into the Equation (3), we get

$$\begin{aligned} S(t) = &\int_0^t \pi e^{(q_1+\mu)y+\int_0^y \eta\, dx} dy \times e^{-(q_1+\mu)t-\int_0^t \eta\, ds} \\ &+ S(0) e^{-(q_1+\mu)t-\int_0^t \eta\, ds}. \end{aligned}$$

So, $S(t)$ is positive for $t \geq 0$.

2. Take the fifth equation of the system (Equation 1) as follows:

$$\frac{dQ}{dt} = q_1 S - \frac{\rho_1 \beta_1 QI}{N} - \frac{\rho_2 \beta_2 QC}{N} - r_3 Q - \mu Q.$$

Let $\omega = \frac{\rho_1 \beta_1 I}{N} + \frac{\rho_2 \beta_2 C}{N}$.

$$\begin{aligned} \frac{dQ}{dt} &= q_1 S - Q(\omega + r_3 + \mu), \\ \frac{dQ}{dt} + Q(\omega + r_3 + \mu) &= q_1 S, \\ \frac{d\left(e^{(r_3+\mu)t+\int_0^t \omega ds} Q(t)\right)}{dt} &= q_1 S e^{(r_3+\mu)t+\int_0^t \omega ds}, \end{aligned} \tag{5}$$

then a homogeneous solution is obtained

$$\begin{aligned} \frac{d\left(e^{(r_3+\mu)t+\int_0^t \omega ds} Q(t)\right)}{dt} &= 0, \\ Q(t) &= k e^{-(r_3+\mu)t-\int_0^t \omega ds}. \end{aligned}$$

Thus, let us assume that the solution is non-homogeneous

$$Q(t) = k e^{-(r_3+\mu)t-\int_0^t \omega ds}. \tag{6}$$

Next, substituting the Equation (6) into the Equation (5) to get

$$\begin{aligned} \frac{dk(t)}{dt} &= q_1 S e^{(r_3+\mu)t+\int_0^t \omega ds}, \\ k(t) &= \int_0^t q_1 S e^{(r_3+\mu)y+\int_0^y \omega dx} dy + K. \end{aligned} \tag{7}$$

The the Equation (7) is substituted into the Equation (6), we get

$$\begin{aligned} Q(t) = &\int_0^t q_1 S e^{(r_3+\mu)y+\int_0^y \omega\, dx} dy \times e^{-(r_3+\mu)t-\int_0^t \omega\, ds} \\ &+ Q(0) e^{-(r_3+\mu)t-\int_0^t \omega\, ds}. \end{aligned}$$

So, $Q(t)$ is positive for $t \geq 0$.

3. Take the second equation of the system (Equation 1) as follows:

$$\frac{dE}{dt} = \frac{\beta_1 SI}{N} + \frac{\beta_2 SC}{N} - \alpha E - \mu E \geq -\alpha E - \mu E,$$

or

$$\begin{aligned} \frac{dE(t)}{dt} &\geq -E(\alpha + \mu), \\ \int \frac{dE(t)}{E} &\geq \int -(\alpha + \mu)\, dt, \\ E(t) &\geq e^{-(\alpha+\mu)t+k}, \\ E(t) &\geq E(0) e^{-(\alpha+\mu)t}. \end{aligned}$$

Thus, $E(t)$ is positive for $t \geq 0$. Furthermore, in the same way as proof number 3, $I(t)$, $C(t)$, $H(t)$, $J(t)$, and $R(t)$ can be shown respectively to be positive. □

3.3. Equilibrium point and basic reproduction number

The equilibrium point of the system (Equation 1) is obtained by setting the right-hand side to zeros. Therefore, the first equilibrium point is obtained, namely the disease-free equilibrium point, as follows:

$$\begin{aligned} X^0 &= \left(S^0, E^0, I^0, C^0, Q^0, H^0, J^0, R^0\right) \\ &= \left(\frac{\pi}{a_1}, 0, 0, 0, \frac{\pi q_1}{a_1 a_5}, 0, 0, \frac{\pi q_1 r_3}{a_1 a_5 \mu}\right). \end{aligned}$$

Where $a_1 = q_1 + \mu$ and $a_5 = r_3 + \mu$.

Furthermore, the basic reproduction number, denoted by R_0, is obtained using the next-generation matrix method

[55, 56]. The constituent components of the next-generation matrix method only consist of infected subpopulation groups, namely:

$$f = \begin{bmatrix} \frac{\beta_1 SI}{N} + \frac{\beta_2 SC}{N} \\ 0 \\ 0 \end{bmatrix}, \text{ and } v = \begin{bmatrix} a_2 E \\ -\xi\alpha E + a_3 I \\ -(1-\xi)\alpha E + a_4 C \end{bmatrix}.$$

The partial derivative evaluated at X^0 gives

$$F\left(X^0\right) = \begin{bmatrix} 0 & \frac{\beta_1 a_5 \mu}{(a_5\mu + q_1\mu + q_1 r_3)} & \frac{\beta_2 a_5 \mu}{(a_5\mu + q_1\mu + q_1 r_3)} \\ 0 & 0 & 0 \\ 0 & 0 & 0 \end{bmatrix}$$

$$\text{and } V\left(X^0\right) = \begin{bmatrix} a_2 & 0 & 0 \\ -\xi\alpha & a_3 & 0 \\ -(1-\xi)\alpha & 0 & a_4 \end{bmatrix}.$$

The inverse of the $V\left(X^0\right)$ matrix is

$$V^{-1} = \begin{bmatrix} \frac{1}{a_2} & 0 & 0 \\ \frac{\xi\alpha}{a_2 a_3} & \frac{1}{a_3} & 0 \\ \frac{(1-\xi)\alpha}{a_2 a_4} & 0 & \frac{1}{a_4} \end{bmatrix}.$$

Based on the $F\left(X^0\right)$ and $V^{-1}\left(X^0\right)$ matrices, the next-generation matrix FV^{-1} can be formed so that we can obtain

$$FV^{-1} = \begin{bmatrix} \frac{\beta_1 a_5 \mu \xi \alpha}{a_2 a_3 (a_5\mu + q_1\mu + q_1 r_3)} + \frac{\beta_2 a_5 \mu \alpha (1-\xi)}{a_2 a_4 (a_5\mu + q_1\mu + q_1 r_3)} & \frac{\beta_1 a_5 \mu}{a_3 (a_5\mu + q_1\mu + q_1 r_3)} & \frac{\beta_1 a_5 \mu}{a_4 (a_5\mu + q_1\mu + q_1 r_3)} \\ 0 & 0 & 0 \\ 0 & 0 & 0 \end{bmatrix}.$$

So, the basic reproduction number is obtained based on the eigenvalues of the FV^{-1} matrix as follows:

$$R_0 = \rho(M) = \frac{a_5 \mu \alpha (\beta_1 \xi a_4 + \beta_2 a_3 (1-\xi))}{a_2 a_3 a_4 \left(a_5\mu + q_1\mu + q_1 r_3\right)}.$$

Next, the second equilibrium point is obtained, namely the endemic equilibrium point $X^* = \left(S^*, E^*, I^*, C^*, Q^*, H^*, J^*, R^*\right)$ with

$$\begin{aligned} S^* &= \frac{\pi a_5}{A_1 R_0}, \\ E^* &= \frac{\pi}{a_2 R_0}(R_0 - 1), \\ I^* &= \frac{\pi \xi \alpha}{a_2 a_3 R_0}(R_0 - 1), \\ C^* &= \frac{(1-\xi)\pi\alpha}{a_2 a_4 R_0}(R_0 - 1), \\ Q^* &= \frac{a_2 a_3 a_4 a_5 q_1 \pi}{A_3}, \\ H^* &= (R_0 - 1) A_4, \\ J^* &= (R_0 - 1) A_5, \\ R^* &= (R_0 - 1) A_6 + \frac{r_3 a_2 a_3 a_4 a_5 q_1 \pi}{\mu A_3}, \end{aligned}$$

with $A_1 = a_5\mu + \mu q_1 + q_1 r_3$, $A_2 = \rho_1\beta_1 a_4 \mu\alpha\xi + \rho_2\beta_2 a_3 \mu\alpha(1-\xi)$, $A_3 = A_1 A_2 (R_0 - 1) + a_2 a_3 a_4 a_5 A_1 R_0$, $A_4 = \frac{\pi\alpha}{a_6 R_0}\left(\frac{\theta h_1 \xi}{a_2 a_3} + \frac{\delta h_2 (1-\xi)}{a_2 a_4} + \frac{p\rho_1\beta_1 q_1 a_4 a_5 \mu\xi}{A_3} + \frac{q\rho_2\beta_2 q_1 a_3 a_5 \mu (1-\xi)}{A_3}\right)$, $A_5 = \frac{\pi\alpha}{a_7 R_0}(\frac{(1-\theta)h_1\xi}{a_2 a_3} + \frac{(1-\delta)h_2(1-\xi)}{a_2 a_4} + \frac{(1-p)\rho_1\beta_1\mu\xi a_4 a_5 q_1}{A_3} + \frac{(1-q)\rho_2\beta_2\mu a_3 a_5 q_1 (1-\xi)}{A_3})$, and $A_6 = \frac{r_1\pi\alpha\xi}{\mu a_2 a_3 R_0} + \frac{r_2\pi\alpha(1-\xi)}{\mu a_2 a_4 R_0} + \frac{r_4 A_4}{\mu} + \frac{r_5 A_5}{\mu}$.

The existence of the endemic equilibrium point X^* depends on the value of R_0. If the value of $R_0 < 1$ is taken, then the endemic equilibrium point X^* does not exist because it is clear that E^*, I^*, C^*, H^*, and J^* are obtained negative. If $R_0 = 1$, then we get the equilibrium point $X^* = X^0$, which causes the equilibrium point X^* not to exist. Furthermore, if $R_0 > 1$, then we get S^*, E^*, I^*, C^*, Q^*, H^*, J^*, and R^* are positive and the endemic equilibrium point X^* exists.

3.4. Local stability

The local stability of the equilibrium point is obtained by linearizing system (Equation 1), which yields the following jacobian matrix below:

$$J = \begin{bmatrix} B_1 - B_2 - a_1 & B_1 & B_1 - \frac{\beta_1 S}{N} & B_1 - \frac{\beta_2 S}{N} & B_1 & B_1 & B_1 & B_1 \\ B_2 - B_1 & -B_2 - a_2 & \frac{\beta_1 S}{N} - B_1 & \frac{\beta_2 S}{N} - B_1 & -B_1 & -B_1 & -B_1 & -B_1 \\ 0 & \xi\alpha & -a_3 & 0 & 0 & 0 & 0 & 0 \\ 0 & (1-\xi)\alpha & 0 & -a_4 & 0 & 0 & 0 & 0 \\ q_1 + B_3 & B_3 & B_3 - \frac{\rho_1\beta_1 Q}{N} & B_3 - \frac{\rho_2\beta_2 Q}{N} & B_3 - B_4 - a_5 & B_3 & B_3 & B_3 \\ -B_5 & -B_5 & B_6 - B_5 & B_7 - B_5 & B_8 - B_5 & -B_5 - a_6 & -B_5 & -B_5 \\ -B_9 & -B_9 & B_{10} - B_9 & B_{11} - B_9 & B_{12} - B_9 & -B_9 & -B_9 - a_7 & -B_9 \\ 0 & 0 & r_1 & r_2 & r_3 & r_4 & r_5 & -\mu \end{bmatrix} \quad (8)$$

With $B_1 = \frac{\beta_1 SI}{N^2} + \frac{\beta_2 SC}{N^2}$, $B_2 = \frac{\beta_1 I}{N} + \frac{\beta_2 C}{N}$, $B_3 = \frac{\rho_1\beta_1 QI}{N^2} + \frac{\rho_2\beta_2 QC}{N^2}$, $\$B_4 = \frac{\rho_1\beta_1 I}{N} + \frac{\rho_2\beta_2 C}{N}$, $B_5 = \frac{p\rho_1\beta_1 QI}{N^2} + \frac{q\rho_2\beta_2 QC}{N^2}$, $B_6 =$

$\theta h_1 + \frac{p\rho_1\beta_1 Q}{N}, B_7 = \delta h_2 + \frac{q\rho_2\beta_2 Q}{N}, B_8 = \frac{p\rho_1\beta_1 I}{N} + \frac{q\rho_2\beta_2 C}{N}, B_9 = \frac{(1-p)\rho_1\beta_1 QI}{N^2} + \frac{(1-q)\rho_2\beta_2 QC}{N^2}, B_{10} = (1-\theta)\, h_1 + \frac{(1-p)\rho_1\beta_1 Q}{N}$, $B_{11} = (1-\delta)\, h_2 + \frac{(1-q)\rho_2\beta_2 Q}{N}$, and $B_{12} = \frac{(1-p)\rho_1\beta_1 I}{N} + \frac{(1-q)\rho_2\beta_2 C}{N}$.

3.4.1. Local stability of disease-free equilibrium point

Evaluating (8) at X^0 yields

$$J\left(X^0\right) = \begin{bmatrix} -a_1 & 0 & -\beta_1 C_1 & -\beta_2 C_1 & 0 & 0 & 0 & 0 \\ 0 & -a_2 & \beta_1 C_1 & \beta_2 C_1 & 0 & 0 & 0 & 0 \\ 0 & \xi\alpha & -a_3 & 0 & 0 & 0 & 0 & 0 \\ 0 & (1-\xi)\,\alpha & 0 & -a_4 & 0 & 0 & 0 & 0 \\ q_1 & 0 & -\rho_1\beta_1 C_2 & -\rho_2\beta_2 C_2 & -a_5 & 0 & 0 & 0 \\ 0 & 0 & \theta h_1 + p\rho_1\beta_1 C_2 & \delta h_2 + q\rho_2\beta_2 C_2 & 0 & -a_6 & 0 & 0 \\ 0 & 0 & (1-\theta)\, h_1 + (1-p)\,\rho_1\beta_1 C_2 & (1-\delta)\, h_2 + (1-q)\,\rho_2\beta_2 C_2 & 0 & 0 & -a_7 & 0 \\ 0 & 0 & r_1 & r_2 & r_3 & r_4 & r_5 & -\mu \end{bmatrix},$$

With $C_1 = \frac{a_5\mu}{(a_5+q_1)\mu+q_1 r_3}$ and $C_2 = \frac{q_1\mu}{(a_5+q_1)\mu+q_1 r_3}$. The characteristic equation for the $\left|J\left(X^0\right) - \lambda I\right| = 0$ is as follows:

$$(-a_1-\lambda)\,(-a_5-\lambda)\,(-a_6-\lambda)\,(-a_7-\lambda)\,(-\mu-\lambda) \begin{vmatrix} -a_2-\lambda & \beta_1 C_1 & \beta_2 C_1 \\ \xi\alpha & -a_3-\lambda & 0 \\ (1-\xi)\,\alpha & 0 & -a_4-\lambda \end{vmatrix} = 0. \tag{9}$$

Based on the Equation (9), we obtain the eigenvalues $\lambda_1 = \lambda_2 = \lambda_3 = \lambda_4 = \lambda_5 < 0$. Therefore, the stability of the disease-free equilibrium point depends on

$$M_1 = \begin{vmatrix} -a_2-\lambda & \beta_1 C_1 & \beta_2 C_1 \\ \xi\alpha & -a_3-\lambda & 0 \\ (1-\xi)\,\alpha & 0 & -a_4-\lambda \end{vmatrix}. \tag{10}$$

From the Equation (10), we obtain the following characteristic equation:

$$\lambda^3 + k_1\lambda^2 + k_2\lambda + k_3 = 0, \tag{11}$$

with

$$k_1 = a_2 + a_3 + a_4,$$
$$k_2 = a_2a_3\,(1-R_0) + a_2a_4\,(1-R_0) + a_3a_4 + \frac{a_4\beta_1\alpha C_1\xi}{a_3} + \frac{a_3\beta_2\alpha C_1\,(1-\xi)}{a_4}, \text{ and}$$
$$k_3 = a_2a_3a_4\,(1-R_0).$$

In the Equation (11), it is clear that $k_1 > 0$, and if $R_0 < 1$, then $k_2 > 0$ and $k_3 > 0$. Therefore, the stability property of the equilibrium point X^0 is established using the Routh–Hurwitz criterion. Furthermore, the equilibrium point X^0 is asymptotically stable if and only if it satisfies the following criteria:

1. $k_1 > 0$,
2. $k_3 > 0$, and
3. $k_1k_2 - k_3 > 0$.

Criteria Equations (1) and (2) have been met so that the disease-free equilibrium point X^0 is locally asymptotically stable if it meets $k_1k_2 - k_3 > 0$ where

$$k_1k_2 - k_3 > 0,$$
$$(a_2+a_3+a_4)\left(a_2a_4\,(1-R_0) + a_3a_4 + \frac{a_4\beta_1\alpha C_1\xi}{a_3} + \frac{a_3\beta_2\alpha C_1\,(1-\xi)}{a_4}\right)$$
$$+a_2^2a_3\,(1-R_0) + a_2a_3^2\,(1-R_0) > 0.$$

It is clear that the Routh–Hurwitz criteria are satisfied; thus, the roots of the characteristic Equation (11) have negative real parts. Therefore, the disease-free equilibrium point is asymptotically locally stable if $R_0 < 1$.

3.4.2. Local stability of the endemic equilibrium point

Evaluating (8) at X^* yields

$$J\left(X^*\right) = \begin{bmatrix} B_1 - B_{13} & B_1 & B_1 - \frac{\beta_1 S^*}{N} & B_1 - \frac{\beta_2 S^*}{N} & B_1 & B_1 & B_1 & B_1 \\ B_2 - B_1 & -B_{14} & \frac{\beta_1 S^*}{N} - B_1 & \frac{\beta_2 S^*}{N} - B_1 & -B_1 & -B_1 & -B_1 & -B_1 \\ 0 & \xi\alpha & -a_3 & 0 & 0 & 0 & 0 & 0 \\ 0 & (1-\xi)\,\alpha & 0 & -a_4 & 0 & 0 & 0 & 0 \\ q_1 + B_3 & B_3 & B_3 - \frac{\rho_1\beta_1 Q^*}{N} & B_3 - \frac{\rho_2\beta_2 Q^*}{N} & B_3 - B_{15} & B_3 & B_3 & B_3 \\ -B_5 & -B_5 & B_6 - B_5 & B_7 - B_5 & B_8 - B_5 & -B_{16} & -B_5 & -B_5 \\ -B_9 & -B_9 & B_{10} - B_9 & B_{11} - B_9 & B_{12} - B_9 & -B_9 & -B_{17} & -B_9 \\ 0 & 0 & r_1 & r_2 & r_3 & r_4 & r_5 & -\mu \end{bmatrix},$$

With $B_1 = \frac{\beta_1 S^* I^*}{N^2} + \frac{\beta_2 S^* C^*}{N^2}$, $B_2 = \frac{\beta_1 I^*}{N} + \frac{\beta_2 C^*}{N}$, $B_3 = \frac{\rho_1\beta_1 Q^* I^*}{N^2} + \frac{\rho_2\beta_2 Q^* C^*}{N^2}$, $B_4 = \frac{\rho_1\beta_1 I^*}{N} + \frac{\rho_2\beta_2 C^*}{N}$, $B_5 = \frac{p\rho_1\beta_1 Q^* I^*}{N^2} + \frac{q\rho_2\beta_2 Q^* C^*}{N^2}$, $B_6 = \theta h_1 + \frac{p\rho_1\beta_1 Q^*}{N}$, $B_7 = \delta h_2 + \frac{q\rho_2\beta_2 Q^*}{N}$, $B_8 = \frac{p\rho_1\beta_1 I^*}{N} + \frac{q\rho_2\beta_2 C^*}{N}$, $B_9 = \frac{(1-p)\rho_1\beta_1 Q^* I^*}{N^2} +$

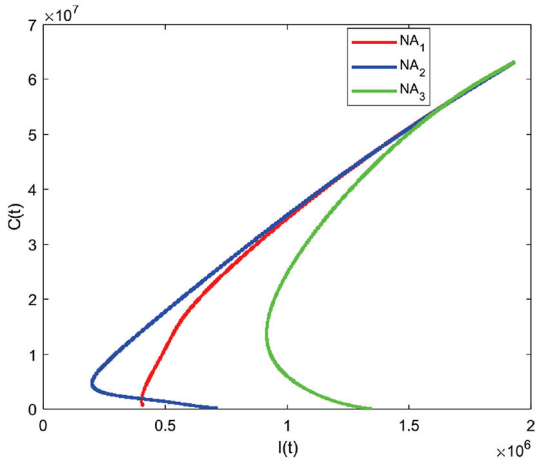

FIGURE 3
Projection of three orbits of the model on the $I - C$ plane.

$\frac{(1-q)\rho_2\beta_2 Q^* C^*}{N^2}$, $B_{10} = (1-\theta)h_1 + \frac{(1-p)\rho_1\beta_1 Q^*}{N}$, $B_{11} = (1-\delta)h_2 + \frac{(1-q)\rho_2\beta_2 Q^*}{N}$, $B_{12} = \frac{(1-p)\rho_1\beta_1 I}{N} + \frac{(1-q)\rho_2\beta_2 C}{N}$, $B_{13} = B_2 + a_1, B_{14} = B_2 + a_2, B_{15} = B_4 + a_5, B_{16} = B_5 + a_6$, and $B_{17} = B_9 + a_7$.

The characteristic equation of the $|J(X^*) - \lambda I| = 0$ is

$$\lambda^8 + k_1\lambda^7 + k_2\lambda^6 + k_3\lambda^5 + k_4\lambda^4 + k_5\lambda^3 + k_6\lambda^2 + k_7\lambda + k_8 = 0, \tag{12}$$

It is difficult to prove analytically that all eigenvalues of J have negative real parts for $R_0 > 1$. However, from our numerical simulations (case $R_0 > 1$), all eigenvalues have negative real parts.

Figure 3 gives the projection of three orbits of three different initial conditions when $R_0 > 1$ on the $I - C$ plane. The component (I, C) of the equilibrium X^* is not $(0, 0)$. This simulation indicates that the endemic equilibrium X^* is locally asymptotically stable when $R_0 > 1$.

3.5. Global stability analysis

In this study, we prove the global stability of disease-free and endemic equilibrium points by constructing the suitable Lyapunov function and following the theorem from Alligood et al. [57].

3.5.1. Global stability of the disease-free equilibrium point

Theorem 2. Disease-free equilibrium point X^0 is globally asymptotically stable if $R_0 < 1$ and unstable if $R_0 > 1$.

Proof. Defined Lyapunov function

$$L = \kappa_1 E + \kappa_2 I + \kappa_3 C, \tag{13}$$

where

$$\begin{aligned} \kappa_1 &= a_1 a_2 a_3 a_4, \\ \kappa_2 &= \frac{\pi\beta_1 a_2 a_4}{N}, \text{ and} \\ \kappa_3 &= \frac{\pi\beta_2 a_2 a_3}{N}. \end{aligned}$$

The function L needs to be proven to determine whether Lyapunov is strong or weak for X^0.

$$\begin{aligned} L\left(\overrightarrow{x}^*\right) &= L\left(S^0, E^0, I^0, C^0, Q^0, H^0, J^0, R^0\right), \\ L\left(\overrightarrow{x}^*\right) &= \kappa_1 E^0 + \kappa_2 I^0 + \kappa_3 C^0 = 0. \end{aligned}$$

It is proven that $L\left(\overrightarrow{x}^*\right) = 0$. Next,

$$L\left(\overrightarrow{x}\right) = \kappa_1 E + \kappa_2 I + \kappa_3 C,$$

Because $\forall (S, E, I, C, Q, H, J, R) \neq (S^0, E^0, I^0, C^0, Q^0, H^0, J^0, R^0)$, so it is proved that $L\left(\overrightarrow{x}\right) > 0$.

Thus, the Equation (13) can be reduced to

$$\begin{aligned} \frac{\partial L}{\partial t} &= \kappa_1 \frac{dE}{dt} + \kappa_2 \frac{dI}{dt} + \kappa_3 \frac{dC}{dt} \\ &= \kappa_1 \left(\frac{\beta_1 SI + \beta_2 SC}{N} - a_2 E\right) \\ &\quad + \kappa_2 (\xi\alpha E - a_3 I) + \kappa_3 ((1-\xi)\alpha E - a_4 C), \end{aligned}$$

so, we obtain

$$\begin{aligned} &= a_1 a_2 a_3 a_4 \left(\frac{\beta_1 SI + \beta_2 SC}{N} - a_2 E + \frac{\pi\beta_1 a_2 a_4 \xi\alpha E}{a_1 a_2 a_3 a_4 N}\right. \\ &\left. + \frac{\pi\beta_2 a_2 a_3 (1-\xi)\alpha E}{a_1 a_2 a_3 a_4 N} - \frac{\pi\beta_1 I}{a_1 N} - \frac{\pi\beta_2 C}{a_1 N}\right). \end{aligned}$$

Let $S = \frac{\pi}{a_1}$, so we get

$$\frac{\partial L}{\partial t} = a_1 a_2^2 a_3 a_4 E (R_0 - 1).$$

Based on the description above, it can be concluded that $\frac{\partial L}{\partial t} < 0$ if $R_0 < 1$ and $\frac{\partial L}{\partial t} = 0$ if $E = 0$. Hence, by Lasalle's invariance principle, the disease-free equilibrium point in the spread of COVID-19 (X^0) is globally asymptotically stable if $R_0 < 1$. □

3.5.2. Global stability of the endemic equilibrium point

Theorem 3. If $R_0 > 1$, then the endemic equilibrium point X^* is said to be globally asymptotically stable.

TABLE 2 Stability conditions.

Equilibrium point	Existence requirement	Global stability type	Stability condition
X^0	None	Asymptotically stable	$R_0 < 1$
X^*	$R_0 > 1$	Asymptotically stable	$R_0 > 1$ and strong Lyapunov function

Proof. The Lyapunov function is defined as follows:

$$L = \frac{1}{2}\left[S_S + E_E + I_I + C_C + Q_Q + H_H + J_J + R_R\right]^2, \quad (14)$$

Where $S_S = \left(S - S^*\right)$, $E_E = \left(E - E^*\right)$, $I_I = \left(I - I^*\right)$, $C_C = \left(C - C^*\right)$, $Q_Q = \left(Q - Q^*\right)$, $H_H = \left(H - H^*\right)$, $J_J = \left(J - J^*\right)$, and dan $R_R = \left(R - R^*\right)$.

The function L needs to be proven to determine whether the Lyapunov function is strong or weak for X^*.

$$\begin{aligned} L\left(\overrightarrow{x}^*\right) &= L\left(S^*, E^*, I^*, C^*, Q^*, H^*, J^*, R^*\right), \\ L\left(\overrightarrow{x}^*\right) &= \frac{1}{2}\left[S_S^* + E_E^* + I_I^* + C_C^* + Q_Q^* + H_H^* + J_J^* + R_R^*\right]^2 \\ &= 0. \end{aligned}$$

Where $S_S^* = \left(S^* - S^*\right)$, $E_E^* = \left(E^* - E^*\right)$, $I_I^* = \left(I^* - I^*\right)$, $C_C^* = \left(C^* - C^*\right)$, $Q_Q^* = \left(Q^* - Q^*\right)$, $H_H^* = \left(H^* - H^*\right)$, $J_J^* = \left(J^* - J^*\right)$, and $R_R^* = \left(R^* - R^*\right)$. It is proven that $L\left(\overrightarrow{x}^*\right) = 0$.

Next,

$$L\left(\overrightarrow{x}\right) = \frac{1}{2}\left[S_S + E_E + I_I + C_C + Q_Q + H_H + J_J + R_R\right]^2.$$

Because $\forall\,(S, E, I, C, Q, H, J, R) \neq \left(S^0, E^0, I^0, C^0, Q^0, H^0, J^0, R^0\right)$, so that it is proven that $L\left(\overrightarrow{x}\right) > 0$. Next, we check that the Equation (14) is reduced to

$$\begin{aligned} \frac{\partial L}{\partial t} &= \left[S_S + E_E + I_I + C_C + Q_Q + H_H + J_J + R_R\right] \\ &\quad \frac{d}{dt}\left[S + E + I + C + Q + H + J + R\right], \\ &= \left[S_S + E_E + I_I + C_C + Q_Q + H_H + J_J + R_R\right] \\ &\quad [\pi - \mu\left(S + E + I + C + Q + H + J + R\right) \\ &\quad -d_1 I - d_2 C - d_3 H - d_4 J], \end{aligned}$$

Let $\pi = \mu\left(S^* + E^* + I^* + C^* + Q^* + H^* + J^* + R^*\right) + d_1 I^* + d_2 C^* + d_3 H^* + d_4 J^*$. So that it gives

$$\begin{aligned} &= \left[S_S + E_E + I_I + C_C + Q_Q + H_H + J_J + R_R\right] \\ &\times[-\left[\mu(S_S + E_E + I_I + C_C + Q_Q + H_H + J_J + R_R) + d_1\left(I - I^*\right)\right. \\ &\left.+d_2\left(C - C^*\right) + d_3\left(H - H^*\right) + d_4\left(J - J^*\right)\right]], \\ &= -\left[S_S + E_E + I_I + C_C + Q_Q + H_H + J_J + R_R\right] \\ &\times\left[\mu(S_S + E_E + I_I + C_C + Q_Q + H_H + J_J + R_R) + d_1\left(I - I^*\right)\right. \\ &\left.+d_2\left(C - C^*\right) + d_3\left(H - H^*\right) + d_4\left(J - J^*\right)\right]]. \end{aligned}$$

Based on the description above, it can be concluded that $\frac{\partial L}{\partial t} < 0$ if $R_0 > 1$ and $\frac{\partial L}{\partial t} = 0$ if $S = S^*$, $E = E^*$, $I = I^*$, $C = C^*$, $Q = Q^*$, $H = H^*$, $J = J^*$, and $R = R^*$. Hence, by Lasalle's invariance principle, it means that the endemic equilibrium point in the spread of COVID-19 $\left(X^*\right)$ is globally asymptotically stable if $R_0 > 1$. □

The terms of existence and the type of stability of the equilibrium point of the system of equations are summarized in Table 2.

3.6. Sensitivity analysis

The sensitivity analysis aims to determine the parameters that cause the spread of the COVID-19 virus. The sensitivity index of the basic reproduction number depends on the differentiation of the parameters contained in the basic reproduction number [58, 59]. Sensitivity index R_0 to the parameters is as follows:

$$\begin{aligned} I_\alpha^{R_0} &= \frac{\partial R_0}{\partial \alpha}\frac{\alpha}{R_0} = \frac{\mu}{\alpha + \mu}, \\ I_{\beta_1}^{R_0} &= \frac{\partial R_0}{\partial \beta_1}\frac{\beta_1}{R_0} = \frac{\beta_1 \xi a_4}{\beta_1 \xi a_4 + \beta_2 a_3\left(1 - \xi\right)}, \\ I_{\beta_2}^{R_0} &= \frac{\partial R_0}{\partial \beta_2}\frac{\beta_2}{R_0} = \frac{\beta_2 a_3\left(1 - \xi\right)}{\beta_1 \xi a_4 + \beta_2 a_3\left(1 - \xi\right)}, \\ I_\xi^{R_0} &= \frac{\partial R_0}{\partial \xi}\frac{\xi}{R_0} = \frac{\beta_1 \xi a_4 - \beta_2 \xi a_3}{\beta_1 \xi a_4 + \beta_2 a_3\left(1 - \xi\right)}, \\ I_{q_1}^{R_0} &= \frac{\partial R_0}{\partial q_1}\frac{q_1}{R_0} = -\frac{q_1}{q_1 + \mu}, \\ I_{h_1}^{R_0} &= \frac{\partial R_0}{\partial h_1}\frac{h_1}{R_0} = \frac{a_4 \beta_1 h_1 \xi}{-a_3\left(\beta_2 a_3\left(1 - \xi\right) + \beta_1 a_4 \xi\right)}, \\ I_{r_1}^{R_0} &= \frac{\partial R_0}{\partial r_1}\frac{r_1}{R_0} = \frac{\beta_1 r_1 a_4 \xi}{-a_3\left(\beta_2 a_3\left(1 - \xi\right) + \beta_1 a_4 \xi\right)}, \\ I_{d_1}^{R_0} &= \frac{\partial R_0}{\partial d_1}\frac{d_1}{R_0} = \frac{\beta_1 d_1 a_4 \xi}{-a_3\left(\beta_2 a_3\left(1 - \xi\right) + \beta_1 a_4 \xi\right)}, \\ I_{h_2}^{R_0} &= \frac{\partial R_0}{\partial h_2}\frac{h_2}{R_0} = \frac{\beta_2 h_2 a_3\left(1 - \xi\right)}{-a_4\left(\beta_2 a_3\left(1 - \xi\right) + \beta_1 a_4 \xi\right)}, \\ I_{r_2}^{R_0} &= \frac{\partial R_0}{\partial r_2}\frac{r_2}{R_0} = \frac{\beta_2 r_2 a_3\left(1 - \xi\right)}{-a_4\left(\beta_2 a_3\left(1 - \xi\right) + \beta_1 a_4 \xi\right)}, \\ I_{d_2}^{R_0} &= \frac{\partial R_0}{\partial d_2}\frac{d_2}{R_0} = \frac{\beta_2 r_2 a_3\left(1 - \xi\right)}{-a_4\left(\beta_2 a_3\left(1 - \xi\right) + \beta_1 a_4 \xi\right)}, \end{aligned}$$

TABLE 3 Sensitivity analysis.

No	Parameter	Sensitivity index
1	q_1	−0.9761
2	β_2	0.9754
3	μ	0.5715
4	d_2	−0.5636
5	r_2	−0.0625
6	α	0.0522
7	β_1	0.0246
8	h_2	−0.0084
9	h_1	−0.0066
10	r_1	−0.0057
11	ξ	0.0025
12	d_1	−0.0007

Next, the graph of the solution $R_0 < 1$ is obtained in Figure 4.

The analysis results from 3.4.1, and Theorem 2 are illustrated numerically. Numerical simulations with some initial values show that the graph solution is toward and close to the disease-free equilibrium point X^0 (converging toward the disease-free equilibrium point X_0). Based on the graph, this means that after all this time, no individual has been infected with COVID-19. The numerical results support the analysis that if $R_0 < 1$, then the disease-free equilibrium point X^0 is asymptotically stable locally and globally given different initial values.

We show the stability of the endemic equilibrium point, the parameter values in Table 1 are used, and three different values, so we get $R_0 = 1.47 > 1$. Similarly, the disease-free equilibrium point is obtained

$$X^0 = (21071493,\ 0,\ 0,\ 0,\ 79018695,\ 0,\ 0,\ 174052991)$$

and the endemic equilibrium point is given as

$$I_\mu^{R_0} = \frac{\partial R_0}{\partial \mu}\frac{\mu}{R_0} = \frac{-\left(\alpha\left(\left(-2\xi+2\right)\beta_2 + 2\beta_1\xi\right)\mu^5 + a_8\left(1-\xi\right)\beta_2 + \beta_1 a_9\xi\right)\mu^4 + 2a_{10}\left(\left(1-\xi\right)a_3\beta_2 + \beta_1\xi a_4\right)\mu^3}{a_1^2a_2^2a_3^2a_4^2}$$
$$- \frac{\left(\left(\left(-a_{12}\right)q_1 + a_{11}^2\right)\alpha + a_{11}^2\left(a_{12}+q_1\right)\left(\xi-1\right)\beta_2 - \left(\left(\left(a_{11}\right)q_1 - a_{12}^2\right)\alpha - a_{12}^2\left(a_{11}+q_1\right)\right)\beta_1\xi\right)\mu^2}{a_1^2a_2^2a_3^2a_4^2}$$
$$- \frac{2\left(a_{11}\alpha q_1\left(\beta_1\xi + \beta_2\left(1-\xi\right)\right)a_{11}\mu + a_{12}\alpha\left(\left(\xi-1\right)a_{11}\beta_2 - \beta_1\xi a_{12}\right)q_1a_{11}\right)}{a_1^2a_2^2a_3^2a_4^2},$$

With $a_8 = \left(4d_1 + \alpha + d_2 + h_1 + h_2 + q_1 + 4r_1 + r_2\right)$, $a_9 = d_1 + \alpha + 4d_2 + h_1 + 4h_2 + q_1 + r_1 + 4r_2$, $a_{10} = \left(d_1 + \alpha + d_2 + h_1 + h_2 + q_1 + r_1 + r_2\right)$, $a_{11} = h_1 + r_1 + d_1$, and $a_{12} = h_2 + r_2 + d_2$.

The parameter sensitivity index is shown in Table 3.

From Table 3, we can see that the most sensitive parameters are q_1 and β_2. A positive index means that if we reduce the parameter by almost 10%, then the value of the basic reproduction number can decrease by 10%.

4. Simulation of the model without control

This section presents a numerical solution of system (1) using the Fourth-order Runge–Kutta method. The parameter values used in this simulation are shown in Table 1 and three different initial values. In this simulation, the stability of the disease-free equilibrium point is shown from the parameter values given in Table 1, except for the parameter $q_1 = 0.56574$, the value is $R_0 = 0.456 < 1$. Based on the value of these parameters, the disease-free equilibrium point is obtained, namely

$X^0 = (6527542,\ 0,\ 0,\ 0,\ 83496205,\ 0,\ 0,\ 183499868)$.

$$X^* = \left(S^*,\ E^*,\ I^*,\ C^*,\ Q^*,\ H^*,\ J^*,\ R^*\right),$$
$$= (6031017,\ 10196616,\ 1933377,\ 63222893,$$
$$2119885,\ 362896,\ 798735,\ 30671327).$$

The solution graph for the case of $R_0 > 1$ is obtained as follows in Figure 5.

The numerical simulation results support the analysis from 3.4.2 and Theorem 3 that some of the initial values given are obtained by the graph of the solution leading to the endemic equilibrium point X^* (converging to the endemic equilibrium point X^*), which means there is a spread of disease due to COVID-19. The numerical simulation results follow the analysis that if $R_0 > 1$, the endemic equilibrium point X^* is asymptotically stable locally and globally with different initial values. Based on the given parameter values, we obtain $R_0 > 1$. This means that there is an outbreak of disease due to COVID-19. Therefore, it is necessary to take control measures to reduce the outbreak.

4.1. Effect parameters

The effect of parameters on R_0 was analyzed using contour plots. We choose two significant parameters, q_1

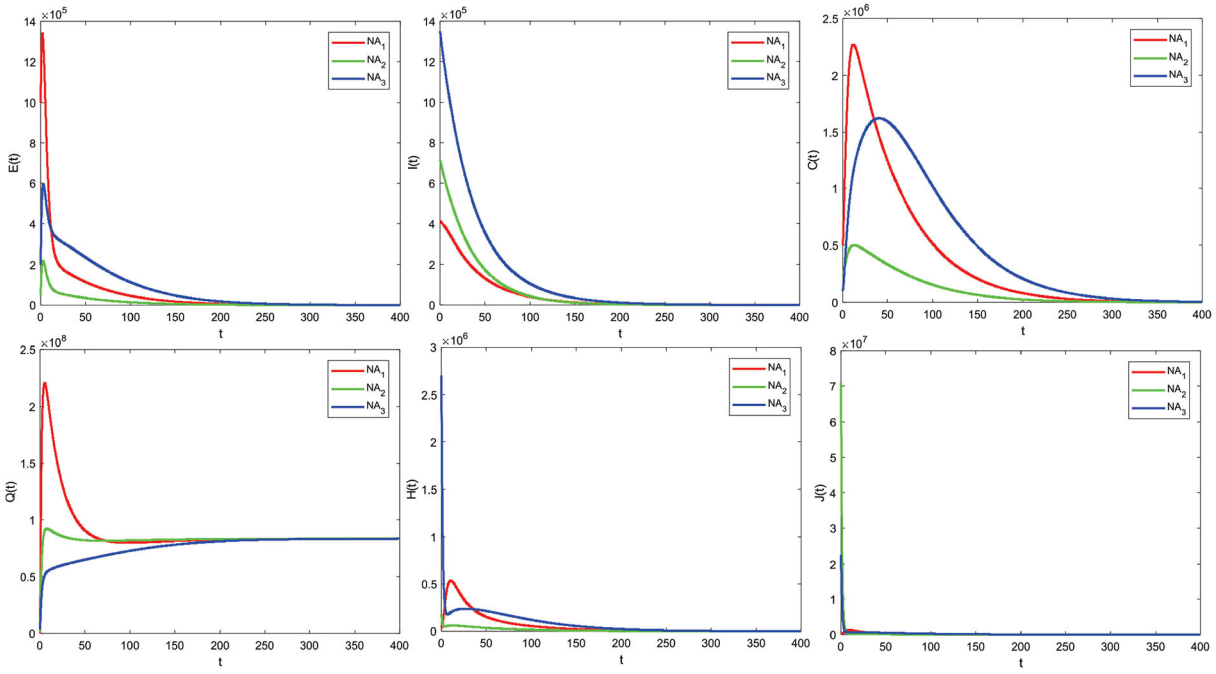

FIGURE 4
COVID-19 model solution graph for $R_0 < 1$.

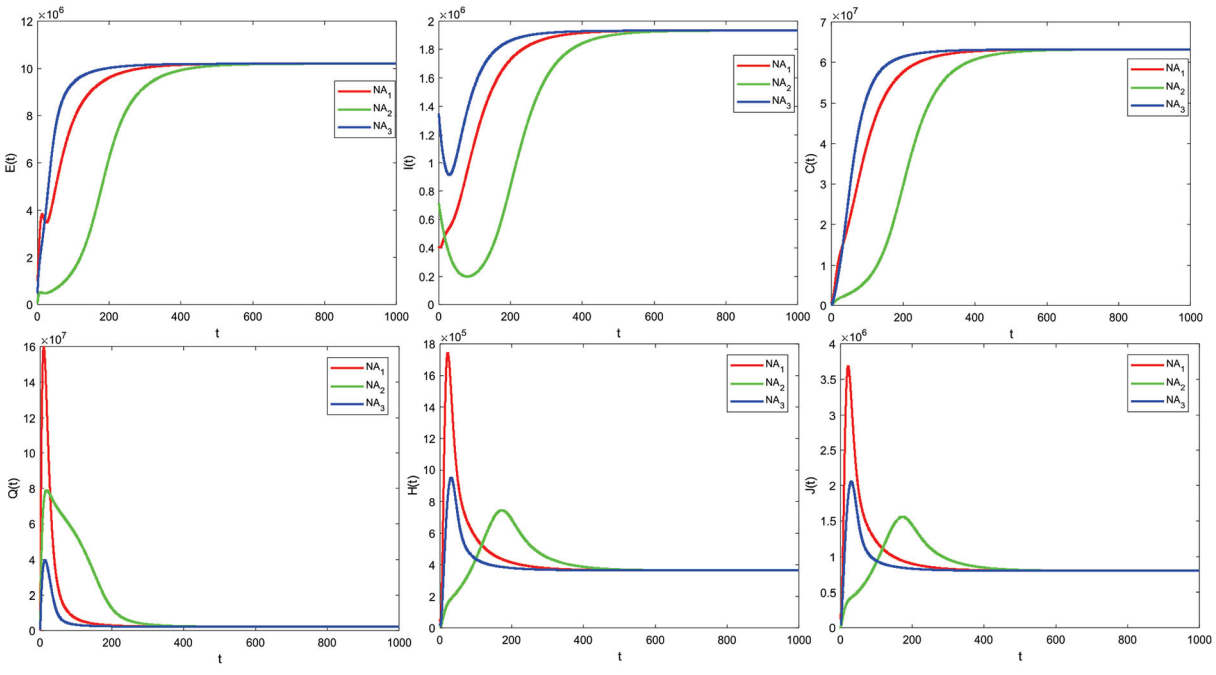

FIGURE 5
The COVID-19 model solution graph for $R_0 > 1$.

and β_2, and provide a contour plot as a function of R_0. The impact of some R_0 parameters is further investigated in Figure 6. Figure 6 shows that increasing the parameter q_1 decreases the value of R_0. This implies that increasing quarantines has the effect of reducing the spread of COVID-19. Meanwhile, an increase in the β_2 parameter resulted in an increase in the R_0 value and implied that an increase in contacts of individuals with comorbidities would increase the spread of COVID-19, especially individuals with comorbidities. Therefore, increasing quarantine and reducing contact with individuals with comorbidities are important.

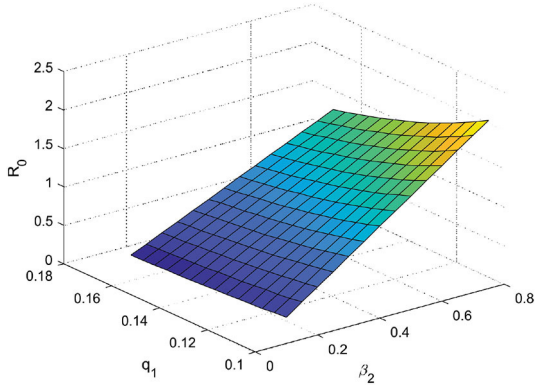

FIGURE 6
Effect parameters of R_0
($\beta_2 \times q_1 \in [0.1 : 0.79664] \times [0.1 : 0.16574]$).

5. Optimal control problem

5.1. Comorbidity COVID-19 model with optimal control

The control variable given to the COVID-19 model consists of preventive measures through education (u_1) and individual treatment efforts for infected (u_2) . So the model with control is given as follows:

$$\begin{aligned}
\frac{dS}{dt} &= \pi - (1-u_1)\frac{(\beta_1 SI + \beta_2 SC)}{N} - q_1 S - \mu S,\\
\frac{dE}{dt} &= (1-u_1)\frac{(\beta_1 SI + \beta_2 SC)}{N} - \alpha E - \mu E,\\
\frac{dI}{dt} &= \xi\alpha E - (h_1+u_2) I - r_1 I - d_1 I - \mu I,\\
\frac{dC}{dt} &= (1-\xi)\alpha E - (h_2+u_2) C - r_2 C - d_2 C - \mu C,\\
\frac{dQ}{dt} &= q_1 S - \frac{\rho_1\beta_1 QI}{N} - \frac{\rho_2\beta_2 QC}{N} - r_3 Q - \mu Q,\\
\frac{dH}{dt} &= (\theta h_1 + u_2) I + \frac{p\rho_1\beta_1 QI}{N}\\
&+ \frac{q\rho_2\beta_2 QC}{N} + (\delta h_2 + u_2) C - r_4 H - d_3 H - \mu H,\\
\frac{dJ}{dt} &= ((1-\theta)h_1 + u_2) I\\
&+ ((1-\delta)h_2 + u_2) C + \frac{(1-p)\rho_1\beta_1 QI}{N}\\
&+ \frac{(1-q)\rho_2\beta_2 QC}{N} - a_7 J,\\
\frac{dR}{dt} &= r_1 I + r_2 C + r_3 Q + r_4 H + r_5 J - \mu R.
\end{aligned} \tag{15}$$

The function that minimizes the number of infected cases without comorbidity (I) and the number of infected cases with comorbidity (C) over a time interval $[0, T]$ can be defined as

$$J(u_1, u_2) = \int_0^T \left(I(t) + C(t) + \frac{1}{2}(A_1 u_1^2 + A_2 u_2^2) \right), \tag{16}$$

Where A_1 and A_2 are the relative cost associated with the controls u_1 and u_2, and T is the final time. The aim of the control is to minimize the cost function.

$$J(u_1^*, u_2^*) = \min J(u_1, u_2),$$

Subject to the system (Equation 15), where $0 \le (u_1, u_2) \le 1$ and $t \in (0, T)$.

5.2. Optimal control analysis

The Hamilton function can be defined as follows:

$$\begin{aligned}
\mathcal{H} &= I + C + \frac{1}{2}\left(A_1 u_1^2 + A_2 u_2^2\right)\\
&+\lambda_1 \left(\pi - (1-u_1)\frac{(\beta_1 SI + \beta_2 SC)}{N} - q_1 S - \mu S \right)\\
&+\lambda_2 \left((1-u_1)\frac{(\beta_1 SI + \beta_2 SC)}{N} - \alpha E - \mu E \right)\\
&+\lambda_3 \left(\xi\alpha E - (h_1+u_2) I - r_1 I - d_1 I - \mu I \right)\\
&+\lambda_4 \left((1-\xi)\alpha E - (h_2+u_2) C - r_2 C - d_2 C - \mu C \right)\\
&+\lambda_5 \left(q_1 S - \frac{\rho_1\beta_1 QI}{N} - \frac{\rho_2\beta_2 QC}{N} - r_3 Q - \mu Q \right)\\
&+\lambda_6 \left((\theta h_1 + u_2) I + \frac{p\rho_1\beta_1 QI}{N} \right.\\
&\left. + \frac{q\rho_2\beta_2 QC}{N} + (\delta h_2 + u_2) C - r_4 H - d_3 H - \mu H \right)\\
&+\lambda_7 \left(((1-\theta)h_1 + u_2) I + ((1-\delta)h_2 + u_2) C \right.\\
&\left. + \frac{(1-p)\rho_1\beta_1 QI}{N} + \frac{(1-q)\rho_2\beta_2 QC}{N} - a_7 J \right)\\
&+\lambda_8 \left(r_1 I + r_2 C + r_3 Q + r_4 H + r_5 J - \mu R \right).
\end{aligned} \tag{17}$$

Based on Pontryagin's principle, the Hamilton function will reach an optimal solution if it satisfies the state equation

and the costate equation, and the condition is stationary. The equation state is obtained by deriving the Hamilton function (Equation 17) for each variable costate as Equation (15). Next, the equation costate is the negative value of the derivative of the Hamilton function (Equation 17) for each variable state as follows:

$$
\begin{aligned}
&\frac{d\lambda_1}{dt} = -\frac{\partial H}{\partial S} = (\lambda_1 - \lambda_2) \\
&\left(\frac{(1-u_1)(\beta_1 I + \beta_2 C)}{N} + \frac{(1-u_1)(\beta_1 SI + \beta_2 SC)}{N^2}\right) \\
&+q_1(\lambda_1 - \lambda_5) + \lambda_1 \mu \\
&+\frac{\rho_1 \beta_1 QI}{N^2}\left(p\lambda_6 + (1-p)\lambda_7 - \lambda_5\right) \\
&+\frac{\rho_2 \beta_2 QC}{N^2}\left(q\lambda_6 + (1-q)\lambda_7 - \lambda_5\right), \\
&\frac{d\lambda_2}{dt} = -\frac{\partial H}{\partial E} = (\lambda_2 - \lambda_1)\frac{(1-u_1)(CS\beta_2 + IS\beta_1)}{N^2} \\
&+\lambda_2\alpha + \lambda_2\mu - \lambda_3\alpha\xi - \lambda_4\alpha(1-\xi) \\
&+\frac{\rho_1 \beta_1 QI}{N^2}\left(\lambda_6 p + (1-p)\lambda_7 - \lambda_5\right) + \frac{\rho_2 \beta_2 QC}{N^2} \\
&\left(\lambda_6 q + (1-q)\lambda_7 - \lambda_5\right), \\
&\frac{d\lambda_3}{dt} = -\frac{\partial H}{\partial I} = (\lambda_1 - \lambda_2)\left(\frac{(1-u_1)S\beta_1}{N} - \frac{(1-u_1)S\beta_1}{N}\right) \\
&+h_1(\lambda_3 - \theta\lambda_6 - (1-\theta)\lambda_7) \\
&+u_2(\lambda_3 - \lambda_6 - \lambda_7) + r_1(\lambda_3 - \lambda_8) - \lambda_3(-d_1 - \mu) \\
&+\frac{\rho_1 \beta_1 Q}{N}\left(\lambda_5 - \lambda_6 p - \lambda_7(1-p)\right) - 1, \qquad (18) \\
&\frac{d\lambda_4}{dt} = -\frac{\partial H}{\partial C} \\
&= (\lambda_2 - \lambda_1)\left(-\frac{(1-u_1)S\beta_2}{N} + \frac{(1-u_1)(CS\beta_2 + IS\beta_1)}{N^2}\right) \\
&+h_2(\lambda_4 - \lambda_6\delta - \lambda_7(1-\delta)) \\
&+r_2(\lambda_4 - \lambda_8) + u_2(\lambda_4 - \lambda_6 - \lambda_7) - \lambda_4(-d_2 - \mu) \\
&+\frac{\rho_1 \beta_1 QI}{N^2}\left(-\lambda_5 + \lambda_6 p + \lambda_7(1-p)\right) \\
&+\left(\frac{\rho_2 \beta_2 Q}{N} - \frac{\rho_2 \beta_2 QC}{N^2}\right)\left(\lambda_5 - \lambda_6 q - \lambda_7(1-q)\right) - 1, \\
&\frac{d\lambda_5}{dt} = -\frac{\partial H}{\partial Q} = (\lambda_2 - \lambda_1)\left(\frac{(1-u_1)(CS\beta_2 + IS\beta_1)}{N^2}\right) \\
&+r_3(\lambda_5 - \lambda_8) \\
&+\left(\frac{\rho_1 \beta_1 I}{N} - \frac{\rho_1 \beta_1 QI}{N^2}\right)\left(\lambda_5 - p\lambda_6 - (1-p)\lambda_7\right) \\
&+\left(\frac{\rho_2 \beta_2 C}{N} - \frac{\rho_2 \beta_2 QC}{N^2}\right)\left(\lambda_5 - \lambda_6 q - \lambda_7(1-q)\right) + \lambda_5\mu, \\
&\frac{d\lambda_6}{dt} = -\frac{\partial H}{\partial H} = (\lambda_2 - \lambda_1)\left(\frac{(1-u_1)(CS\beta_2 + IS\beta_1)}{N^2}\right) \\
&+r_4(\lambda_6 - \lambda_8) + \frac{\rho_1 \beta_1 QI}{N^2}\left(-\lambda_5 + \lambda_6 p + \lambda_7(1-p)\right) \\
&+\frac{\rho_2 \beta_2 QC}{N^2}\left(-\lambda_5 + \lambda_6 q + \lambda_7(1-q)\right), \\
&\frac{d\lambda_7}{dt} = -\frac{\partial H}{\partial J} = (\lambda_2 - \lambda_1)\left(\frac{(1-u_1)(CS\beta_2 + IS\beta_1)}{N^2}\right) \\
&+r_5(\lambda_7 - \lambda_8) + \frac{\rho_1 \beta_1 QI}{N^2}\left(-\lambda_5 + \lambda_6 p + \lambda_7(1-p)\right) \\
&+\frac{\rho_2 \beta_2 QC}{N^2}\left(-\lambda_5 + \lambda_6 q + \lambda_7(1-q)\right) + \lambda_7(d_4 + \mu), \\
&\frac{d\lambda_8}{dt} = -\frac{\partial H}{\partial R} = (\lambda_2 - \lambda_1)\left(\frac{(1-u_1)(CS\beta_2 + IS\beta_1)}{N^2}\right) \\
&+\frac{\rho_1 \beta_1 QI}{N^2}\left(-\lambda_5 + \lambda_6 p + \lambda_7(1-p)\right) \\
&+\frac{\rho_2 \beta_2 QC}{N^2}(-\lambda_5 + \lambda_6 q + \lambda_7(1-q)) + \lambda_8\mu.
\end{aligned}
$$

With transverse condition $\lambda_1(T) = \lambda_2(T) = \lambda_3(T) = \lambda_4(T) = \lambda_5(T) = \lambda_6(T) = \lambda_7(T) = \lambda_8(T) = 0$.

The stationary condition for the optimal control problem (16) is obtained by deriving the Hamilton function (17) on the control variables u_1 and u_2 $\left(\frac{\partial \mathcal{H}}{\partial u_1} = 0,\ \frac{\partial \mathcal{H}}{\partial u_2} = 0\right)$, successively obtained

$$
\begin{aligned}
u_1 &= \frac{(\beta_1 SI + \beta_2 SC)(\lambda_2 - \lambda_1)}{NA_1} \text{ and} \\
u_2 &= \frac{I(\lambda_3 - \lambda_6 - \lambda_7) + C(\lambda_4 - \lambda_6 - \lambda_7)}{A_2}.
\end{aligned}
$$

The control variables in the COVID-19 model with preventive measures through education and treatment efforts for infected individuals are defined as $0 \le u_1 \le 1$ and $0 \le u_2 \le 1$. So, the optimal control u_1^* and u_2^* can be expressed as

$$
\begin{aligned}
u_1^* &= \text{maks}\left\{0, \min\left(\frac{(\beta_1 S^* I^* + \beta_2 S^* C^*)(\lambda_2 - \lambda_1)}{NA_1}, 1\right)\right\} \text{ and} \\
u_2^* &= \text{maks}\left\{0, \min\left(\frac{I^*(\lambda_3 - \lambda_6 - \lambda_7) + C^*(\lambda_4 - \lambda_6 - \lambda_7)}{A_2}, 1\right)\right\}.
\end{aligned}
$$

The optimal system is obtained by substituting the optimal control variables u_1^* and u_2^* into the system of state (Equation 15) and costate (Equation 18) equations.

6. Simulation of the model with control

The method used in solving this optimal control problem is the forward–backward sweep method. In this numerical simulation, the parameter values used are presented in Table 1 according to the state of the COVID-19 case in Indonesia. Next, the initial values given are as follows $S_0 = 270,911,990$, $E_0 = 1,000,000$, $I_0 = 412,784$, $C_0 = 500,000$, $Q_0 = 100,000$, $H_0 = 56,899$, $J_0 = 200,000$, and $R_0 = 341,942$, with simulation intervals $t \in [0, 100]$. The results of the optimal numerical control simulation are presented as follows:

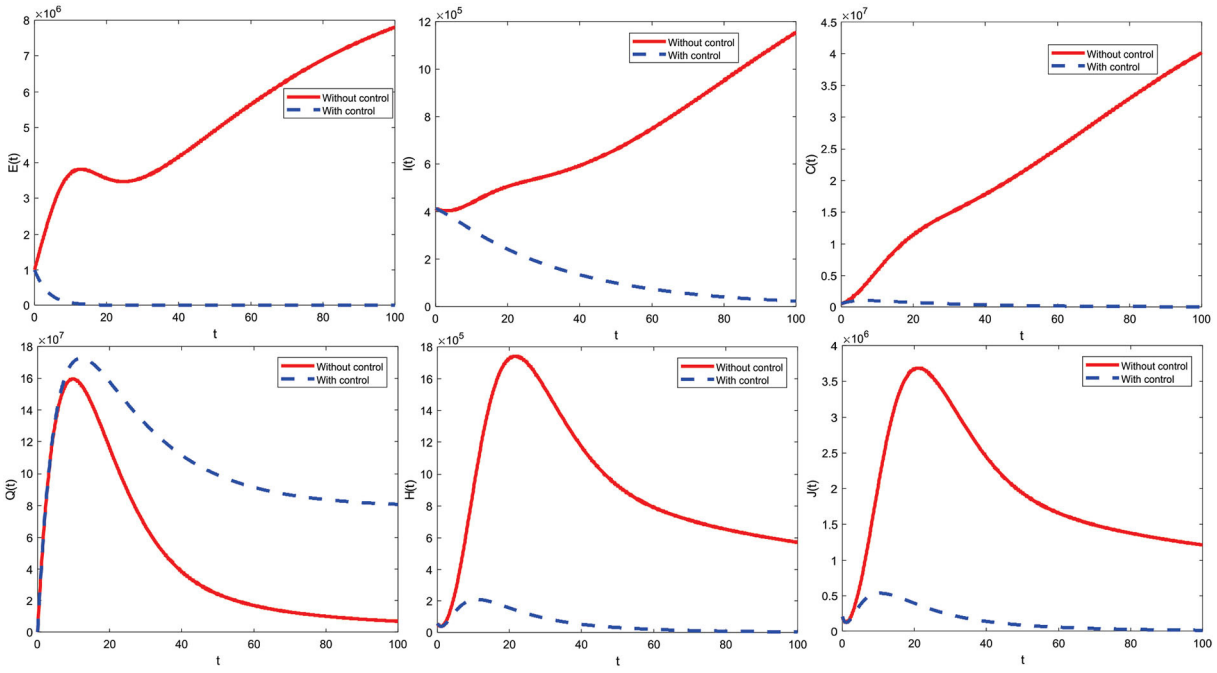

FIGURE 7
The optimal control simulation results with $u_1 \neq 0$.

6.1. Using the control strategy $u_1 \neq 0$ and $u_2 = 0$

Figure 7 shows the control strategy $u_1 \neq 0$ and $u_2 = 0$. This is the result of education that makes all individuals always be careful, such as interacting outside the home. Implementing this strategy on subpopulations exposed, infected with comorbidity, infected without comorbidity, and isolation is significantly reduced. Implementing the control strategy $u_1 \neq 0$ and $u_2 = 0$ can also increase the subpopulation of quarantine. Furthermore, the control strategy profiles $u_1 \neq 0$ and $u_2 = 0$ to reduce the number of COVID-19 cases during $t = 100$ are presented in Figure 8.

The control strategy $u_1 \neq 0$ and $u_2 = 0$ is given by one (maximum) from the beginning of the period to $t = 99.9$ and decreases significantly to zero at the end of the period. Control is terminated at the period's end, meaning no more control is given.

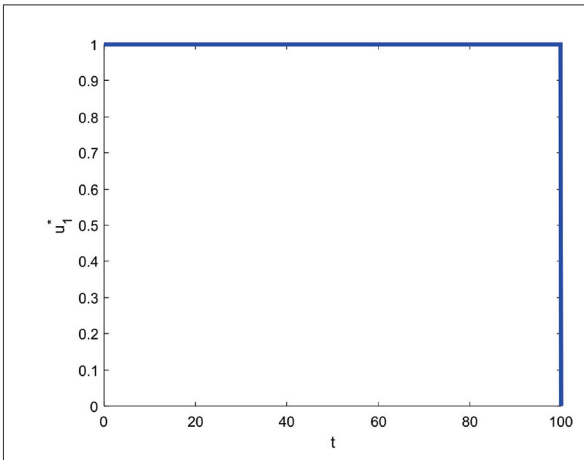

FIGURE 8
The optimal control profile with $u_1 \neq 0$.

6.2. Using the control strategy $u_1 = 0$ and $u_2 \neq 0$

Figure 9 shows the control strategy $u_1 = 0$ and $u_2 \neq 0$. This strategy can reduce the subpopulation infected with comorbid and without comorbid because there is an increase in the care of infected individuals. Implementing this strategy on subpopulations exposed, infected with comorbidity, infected without comorbidity, and isolation is significantly reduced. Implementing the control strategies $u_1 = 0$ and $u_2 \neq 0$ can also increase the subpopulation of quarantine. Furthermore, the profiles of $u_1 = 0$ and $u_2 \neq 0$ control strategies to reduce the number of COVID-19 cases for $t = 100$ are presented in Figure 10.

The control strategy $u_1 = 0$ and $u_2 \neq 0$ is given by one (maximum) from the beginning to $t = 48.6$ and decreases slowly

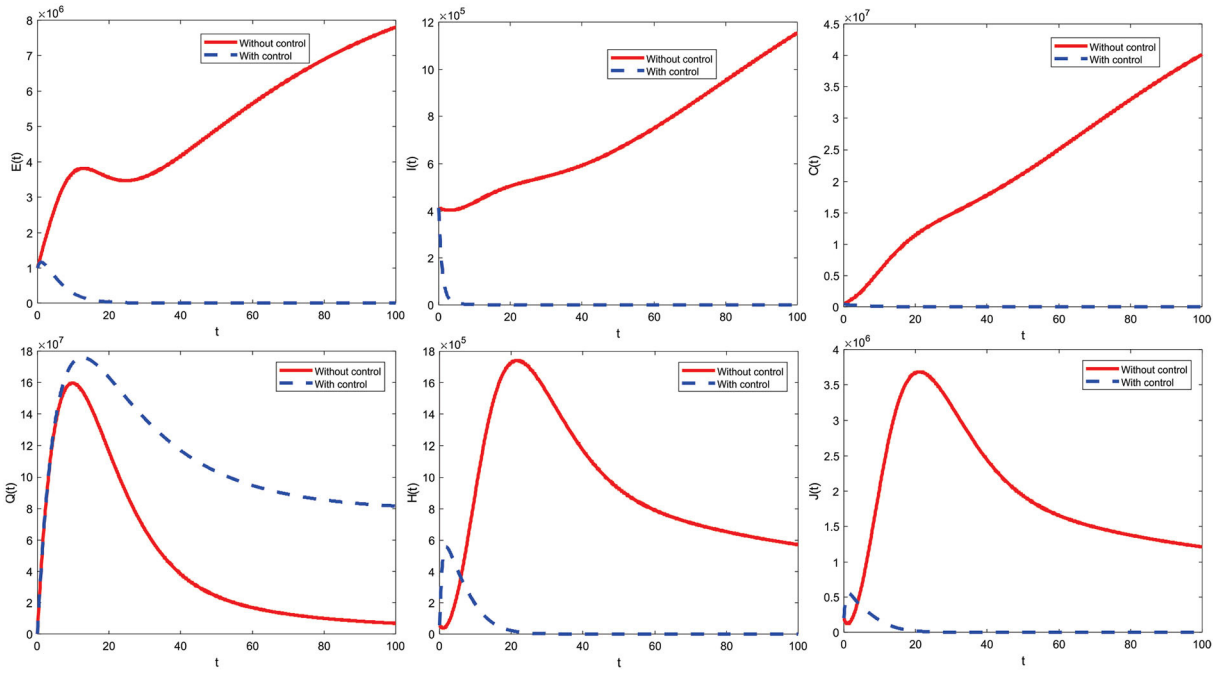

FIGURE 9
The optimal control simulation results with $u_2 \neq 0$.

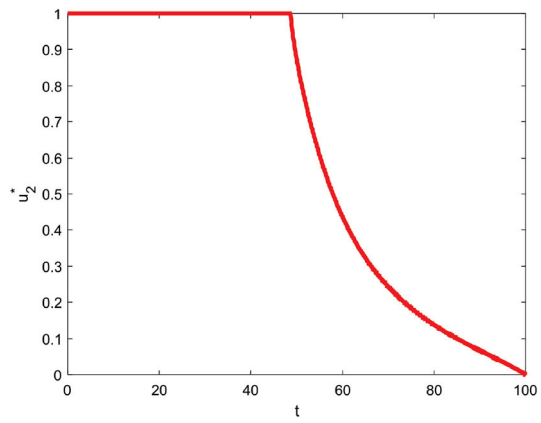

FIGURE 10
Optimal control profile with $u_2 \neq 0$.

until $t = 100$ reaches zero which means control is stopped at the end of the period.

6.3. Using the control strategy $u_1 \neq 0$ and $u_2 \neq 0$

Figure 11 indicates a combined control strategy. This results from education that makes all individuals always be careful (such as interacting outside the home) and increased care for infected individuals. Combined control strategies can control or reduce deployment significantly. Furthermore, the combined control strategy profile to reduce the number of COVID-19 cases during $t = 100$ is presented in Figure 12.

The combined control strategy consists of two concurrent administrations of control. The control u_1 is given by one (maximum) up to $t = 65.4$ and decreases significantly until the end of the period reaches zero. Then, control u_2 is assigned one (maximum) until $t = 39.5$ and then decreases until $t = 100$ slowly reaches zero. Both controls are terminated at the end of the period, which means they are no longer given control of u_1 and u_2.

6.4. Comparison of total infections using all strategic control scenarios

The varying initial values of the exposed subpopulations are given. Total infected subpopulations for different initial conditions from exposed subpopulations are $E(0) = 200000, E(0) = 1000000, E(0) = 10000000$, and $E(0) = 100000000$ successively from left to right using the three control strategies shown in Figure 13.

From Figure 13, it can be seen that the number of infected subpopulations was reduced by applying the third strategy compared to other strategies. Based on strategies 1–3, it can be

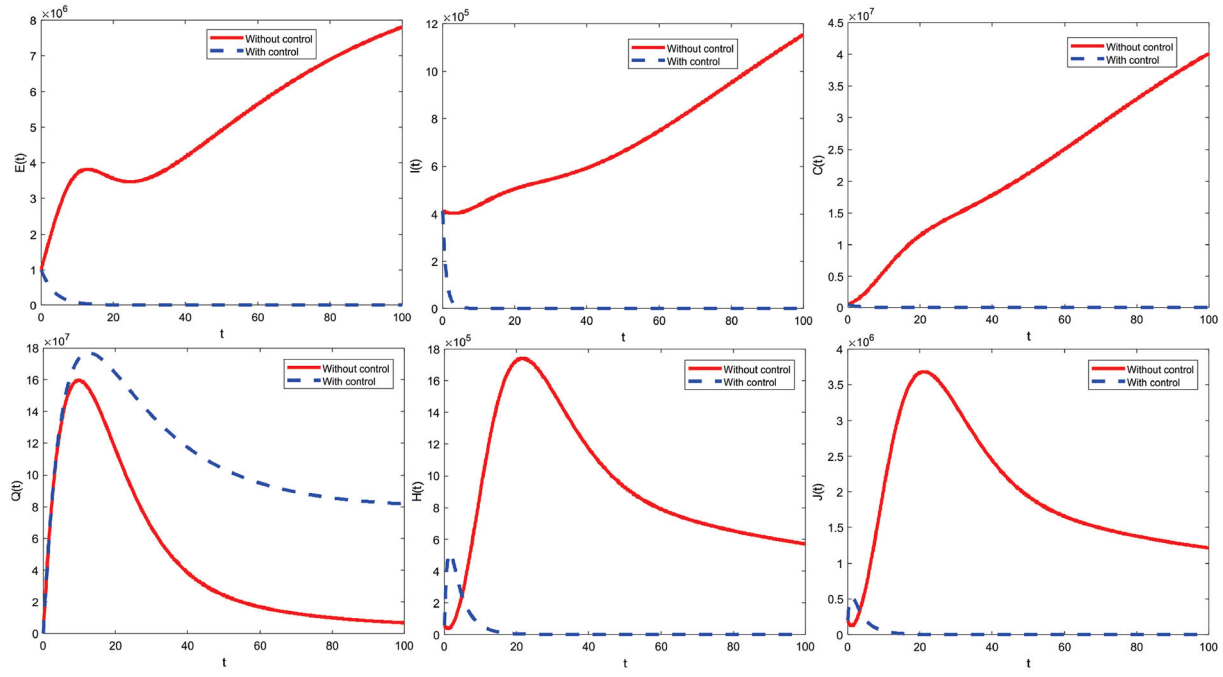

FIGURE 11
Combined optimal control simulation results.

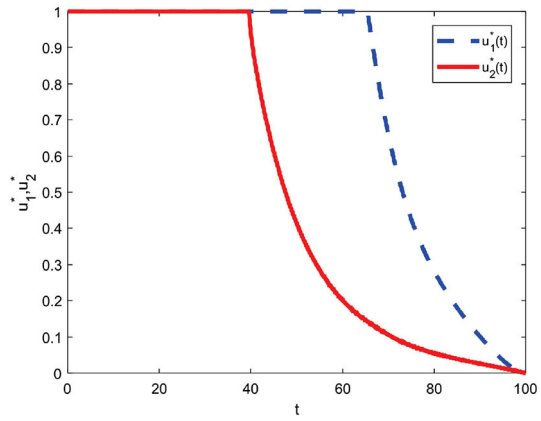

FIGURE 12
Combined control profile.

concluded that strategy 3 is the best strategy to minimize the number of people infected with COVID-19 in the community.

7. Cost evaluation

The cost evaluation aims to determine the most minimal cost-effectiveness strategy of COVID-19 spread control measures. Cost evaluation in this study uses average cost-effectiveness ratio (ACER) and incremental cost-effectiveness ratio (ICER). According to the approach to cost-effectiveness analysis, ACER is defined mathematically as follows:

$$ACER = \frac{\text{Objective function } (J)}{\text{Total number of infections averted}}.$$

The strategy with the smallest ACER value is the most cost-effective and is obtained in Table 4 as follows:

The incremental cost-effectiveness ratio, which compares two intervention options vying for the same scarce resources, typically tracks costs and health benefits changes. ICER is defined as follows when considering strategies p and q as two competing control intervention techniques:

$$ICER = \frac{\text{Change in total costs in strategies p and q}}{\text{Change in control benefits in strategies p and q}}.$$

Next, ICER was calculated to determine the most cost-effective strategy out of all the control strategies. First, the competition for strategies 1 and 2 is calculated as follows:

$$ICER\,(1) = \frac{49,247,000,000 - 0}{53,846,000,000 - 0} = 0.9146,$$

$$ICER\,(2) = \frac{2,991,000,000 - 49,247,000,000}{53,893,000,000}$$

$$-53,846,000,000 = -\frac{46,256,000,000}{47,000,000} = -984.1702,$$

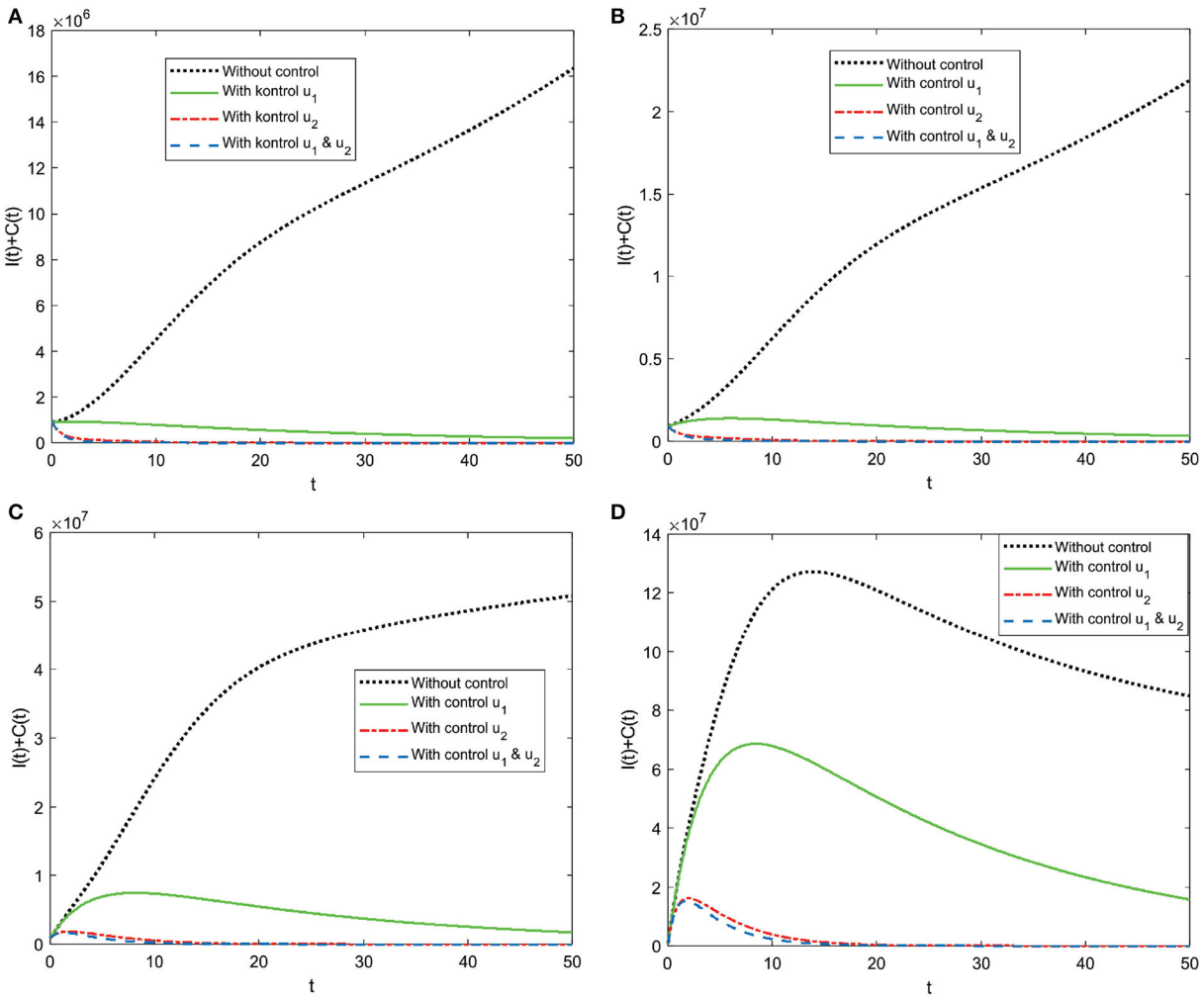

FIGURE 13
(A–D) Total subpopulation infected using various strategies.

The ICER results in strategy 1 were greater than in strategy 2, so educational controls alone were more expensive and ineffective than medical care enhancement controls. Therefore, strategy 1 is removed from the possible control strategies. Next, the ICER for strategies 2 and 3 is recalculated as follows:

$$ICER\,(2) = \frac{2,991,000,000 - 0}{53,893,000,000 - 0} = 0.5130,$$

$$ICER\,(3) = \frac{1,794,700,000 - 2,991,000,000}{53,894,000,000 - 53,893,000,000} = -\frac{1,196,300,000}{1,000,000} = -1,196.3.$$

Strategy 2 has a higher ICER value than strategy 3. So, strategy 3 (combined control) is the best control strategy of all options because of its cost-effectiveness and prevention of the spread of infectious diseases.

TABLE 4 Total infections prevented, total costs, and ACER for strategies 1, 2, and 3.

Strategy	Infections prevented	Total cost	ACER
No strategy	0	0	0
Strategy 1	53,846,000,000	49,247,000	0.9146
Strategy 2	53,893,000,000	2,991,000	0.0555
Strategy 3	53,894,000,000	1,794,700	0.0333

8. Conclusion

In this study, we have proposed a mathematical model of COVID-19 with comorbidities and added control of community education and improvement of medical care. The proposed

model has been calibrated using cumulative confirmed infection cases in Indonesia. The basic reproduction number has been calculated by the next-generation matrix method. The model has an asymptotically stable disease-free equilibrium, provided that the basic reproduction number is <1. Furthermore, the model has an asymptotically stable endemic equilibrium, provided that the basic reproduction number is more than one. Individuals with comorbidity have a greater risk of infection, so there is a need for more supervision and preventive measures such as wearing masks, maintaining distance, and proper sanitation. Public education can be through social media, TV, radio, print media, and others to control the COVID-19 pandemic in Indonesia. Based on the model analysis, it is found that the COVID-19 pandemic can be controlled and eradicated if the value of $R_0 < 1$ by providing public education control and improving medical care. The sensitivity analysis results show that the most influential parameters are quarantine and contact with infected individuals, so educating the public to reduce disease transmission is important. After public education was given, the community became aware of the COVID-19 outbreak and began to reduce contact with other people. Likewise, the Indonesian government imposed large-scale social restrictions (PSBB) and enforced restrictions on community activities (PPKM) with four levels aiming to reduce infection and reduce social contact, educational institutions conducted online classes, webinars, etc. In addition to public education, increased medical care also need to be given to individuals who are already infected so that they recover quickly and that the epidemic is resolved soon. Furthermore, from the numerical results and cost-effectiveness analysis on the optimal control problem, it is found that applying a combination of controls can give the best results compared to a single control. This study can be extended in various ways, including considering the stochastic, time delay, and fractional derivative versions of this model. In addition, providing control variations (such as the presence of vaccination) combines the dynamics of two COVID-19 strains with another comorbidity and considers the COVID-19 vaccination model.

Data availability statement

The raw data supporting the conclusions of this article will be made available by the authors, without undue reservation.

Author contributions

MAR and F: conceptualization. MAR: methodology, software, writing—original draft preparation, and visualization. MAR, F, CA, and CWC: validation, investigation, and data curation. F, CA, and CWC: formal analysis. MAR, F, and CA: writing—review and editing. F and CA: supervision. All authors have read and agreed to the published version of the manuscript.

Conflict of interest

The authors declare that the research was conducted in the absence of any commercial or financial relationships that could be construed as a potential conflict of interest.

Publisher's note

All claims expressed in this article are solely those of the authors and do not necessarily represent those of their affiliated organizations, or those of the publisher, the editors and the reviewers. Any product that may be evaluated in this article, or claim that may be made by its manufacturer, is not guaranteed or endorsed by the publisher.

References

1. WHO. *Novel Coronavirus.* (2020). Available online at: https://www.who.int/indonesia/news/novel-coronavirus

2. Wu Z, McGoogan JM. Characteristics of and important lessons from the coronavirus disease 2019 (COVID-19) outbreak in China: summary of a report of 72 314 cases from the Chinese center for disease control and prevention. *JAMA.* (2020) 323:1239–42. doi: 10.1001/jama.2020.2648

3. Kemkes. *Pertanyaan dan Jawaban Terkait COVID-19 Kementerian Kesehatan.* (2020). Available online at: https://www.kemkes.go.id/article/view/20030400008/FAQ-Coronavirus.html

4. WHO. *Novel Coronavirus (COVID-19).* (2021). Available online at: https://www.moh.gov.sa/en/HealthAwareness/EducationalContent/Corona/Pages/corona.aspx

5. WHO. *Novel Coronavirus (2019-nCoV): Situation Report 1.* (2020). Available online at: https://apps.who.int/iris/handle/10665/330760

6. Wu YC, Chen CS, Chan YJ. The outbreak of COVID-19: an overview. *J Chin Med Assoc.* (2020) 83:217–20. doi: 10.1097/JCMA.0000000000000270

7. Guan W, Liang W, Zhao Y, Liang H, Chen Z, Li Y, et al. Comorbidityity and its impact on 1590 patients with COVID-19 in China: a nationwide analysis. *Eur Respir J.* (2020) 55:2000547. doi: 10.1183/13993003.00547-2020

8. Yang J, Zheng Y, Gou X, Pu K, Chen Z, Guo Q. International journal of infectious diseases prevalence of comorbidities and its effects in patients infected with SARS-CoV-2: a systematic review and meta-analysis. *Int J Infect Dis.* (2020) 94:91–5. doi: 10.1016/j.ijid.2020.03.017

9. Satgas. *Peta Sebaran COVID-19.* (2021). Available online at: https://covid19.go.id/peta-sebaran

10. Adisasmito W, Suwandono A, Trihono, Gani A, Aisyah DN, Solikha DA, et al. Studi komparasi pembelajaran penanganan COVID-19 Indonesia-Korea Selatan. In: *Direktorat Kesehatan dan Gizi Masyarakat Kementerian PPN/BAPPENAS.* (2021). Available online at: https://infeksiemerging.kemkes.go.id/document/download/3ax61Bxrn5

11. Worldometers. *Report Coronavirus Cases* (2021). Available online at: https://www.worldometers.info/coronavirus/

12. Lemon SM, Hamburg MA, Frederick P, Choffnes ER, Mack A. *Ethical and Legal Considerations in Mitigating Pandemic Disease: Workshop Summary*. Washington, DC: National Academic Press (2007).

13. WHO. *COVID-19 Strategy Update*. (2020). Available online at: https://www.who.int/publications/m/item/covid-19-strategy-update

14. WHO. *Pertimbangan-Pertimbangan Untuk Karantina Individu Dalam Konteks Penanggulangan Penyakit Coronavirus (COVID-19)*. (2020). Available online at: https://www.who.int/docs/default-source/searo/indonesia/covid19/who-2019-covid19-ihr-quarantine-2020-indonesian.pdf?sfvrsn=31d7cbd8_2

15. Tang B, Wang X, Li Q, Bragazzi NL, Tang S, Xiao Y, et al. Estimation of the transmission risk of the 2019-nCoV and its implication for public health interventions. *J Clin Med*. (2020) 9:462. doi: 10.3390/jcm9020462

16. Müller J, Kuttler C. *Methods and Models in Mathematical Biology*. Berlin; Heidelberg: Springer-Verlag (2015).

17. Murray JD. *Mathematical Biology I: An Introduction*. Berlin; Heidelberg: Springer-Verlag (2002).

18. Feng Z. Final and peak epidemic sizes for SEIR models with quarantine and isolation. *Math Biosci Eng*. (2007). 4:675–86. doi: 10.3934/mbe.2007.4.675

19. Tahir M, Shah SIA, Zaman G, Khan T. Stability behaviour of mathematical model MERS corona virus spread in population. *Filomat*. (2019) 33:3947–60. doi: 10.2298/FIL1912947T

20. Usaini S, Hassan AS, Garba SM, Lubuma JMS. Modeling the transmission dynamics of the middle east respiratory syndrome coronavirus (MERS-CoV) with latent immigrants. *J Interdisc Math*. (2019) 22:903–30. doi: 10.1080/09720502.2019.1692429

21. Soewono E. On the analysis of COVID-19 transmission in wuhan, diamond princess and jakarta-cluster. *Commun Biomath Sci*. (2020) 3:9–18. doi: 10.5614/cbms.2020.3.1.2

22. Das P, Upadhyay RK, Misra AK, Rihan FA, Das P, Ghosh D. Mathematical model of COVID-19 with comorbidity and controlling using non-pharmaceutical interventions and vaccination. *Nonlinear Dyn*. (2021) 106:1213–27. doi: 10.1007/s11071-021-06517-w

23. Omame A, Sene N, Nometa I, Nwakanma CI, Nwafor EU, Iheonu NO, et al. Analysis of COVID-19 and comorbidity co-infection model with optimal control. *Optimal Control Appl Methods*. (2021) 42:1568–90. doi: 10.1002/oca.2748

24. Jia J, Ding J, Liu S, Liao G, Li J, Duan B, et al. Modeling the control of COVID-19: impact of policy interventions and meteorological factors. *Electron J Diff Equ*. (2020) 2020:23.

25. Prathumwan D, Trachoo K, Chaiya I. Mathematical modeling for prediction dynamics of the coronavirus disease 2019 (COVID-19) pandemic, quarantine control measures. *Symmetry*. (2020) 12:1404. doi: 10.3390/sym12091404

26. Deressa CT, Duressa GF. Modeling and optimal control analysis of transmission dynamics of COVID-19: The case of Ethiopia. *Alexandria Eng J*. (2020) 60:719–32. doi: 10.1016/j.aej.2020.10.004

27. Olaniyi S, Obabiyi OS, Okosun KO, Oladipo AT, Adewale SO. Mathematical modelling and optimal cost-effective control of COVID-19 transmission dynamics. *Eur Phys J Plus*. (2020) 135:938. doi: 10.1140/epjp/s13360-020-00954-z

28. Aldila D, Khoshnaw SHA, Safitri E, Rais YA, Bakry ARQ, Samiadji BM, et al. A mathematical study on the spread of COVID-19 considering social distancing and rapid assessment: the case of Jakarta, Indonesia. *Chaos Solit Fractals*. (2020) 139:110042. doi: 10.1016/j.chaos.2020.110042

29. Aldila D, Ndii MZ, Samiadji BM. Optimal control on COVID-19 eradication program in Indonesia under the effect of community awareness. *Math Biosci Eng*. (2020) 17:6355–89. doi: 10.3934/mbe.2020335

30. Ali M, Shah STH, Imran M, Khan A. The role of asymptomatic class, quarantine and isolation in the transmission of COVID-19. *J Biol Dyn*. (2020) 14:389–408. doi: 10.1080/17513758.2020.1773000

31. Rois MA, Tafrikan M, Norasia Y, Anggriani I, Ghani M. SEIHR model on spread of COVID-19 and its simulation. *Telematika*. (2022) 15.

32. Annas S, Pratama MI, Rifandi M, Sanusi W, Side S. Stability analysis and numerical simulation of SEIR model for pandemic COVID-19 spread in Indonesia. *Chaos Solit Fractals*. (2020) 139:110072. doi: 10.1016/j.chaos.2020.110072

33. Baba IA, Nasidi BA, Baleanu D. Optimal control model for the transmission of novel COVID-19. *Comput Mater Continua*. (2021) 66:3089–106. doi: 10.32604/cmc.2021.012301

34. Li XP, Darassi MH, Khan MA, Chukwu CW, Alshahrani MY, Shahrani MA, et al. Assessing the potential impact of COVID-19 Omicron variant: insight through a fractional piecewise model. *Results Phys*. (2022) 38:105652. doi: 10.1016/j.rinp.2022.105652

35. Bajiya VP, Bugalia S, Tripathi JP. Mathematical modeling of COVID-19: impact of non-pharmaceutical interventions in india mathematical modeling of COVID-19: impact of non-pharmaceutical interventions in India. *Chaos*. (2020) 30:113143. doi: 10.1063/5.0021353

36. Das P, Nadim SS, Das S, Das P. Dynamics of COVID-19 transmission with comorbidity: a data driven modelling based approach. *Nonlinear Dyn*. (2021) 106:1197–211. doi: 10.1007/s11071-021-06324-3

37. Diagne ML, Rwezaura H, Tchoumi SY, Tchuenche JM. Mathematical model of COVID-19 with vaccination and treatment. *Comput Math Methods Med*. (2021) 2021:1250129. doi: 10.1155/2021/1250129

38. Ghostine R, Gharamti M, Hassrouny S, Hoteit I. An extended SEIR model with vaccination for forecasting the COVID-19 pandemic in Saudi Arabia using an ensemble Kalman filter. *Mathematics*. (2021) 9:636. doi: 10.3390/math9060636

39. Kouidere A, Khajji B, Bhih AE, Balatif O, Rachik MA. Mathematical modeling with optimal control strategy of transmission of COVID-19 pandemic virus. *Commun Math Biol Neurosci*. (2020) 2020:24. doi: 10.28919/cmbn/4599

40. Madubueze CE, Onwubuya IO, Dachollom S. Controlling the spread of COVID-19: optimal control analysis. *Comput Math Methods Med*. (2020) 2020:6862516. doi: 10.1101/2020.06.08.20125393

41. Naveed M, Baleanu D, Rafiq M, Raza A, Soori A, Hasan, et al. Dynamical behavior and sensitivity analysis of a delayed coronavirus epidemic model. *Comput Mater Continua*. (2020) 65:225–41. doi: 10.32604/cmc.2020.011534

42. Riyapan P, Shuaib SE, Intarasit A. A mathematical model of COVID-19 pandemic: a case study of Bangkok, Thailand. *Comput Math Methods Med*. (2021) 2021:6664483. doi: 10.1155/2021/6664483

43. Yang C, Wang J. A mathematical model for the novel coronavirus epidemic in Wuhan, China. *Math Biosci Eng*. (2020) 17:2708–24. doi: 10.3934/mbe.2020148

44. Youssef HM, Alghamdi NA, Ezzat MA, El-bary AA, Shawky AM. Study on the SEIQR model and applying the epidemiological rates of COVID-19 epidemic spread in Saudi Arabia. *Infect Dis Model*. (2021) 6:678–92. doi: 10.1016/j.idm.2021.04.005

45. Youssef HM, Alghamdi NA, Ezzat MA, El-Bary AA, Shawky AM. A new dynamical modeling SEIR with global analysis applied to the real data of spreading COVID-19 in Saudi Arabia. *Math Biosci Eng*. (2020) 17:7018–44. doi: 10.3934/mbe.2020362

46. Rois MA, Trisilowati T, Habibah U. Dynamic analysis of COVID-19 model with quarantine and isolation. *JTAM*. (2021) 5:418–33.

47. Rois MA, Trisilowati, Habibah U. Optimal control of mathematical model for COVID-19 with quarantine and isolation. *Int J Eng Trends Technol*. (2021) 69:154–60. doi: 10.14445/22315381/IJETT-V69I6P223

48. Musa SS, Qureshi S, Zhao S, Yusuf A, Mustapha UT, He D. Mathematical modeling of COVID-19 epidemic with effect of awareness programs. *Infect Dis Model*. (2021) 6:448–60. doi: 10.1016/j.idm.2021.01.012

49. Chukwu CW, Fatmawati. Modelling fractional-order dynamics of COVID-19 with environmental transmission and vaccination: a case study of Indonesia. *AIMS Math*. (2022) 7:4416–38. doi: 10.3934/math.2022246

50. Zeb A, Alzahrani E, Erturk VS, Zaman G. Mathematical Model for coronavirus disease 2019 (COVID-19) containing isolation class. *BioMed Res Int*. (2020) 2020:3452402. doi: 10.1155/2020/3452402

51. Bonyah E, Juga M, Fatmawati. Fractional dynamics of coronavirus with comorbidity via Caputo-Fabrizio derivative. *Commun Math Biol Neurosci*. (2022) 2022:12. doi: 10.28919/cmbn/6964

52. Fatmawati, Yuliani E, Alfiniyah C, Juga ML, Chukwu CW. On the modeling of COVID-19 transmission dynamics with two strains: insight through caputo fractional derivative. *Fractal Fract*. (2022) 6:346. doi: 10.3390/fractalfract6070346

53. Majumder M, Tiwari PK, Pal S. Impact of saturated treatments on HIV-TB dual epidemic as a consequence of COVID-19: optimal control with awareness and treatment. *Nonlinear Dyn*. (2022) 109:143–76. doi: 10.1007/s11071-022-07395-6

54. Rai RK, Khajanchi S, Tiwari PK, Venturino E, Misra AK. Impact of social media advertisements on the transmission dynamics of COVID-19 pandemic in India. *J Appl Math Comput*. (2022) 68:19–44. doi: 10.1007/s12190-021-01507-y

55. Brauer F, Castillo-Chavez C. *Mathematical Models in Population Biology and Epidemiology*. New York, NY: Springer-Verlag New York (2012).

56. Driessche PVD, Watmough J. Reproduction numbers and sub-threshold endemic equilibria for compartmental models of disease transmission. *Math Biosci*. (2002) 180:29–48. doi: 10.1016/S0025-5564(02)00108-6

57. Alligood KT, Sauer TD, Yorke JA. CHAOS: an Introduction to dynamical systems. In: *Introduction To Computational Modeling Using C and Open-Source Tools*. New York, NY; Berlin; Heidelberg: Springer-Verlag (2000).

58. Chitnis N, Hyman JM, Cushing JM. Determining important parameters in the spread of malaria through the sensitivity analysis of a mathematical model. *Bull Math Biol*. (2008) 70:1272. doi: 10.1007/s11538-008-9299-0

59. Rois MA, Trisilowati T, Habibah U. Local sensitivity analysis of COVID-19 epidemic with quarantine and isolation using normalized index. *Telematika*. (2021) 14:13–24. doi: 10.35671/telematika.v14i1.1191

frontiers | Frontiers in Applied Mathematics and Statistics

TYPE Original Research
PUBLISHED 06 January 2023
DOI 10.3389/fams.2022.1077831

OPEN ACCESS

EDITED BY
Bapan Ghosh,
Indian Institute of Technology Indore, India

REVIEWED BY
Huda Abdul Satar,
University of Baghdad, Iraq
Prabir Panja,
Haldia Institute of Technology, India

*CORRESPONDENCE
Hasan S. Panigoro
✉ hspanigoro@ung.ac.id

SPECIALTY SECTION
This article was submitted to Mathematical Biology, a section of the journal Frontiers in Applied Mathematics and Statistics

RECEIVED 23 October 2022
ACCEPTED 25 November 2022
PUBLISHED 06 January 2023

CITATION
Panigoro HS, Rahmi E and Resmawan R (2023) Bifurcation analysis of a predator–prey model involving age structure, intraspecific competition, Michaelis–Menten type harvesting, and memory effect. *Front. Appl. Math. Stat.* 8:1077831. doi: 10.3389/fams.2022.1077831

Bifurcation analysis of a predator–prey model involving age structure, intraspecific competition, Michaelis–Menten type harvesting, and memory effect

Hasan S. Panigoro*, Emli Rahmi and Resmawan Resmawan

Biomathematics Research Group, Department of Mathematics, Universitas Negeri Gorontalo, Gorontalo, Indonesia

The complexity of the dynamical behaviors of interaction between prey and its predator is studied. The prey and predator relationship involves the age structure and intraspecific competition on predators and the nonlinear harvesting of prey following the Michaelis–Menten type term. Some biological validities are shown for the constructed model such as the existence and uniqueness as well as the non-negativity and boundedness of solutions. Three equilibrium points, namely the origin, axial, and interior points, are found including their global dynamics by employing the Lyapunov function along with the generalized Lassale invariant principle. The changes in dynamical behaviors driven by the harvesting and the memory effect are exhibited, including transcritical, saddle-node, backward, and Hopf bifurcations. The appearance of these interesting phenomena is strengthened by giving numerical simulations consisting of bifurcation diagrams, phase portraits, and their time series.

KEYWORDS

bifurcation, age structure, intraspecific competition, harvesting, memory effect

1. Introduction

Since Lotka and Volterra introduced the classical predator–prey model, theoretical studies of predation without age structure have attracted the attention of many authors, for example Deng et al. [1], Huang et al. [2], Tahara et al. [3], and Zeng et al. [4]. However, in nature, many species of plants and animals could have life histories that can simply be partitioned into two age stages: immature and mature stages. In each stage, individuals of species have identical biological characteristics, such as the ability to reproduce, motile, ingest food, and survive [5]. In particular, there are amphibians, insects, birds, and mammals with life cycles that can last from only several days or weeks to more than a century. For this reason, some researchers have developed the predator–prey model by incorporating age structure either in prey or/and predator population with other factors that also influence the dynamics of the predator–prey model, mainly restricted to the classical integer-order, stochastic, or delay equations [6–13].

In Wang and Chen [14] considered the predator–prey model with age structure for the predator population using time delays. If we ignore the effect of time delay, the model can be written as follows:

$$\begin{aligned}\frac{dx}{dt} &= rx\left(1-\frac{x}{K}\right)-mxz,\\ \frac{dy}{dt} &= nxz-\beta y-\delta_1 y,\\ \frac{dz}{dt} &= \beta y-\delta_2 z.\end{aligned} \tag{1}$$

Here $x(t), y(t)$, and $z(t)$ represent the population densities of prey, immature predator, and mature predator, at time t, respectively. Model (Equation 1) assumes that the prey grows logistically with r as the intrinsic growth rate, K is the carrying capacity; m is the linear Holling type I functional response, n is the conversion rate with which captured prey are converted to new immature predator, β is the maturity rate of the predator, δ_1 and δ_2 are the death rate of the immature and mature predators, respectively. It is also assumed that only the mature predator can feed the prey through the term mxz. If we do not consider the age structure of the predator population, then model (Equation 1) is reduced to the classical Lotka–Volterra model for which the positive equilibrium or the boundary equilibrium of this model is globally asymptotically stable. This means that the model has no periodic solution. On the other hand, Wang and Chen [14] prove that in the model (Equation 1), there exists an orbitally asymptotically stable periodic solution around the interior equilibrium point which suggests that the age structure can cause periodic oscillation of populations.

From the point of view of human needs, harvesting of populations generally occurs in wildlife, forestry, and fisheries management. When harvesting is integrated into the predator–prey model, there are three types of harvesting, namely constant harvesting [15], linear harvesting [16], and non-linear harvesting [17]. In this article, we assume that the predator is not a commercial species and there is intraspecific competition among immature predators. Therefore, the predator–prey model with age structure and intraspecific competition in predator (Equation 1), where the prey population is subject to Michaelis–Menten type harvesting, is given by

$$\begin{aligned}\frac{dx}{dt} &= rx\left(1-\frac{x}{K}\right)-mxz-\frac{hx}{c+x},\\ \frac{dy}{dt} &= nxz-\beta y-\delta_1 y-\omega y^2,\\ \frac{dz}{dt} &= \beta y-\delta_2 z.\end{aligned} \tag{2}$$

An example of prey-predator interactions whose biological phenomena are described in the model (Equation 2) can be found in the African wild dog with its prey impala. The African wild dogs are a social structure that lives in packs. For 3–4 weeks, young African wild dogs were in the den with their mother. All adult members of African wild dogs are care for their young ones and provide food for them. The hunting members of the pack will return to the den where they regurgitate meat for the nursing female and young. In some cases, young ones fail to survive because the hunting member does not bring back sufficient food for the young, which leads to intraspecific competition in immature predator [18]. On the other hand, the prey, impala, even though there are no major threats to their survival, poaching has become significantly contributed to the decline in its number [19].

Note that the growth rates of the prey, immature, and mature predator populations in the model (Equation 2) depend only on the local state as the left-hand side is the integer-order derivative. On the other hand, most biological systems have properties where the current state is affected by all of the past states or it is called the memory effect. Therefore, modeling with memory effects can be done by analyzing the system using fractional-order calculus [20, 21]. The operators of the fractional-order derivative have non-local properties to make them more suitable for dynamical systems that have memory influences on their state variables.

After Riemann and Liouville generalized the concept of integer-order calculus to the fractional-order calculus over two decades ago, the studies about the predator–prey models with fractional-order differential equation have gained much attention, for example, Rahmi et al. [22], Owolabi [23], Barman et al. [24], Ghanbari and Djilali [25], Yousef et al. [26], Ghosh et al. [27], and Panigoro et al. [28]. The fractional-order derivatives are defined as an integration that provides the ability to store the whole memory over time, and hence, it could give an exact description of different ecological phenomena. For this reason, the new structure for the model (Equation 2) is given in the following form:

$$\begin{aligned}{}^{C}\mathcal{D}_t^{\alpha} x(t) &= rx\left(1-\frac{x}{K}\right)-mxz-\frac{hx}{c+x}=F_1(x,y,z),\\ {}^{C}\mathcal{D}_t^{\alpha} y(t) &= nxz-\beta y-\delta_1 y-\omega y^2=F_2(x,y,z),\\ {}^{C}\mathcal{D}_t^{\alpha} z(t) &= \beta y-\delta_2 z=F_3(x,y,z).\end{aligned} \tag{3}$$

The existence and local stability of all equilibrium points of the model (Equation 3) are discussed in Panigoro et al. [29]. However, to the best of our knowledge, the global dynamics and bifurcation analysis of the model (Equation 3), to this day, have not been investigated. Here, ${}^{C}\mathcal{D}_t^{\alpha} f(t)$ is the standard Caputo derivative for a continuous function $f(x) \in \mathbb{C}([0,+\infty),\mathbb{R})$, which is defined as follows:

$${}^{C}\mathcal{D}_t^{\alpha} f(t) = \frac{1}{\Gamma(1-\alpha)}\int_0^t \frac{f'(\tau)}{(t-\tau)^{\alpha}}d\tau, \tag{4}$$

where $\Gamma(*)$ is the gamma function, $t \geq 0$, and $0 < \alpha \leq 1$ is known as the order of the fractional derivative.

Based on the above discussion, we have organized our work in several sections: In Section 3, we develop the existence and

uniqueness solution of the model (Equation 3). To check the biologically well-posedness of the model, we establish the non-negativity and boundedness of solutions of the model in Section 3. In Section 4, we derive some sufficient conditions to ensure the global asymptotic stability of each locally asymptotically stable equilibrium point by applying the Lyapunov functions. We then analyze the existing conditions of transcritical, saddle-node, backward, and Hopf bifurcations in Section 5. Some numerical simulations of our obtained results are carried out in Section 6. Finally, the conclusions are given in Section 7.

2. Existence and uniqueness

In this section, we will show that the model (Equation 3) has a unique solution. A similar manner given by Mahata et al. [30] is adopted. We first take the Riemann–Liouville integral (Definition 1 in Yavuz and Sene [31]) on both sides of Equation (3) to achieve the following Volterra-type integral equations.

$$\begin{aligned} x(t)-x(0) &= \frac{1}{\Gamma(\alpha)}\int_0^t F_1(x(\tau),y(\tau),z(\tau))(t-)^{\alpha-1}\,d\tau,\\ y(t)-y(0) &= \frac{1}{\Gamma(\alpha)}\int_0^t F_2(x(\tau),y(\tau),z(\tau))(t-\tau)^{\alpha-1}\,d\tau,\\ z(t)-z(0) &= \frac{1}{\Gamma(\alpha)}\int_0^t F_3(x(\tau),y(\tau),z(\tau))(t-\tau)^{\alpha-1}\,d\tau, \end{aligned} \tag{5}$$

Now, we will show that the kernels $F_i(x,y,z)$, $i=1,2,3$, satisfy the Lipschitz condition. For $\|.\|$ is the Euclidean norm, we suppose that $\|x(t)\|\le a_1$, $\|\bar{x}(t)\|\le a_2$, $\|y(t)\|\le a_3$, $\|\bar{y}(t)\|\le a_4$, $\|z(t)\|\le a_5$, and $\|\bar{z}(t)\|\le a_6$ are bounded functions. For x, $\bar{x}$, y, $\bar{y}$, z, and $\bar{z}$, we have

$$\begin{aligned} &\|F_1(x,y,z)-F_1(\bar{x},y,z)\|\\ &=\|\left[rx\left(1-\frac{x}{K}\right)-mxz-\frac{hx}{c+x}\right]\\ &-\left[r\bar{x}\left(1-\frac{\bar{x}}{K}\right)-m\bar{x}z-\frac{h\bar{x}}{c+\bar{x}}\right]\|\\ &=\|r(x-\bar{x})-\frac{r}{K}(x+\bar{x})(x-\bar{x})-mz(x-\bar{x})\\ &-ch\left(\frac{x-\bar{x}}{(c+x)(c+\bar{x})}\right)\|\\ &\le r\|x-\bar{x}\|+\frac{(a_1+a_2)r}{K}\|x-\bar{x}\|+a_5m\|x-\bar{x}\|+\frac{h}{c}\|x-\bar{x}\|\\ &=g_1\|x-\bar{x}\|, \end{aligned}$$

$$\begin{aligned} &\|F_2(x,y,z)-F_2(x,\bar{y},z)\|\\ &=\left\|\left[nxz-\beta y-\delta_1 y-\omega y^2\right]-\left[nxz-\beta\bar{y}-\delta_1\bar{y}-\omega\bar{y}^2\right]\right\|\\ &=\|-\beta(y-\bar{y})-\delta_1(y-\bar{y})-\omega(y+\bar{y})(y-\bar{y})\|\\ &\le\beta\|y-\bar{y}\|+\delta_1\|y-\bar{y}\|+\omega(a_3+a_4)\|y-\bar{y}\|\\ &=g_2\|y-\bar{y}\|, \end{aligned}$$

$$\begin{aligned} &\|F_3(x,y,z)-F_3(x,y,\bar{z})\|\\ &=\|[\beta y-\delta_2 z]-[\beta y-\delta_2\bar{z}]\|\\ &\le g_3\|z-\bar{z}\|, \end{aligned}$$

where $g_1=r+\frac{(a_1+a_2)r}{K}+a_5m+\frac{h}{c}$, $g_2=\beta+\delta_1+\omega(a_3+a_4)$, and $g_3=\delta_2$. Therefore, we conclude that $F_i(x,y,z)$, $i=1,2,3$, satisfy the Lipschitz condition. Furthermore, it is clear that if $0\le g_i<1$, then $F_i(x,y,z)$ are contractions for $i=1,2,3$. Therefore, the following theorem is obtained.

Theorem 1. The kernel $F_i(x,y,z)$, $i=1,2,3$ satisfy the Lipschitz condition and contractions if $0<g_i<1$, $i=1,2,3$.

Next, Equation (5) can be written as follows:

$$\begin{aligned} x(t) &= x(0)+\frac{1}{\Gamma(\alpha)}\int_0^t F_1(x(\tau),y(\tau),z(\tau))(t-\tau)^{\alpha-1}\,d\tau,\\ y(t) &= y(0)+\frac{1}{\Gamma(\alpha)}\int_0^t F_2(x(\tau),y(\tau),z(\tau))(t-\tau)^{\alpha-1}\,d\tau,\\ z(t) &= z(0)+\frac{1}{\Gamma(\alpha)}\int_0^t F_3(x(\tau),y(\tau),z(\tau))(t-\tau)^{\alpha-1}\,d\tau, \end{aligned}$$

Which can be written by the following recursive formula

$$\begin{aligned} x_n(t) &= x(0)+\frac{1}{\Gamma(\alpha)}\int_0^t F_1(x_{n-1},y,z)(t-\tau)^{\alpha-1}\,d\tau,\\ y_n(t) &= y(0)+\frac{1}{\Gamma(\alpha)}\int_0^t F_2(x,y_{n-1},z)(t-\tau)^{\alpha-1}\,d\tau,\\ z_n(t) &= z(0)+\frac{1}{\Gamma(\alpha)}\int_0^t F_3(x,y,z_{n-1})(t-\tau)^{\alpha-1}\,d\tau, \end{aligned}$$

with initial conditions $x_0(t)=x(0)$, $y_0(t)=y(0)$, and $z_0(t)=z(0)$. Therefore, we have

$$\begin{aligned} \varphi_{1_n}(t) &= x_n(t)-x_{n-1}(t)\\ &= \frac{1}{\Gamma(\alpha)}\int_0^t\left(F_1(x_{n-1},y,z)-F_1(x_{n-2},y,z)\right)(t-\tau)^{\alpha-1}\,d\tau,\\ \varphi_{2_n}(t) &= y_n(t)-y_{n-1}(t)\\ &= \frac{1}{\Gamma(\alpha)}\int_0^t\left(F_2(x,y_{n-1},z)-F_2(x,y_{n-2},z)\right)(t-\tau)^{\alpha-1}\,d\tau,\\ \varphi_{3_n}(t) &= z_n(t)-z_{n-1}(t)\\ &= \frac{1}{\Gamma(\alpha)}\int_0^t\left(F_3(x,y,z_{n-1})-F_3(x,y,z_{n-2})\right)(t-\tau)^{\alpha-1}\,d\tau, \end{aligned} \tag{6}$$

where $x_n(t)=\sum_{j=1}^n\varphi_{1_n}(t)$, $y_n(t)=\sum_{j=1}^n\varphi_{2_n}(t)$, and $z_n(t)=\sum_{j=1}^n\varphi_{3_n}(t)$. Now, we evaluate the norm of Equation (6). We achieve

$$\begin{aligned} \|\varphi_{1_n}(t)\| &= \|x_n(t)-x_{n-1}(t)\|\\ &\le \frac{1}{\Gamma(\alpha)}\int_0^t\|\left(F_1(x_{n-1},y,z)\right.\end{aligned}$$

$$
\begin{aligned}
&-F_1(x_{n-2},y,z)\big)\,(t-\tau)^{\alpha-1}\,d\tau,\\
\left\|\varphi_{2_n}(t)\right\| &= \left\|y_n(t)-y_{n-1}(t)\right\|\\
&\le \frac{1}{\Gamma(\alpha)}\int_0^t \|\big(F_2(x,y_{n-1},z)\\
&-F_2(x,y_{n-2},z)\big)\,(t-\tau)^{\alpha-1}\,d\tau\|, \qquad (7)\\
\left\|\varphi_{3_n}(t)\right\| &= \left\|z_n(t)-z_{n-1}(t)\right\|\\
&\le \frac{1}{\Gamma(\alpha)}\int_0^t \|\big(F_3(x,y,z_{n-1})\\
&-F_3(x,y,z_{n-2})\big)\,(t-\tau)^{\alpha-1}\,d\tau\|.
\end{aligned}
$$

From Theorem 1, we have that the kernel satisfy the Lipschitz condition and hence Equation (7) becomes

$$
\begin{aligned}
\left\|x_n(t)-x_{n-1}(t)\right\| &\le \frac{g_1}{\Gamma(\alpha)}\int_0^t \left\|x_{n-1}-x_{n-2}\right\|(t-\tau)^{\alpha-1}\,d\tau,\\
\left\|y_n(t)-y_{n-1}(t)\right\| &\le \frac{g_2}{\Gamma(\alpha)}\int_0^t \left\|y_{n-1}-y_{n-2}\right\|(t-\tau)^{\alpha-1}\,d\tau,\\
\left\|z_n(t)-z_{n-1}(t)\right\| &\le \frac{g_3}{\Gamma(\alpha)}\int_0^t \left\|z_{n-1}-z_{n-2}\right\|(t-\tau)^{\alpha-1}\,d\tau.
\end{aligned}
$$

The last inequality gives

$$
\begin{aligned}
\left\|\varphi_{1_n}(t)\right\| &\le \frac{g_1}{\Gamma(\alpha)}\int_0^t \left\|\varphi_{1_{n-1}}(\tau)\right\|\,d\tau,\\
\left\|\varphi_{2_n}(t)\right\| &\le \frac{g_2}{\Gamma(\alpha)}\int_0^t \left\|\varphi_{2_{n-1}}(\tau)\right\|\,d\tau, \qquad (8)\\
\left\|\varphi_{3_n}(t)\right\| &\le \frac{g_3}{\Gamma(\alpha)}\int_0^t \left\|\varphi_{3_{n-1}}(\tau)\right\|\,d\tau.
\end{aligned}
$$

Finally, the existence of a solution is given by the following theorem.

Theorem 2. The solution of model (Equation 3) has a solution under the condition if we have t_1 such that $\left(\frac{t_1 g_i}{\Gamma(\alpha+1)}\right) < 1,\ i=1,2,3.$

Proof. We assume that $x(t)$, $y(t)$, and $z(t)$ are bounded and their kernel $F_i,\ i=1,2,3$ satisfy the Lipschitz condition. According to Equation (8), we obtain

$$
\begin{aligned}
\left\|\varphi_{1_n}(t)\right\| &\le \left\|x_0(t)\right\|\left[\frac{t_1 g_1}{\Gamma(\alpha+1)}\right]^n,\\
\left\|\varphi_{2_n}(t)\right\| &\le \left\|y_0(t)\right\|\left[\frac{t_1 g_2}{\Gamma(\alpha+1)}\right]^n, \qquad (9)\\
\left\|\varphi_{3_n}(t)\right\| &\le \left\|z_0(t)\right\|\left[\frac{t_1 g_3}{\Gamma(\alpha+1)}\right]^n,
\end{aligned}
$$

which represent the existence and continuity of the system. To show that the solution of the model (Equation 3) can be set up from the functions in Equation (9), we assume

$$
\begin{aligned}
x(t)-x(0) &= x_n(t)-Q_{1_n}(t),\\
y(t)-y(0) &= y_n(t)-Q_{2_n}(t), \qquad (10)\\
z(t)-z(0) &= z_n(t)-Q_{3_n}(t).
\end{aligned}
$$

where $Q_{i_n},\ i=1,2,3$ are the remaining terms. Furthermore, the given terms would be demonstrated to hold $\left\|Q_{i_\infty}\right\| \to 0\ \forall i = 1,2,3$. Denoting that

$$
\begin{aligned}
\|Q_{1n}\|(t) &\le \left\|\frac{1}{\Gamma(\alpha)}\int_0^t \big(F_1(x,y,z)-F_1(x_{n-1},y,z)\big)\,d\tau\right\|\\
&\le \frac{1}{\Gamma(\alpha)}\int_0^t \left\|F_1(x,y,z)-F_1(x_{n-1},y,z)\right\|\,d\tau\\
&\le \frac{tg_1}{\Gamma(\alpha+1)}\left\|x-x_{n-1}\right\|,\\
\|Q_{2n}\|(t) &\le \left\|\frac{1}{\Gamma(\alpha)}\int_0^t \big(F_2(x,y,z)-F_2(x,y_{n-1},z)\big)\,d\tau\right\|\\
&\le \frac{1}{\Gamma(\alpha)}\int_0^t \left\|F_2(x,y,z)-F_2(x,y_{n-1},z)\right\|\,d\tau \qquad (11)\\
&\le \frac{tg_2}{\Gamma(\alpha+1)}\left\|y-y_{n-1}\right\|.\\
\|Q_{3n}\|(t) &\le \left\|\frac{1}{\Gamma(\alpha)}\int_0^t \big(F_3(x,y,z)-F_3(x,y,z_{n-1})\big)\,d\tau\right\|\\
&\le \frac{1}{\Gamma(\alpha)}\int_0^t \left\|F_3(x,y,z)-F_3(x,y,z_{n-1})\right\|\,d\tau\\
&\le \frac{tg_3}{\Gamma(\alpha+1)}\left\|z-z_{n-1}\right\|.
\end{aligned}
$$

By applying a recursive pattern, we acquire

$$
\begin{aligned}
\left\|Q_{1_n}(t)\right\| &\le \left[\frac{t}{\Gamma(\alpha+1)}\right]^{n+1} g_1^n k,\\
\left\|Q_{2_n}(t)\right\| &\le \left[\frac{t}{\Gamma(\alpha+1)}\right]^{n+1} g_2^n k, \qquad (12)\\
\left\|Q_{3_n}(t)\right\| &\le \left[\frac{t}{\Gamma(\alpha+1)}\right]^{n+1} g_3^n k.
\end{aligned}
$$

At the point t_1, we have

$$
\begin{aligned}
\left\|Q_{1_n}(t)\right\| &\le \left[\frac{t_1}{\Gamma(\alpha+1)}\right]^{n+1} g_1^n k,\\
\left\|Q_{2_n}(t)\right\| &\le \left[\frac{t_1}{\Gamma(\alpha+1)}\right]^{n+1} g_2^n k, \qquad (13)\\
\left\|Q_{3_n}(t)\right\| &\le \left[\frac{t_1}{\Gamma(\alpha+1)}\right]^{n+1} g_3^n k.
\end{aligned}
$$

By considering the results of Theorem 1 and applying $n \to \infty$ to both sides, we have $\left\|Q_{i_\infty}\right\| \to 0\ \forall i = 1,2,3$.

In the end, we will show that the solution is unique for each initial value by utilizing the contradiction approach. Suppose that there exists another solution of the model (Equation 3), namely $x_1(t)$, $y_1(t)$, and $z_1(t)$. Then, we have

$$
\begin{aligned}
x(t)-x_1(t) &= \frac{1}{\Gamma(\alpha)}\int_0^t \big(F_1(x,y,z)-F_1(x_{n-1},y,z)\big)\,d\tau,\\
y(t)-y_1(t) &= \frac{1}{\Gamma(\alpha)}\int_0^t \big(F_2(x,y,z)-F_2(x,y_{n-1},z)\big)\,d\tau, \qquad (14)
\end{aligned}
$$

$$z(t) - z_1(t) = \frac{1}{\Gamma(\alpha)} \int_0^t \left(F_3(x,y,z) - F_3(x,y,z_{n-1})\right)\, d\tau.$$

Applying the norm on both sides, we achieve

$$\begin{aligned}
\left\|x(t) - x_1(t)\right\| &\leq \frac{1}{\Gamma(\alpha)} \int_0^t \left\|F_1(x,y,z) - F_1(x_{n-1},y,z)\right\|\, d\tau,\\
\left\|y(t) - y_1(t)\right\| &\leq \frac{1}{\Gamma(\alpha)} \int_0^t \left\|F_2(x,y,z) - F_2(x,y_{n-1},z)\right\|\, d\tau,\\
\left\|z(t) - z_1(t)\right\| &\leq \frac{1}{\Gamma(\alpha)} \int_0^t \left\|F_3(x,y,z) - F_3(x,y,z_{n-1})\right\|\, d\tau.
\end{aligned} \tag{15}$$

By considering Theorem 1, we obtain

$$\begin{aligned}
\left\|x(t) - x_1(t)\right\| &\leq \frac{tg_1}{\Gamma(\alpha+1)} \left\|x(t) - x_1(t)\right\|,\\
\left\|y(t) - y_1(t)\right\| &\leq \frac{tg_2}{\Gamma(\alpha+1)} \left\|y(t) - y_1(t)\right\|,\\
\left\|z(t) - z_1(t)\right\| &\leq \frac{tg_3}{\Gamma(\alpha+1)} \left\|z(t) - z_1(t)\right\|.
\end{aligned}$$

Therefore, the following equations are obtained.

$$\begin{aligned}
\left\|x(t) - x_1(t)\right\| \left(1 - \frac{tg_1}{\Gamma(\alpha+1)}\right) &\leq 0,\\
\left\|y(t) - y_1(t)\right\| \left(1 - \frac{tg_2}{\Gamma(\alpha+1)}\right) &\leq 0,\\
\left\|z(t) - z_1(t)\right\| \left(1 - \frac{tg_3}{\Gamma(\alpha+1)}\right) &\leq 0.
\end{aligned} \tag{16}$$

As a result, we achieve $\left\|x(t) - x_1(t)\right\| = 0$, $\left\|y(t) - y_1(t)\right\| = 0$, and $\left\|z(t) - z_1(t)\right\| = 0$, which impact $x(t) = x_1(t)$, $y(t) = y_1(t)$, and $z(t) = z_1(t)$. Then, we finally give the following theorem.

Theorem 3. The Caputo fractional-order predator–prey model (Equation 3) has a unique solution.

3. Non-negativity and boundedness

In this section, we will show that for any initial condition is in $\mathbb{R}^3_+$ where

$$\mathbb{R}^3_+ := \left\{(x,y,z) : x \geq 0,\ y \geq 0,\ z \geq 0,\ x \in \mathbb{R},\ y \in \mathbb{R}\right\}.$$

The solution not only exists and is unique but also bounded and always in $\mathbb{R}^3_+$ as $t \to \infty$. Therefore, we have the following two theorems.

Theorem 4. If the initial condition in $\mathbb{R}^3_+$ then both population densities of prey and predator given by model (Equation 3) remain in $\mathbb{R}^3_+$.

Proof. To prove this non-negativity condition, we apply *reductio ad absurdum* (contradiction method), which is also used in Barman et al. [24] and Maji [32]. We assume that there exists $\hat{t} > 0$ such that

$$\begin{cases}
x(t) & > 0, \text{ when } 0 \leq t < \hat{t},\\
x(\hat{t}) & = 0, \text{ when } t = \hat{t}\\
x(\hat{t}^+) & < 0, \text{ when } t = \hat{t}^+.
\end{cases} \tag{17}$$

From the first equation in Equation (3) along with Equation (17), we have

$${}^C\mathcal{D}_t^{\alpha} x(t)|_{x(\hat{t})} = 0. \tag{18}$$

According to Lemma 3.1 in Barman et al. [33], we get $x(\hat{t}^+) = 0$ which contradicts with Equation (17) where $x(\hat{t}^+) < 0$. This means that $x(t) \geq 0$ for all $t \in [0,\infty]$. Similarly, we can show that $y(t) \geq 0$ and $z(t) \geq 0$ for all $t \in [0,\infty]$. In conclusion, we have the non-negative solution for model (Equation 3) when the initial values are in $\mathbb{R}^3_+$.

Theorem 5. The solution of model (Equation 3) is always bounded in $\mathbb{R}^3_+$ for the initial condition in $\mathbb{R}^3_+$.

Proof. Since we work the population model, it is natural that the population must be bounded due to the limitation of their biological resources, which is also known as environmental carrying capacity. Thus, the boundedness of the solution of the model (Equation 3) is also important to learn and prove. From Theorem 4, we can define a positive function as follows:

$$\mathcal{N}(t) = x + \frac{my}{n} + \frac{mz}{n}. \tag{19}$$

For any $\gamma > 0$, the following fractional-order differential equation holds.

$$\begin{aligned}
&{}^C\mathcal{D}_t^{\alpha}\mathcal{N}(t) + \gamma\mathcal{N}(t)\\
&= {}^C\mathcal{D}_t^{\alpha} x(t) + \frac{m}{n}{}^C\mathcal{D}_t^{\alpha} y(t) + \frac{m}{n}{}^C\mathcal{D}_t^{\alpha} y(t) + \gamma\mathcal{N}(t)\\
&= \left(rx\left(1 - \frac{x}{K}\right) - mxz - \frac{hx}{c+x}\right)\\
&\quad + \frac{m}{n}(nxz - \beta y - \delta_1 y - \omega y^2)\\
&\quad + \frac{m}{n}(\beta y - \delta_2 z) + \gamma x + \frac{\gamma my}{n} + \frac{\gamma mz}{n}\\
&= rx - \frac{rx^2}{K} - \frac{hx}{c+x} - \frac{\delta_1 my}{n} - \frac{\omega my^2}{n}\\
&\quad - \frac{\delta_2 mz}{n} + \gamma x + \frac{\gamma my}{n} + \frac{\gamma mz}{n}\\
&\leq rx - \frac{rx^2}{K} - \frac{\delta_1 my}{n} - \frac{\delta_2 mz}{n} + \gamma x + \frac{\gamma my}{n} + \frac{\gamma mz}{n}\\
&= (r+\gamma)x - \frac{rx^2}{K} + (\gamma - \delta_1)\frac{my}{n} + (\gamma - \delta_2)\frac{mz}{n}
\end{aligned}$$

By choosing $\gamma < \min\{\delta_1, \delta_2\}$, we obtain

$${}^C\mathcal{D}_t^{\alpha}\mathcal{N}(t) + \gamma\mathcal{N}(t) \leq (r+\gamma)x - \frac{rx^2}{K}$$

$$
\begin{aligned}
&= -\frac{r}{K}\left(x^2 - \frac{(r+\gamma)Kx}{r}\right)\\
&= -\frac{r}{K}\left(x^2 - \frac{(r+\gamma)Kx}{r} + \frac{(r+\gamma)^2K^2}{4r^2} - \frac{(r+\gamma)^2K^2}{4r^2}\right)\\
&= -\frac{r}{K}\left[\left(x - \frac{(r+\gamma)K}{2r}\right)^2 - \frac{(r+\gamma)^2K^2}{4r^2}\right]\\
&= -\frac{r}{K}\left(x - \frac{(r+\gamma)K}{2r}\right)^2 + \frac{(r+\gamma)^2K}{4r}\\
&\leq \frac{(r+\gamma)^2K}{4r}
\end{aligned}
$$

According to Lemma 3 in Panigoro et al. [34], we apply the comparison principle and obtain

$$\mathcal{N}(t) \leq \left(\mathcal{N}(0) - \frac{(r+\gamma)^2K}{4\gamma r}\right)E_\alpha[-\gamma t^\alpha] + \frac{(r+\gamma)^2K}{4\gamma r}. \quad (20)$$

For $t \to \infty$, we achieve $\mathcal{N}(t) \to \frac{(r+\gamma)^2K}{4\gamma r}$, which means all solutions of model (Equation 3) with non-negative initial conditions are confined to $\hat{\Omega}$ where

$$\hat{\Omega} := \left\{(x,y,z) \in \mathbb{R}^3_+ : \mathcal{N}(t) = x(t) + \frac{my(t)}{n} + \frac{mz(t)}{n} \leq \sigma,\ \sigma = \frac{(r+\gamma)^2K}{4\gamma r} + \varepsilon,\ \varepsilon > 0\right\}. \quad (21)$$

4. Global dynamics

In this section, the global dynamics of model (Equation 3) are investigated. Note that all biological equilibrium points, their existence conditions, and their local stability are successfully described in Panigoro et al. [29], which can be rewritten by the following theorem.

Theorem 6. (i) The origin point $\mathcal{E}_o = (0,0,0)$ always exists. It is locally asymptotically stable (LAS) if $r < \frac{h}{c}$.

(ii) The axial point $\mathcal{E}_A = (\hat{x},0,0)$ where $\hat{x}$ is the positive root of $x^2 + (c-K)x + \left(\frac{h}{r} - c\right)K = 0$, which has

(a) an equilibrium point if $c > \frac{h}{r}$.

(b) a pair of equilibrium points if $c < \min\left\{K, \frac{h}{r}\right\}$.

Moreover, it is LAS if $h < \frac{(c+\hat{x})^2 r}{K}$ and $\hat{x} < \frac{(\beta+\delta_1)\delta_2}{\beta n}$.

(iii) The interior point $\mathcal{E}_I = (x^*, y^*, z^*)$ exists, if $a_i,\ i = 2,3$ in Panigoro et al. [29] satisfies the following statements.

(a) An equilibrium point in $\mathbb{R}^3_+$ if $a_3 < 0$.

(b) Two equilibrium points in $\mathbb{R}^3_+$ if $a_2 < 0$ and $a_3 > 0$.

The LAS condition of $\mathcal{E}_I$ can be seen in Theorem 4 in Panigoro et al. [29].

Note that all equilibrium points may attain local asymptotic stability with several biological conditions. Now, we will identify the biological properties to obtain globally asymptotically stable (GAS) for each equilibrium point. The analytical results are given by the following three theorems.

Theorem 7. The origin point $\mathcal{E}_o = (0,0,0)$ is GAS if $r \leq \frac{h}{c+\sigma}$.

Proof. We define the positive definite Lyapunov function as follows:

$$\mathcal{V}_1(x,y,z) = x + \frac{my}{n} + \frac{mz}{n} \quad (22)$$

By applying Lemma 3.1 in Vargas-De-León [35], we compute the $\alpha-$order derivative of $\mathcal{V}_1(x,y,z)$ along the solution of the model (Equation 3) as follows:

$$
\begin{aligned}
{}^C\mathcal{D}_t^\alpha \mathcal{V}_1(x,y,z) &\leq {}^C\mathcal{D}_t^\alpha x + \frac{m}{n}{}^C\mathcal{D}_t^\alpha y + \frac{m}{n}{}^C\mathcal{D}_t^\alpha z\\
&= \left(rx\left(1 - \frac{x}{K}\right) - mxz - \frac{hx}{c+x}\right)\\
&\quad + \frac{m}{n}(nxz - \beta y - \delta_1 y - \omega y^2)\\
&\quad + \frac{m}{n}(\beta y - \delta_2 z)\\
&= rx - \frac{rx^2}{K} - mxz - \frac{hx}{c+x} + mxz\\
&\quad - \frac{\beta my}{n} - \frac{\delta_1 my}{n} - \frac{\omega my^2}{n} + \frac{\beta my}{n} - \frac{\delta_2 mz}{n}\\
&= rx - \frac{rx^2}{K} - \frac{hx}{c+x} - \frac{\delta_1 my}{n} - \frac{\omega my^2}{n} - \frac{\delta_2 mz}{n}\\
&\leq rx - \frac{hx}{c+x} - \frac{\delta_1 my}{n} - \frac{\delta_2 mz}{n}.
\end{aligned}
$$

From Equation (21), we have $x \leq \sigma$ and hence

$$
\begin{aligned}
{}^C\mathcal{D}_t^\alpha \mathcal{V}_1(x,y,z) &\leq rx - \frac{hx}{c+\sigma} - \frac{\delta_1 my}{n} - \frac{\delta_2 mz}{n}\\
&= -\left(\frac{h}{c+\sigma} - r\right)x - \frac{\delta_1 my}{n} - \frac{\delta_2 mz}{n}
\end{aligned}
$$

Therefore, ${}^C\mathcal{D}_t^\alpha \mathcal{V}_1(x,y,z) \leq 0$ for all $(x,y,z) \in \mathbb{R}^3_+$, if $r \leq \frac{h}{c+\sigma}$. We also find that ${}^C\mathcal{D}_t^\alpha \mathcal{V}_1(x,y,z) = 0$, if $(x,y,z) = (0,0,0)$. This conveys that $\{\mathcal{E}_o\}$ is the only invariant set on which ${}^C\mathcal{D}_t^\alpha \mathcal{V}_1(x,y,z) = 0$. Obeying Lemma 4.6 in Huo et al. [20], $r \leq \frac{h}{c+\sigma}$ obviously becomes the biological condition of $\mathcal{E}_o$ to reach GAS.

Theorem 8. The axial point $\mathcal{E}_A = (\hat{x},0,0)$ is GAS if $\frac{hK}{cr} < \hat{x} < \frac{\delta_2}{n}$.

Proof. We construct a positive definite Lyapunov function based on the Volterra equation as follows:

$$\mathcal{V}_2(x,y,z) = \left(x - \hat{x} - \hat{x}\ln\frac{x}{\hat{x}}\right) + \frac{my}{n} + \frac{mz}{n}. \tag{23}$$

The α-order derivative of $\mathcal{V}_2(x,y,z)$ along the solution of the model (Equation 3) given by Lemma 3.1 in Vargas-De-León [35] is given by

$$\begin{aligned}
{}^{C}\mathcal{D}_t^{\alpha}\mathcal{V}_2(x,y,z) &\leq \left(\frac{x-\hat{x}}{x}\right){}^{C}\mathcal{D}_t^{\alpha}x + \frac{m\,{}^{C}\mathcal{D}_t^{\alpha}y}{n} + \frac{m\,{}^{C}\mathcal{D}_t^{\alpha}z}{n}\\
&= \left(\frac{x-\hat{x}}{x}\right)\left(rx\left(1-\frac{x}{K}\right) - mxz - \frac{hx}{c+x}\right)\\
&\quad Z + \frac{m}{n}\left(nxz - \beta y - \delta_1 y - \omega y^2\right) +\\
&\quad \frac{m}{n}\left(\beta y - \delta_2 z\right)\\
&= (x-\hat{x})\left(r - \frac{rx}{K} - mz - \frac{h}{c+x}\right) + mxz\\
&\quad - \frac{m\delta_1 y}{n} - \frac{m\omega y^2}{n} - \frac{m\delta_2 z}{n}\\
&= (x-\hat{x})\left(-\frac{r}{K}(x-\hat{x}) + \frac{h(x-\hat{x})}{(c+x)(c+\hat{x})} - mz\right)\\
&\quad + mxz - \frac{m\delta_1 y}{n} - \frac{m\omega y^2}{n} - \frac{m\delta_2 z}{n}\\
&= -\frac{r}{K}(x-\hat{x})^2 + \frac{h(x-\hat{x})^2}{(c+x)(c+\hat{x})} + m\hat{x}z\\
&\quad - \frac{m\delta_1 y}{n} - \frac{m\omega y^2}{n} - \frac{m\delta_2 z}{n}\\
&\leq -\frac{r}{K}(x-\hat{x})^2 + \frac{h(x-\hat{x})^2}{c\hat{x}}\\
&\quad + m\hat{x}z - \frac{m\delta_1 y}{n} - \frac{m\delta_2 z}{n}\\
&= -\left(\frac{r}{K} - \frac{h}{c\hat{x}}\right)(x-\hat{x})^2 - \frac{m\delta_1 y}{n}\\
&\quad - \left(\frac{\delta_2}{n} - \hat{x}\right)mz
\end{aligned}$$

Since $\frac{hK}{cr} < \hat{x} < \frac{\delta_2}{n}$, we have ${}^{C}\mathcal{D}_t^{\alpha}\mathcal{V}_2(x,y,z) \leq 0$ for all $(x,y,z) \in \mathbb{R}^3_+$. It is also clear that ${}^{C}\mathcal{D}_t^{\alpha}\mathcal{V}_2(x,y,z) = 0$ if $(x,y,z) = (\hat{x},0,0)$. This confirms that $\{\mathcal{E}_A\}$ is the only invariant set on which ${}^{C}\mathcal{D}_t^{\alpha}\mathcal{V}_2(x,y,z) = 0$. Therefore, $\mathcal{E}_A$ is GAS due to Lemma 4.6 in Huo et al. [20]. This confirms the justifiability of Theorem 8.

Theorem 9. Let $\Omega_X := \left\{(x,y,z) : \frac{z^*}{z} < \frac{(1-mx^*)my^* - n\sigma}{(1+\sigma m)my^*}\right\}$ and $h < \frac{c^2 r}{K}$. The interior point $\mathcal{E}_I = (x^*,y^*,z^*)$ is GAS in Ω_X.

Proof. Consider a positive definite Lyapunov function as follows:

$$\mathcal{V}_3(x,y,z) = \left(x - x^* - x^*\ln\frac{x}{x^*}\right) + \frac{m}{n}\left(y - y^* - y^*\ln\frac{x}{y^*}\right) + \frac{1}{\delta_2}\frac{(z-z^*)^2}{2z^*}. \tag{24}$$

By applying Lemma 3.1 in Vargas-De-León [35] and Lemma 1 in Aguila-Camacho et al. [36], we obtain the α-order derivative of $\mathcal{V}_3(x,y,z)$ as follows:

$$\begin{aligned}
{}^{C}\mathcal{D}_t^{\alpha}\mathcal{V}_3(x,y,z) &\leq \left(\frac{x-x^*}{x}\right){}^{C}\mathcal{D}_t^{\alpha}x + \frac{m}{n}\left(\frac{y-y^*}{y}\right)\\
&\quad {}^{C}\mathcal{D}_t^{\alpha}y + \frac{1}{\delta_2}\left(\frac{z-z^*}{z^*}\right){}^{C}\mathcal{D}_t^{\alpha}z\\
&= \left(\frac{x-x^*}{x}\right)\left(rx\left(1-\frac{x}{K}\right) - mxz - \frac{hx}{c+x}\right)\\
&\quad + \frac{m}{n}\left(\frac{y-y^*}{y}\right)\left(nxz - \beta y - \delta_1 y - \omega y^2\right)\\
&\quad + \frac{1}{\delta_2}\left(\frac{z-z^*}{z^*}\right)\left(\beta y - \delta_2 z\right)\\
&= (x-x^*)\left(-\frac{r}{K}(x-x^*) - m(z-z^*)\right.\\
&\quad \left. + \frac{h(x-x^*)}{(c+x)(c+x^*)}\right)\\
&\quad + (y-y^*)\left(\frac{mxz}{y} - \frac{mx^*z^*}{y^*} - \frac{m\omega(y-y^*)}{n}\right)\\
&\quad + (z-z^*)\left(\frac{y}{y^*} - 1 - \frac{z-z^*}{z^*}\right)\\
&= -\frac{r}{K}(x-x^*)^2 + mz^*x + mx^*z\\
&\quad + \frac{h(x-x^*)^2}{(c+x)(c+x^*)}\\
&\quad * - \frac{my^*xz}{y} - \frac{mx^*z^*y}{y^*}\\
&\quad - \frac{m\omega(y-y^*)^2}{n} + \frac{yz}{y^*} - \frac{z^*y}{y^*}\\
&\quad - z + z^* - \frac{(z-z^*)^2}{z^*}.
\end{aligned}$$

Applying Equation (21), we have

$$\begin{aligned}
{}^{C}\mathcal{D}_t^{\alpha}\mathcal{V}_3(x,y,z) &\leq -\left(\frac{r}{K} - \frac{h}{c^2}\right)(x-x^*)^2\\
&\quad - \frac{m\omega(y-y^*)^2}{n} - \frac{(z-z^*)^2}{z^*}\\
&\quad - \left(1 - mx^* - \frac{\sigma n}{my^*}\right)z + (1+\sigma m)z^*.
\end{aligned}$$

Since $\frac{z^*}{z} < \frac{(1-mx^*)my^* - n\sigma}{(1+\sigma m)my^*}$, we achieve

$$\begin{aligned}
{}^{C}\mathcal{D}_t^{\alpha}\mathcal{V}_2(x,y,z) &\leq -\left(\frac{r}{K} - \frac{h}{c^2}\right)(x-x^*)^2\\
&\quad - \frac{m\omega(y-y^*)^2}{n} - \frac{(z-z^*)^2}{z^*}.
\end{aligned}$$

Thus, ${}^{C}\mathcal{D}_t^{\alpha}\mathcal{V}_3(x,y,z) \leq 0$ for all $(x,y,z) \in \mathbb{R}^3_+$, when $h < \frac{c^2 r}{K}$. We also confirm that ${}^{C}\mathcal{D}_t^{\alpha}\mathcal{V}_3(x,y,z) = 0$ if $(x,y,z) =$

(x^*, y^*, z^*) and hence $\{\mathcal{E}_I\}$ is the only invariant set on which ${}^C\mathcal{D}_t^{\alpha}\mathcal{V}_3(x, y, z) = 0$. Based on Lemma 4.6 in Huo et al. [20], the interior point $\mathcal{E}_I$ is GAS in Ω_X. This ends the proof.

5. Bifurcation analysis

In this section, we will study the occurrence of several phenomena namely transcritical, saddle-node, backward, and Hopf bifurcations. Two parameters are chosen, namely the harvesting rate (h) and the order of the derivative (α), as the memory index. For the analytical purpose, we define the following parameter.

$$h_1^* = cr,$$
$$h_2^* = \frac{(c+K)^2 r}{4K},$$
$$\alpha^* = \frac{2}{\pi}\arctan\left|\frac{\zeta_2}{\zeta_1}\right|.$$

Next, the following theorem is given for describing the occurrence of transcritical bifurcation driven by the harvesting rate (h) as the bifurcation parameter.

Theorem 10. The origin point $\mathcal{E}_o$ and the axial point $\mathcal{E}_A$ exchange their stability *via* transcritical bifurcation when h passes through h_1^*.

Proof. Since the axial consists of two equilibrium points, we focus on the axial point nearest to the origin point. When $h = h_1^*$, the axial point merge with the origin point $\mathcal{E}_0 = \mathcal{E}_A = (0, 0, 0)$ where the eigenvalues of the Jacobian matrix are: $\lambda_1 = 0$, $\lambda_2 = (\beta + \delta_1)$, and $\lambda_3 = -\delta_2$. We obtain $\left|\arg(\lambda_{2,3})\right| = \pi > \alpha\pi/2$ while $\left|\arg(\lambda_1)\right| = \alpha\pi/2$. This means $\mathcal{E}_0 = \mathcal{E}_A = (0, 0, 0)$ is non-hyperbolic. When $h_1^* < h < \frac{(c+K)^2 r}{4K}$, by applying Theorems 2 and 3 in Panigoro et al. [29], $\mathcal{E}_0$ becomes LAS while the nearest $\mathcal{E}_A$ becomes a saddle point. For $0 < h < h_1^*$, The origin $\mathcal{E}_0$ becomes unstable and the nearest $\mathcal{E}_A \notin \mathbb{R}_+^3$ becomes unstable. This condition shows the existence of transcritical bifurcation, where h becomes the bifurcation parameter while $h = h_1^*$ is the bifurcation point.

Now, the existence of saddle-node bifurcation on axial will be proven by still regarding the harvesting rate (h) as the bifurcation parameter. As a result, the following theorem is proposed.

Theorem 11. Suppose that $c < \min\left\{\frac{h}{r}, K\right\}$. The axial point $\mathcal{E}_A$ undergoes saddle-node bifurcation when h passes through the bifurcation point h_2^*.

Proof. According to Theorem 1 in Panigoro et al. [29], the axial point does not exist when $h > h_2^*$. When $h = h_2^*$, a unique equilibrium point $\mathcal{E}_A = \left(\frac{K-c}{2}, 0, 0\right)$ occurs in axial where its Jacobian matrix has three eigenvalues: $\lambda_1 = 0$ and $\lambda_{2,3} = -\frac{1}{2}\left[\beta + \delta_1 + \delta_2 + \sqrt{(\beta + \delta_1 - \delta_2)^2 + 2\beta n(K - c)}\right]$. Since $\left|\arg(\lambda_1)\right| = \alpha\pi/2$, this axial point is non-hyperbolic. When $h < h^*$, two axial points occurs given by $\mathcal{E}_A^a = (\hat{x}_a, 0, 0)$ and $\mathcal{E}_A^b = (\hat{x}_b, 0, 0)$, where $\hat{x}_a = \frac{K-c}{2} + \sqrt{\frac{(h^*-h)K}{r}}$ and $\hat{x}_b = \frac{K-c}{2} - \sqrt{\frac{(h^*-h)K}{r}}$. It is easy to validate that both $\mathcal{E}_A^a$ and $\mathcal{E}_A^b$ are in $\mathbb{R}_+^3$ and have different stability. As a consequence, all the given circumstances express the occurrence of saddle-node bifurcation.

Based on Theorems 10 and 11, we obtain more global bifurcation namely backward bifurcation given by the following lemma.

Lemma 1. The model (Equation 3) undergoes backward bifurcation driven by the harvesting rate (h).

Proof. From previous theorems, the axial point $\mathcal{E}_A^a$ exists and is LAS, while $\mathcal{E}_o$ is unstable when $h < h_1^*$. When $h_1^* < h < h_2^*$, $\mathcal{E}_o$ becomes LAS, $\mathcal{E}_A^a$ still exists and is LAS, and unstable $\mathcal{E}_A^b$ occurs. The bistability condition is held for this interval of h which means that the convergence of the solution is very sensitive to the initial condition. Finally, those two axial points merge when $h = h_2^*$ and disappear when $h > h_2^*$. This completes the proof.

Finally, we will show that the memory index in this case, that is, the order of the derivative (α), affects the dynamical behaviors of the model (Equation 3) indicated by the appearance of Hopf bifurcation around the interior point $\mathcal{E}_I$.

Theorem 12. Suppose the characteristic equation of the Jacobian matrix evaluated at $\mathcal{E}_I$ can be written as $\lambda^3 + \xi_1\lambda^2 + \xi_2\lambda + \xi_3 = 0$, which has a pair of complex conjugate eigenvalues $\lambda_{1,2} = \zeta_1 \pm i\zeta_2$, where $\zeta_1 > 0$ and one real negative eigenvalue ($\lambda_3 < 0$). The model (Equation 3) undergoes a Hopf bifurcation when the order of the fractional derivative α crosses out the critical value $\alpha^* = \frac{2}{\pi}\arctan\left|\frac{\zeta_2}{\zeta_1}\right|$.

Proof. From the earlier assumptions, we have $\min_{1\le i\le 3}\left|\arg(\lambda_i)\right| = \arctan\left|\frac{\zeta_2}{\zeta_1}\right|$. Therefore, the solution of $m(\alpha^*) = \alpha^*\frac{\pi}{2} - \min\left|\arg(\lambda_i)\right| = 0$ is only when $\alpha^* = \frac{2}{\pi}\arctan\left|\frac{\zeta_2}{\zeta_1}\right|$. If we check the transversal condition: $\frac{dm(\alpha)}{d\alpha}|_{\alpha=\alpha^*} = \frac{\pi}{2}$ which is not equal to 0, we can assure that the sign of $m(\alpha)$ changes when the bifurcation parameter α passing by α^*. It means that the equilibrium point $\mathcal{E}_I$ is stable when $\alpha \in (0, \alpha^*)$ and is unstable for $\alpha^* < \alpha < 1$.

6. Numerical simulations

In this section, we explore the dynamical behaviors of the model (Equation 3) numerically to support analytical findings,

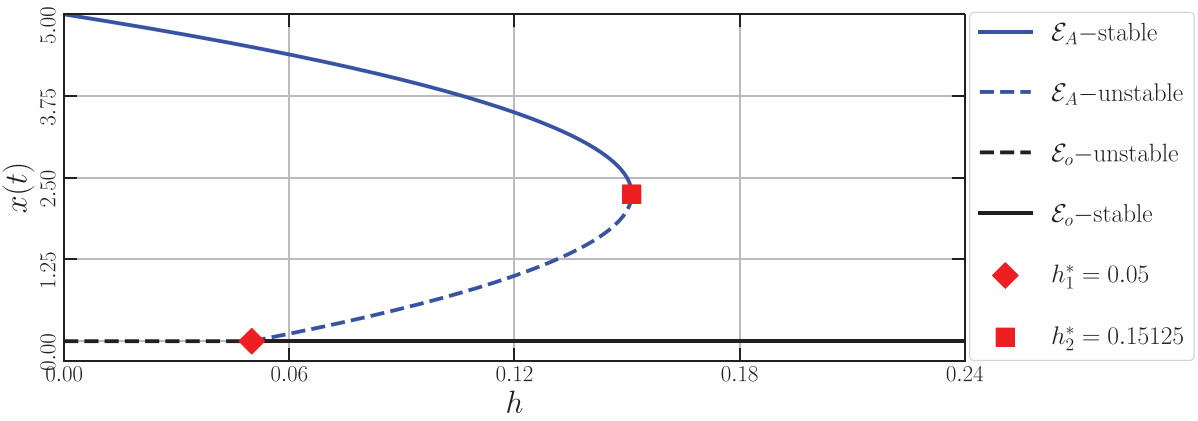

FIGURE 1
Bifurcation diagram driven by the harvesting rate (h) of the model (Equation 3) around the axial point using the parameter values: $r = 0.1$, $K = 5$, $m = 0.25$, $c = 0.5$, $n = 0.01$, $\beta = 0.06$, $\delta_1 = 0.05$, $\delta_2 = 0.05$, $\omega = 0.1$, and $\alpha = 0.9$.

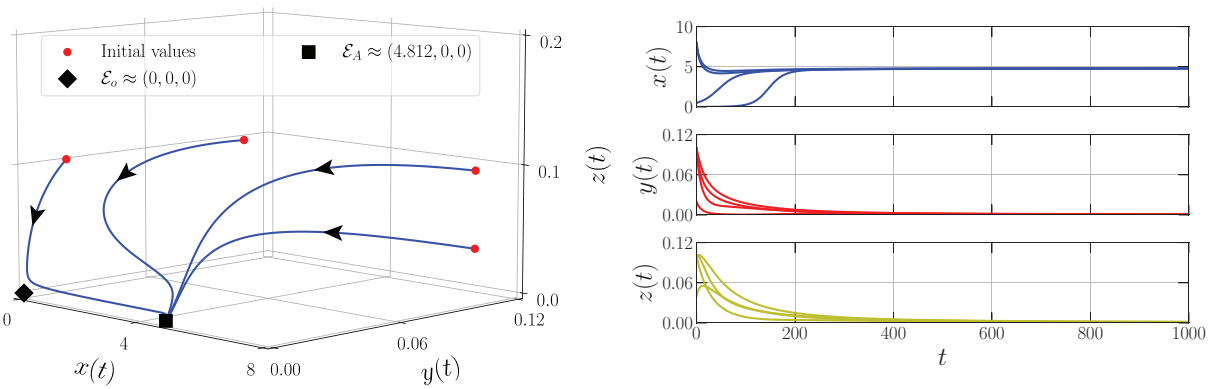

FIGURE 2
Phase portrait and time series of the model (Equation 3) using parameter values: $r = 0.1$, $K = 5$, $m = 0.25$, $c = 0.5$, $n = 0.01$, $\beta = 0.06$, $\delta_1 = 0.05$, $\delta_2 = 0.05$, $\omega = 0.1$, $\alpha = 0.9$, and $h = 0.02$.

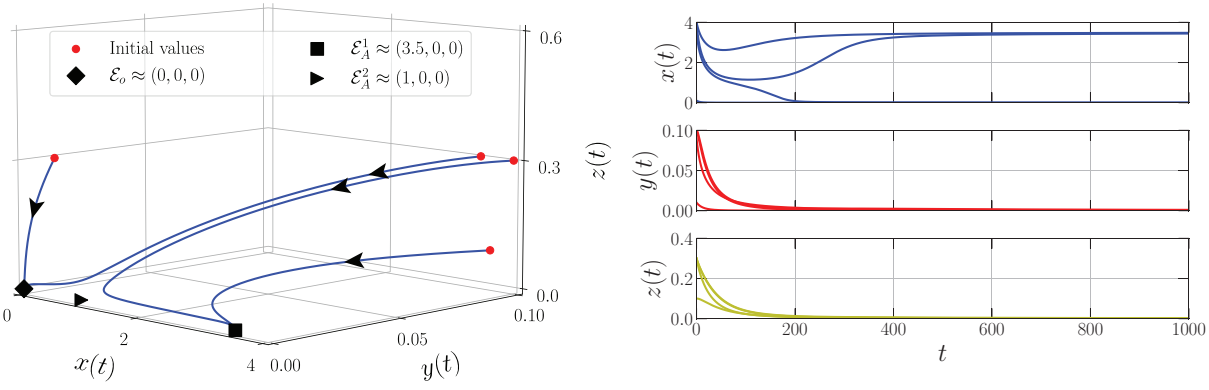

FIGURE 3
Phase portrait and time series of the model (Equation 3) using parameter values: $r = 0.1$, $K = 5$, $m = 0.25$, $c = 0.5$, $n = 0.01$, $\beta = 0.06$, $\delta_1 = 0.05$, $\delta_2 = 0.05$, $\omega = 0.1$, $\alpha = 0.9$, and $h = 0.12$.

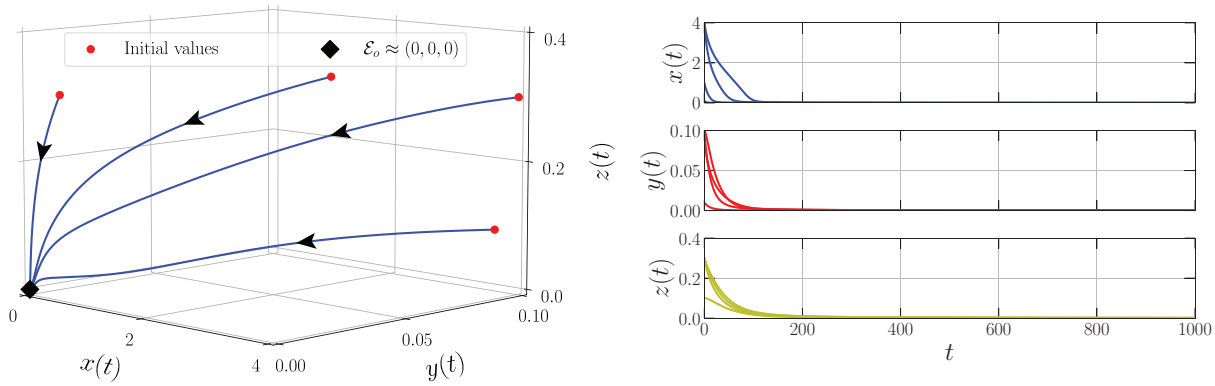

FIGURE 4
Phase portrait and time series of the model (Equation 3) using parameter values: $r = 0.1$, $K = 5$, $m = 0.25$, $c = 0.5$, $n = 0.01$, $\beta = 0.06$, $\delta_1 = 0.05$, $\delta_2 = 0.05$, $\omega = 0.1$, $\alpha = 0.9$, and $h = 0.18$.

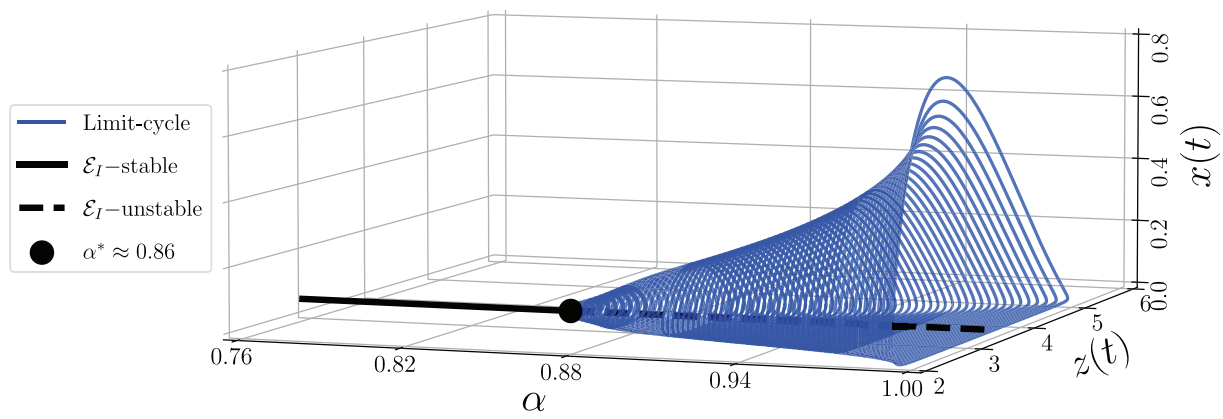

FIGURE 5
Bifurcation diagram driven by the order of the derivative (α) of model (Equation 3) around the axial point $\mathcal{E}_I$ using parameter values: $r = 0.8$, $K = 5$, $m = 0.25$, $h = 0.01$, $c = 0.08$, $n = 0.2$, $\beta = 0.4$, $\delta_1 = 0.01$, $\delta_2 = 0.01$, $\delta_2 = 0.01$, and $\omega = 0.1$.

especially the occurrence of bifurcation. The predictor–corrector scheme given by Diethelm et al. [37] is employed. All of the parameters used in these simulations are assumptions matched with the biological conditions given by the previous analysis results. This decision was taken because this work does not specifically address an ecological case involving a particular organism.

To show the occurrence of several bifurcations driven by the harvesting rate (h), we first set the parameter as follows:

$$r = 0.1,\ K = 5,\ m = 0.25,\ c = 0.5,\ n = 0.01,$$
$$\beta = 0.06,\ \delta_1 = 0.05,\ \delta_2 = 0.05,\ \omega = 0.1,\ \alpha = 0.9. \quad (25)$$

By varying the harvesting rate in the interval $0 \leq h \leq 0.24$, the bifurcation diagram is portrayed as in Figure 1. We have three types of dynamic behaviors around the axial point. When $0 \leq h < h_1^* = 0.05$, we have unstable origin point $\mathcal{E}_o$ and LAS $\mathcal{E}_A$. The origin point losses its stability *via* transcritical bifurcation when h crosses h_1^* and the unstable axial point $\mathcal{E}_A$ occurs simultaneously. These dynamics are maintained for interval $h_1^* < h < h_2^* = 0.15125$. On the other hand, the stable branch of axial point $\mathcal{E}_A$ is preserved for $0 \leq h < h_2^*$. The LAS point and unstable point of $\mathcal{E}_A$ merge into the non-hyperbolic point when $h = h_2^*$. The axial point finally disappeared when h passes through h_2^* while the sign of $\mathcal{E}_o$ does not change. Thus, we have saddle-node bifurcation on axial with h_2^* as the bifurcation point. If we observe from a more global point of view, these interesting phenomena represent the existence of backward bifurcation marked by the occurrence of bistability condition. To show these dynamical behaviors, we choose three values of harvesting rate in each interval: $h = 0.02, 0.12$, and 0.18 and portray them as phase portraits and time series (see Figures 2–4). The interesting phenomenon called bistability is portrayed in Figure 3. Two equilibrium points LAS

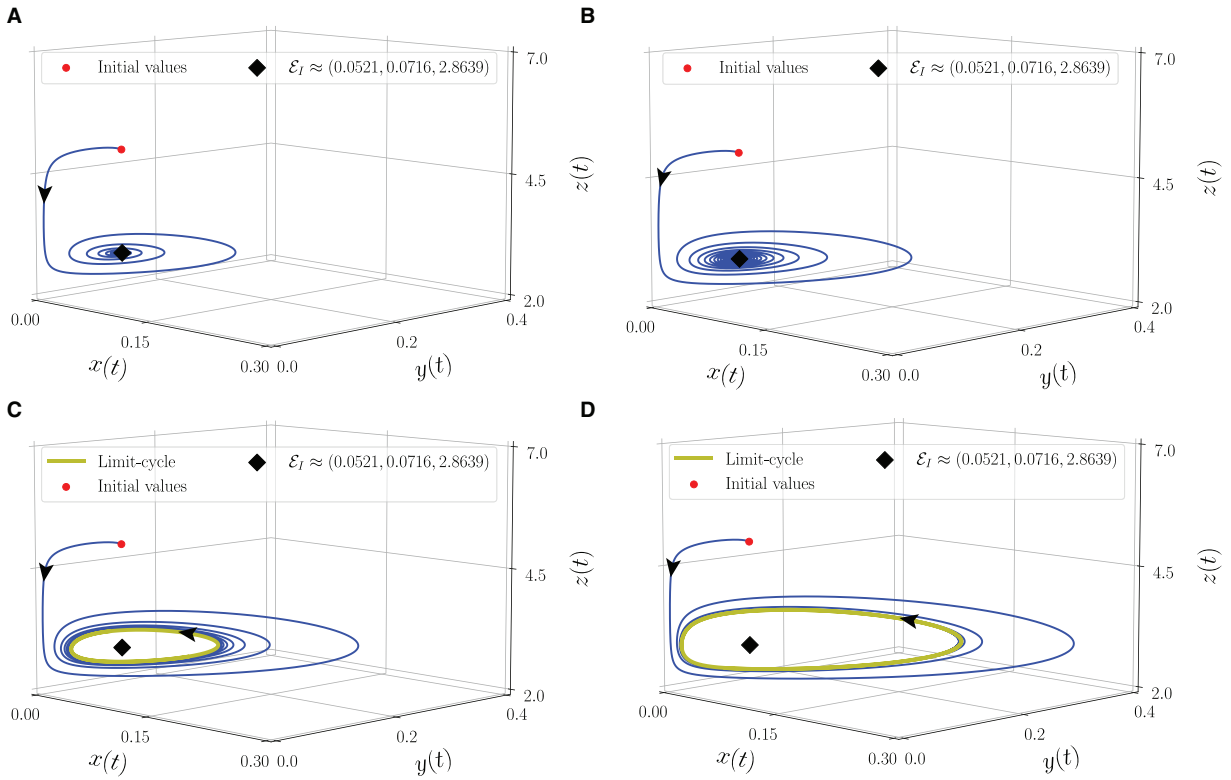

FIGURE 6
Phase portrait of the model (Equation 3) around interior point $\mathcal{E}_I$ using parameter values from Equation (26). **(A)** $\alpha = 0.81$, **(B)** $\alpha = 0.84$, **(C)** $\alpha = 0.87$, and **(D)** $\alpha = 0.9$.

simultaneously impact the sensitivity of the convergence of the solution to the selection of the initial value. The two closest initial values are set which converge to the different equilibrium points. One of them convergent to the origin point and the other solution convergent to the axial point. This means, two conditions may arrive, namely the extinction of all populations and the only prey existence point. Several references show that the bistability condition occurs as the consequence of saddle-node bifurcation, see Adhikary et al. [38] and several references therein.

From the biological point of view, these numerical bifurcations describe the possibility for the prey to extinct or survive due to the change in the harvesting rate while the predator both mature and immature is always extinct (Figure 1). Three feasible conditions may happen. First, for any sufficiently small harvesting rate ($0 \leq h < h_1^* = 0.05$), the prey population may maintain its existence in this ecosystem (Figure 2). Second, if the harvesting rate increases ($h_1^* < h < h_2^*$), two possible conditions may occur namely the extinction of prey or the viability of prey. These circumstances depend on the initial condition, where if the initial condition is quite close to the origin point, the prey will be extinct, and for the initial condition is far enough from the origin point, the prey can survive extinction (Figure 3). Third, if the harvesting rate is again increased ($h > h_2^*$), the population of prey will finally extinct and there are no population again in this ecosystem (Figure 4).

The next circumstance occurs in the interior point of the model (Equation 3), which demonstrates the influence of the order of the derivative as the memory index on the dynamical behaviors around the interior point. We set the parameter as follows:

$$r = 0.8,\ K = 5,\ m = 0.25,\ h = 0.01,\ c = 0.08,\ n = 0.2,$$
$$\beta = 0.4,\ \delta_1 = 0.01,\ \delta_2 = 0.01,\ \delta_2 = 0.01,\ \omega = 0.1. \quad (26)$$

To identify the dynamical behaviors, we vary the values of α in the interval $0.76 \leq \alpha \leq 1$. As a result, we obtain the bifurcation diagram given in Figure 5. For $\alpha < \alpha^* \approx 0.86$, the interior point $\mathcal{E}_I$ is LAS. To show this condition, we give the phase portraits by selecting $\alpha = 0.81$ and $\alpha = 0.84$ as given in Figures 6A, B. Nearby solution oscillates and convergent to $\mathcal{E}_I$. When α crosses $\alpha^* \approx 0.86$, $\mathcal{E}_I$ losses its stability *via* Hopf bifurcation which is indicated by the occurrence of periodic signal namely limit-cycle. The nearby solution stays away from $\mathcal{E}_I$ and convergent to the limit-cycle. The evolution of the limit-cycle given in Figure 5 also shows that the diameter of the limit-cycle increases when alpha increases. We portray the phase portraits in Figures 6C, D to show the dynamics

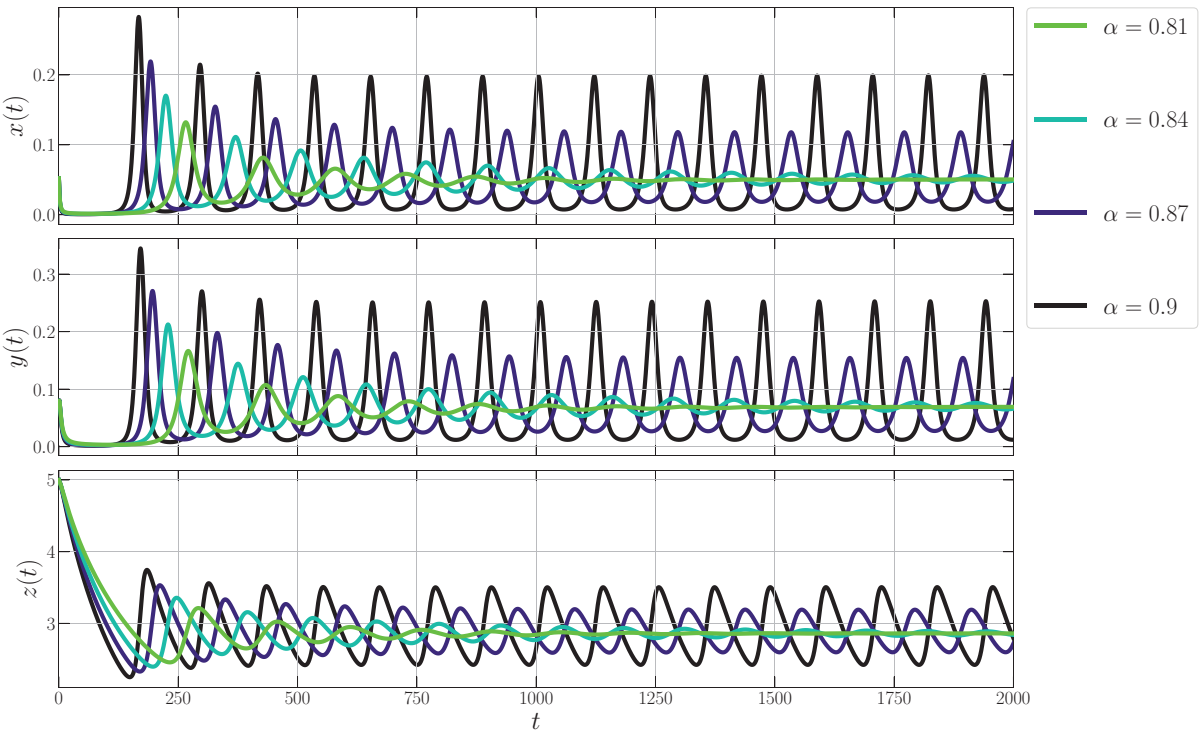

FIGURE 7
Phase portrait of the model (Equation 3) around interior point $\mathcal{E}_I$ using parameter values from Equation (26).

of solutions around $\mathcal{E}_I$ for $\alpha = 0.87$ and $\alpha = 0.9$. It is shown that the densities of all populations are oscillated and finally converge to the limit cycle. The physical interpretations of Hopf bifurcation driven by α are closely related to the influence of the memory on the change of behaviors around the interior point. The stronger the influence of memory, the higher the ability of prey and predators to maintain their existence ($\alpha < \alpha^*$). For less memory effect which is indicated by $\alpha > \alpha^*$, all populations lose the ability to stabilize their number of individuals. The population density fluctuates according to seasonal patterns which indicates by the appearance of a limit cycle (Figures 6C, D), and the peak of each population also increases for less memory effect (Figure 7). Although the density for each population cannot tend to a constant number, in this case, the memory effect cannot cause the extinction of every population.

7. Conclusion

The dynamics of a predator–prey model incorporating four biological conditions, namely age structure, intraspecific competition, Michaelis–Menten type harvesting, and memory effect, have been studied. All biological validities have been presented such as the existence, uniqueness, non-negativity, and boundedness of the solution. The dynamics of the model have been explored by showing the global stability conditions for three equilibrium points namely the origin, the axial, and the interior points. We have shown that three bifurcations phenomena driven by the harvesting rate occur around the axial point namely transcritical, saddle-node, and backward bifurcations. The bistability condition exists as the impact of saddle-node bifurcation which states that the existence of prey depends on the initial condition. A bifurcation driven by the memory effect also has been shown around the interior point which is called Hopf bifurcation. All the bifurcation phenomena having an impact on the densities of the population not only may reduce their densities but also threaten the existence of several populations.

Data availability statement

The original contributions presented in the study are included in the article/supplementary material, further inquiries can be directed to the corresponding author/s.

Author contributions

All authors listed have made a substantial, direct, and intellectual contribution to the work and approved it for publication.

Funding

This research was funded by LPPM-UNG *via* PNBP-Universitas Negeri Gorontalo according to DIPA-UNG No. 023.17.2.677521/2021, under contract No. B/176/UN47.DI/PT.01.03/2022.

Acknowledgments

The authors intended to express our gratitude and appreciation to the editors, reviewers, and all those who have supported us in improving this article.

Conflict of interest

The authors declare that the research was conducted in the absence of any commercial or financial relationships that could be construed as a potential conflict of interest.

Publisher's note

References

1. Deng H, Chen F, Zhu Z, Li Z. Dynamic behaviors of Lotka-Volterra predator-prey model incorporating predator cannibalism. *Adv Diff Equat*. (2019) 2019:359. doi: 10.1186/s13662-019-2289-8

2. Huang Q, Lin Y, Zhong Q, Ma F, Zhang Y. The impact of microplastic particles on population dynamics of predator and prey: implication of the Lotka-Volterra model. *Sci Rep*. (2020) 10:1–10. doi: 10.1038/s41598-020-61414-3

3. Tahara T, Gavina MKA, Kawano T, Tubay JM, Rabajante JF, Ito H, et al. Asymptotic stability of a modified Lotka-Volterra model with small immigrations. *Sci Rep*. (2018) 8:1–7. doi: 10.1038/s41598-018-25436-2

4. Zeng X, Liu L, Xie W. Existence and uniqueness of the positive steady state solution for a Lotka-Volterra predator-prey model with a crowding term. *Acta Math Sci*. (2020) 40:1961–80. doi: 10.1007/s10473-020-0622-7

5. Gui Z, Ge W. The effect of harvesting on a predator-prey system with stage structure. *Ecol Modell*. (2005) 187:329–40. doi: 10.1016/j.ecolmodel.2005.01.052

6. Magnússon KG. Destabilizing effect of cannibalism on a structured predator-prey system. *Math Biosci*. (1999) 155:61–75. doi: 10.1016/S0025-5564(98)10051-2

7. Liu C, Zhang Q, Huang J. Stability analysis of a harvested prey-predator model with stage structure and maturation delay. *Math Problems Eng*. (2013) 2013:329592. doi: 10.1155/2013/329592

8. Dubey B, Agarwal S, Kumar A. Optimal harvesting policy of a prey-predator model with Crowley-Martin-type functional response and stage structure in the predator. *Nonlinear Anal Model Control*. (2018) 23:493–514. doi: 10.15388/NA.2018.4.3

9. Xiao Z, Li Z, Zhu Z, Chen F. Hopf bifurcation and stability in a Beddington-DeAngelis predator-prey model with stage structure for predator and time delay incorporating prey refuge. *Open Math*. (2019) 17:141–59. doi: 10.1515/math-2019-0014

10. Zhang X, Liu Z. Periodic oscillations in age-structured ratio-dependent predator-prey model with Michaelis-Menten type functional response. *Physica D*. (2019) 389:51–63. doi: 10.1016/j.physd.2018.10.002

11. Zhang F, Chen Y, Li J. Dynamical analysis of a stage-structured predator-prey model with cannibalism. *Math Biosci*. (2019) 307:33–41. doi: 10.1016/j.mbs.2018.11.004

12. Lu W, Xia Y. Periodic solution of a stage-structured predator-prey model with Crowley-Martin type functional response. *AIMS Math*. (2022) 7:8162–75. doi: 10.3934/math.2022454

13. Li J, Liu X, Wei C. The impact of role reversal on the dynamics of predator-prey model with stage structure. *Appl Math Model*. (2022) 104:339–57. doi: 10.1016/j.apm.2021.11.029

14. Wang W, Chen L. A predator-prey system with stage-structure for predator. *Comput Math Appl*. (1997) 33:83–91. doi: 10.1016/S0898-1221(97)00056-4

15. Chow C, Hoti M, Li C, Lan K. Local stability analysis on Lotka-Volterra predator-prey models with prey refuge and harvesting. *Math Methods Appl Sci*. (2018) 41:7711–32. doi: 10.1002/mma.5234

16. Xiao M, Cao J. Hopf bifurcation and non-hyperbolic equilibrium in a ratio-dependent predator-prey model with linear harvesting rate: analysis and computation. *Math Comput Model*. (2009) 50:360–79. doi: 10.1016/j.mcm.2009.04.018

17. Zhang Z, Upadhyay RK, Datta J. Bifurcation analysis of a modified Leslie-Gower model with Holling type-IV functional response and nonlinear prey harvesting. *Adv Diff Equat*. (2018) 2018:127. doi: 10.1186/s13662-018-1581-3

18. Mulheisen M, Allen C, Parr CS. *Lycaon Pictus*. (*On-line*), *Animal Diversity Web*. (2002). Available online at: https://animaldiversity.org/accounts/Lycaon_pictus/ (accessed on November 13, 2022)

19. IUCN SSC Antelope Specialist Group. *Aepyceros melampus. The IUCN Red List of Threatened Species 2016: eT550A50180828*. (2016). Available online at: https://www.iucnredlist.org/species/550/50180828 (accessed on November 13, 2022)

20. Huo J, Zhao H, Zhu L. The effect of vaccines on backward bifurcation in a fractional order HIV model. *Nonlinear Anal. Real World Appl*. (2015) 26:289–305. doi: 10.1016/j.nonrwa.2015.05.014

21. Moustafa M, Mohd MH, Ismail AI, Abdullah FA. Stage structure and refuge effects in the dynamical analysis of a fractional order Rosenzweig-MacArthur prey-predator model. *Progr Fract Different Appl*. (2019) 5:49–64. doi: 10.18576/pfda/050106

22. Rahmi E, Darti I, Suryanto A, Trisilowati, Panigoro HS. Stability analysis of a fractional-order leslie-gower model with allee effect in predator. *J Phys*. (2021) 1821:012051. doi: 10.1088/1742-6596/1821/1/012051

23. Owolabi KM. Dynamical behaviour of fractional-order predator-prey system of Holling-type. *Discrete Contin Dyn Syst S*. (2020) 13:823–34. doi: 10.3934/dcdss.2020047

24. Barman D, Roy J, Alam S. Modelling hiding behaviour in a predator-prey system by both integer order and fractional order derivatives. *Ecol Inform*. (2022) 67:101483. doi: 10.1016/j.ecoinf.2021.101483

25. Ghanbari B, Djilali S. Mathematical and numerical analysis of a three-species predator-prey model with herd behavior and time fractional-order derivative. *Math Methods Appl Sci*. (2020) 43:1736–52. doi: 10.1002/mma.5999

26. Yousef FB, Yousef A, Maji C. Effects of fear in a fractional-order predator-prey system with predator density-dependent prey mortality. *Chaos Solitons Fractals*. (2021) 145:110711. doi: 10.1016/j.chaos.2021.110711

27. Ghosh U, Pal S, Banerjee M. Memory effect on Bazykin's prey-predator model: stability and bifurcation analysis. *Chaos Solitons Fractals*. (2021) 143:110531. doi: 10.1016/j.chaos.2020.110531

28. Panigoro HS, Rahmi E, Achmad N, Mahmud SL, Resmawan R, Nuha AR. A discrete-time fractional-order rosenzweig-macarthur predator-prey model involving prey refuge. *Commun Math Biol Neurosci*. (2021) 2021:1–19. doi: 10.28919/cmbn/6586

29. Panigoro HS, Resmawan R, Sidik ATR, Walangadi N, Ismail A, Husuna C. A fractional-order predator-prey model with age structure on predator and nonlinear harvesting on prey. *Jambura J Math*. (2022) 4:355–66. doi: 10.34312/jjom.v4i2.15220

30. Mahata A, Paul S, Mukherjee S, Das M, Roy B. Dynamics of caputo fractional order SEIRV epidemic model with optimal control and stability analysis. *Int J Appl Comput Math*. (2022) 8:1–25. doi: 10.1007/s40819-021-01224-x

31. Yavuz M, Sene N. Stability analysis and numerical computation of the fractional predator-prey model with the harvesting rate. *Fractal Fract*. (2020) 4:35. doi: 10.3390/fractalfract4030035

32. Maji C. Impact of fear effect in a fractional-order predator-prey system incorporating constant prey refuge. *Nonlinear Dyn*. (2022) 107:1329–42. doi: 10.1007/s11071-021-07031-9

33. Barman D, Roy J, Alrabaiah H, Panja P, Mondal SP, Alam S. Impact of predator incited fear and prey refuge in a fractional order prey predator model. *Chaos Solitons Fractals*. (2021) 142:110420. doi: 10.1016/j.chaos.2020.110420

34. Panigoro HS, Suryanto A, Kusumahwinahyu WM, Darti I. Dynamics of a fractional-order predator-prey model with infectious diseases in prey. *Commun Biomath Sci*. (2019) 2:105. doi: 10.5614/cbms.2019.2.2.4

35. Vargas-De-León C. Volterra-type Lyapunov functions for fractional-order epidemic systems. *Commun Nonlinear Sci Num Simulat*. (2015) 24:75–85. doi: 10.1016/j.cnsns.2014.12.013

36. Aguila-Camacho N, Duarte-Mermoud MA, Gallegos JA. Lyapunov functions for fractional order systems. *Commun Nonlinear Sci Num Simulat*. (2014) 19:2951–7. doi: 10.1016/j.cnsns.2014.01.022

37. Diethelm K, Ford NJ, Freed AD. A predictor-corrector approach for the numerical solution of fractional differential equations. *Nonlinear Dyn*. (2002) 29:3–22. doi: 10.1023/A:1016592219341

38. Adhikary PD, Mukherjee S, Ghosh B. Bifurcations and hydra effects in Bazykin's predator-prey model. *Theor Populat Biol*. (2021) 140:44–53. doi: 10.1016/j.tpb.2021.05.002

frontiers | Frontiers in Applied Mathematics and Statistics

TYPE Original Research
PUBLISHED 01 February 2023
DOI 10.3389/fams.2022.1101029

OPEN ACCESS

EDITED BY
Yasser Aboelkassem,
University of Michigan–Flint, United States

REVIEWED BY
Vedat Erturk,
Ondokuz Mayıs University, Türkiye
Pushpendra Kumar,
Central University of Punjab, India

*CORRESPONDENCE
Shewafera Wondimagegnhu Teklu
✉ luelzedo2008@gmail.com;
✉ shewaferaw@dbu.edu.et

SPECIALTY SECTION
This article was submitted to Mathematical Biology, a section of the journal Frontiers in Applied Mathematics and Statistics

RECEIVED 17 November 2022
ACCEPTED 30 December 2022
PUBLISHED 01 February 2023

CITATION
Teklu SW and Terefe BB (2023) COVID-19 and syphilis co-dynamic analysis using mathematical modeling approach. *Front. Appl. Math. Stat.* 8:1101029. doi: 10.3389/fams.2022.1101029

COVID-19 and syphilis co-dynamic analysis using mathematical modeling approach

Shewafera Wondimagegnhu Teklu* and Birhanu Baye Terefe

Department of Mathematics, College of Natural and Computational Sciences, Debre Berhan University, Debre Berhan, Ethiopia

In this study, we have proposed and analyzed a new COVID-19 and syphilis co-infection mathematical model with 10 distinct classes of the human population (COVID-19 protected, syphilis protected, susceptible, COVID-19 infected, COVID-19 isolated with treatment, syphilis asymptomatic infected, syphilis symptomatic infected, syphilis treated, COVID-19 and syphilis co-infected, and COVID-19 and syphilis treated) that describes COVID-19 and syphilis co-dynamics. We have calculated all the disease-free and endemic equilibrium points of single infection and co-infection models. The basic reproduction numbers of COVID-19, syphilis, and COVID-19 and syphilis co-infection models were determined. The results of the model analyses show that the COVID-19 and syphilis co-infection spread is under control whenever its basic reproduction number is less than unity. Moreover, whenever the co-infection basic reproduction number is greater than unity, COVID-19 and syphilis co-infection propagates throughout the community. The numerical simulations performed by MATLAB code using the ode45 solver justified the qualitative results of the proposed model. Moreover, both the qualitative and numerical analysis findings of the study have shown that protections and treatments have fundamental effects on COVID-19 and syphilis co-dynamic disease transmission prevention and control in the community.

KEYWORDS

syphilis, COVID-19, COVID-19 and syphilis co-infection, protection, numerical simulation

1. Introduction

Communicable diseases are illnesses caused by pathogenic microbial agents such as bacteria, viruses, fungi, and parasites, which affect human beings throughout the world [1]. The novel coronavirus (COVID-19) infection is a lethal disease that has been a major global public health concern. The COVID-19 pandemic has affected various animals mostly infecting millions of human beings in different nations throughout the world [2–6]. It has been spreading mainly through sneezing, individuals interacting with each other in a certain time frame, or through coughing [7]. Although different species of animals are thought to be the source of COVID-19 transmission, bats have been shown to be coronavirus hosts [8]. Many nations throughout the world have started to practice various prevention and control strategies such as lockdown approach, quarantine, isolation, and closing schools [3, 9].

Syphilis is a major sexually transmitted disease and has been affecting millions of individuals both in low- and high-income countries of the world [10]. It is a chronic systemic disease caused by *Treponema pallidum* bacterium which is mainly transmitted through sex, blood contact, and mother-to-child during birth [4, 10–16]. Diagnosis, treatment, and using a condom are the basic control mechanisms of syphilis spreading in the community [10]. If left untreated, syphilis progresses through four stages: primary, secondary, latent, and tertiary [17–19]. The first three infection stages can transmit the disease to other susceptible groups of individuals, the transmission can occur *via* sexual contact, and in most cases, the tertiary stage is not

transmissible through sexual contact [19]. It can be a cause of different cardiovascular and neurological diseases [17]. Approximately 90% of new syphilis substantial morbidity and mortality data are recorded in low-income countries around the world [11, 16]. Co-infection is an infection of an individual with two or more microorganisms' species [20, 21]. COVID-19 is an opportunistic infection for people with a weak immune system who were already infected by acute and chronic infections such as pneumonia, TB, and HIV/AIDS.

Mathematical modeling approach research done by scholars using a deterministic method [10, 14], a stochastic method [7, 22], or a fractional order method [23–32] has made a great contribution to linking the scientific approach with real-world physical situations and also for the decision-making process for solving real-world problems [33]. Different scholars have formulated and analyzed mathematical models on COVID-19 transmission [7, 8, 22, 24–26, 29, 30, 34–37], syphilis transmission [10, 17–19, 23], and other infectious diseases transmission [20, 21, 27, 28, 33, 38–40]; however, no one has done analysis on COVID-19 and syphilis co-infection transmission dynamics.

Oshinubi et al. [41] proposed and analyzed a new age-dependent compartmental model for COVID-19 transmission. The qualitative analysis of the model includes the non-negativity and boundedness of the model solutions in a given region, and the existence, uniqueness, and stability of the model solutions. Using parameter estimation from three different nations Kuwait, France, and Cameroon, they carried out numerical simulations and have shown the fundamental role of vaccination on COVID-19 transmission. Babaei et al. [34] proposed and examined a model for novel coronavirus transmission with Caputo's fractional order approach. The finding of the study shows that quarantine has a very fundamental role to control transmission. Iboi et al. [17] formulated and analyzed a new multi-stage syphilis model to examine the role of transitory immunity loss in the spreading process. The analysis shows that the disease-free and unique endemic equilibrium points are globally asymptotically stable when the corresponding basic reproduction number is less than unity and greater than unity, respectively. The results show that high treatment rates in the primary and secondary stages have a positive effect on the remaining stages of infection. Nwankwo et al. [38] formulated a mathematical model to examine the interaction between HIV/AIDS and syphilis pathogens with syphilis treatment on the co-infection of syphilis and HIV/AIDS where treatment or HIV is not accessible. High treatment in the primary stage has a fundamental role in reducing both single infections and co-infections in the population. Teklu et al. [42] formulated a six-compartmental COVID-19 transmission model to examine the impacts of intervention measures. The results show that protection, treatment, and vaccinations are fundamental to minimizing infection in the population.

Because different scholars have been mainly concerned with studying COVID-19 and syphilis single infections, no one has studied syphilis and COVID-19 co-infection using a mathematical model approach. Therefore, in this study, we are interested in filling the gap by formulating and analyzing syphilis and COVID-19 model intervention strategies.

The remaining part of the article is organized as follows. Section 2 presents COVID-19 and syphilis co-infection model construction. Section 3 describes the qualitative model analysis. Section 4 presents the numerical and sensitivity analyses. Section 5 presents the discussions and conclusions of the whole research study.

TABLE 1 Variables' definitions.

State variables	Definition
S	Susceptible individuals for both COVID-19 and syphilis
P_c	COVID-19 protected individuals
P_s	Syphilis protected individuals
I_c	COVID-19 infected individuals
Q_c	COVID-19 isolated with treatment individuals
I_{as}	Syphilis asymptomatic infected individuals
I_{ss}	Syphilis symptomatic infected individuals
T_s	Syphilis treated individuals
I_{cs}	COVID-19 and syphilis co-infected individuals
T	Co-infected treated individuals

2. Model construction

We have considered COVID-19 and syphilis co-infection by separating the four syphilis infection stages (primary, secondary, latent, and tertiary) into two, the asymptomatic and symptomatic groups, and we have divided the population $N(t)$ into 10 mutually exclusive states, which are described in Table 1 as follows:

$$N(t) = P_c(t) + P_s(t) + S(t) + I_c(t) + Q_c(t) + I_{as}(t) + I_{ss}(t) + T_s(t) + T_{cs}(t) + T(t).$$

Assumptions and definitions of basic terms:

- Co-infectious humans do not transmit both infections simultaneously.
- COVID-19 infection is transmitted to susceptible individuals from I_c and I_{cs} infectious groups at the transmission rate as follows:

$$\lambda_c = \beta_2(I_c + \phi_1 I_{cs}). \quad (1)$$

- Syphilis infection is transmitted to susceptible individuals from I_{as}, I_{ss}, *and* I_{cs} infectious groups at the force of infection rate as follows:

$$\lambda_s = \beta_1(I_{as} + \phi_2 I_{ss} + \phi_3 I_{cs}). \quad (2)$$

Using variable and parameter definitions given in Tables 1, 2, respectively, the flowchart of the COVID-19 and syphilis co-infection model is represented in Figure 1.

Using the flowchart represented in Figure 1, the corresponding system of differential equations of the complete co-infection model (3) is written as follows:

$$\frac{dP_c}{dt} = \tau_1\Lambda - (\beta + \lambda_s + \mu)P_c,$$
$$\frac{dP_s}{dt} = \tau_3\Lambda - (\pi + \lambda_c + \mu)P_s,$$

TABLE 2 Parameter definitions.

Parameters	Biological definitions
Λ	The annual recruitment number of population in the community
τ_1	Portion of recruitment rate protected from COVID-19
τ_2	Portion of recruitment rate susceptible to both COVID-19 and syphilis
τ_3	Portion of recruitment rate protected from syphilis
β	COVID-19 protection loss rate
π	Syphilis protection loss rate
μ	Natural death rate of individuals
θ_1	Modification parameter
θ_2	Modification parameter
θ_3	Modification parameter
ρ	Treatment rate of COVID-19 infectious
ϵ	Progression rate of asymptomatic syphilis infectious to symptomatic syphilis infectious
ε	Treatment rate of COVID-19 and syphilis co-infections
γ	Treatment rate of symptomatic syphilis infectious
δ	Immunity lose rate against syphilis treatment
β_1	Syphilis transmission rate
β_2	COVID-19 transmission rate
ω_1	COVID-19 infection induced death rate
ω_2	Syphilis infection induced death rate
ω_3	COVID-19 and syphilis co-infection induced death rate
θ	Immunity lose rate against syphilis after treated from co-infection

$$\begin{aligned}
\frac{dS}{dt} &= \tau_2\Lambda + \beta P_c + \pi P_s + \delta T_s + \theta T - (\lambda_s + \lambda_c + \mu)S,\\
\frac{dI_c}{dt} &= \lambda_c S + \lambda_c P_s - (\theta_1\lambda_s + \rho + \mu + \omega_1)I_c,\\
\frac{dQ_c}{dt} &= \rho I_c - \mu Q_c,\\
\frac{dI_{as}}{dt} &= \lambda_s S + \lambda_s P_c - (\theta_2\lambda_c + \epsilon + \mu)I_{as},\\
\frac{dI_{ss}}{dt} &= \epsilon I_{as} - (\theta_3\lambda_c + \gamma + \mu + \omega_2)\, I_{ss},\\
\frac{dI_{cs}}{dt} &= \theta_2\lambda_c I_{as} + \theta_3\lambda_c I_{ss} + \theta_1\lambda_s I_c - (\varepsilon + \mu + \omega_3)I_{cs},\\
\frac{dT_s}{dt} &= \gamma I_{ss} - (\delta + \mu)T_s,\\
\frac{dT}{dt} &= \varepsilon I_{cs} - (\theta + \mu)T.
\end{aligned} \tag{3}$$

2.1. Qualitative properties of the model (3)

System (3) represents the human population; we want to prove that all the solutions of the model are non-negative and bounded, respectively, in the following region:

$$\Omega = \left\{(P_c,\, P_s,\, S,\, I_c,\, Q_c,\, I_{as},\, I_{ss},\, T_s,\, T_{cs},\, T) \in \mathbb{R}_+^{10}, N \le \frac{\Lambda}{\mu}\right\} \tag{4}$$

Theorem 1: Let $P_c(0) > 0$, $S(0) > 0, P_s(0)$, $I_c(0) > 0$, $Q_c(0) > 0$, $I_{as}(0) > 0$, $I_{ss}(0) > 0$, $T_s(0) > 0, I_{cs}(0) > 0$, $T(0) > 0$ be the initial solutions of the system (3), then $P_c(t)$, $P_s(t)$, $S(t)$, $I_c(t)$, $Q_c(t)$, $I_{as}(t)$, $I_{ss}(t)$, $T_s(t)$, $T_{cs}(t)$, and $T(t)$ are positive in the region $\mathbb{R}_+^{10}$ for any time $t > 0$.

Proof: Let $\tau = sup\{t > 0 : P_c(t) > 0,\ S(t) > 0, P_s(t),\ I_c(t) > 0,\ Q_c(t) > 0,\ I_{as}(t) > 0,\ I_{ss}(t) > 0,\ T_s(t) > 0,\ I_{cs}(t) > 0,\ T(t) > 0\}$.

Since $P_c(t)$, $P_s(t)$, $S(t)$, $I_c(t)$, $Q_c(t)$, $I_{as}(t)$, $I_{ss}(t)$, $T_s(t)$, $T_{cs}(t)$, and $T(t)$ are continuous, and we deduce that $\tau > 0$. If $\tau = +\infty$, then positivity holds, but, if $0 < \tau < +\infty$, $P_c(\tau) = 0$ or $P_s(\tau) = 0$ or $S(\tau) = 0$ or $I_c(\tau) = 0$ or $Q_c(\tau) = 0$ or $I_{as}(\tau) = 0$ $I_{ss}(\tau) = 0$ or $T_s(\tau) = 0$ or $T_{cs}(\tau) = 0$ or $T(\tau) = 0$.

From model (3) first equation, we do have

$$\frac{dP_c}{dt} + (\beta + \lambda_s + \mu)P_c = \tau_1\Lambda.$$

After some calculations of integration, we got

$$\begin{aligned}
P_c(\tau) &= a_1 P_c(0) + a_1\int_0^\tau e^{\int(\beta+\lambda_s+\mu)dt}\tau_1\Lambda dt > 0, \text{ where}\\
a_1 &= e^{-\int(\beta+\lambda_s+\mu)dt} > 0,\ P_c(0) > 0, P_c(\tau) > 0, \text{so that}\\
&\quad P_c(\tau) \neq 0.
\end{aligned}$$

From model (3) second equation, we have

$$\frac{dP_s}{dt} = \tau_3\Lambda - (\pi + \lambda_c + \mu)P_s.$$

After some calculations of integration, we have

$$\begin{aligned}
P_s(\tau) &= b_1 P_s(0) + b_1\int_0^\tau e^{\int(\pi+\lambda_c+\mu)dt}\tau_3\Lambda dt > 0, \text{ where}\\
b_1 &= e^{-\int(\pi+\lambda_c+\mu)dt} > 0,\ P_s(0) > 0, P_s(\tau) > 0, \text{so that}\\
&\quad P_s(\tau) \neq 0.
\end{aligned}$$

From model (3) third equation, we have

$$\frac{dS}{dt} = \tau_2\Lambda + \beta P_c + \pi P_s + \delta\gamma T_s - S(\lambda_s + \lambda_c + \mu).$$

After some calculations, we have

$S(\tau) = c_1 S(0) + c_1\int_0^\tau e^{\int(\lambda_s+\lambda_c+\mu)dt}(\tau_2\Lambda + \beta P_c + \pi P_s + \delta\gamma T_s)dt > 0$, where

$c_1 = e^{-\int(\lambda_s+\lambda_c+\mu)dt} > 0$, $S(0) > 0$, and by the definition of τ we have $P_c(t) > 0$, $P_s(t)$, $T_s(t) > 0, S(\tau) > 0$, so that $S(\tau) \neq 0$.

Similarly, by proving the remaining state variable, we have

$I_c(\tau) > 0$, hence $I_c(\tau) \neq 0$, $Q_c(\tau) > 0$ hence $Q_c(\tau) \neq 0$, $I_{as}(\tau) > 0$ hence $I_{as}(\tau) \neq 0, I_{ss}(\tau) > 0$ hence $I_{ss}(\tau) \neq 0, T_s(\tau) > 0$ hence $T_s(\tau) \neq 0$, $T_{cs}(\tau) > 0$ hence $T_{cs}(\tau) \neq 0$, and $T(\tau) > 0$ hence $T(\tau) \neq 0$.

Thus, τ is not finite, and hence $= +\infty$, which means all the model solutions are non-negative.

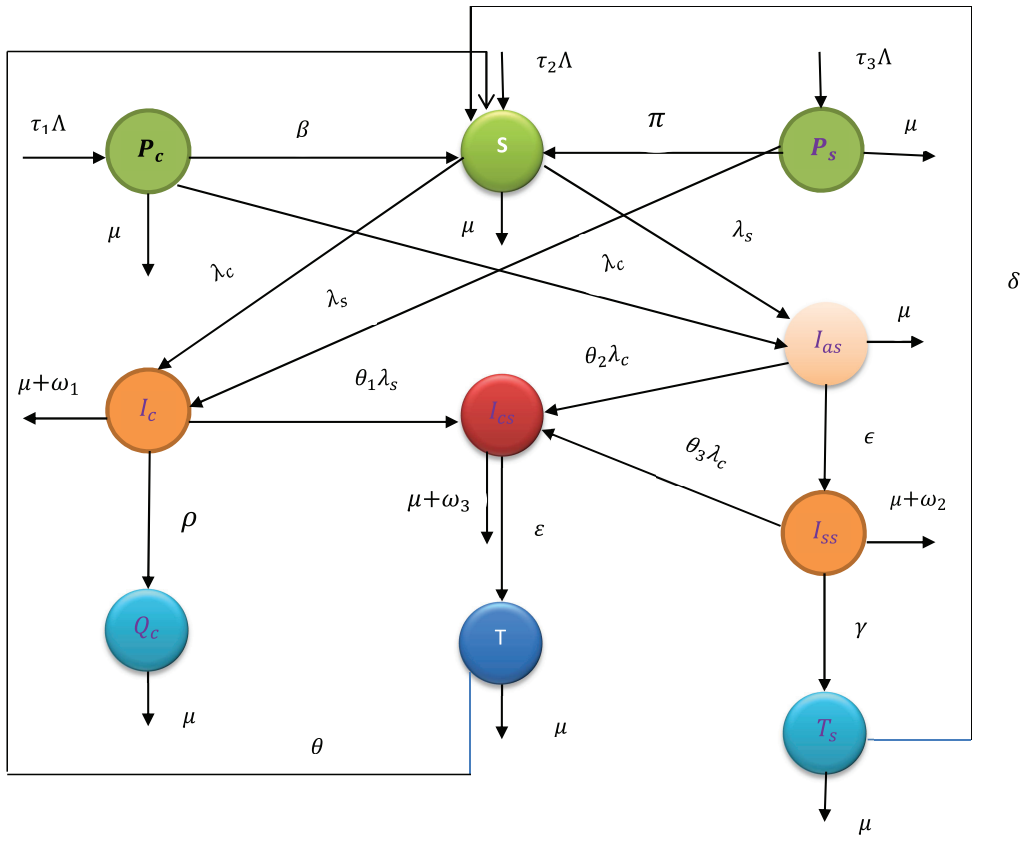

FIGURE 1
Flowchart of the model (3) with forces of infections λ_C and λ_s as in (1) and (2), respectively.

Theorem 2: The model feasible region Ω stated in (4) is bounded in $\mathbb{R}^{10}_{+}$.

Proof: The total human being of the model (3) is as follows:

$$N(t) = P_c(t) + P_s(t) + S(t) + I_c(t) + Q_c(t) + I_{as}(t) + I_{ss}(t) + T_s(t) + T_{cs}(t) + T(t).$$

Differentiating both sides gives the following result

$$\begin{aligned}\frac{dN}{dt} &= \frac{dP_c}{dt} + \frac{dP_s}{dt} + \frac{dS}{dt} + \frac{dI_c}{dt} + \frac{dQ_c}{dt} + \frac{dI_{as}}{dt} + \frac{dI_{ss}}{dt} + \frac{dT_s}{dt} \\ &+ \frac{dT_{cs}}{dt} + \frac{dT}{dt}. \\ &= \Lambda - \mu N - \omega_1 I_c - \omega_2 I_{ss} - \omega_3 I_{cs}, \text{where } \tau_1 + \tau_3 + \tau_2 = 1. \\ \Longrightarrow \frac{dN}{dt} &\leq \Lambda - \mu N.\end{aligned}$$

After some steps, we have $0 \leq N(t) \leq \frac{\Delta}{\mu}$, and hence, the model solutions with positive initial solutions are bounded in Ω.

3. Model analysis in qualitative approach

The complete COVID-19 and syphilis co-infection model (3) depends on the results of the two sub-models analysis.

3.1. COVID-19 mono-infection model analysis

From the complete model (3), we have the COVID-19 mono-infection model taking values $P_s = I_{as} = I_{ss} = T_s = I_{cs} = T = 0$ as follows:

$$\begin{aligned}\frac{dP_c}{dt} &= \tau_1\Lambda - (\beta + \mu)P_c, \\ \frac{dS}{dt} &= \tau_2\Lambda + \beta P_c - (\lambda_c + \mu)S, \\ \frac{dI_c}{dt} &= \lambda_c S - (\rho + \mu + \omega_1)I_c, \\ \frac{dQ_c}{dt} &= \rho I_c - \mu Q_c.\end{aligned} \tag{5}$$

with $N_1(t) = P_c(t) + S(t) + I_c(t) + Q_c(t)$ as a total population and $\lambda_c = \beta_2 I_c$.

3.1.1. COVID-19 infection-free equilibrium

The COVID-19 infection-free equilibrium of the model (5) at $I_c = 0$ is $E^0_c = (P^0_c, S^0\, 0,\, 0,\, 0) = \left(\frac{\tau_1\Lambda}{\beta+\mu}, \frac{\tau_2\Lambda(\beta+\mu)+\beta\tau_1\Lambda}{\mu(\beta+\mu)}, 0,\, 0\right)$.

3.1.2. COVID-19 mono-infection reproduction number

This mono-infection model has one infectious class, I_c, and we can obtain basic reproduction numbers without a method of the next-generation matrix as follows:

$$\begin{aligned}\frac{dI_c}{dt} &= \lambda_c S - (\rho+\mu+\omega_1)I_c,\\ &= \beta_2 I_c S - (\rho+\mu+\omega_1)I_c,\\ &= (\beta_2 S - (\rho+\mu+\omega_1))I_c,\\ &= (\frac{\beta_2\Lambda(\tau_2(\beta+\mu)+\beta\tau_1)}{\mu(\beta+\mu)} - (\rho+\mu+\omega_1))I_c,\\ &= (\rho+\mu+\omega_1)(\frac{\beta_2\Lambda(\tau_2(\beta+\mu)+\beta\tau_1)}{\mu(\beta+\mu)(\rho+\mu+\omega_1))} - 1)I_c,\\ &= (\rho+\mu+\omega_1)(\mathfrak{R}_0^c - 1)I_c, \text{ where}\\ \mathfrak{R}_0^c &= \frac{\beta_2\tau_2\Lambda(\beta+\mu)+\beta_2\beta\tau_1\Lambda}{\mu(\beta+\mu)(\rho+\mu+\omega_1)}.\end{aligned}$$

3.1.3. COVID-19 incidence equilibrium point

The COVID-19 incidence equilibrium point of the system (5) is $E_c^* = (P_c^*, S^*, I_c^*, Q_c^*)$, where

$$\begin{aligned}P_c^* &= \frac{\tau_1\Lambda}{\beta+\mu},\ S^* = \frac{\tau_3\Lambda(\beta+\mu)+\tau_1\beta\Lambda,}{(\lambda_c^*+\mu)(\beta+\mu)},\\ I_c^* &= \frac{(\tau_3\Lambda(\beta+\mu)+\tau_1\beta\Lambda)\lambda_c^*}{(\lambda_c^*+\mu)(\beta+\mu)(\rho+\mu+\omega_1)},\\ Q_c^* &= \frac{(\tau_3\Lambda(\beta+\mu)+\tau_1\beta\Lambda)\rho\lambda_c^*}{\mu(\lambda_c^*+\mu)(\beta+\mu)(\rho+\mu+\omega_1)}.\end{aligned}$$

Theorem 3: The COVID-19 mono-infection model (5) has a unique COVID-19 incidence (endemic) equilibrium point whenever $\mathfrak{R}_0^c > 1$.

Proof: Using equation (1), we have the following:

$$\lambda_c^* = \beta_1 I_c^* = \frac{\beta_1(\tau_3\Lambda(\beta+\mu)+\tau_1\beta\Lambda)\lambda_c^*}{(\lambda_c^*+\mu)(\beta+\mu)(\rho+\mu+\omega_1)}.$$

Then the non-zero value of λ_c^* after a simple simplification is as follows:

$\lambda_c^* = \mu(\mathscr{R}_0^c - 1) > 0$, if and only if $\mathscr{R}_0^c > 1$.

Hence, the COVID-19 mono-infection model (5) has a unique incidence equilibrium point if and only if $\mathscr{R}_0^c > 1$.

Theorem 4: COVID-19 infection-free equilibrium point of the model (5) is locally asymptotically stable if $\mathfrak{R}_0^c < 1$; otherwise, it is unstable.

Proof: The Jacobean matrix of the model (5) at the COVID-19 infection-free equilibrium point is

$$J(E_c^0) = \begin{pmatrix} -(\beta+\mu) & 0 & 0 & 0\\ \beta & -\mu & \frac{-\beta_2(\tau_2\Lambda(\beta+\mu)+\beta\tau_1\Lambda)}{\mu(\beta+\mu)} & 0\\ 0 & 0 & \frac{\beta_2(\tau_2\Lambda(\beta+\mu)+\beta\tau_1\Lambda)-\mu(\beta+\mu)(\rho+\mu+\omega_1)}{\mu(\beta+\mu)} & 0\\ 0 & 0 & \rho & -\mu \end{pmatrix}.$$

Further, the characteristics equation after a certain calculation gives us as follows:

$$\begin{aligned}\lambda_1 &= -(\beta+\mu) < 0 \text{ or } \lambda_2 = -\mu < 0, \text{or}\\ \lambda_3 &= (\rho+\mu+\omega_1)(\mathscr{R}_0^c - 1).\end{aligned}$$

Thus, each eigenvalue of the Jacobian matrix is negative if $\mathscr{R}_0^c < 1$ implies the COVID-19 infection-free equilibrium point is locally asymptotically stable whenever $\mathscr{R}_0^c < 1$.

Theorem 5: The COVID-19 infection-free equilibrium point denoted by E_c^* of the COVID-19 mono-infection model is globally stable if $\mathscr{R}_0^c < 1$; otherwise, it is unstable.

Proof: Take the representative Lyapunov function $l(I_c) = aI_c$, where $a = \frac{1}{(\rho+\mu+\omega_1))}$,

$$\begin{aligned}l(I_c) &= aI_c = \frac{1}{(\rho+\mu+\omega_1)}I_c,\\ \frac{dl}{dt} &= \frac{1}{(\rho+\mu+\omega_1)}((\beta_2 S - (\rho+\mu+\omega_1))I_c),\\ &\le \frac{1}{(\rho+\mu+\omega_1)}\\ &\quad (\frac{\beta_2\Lambda(\tau_2(\beta+\mu)+\beta\tau_1) - \mu(\beta+\mu)(\rho+\mu+\omega_1)}{\mu(\beta+\mu)})I_c,\\ &\le (\frac{\beta_2\Lambda(\tau_2(\beta+\mu)+\beta\tau_1) - \mu(\beta+\mu)(\rho+\mu+\omega_1)}{\mu(\beta+\mu)(\rho+\mu+\omega_1)})I_c,\\ &\le \mu(\beta+\mu)(\rho+\mu+\omega_1)(\frac{\frac{\beta_2\Lambda(\tau_2(\beta+\mu)+\beta\tau_1)}{\mu(\beta+\mu)(\rho+\mu+\omega_1)} - 1}{\mu(\beta+\mu)(\rho+\mu+\omega_1)})I_c,\\ &\le \mu(\beta+\mu)(\rho+\mu+\omega_1)(\frac{\mathscr{R}_0^c - 1}{\mu(\beta+\mu)(\rho+\mu+\omega_1)})I_c,\\ &\le (\mathscr{R}_0^c - 1)I_c.\end{aligned}$$

Thus, $\frac{dl}{dt} < 0$, if $\mathscr{R}_0^c < 1$, and the equality $\frac{dl}{dt} = 0$ holds if $\mathscr{R}_0^c = 1$, and hence the COVID-19 infection-free equilibrium point is globally asymptotically stable if $\mathscr{R}_0^c < 1$.

Theorem 6: The COVID-19 incidence denoted by E_C^* of the COVID-19 mono-infection model (5) is locally asymptotically stable whenever $\mathscr{R}_0^c > 1$; otherwise, it is unstable.

Proof: The Jacobean of the system (5) at E_C^*

$$J(E_C^*) = \begin{pmatrix} -(\beta+\mu) & 0 & 0 & 0\\ \beta & -(\beta_2 {I_c}^* + \mu) & -\beta_2 S^* & 0\\ 0 & \beta_2 I_c^* & \beta_2 S^* - (\rho+\mu+\omega_1) & 0\\ 0 & 0 & \rho & -\mu \end{pmatrix}.$$

From the Jacobean matrix, the characteristics equation, after simplification, gives as follows:

$$(-(\beta+\mu)-\lambda)(-\mu-\lambda)\left[\left(-\left(\beta_2 I_c^* + \mu\right) - \lambda\right)(\beta_2 S^* - (\rho+\mu+\omega_1) - \lambda) + \beta_2 S^* \beta_2 I_c^*\right] = 0.$$

Then we do have the eigenvalues $\lambda_1 = -\mu < 0$ or $\lambda_2 = -(\beta+\mu) < 0$ or

$$\begin{aligned}a_0\lambda^2 + a_1\lambda + a_2 = 0 \text{ where}\\ a_0 &= 1,\\ a_1 &= \left(\frac{\beta_2(\tau_3\Lambda(\beta+\mu)+\tau_1\beta\Lambda)\mu(\mathscr{R}_0^c - 1)}{+\mu(\lambda_c^*+\mu)(\beta+\mu)(\rho+\mu+\omega_1)}{(\lambda_c^*+\mu)(\beta+\mu)(\rho+\mu+\omega_1)}\right)\\ &\quad + \frac{(\beta_2\tau_2\Lambda(\beta+\mu)+\tau_1\beta\Lambda)[(\lambda_c^*+\mu)\mu\mathscr{R}_0^c - 1]}{(\lambda_c^*+\mu)(\beta+\mu)},\\ a_2 &= \frac{\beta_2(\tau_3\Lambda(\beta+\mu)+\tau_1\beta\Lambda)\mu(\mathscr{R}_0^c - 1)}{(\lambda_c^*+\mu)(\beta+\mu)(\rho+\mu+\omega_1)}\end{aligned}$$

$$+\frac{(\beta_2\tau_2\Lambda(\beta+\mu)+\tau_1\beta\Lambda)[(\lambda_c^*+\mu)\mu\mathscr{R}_0^c-1]}{(\lambda_c^*+\mu)(\beta+\mu)}$$
$$+\frac{\beta_2(\tau_2\Lambda(\beta+\mu)+\tau_1\beta\Lambda)\mu(\mathscr{R}_0^c-1)}{(\lambda_c^*+\mu)(\beta+\mu)(\rho+\mu+\omega_1)}.$$

Hence, all the coefficients of the characteristics equations are positive when $\mathscr{R}_0^c > 1$; thus, the COVID-19 incidence equilibrium point has local asymptotic stability when $\mathscr{R}_0^c > 1$.

3.2. Analysis of syphilis sub-model

The syphilis sub-model is obtained from the system (3) by making $P_c = I_c = Q_c = I_{cs} = T = 0$ and is as follows:

$$\begin{aligned}
\frac{dP_s}{dt} &= \tau_3\Lambda-(\pi+\mu)P_s,\\
\frac{dS}{dt} &= \tau_2\Lambda+\pi P_s+\delta\gamma T_s-S(\lambda_s+\mu),\\
\frac{dI_{as}}{dt} &= \lambda_s S-I_{as}(\epsilon+\mu),\\
\frac{dI_{ss}}{dt} &= \epsilon I_{as}-I_{ss}(\gamma+\mu+\omega_2),\\
\frac{dT_s}{dt} &= \gamma I_{ss}-T_s(\delta\gamma+\mu).
\end{aligned} \tag{6}$$

With $N_2(t) = P_s(t)+S(t)+I_{as}(t)+I_{ss}(t)+T_s(t)$, and $\lambda_s = \beta_1(I_{as}+\phi_2 I_{ss})$.

3.2.1. Syphilis infection-free equilibrium

The syphilis infection-free equilibrium point of the model (6) was obtained by making $I_{as} = I_{ss} = 0$ and is given by $E_s^0 = (P_s^0, S^0, I_{as}^0, I_{ss}^0, T_s^0) = \left(\frac{\tau_3\Lambda}{\pi+\mu}, \frac{\tau_2\Lambda(\pi+\mu)+\tau_3\pi\Lambda}{\mu(\pi+\mu)}, 0, 0, 0\right)$.

3.2.2. Syphilis sub-model reproduction number

The syphilis sub-model (6) has two infectious classes, which are I_{as}, and I_{ss}, then applying the next-generation matrix method stated in [43, 44] to obtain the basic reproduction number of the system (6) by computing FV^{-1} as follows:

$$F = \begin{pmatrix}\beta_1 S^0 & \beta_1\phi_2 S^0\\ 0 & 0\end{pmatrix},$$
$$\Longrightarrow F = \begin{pmatrix}\frac{\beta_1\Lambda(\tau_2(\pi+\mu)+\tau_3\pi)}{\mu(\pi+\mu)} & \frac{\beta_1\phi_2\Lambda(\tau_2(\pi+\mu)+\tau_3\pi)}{\mu(\pi+\mu)}\\ 0 & 0\end{pmatrix},$$

and

$$V = \begin{pmatrix}\epsilon+\mu & 0\\ -\epsilon & \gamma+\mu+\omega_2\end{pmatrix}.$$

Then, we applied Mathematica coding; we have

$$V^{-1} = \begin{bmatrix}\frac{1}{\epsilon+\mu} & 0\\ \frac{\epsilon}{(\gamma+\mu+\omega_2)(\epsilon+\mu)} & \frac{1}{(\gamma+\mu+\omega_2)}\end{bmatrix}, \text{ and}$$

$$FV^{-1} = \begin{bmatrix}\frac{\beta_1\Lambda(\tau_2(\pi+\mu)+\tau_3\pi)}{\mu(\pi+\mu)(\epsilon+\mu)} & \\ +\frac{\epsilon\beta_1\phi_2\Lambda(\tau_2(\pi+\mu)+\tau_3\pi)}{\mu(\pi+\mu)(\gamma+\mu+\omega_2)(\epsilon+\mu)} & \frac{\beta_1\phi_2\Lambda(\tau_2(\pi+\mu)+\tau_3\pi)}{\mu(\pi+\mu)(\gamma+\mu+\omega_2)}\\ 0 & 0\end{bmatrix}.$$

Thus, the reproduction number of the syphilis sub-model (6) is given by $\mathscr{R}_0^s = \frac{\beta_1\Lambda[(\gamma+\mu+\omega_2)+\phi_2\epsilon](\tau_2(\pi+\mu)+\tau_3\pi)}{\mu(\pi+\mu)(\gamma+\mu+\omega_2)(\epsilon+\mu)}$.

3.2.3. Syphilis incidence equilibrium point of the system (6)

Making the model (6) equation to zero, we have the syphilis incidence equilibrium point given by $E_s^* = (P_s^*, S^*, I_{as}^*, I_{ss}^*, T_s^*)$, where

$$\begin{aligned}
P_s^* &= \frac{\tau_3\Lambda}{(\pi+\mu)},\\
S^* &= \frac{(\gamma+\mu+\omega_2)(\epsilon+\mu)(\delta\gamma+\mu)(\tau_2\Lambda(\pi+\mu)+\tau_3\Lambda\pi)}{(\pi+\mu)((\gamma+\mu+\omega_2)(\epsilon+\mu)(\lambda_s+\mu)(\delta\gamma+\mu)-\gamma\delta\gamma\epsilon\lambda_s)},\\
I_{as}^* &= \frac{\lambda_s(\gamma+\mu+\omega_2)(\delta\gamma+\mu)(\tau_2\Lambda(\pi+\mu)+\tau_3\Lambda\pi)}{(\pi+\mu)((\gamma+\mu+\omega_2)(\epsilon+\mu)(\lambda_s+\mu)(\delta\gamma+\mu)-\gamma\delta\gamma\epsilon\lambda_s)},\\
I_{ss}^* &= \frac{\epsilon\lambda_s(\delta\gamma+\mu)(\tau_2\Lambda(\pi+\mu)+\tau_3\Lambda\pi)}{(\pi+\mu)((\gamma+\mu+\omega_2)(\epsilon+\mu)(\lambda_s+\mu)(\delta\gamma+\mu)-\gamma\delta\gamma\epsilon\lambda_s)},\\
T_s^* &= \frac{\epsilon\lambda_s\gamma(\tau_2\Lambda(\pi+\mu)+\tau_3\Lambda\pi)}{(\pi+\mu)((\gamma+\mu+\omega_2)(\epsilon+\mu)(\lambda_s+\mu)(\delta\gamma+\mu)-\gamma\delta\gamma\epsilon\lambda_s)}.
\end{aligned}$$

Theorem 7: The syphilis incidence equilibrium point of syphilis in the model (6) is unique whenever $\mathscr{R}_s^0 > 1$.

Proof: From the syphilis infection rate, we have

$$\begin{aligned}
\lambda_s^* &= \beta_1(I_{as}^*+\phi_2 I_{ss}^*).\\
\lambda_s^* &= \beta_1\Big(\frac{\lambda_s(\gamma+\mu+\omega_2)(\delta\gamma+\mu)(\tau_2\Lambda(\pi+\mu)+\tau_3\Lambda\pi)}{(\pi+\mu)((\gamma+\mu+\omega_2)(\epsilon+\mu)(\lambda_s^*+\mu)(\delta\gamma+\mu)-\epsilon\gamma\delta\gamma\lambda_s^*)}\\
&\quad+\frac{\epsilon\lambda_s^*\phi_2(\delta\gamma+\mu)(\tau_2\Lambda(\pi+\mu)+\tau_3\Lambda\pi)}{(\pi+\mu)((\gamma+\mu+\omega_2)(\epsilon+\mu)(\lambda_s^*+\mu)(\delta\gamma+\mu)-\gamma\delta\gamma\epsilon\lambda_s^*)}\Big).\\
&\Longrightarrow \lambda_s^* = (\delta\gamma+\mu)\\
&\quad\frac{\beta_1\Lambda\left[(\gamma+\mu+\omega_2)(\tau_2(\pi+\mu)+\tau_3\pi)+\epsilon\phi_2(\tau_2(\pi+\mu)+\tau_3\pi)\right]-\mu(\pi+\mu)[(\gamma+\mu+\omega_2)(\epsilon+\mu)]}{(\pi+\mu)\left((\gamma+\mu+\omega_2)(\epsilon+\mu)(\delta\gamma+\mu)-\gamma\delta\gamma\epsilon\right)}.\\
&\Longrightarrow \lambda_s^* = \frac{(\delta\gamma+\mu)\mu(\gamma+\mu+\omega_2)(\epsilon+\mu)(\mathscr{R}_0^s-1)}{\left((\gamma+\mu+\omega_2)(\epsilon+\mu)(\delta\gamma+\mu)-\gamma\delta\gamma\epsilon\right)}.\\
&\Longrightarrow \lambda_s^* = k_1(\mathscr{R}_0^s-1), \text{where}\\
k_1 &= \frac{(\delta\gamma+\mu)\mu(\pi+\mu)(\gamma+\mu+\omega_2)(\epsilon+\mu)}{(\pi+\mu)\left((\gamma+\mu+\omega_2)(\epsilon+\mu)(\delta\gamma+\mu)-\gamma\delta\gamma\epsilon\right)}.
\end{aligned}$$

Hence, the syphilis sub-model (6) has a unique incidence equilibrium if $\mathscr{R}_0^s > 1$.

Theorem 8: Syphilis infection-free equilibrium point of the model (3) has local asymptotic stability if $\mathscr{R}_0^s < 1$; otherwise, it is unstable.

Proof: Jacobean of the model (6) at the syphilis infection-free equilibrium point is as follows:

$$J\left(E_0^s\right)=\begin{pmatrix}-(\pi+\mu) & 0 & 0 & 0 & 0\\ \pi & -\mu & \frac{-\beta_1\Lambda(\tau_2(\pi+\mu)+\tau_3\pi)}{\mu(\pi+\mu)} & \frac{-\beta_1\phi_2\Lambda(\tau_2(\pi+\mu)+\tau_3\pi)}{\mu(\pi+\mu)} & \delta\gamma\\ 0 & 0 & \frac{\beta_1\Lambda(\tau_2(\pi+\mu)+\tau_3\pi)-\mu(\pi+\mu)(\epsilon+\mu)}{\mu(\pi+\mu)} & \frac{\beta_1\phi_2\Lambda(\tau_2(\pi+\mu)+\tau_3\pi)}{\mu(\pi+\mu)} & 0\\ 0 & 0 & \epsilon & -(\gamma+\mu+\omega_2) & 0\\ 0 & 0 & 0 & \gamma & -(\delta\gamma+\mu)\end{pmatrix}.$$

From the Jacobian matrix, the characteristics equation after simplification is as follows:

$$(-(\pi+\mu)\lambda)(-\mu-\lambda)(-(\delta\gamma+\mu)\lambda)\left[\left(\frac{\beta_1\Lambda(\tau_2(\pi+\mu)+\tau_3\pi)-\mu(\pi+\mu)(\epsilon+\mu)}{\mu(\pi+\mu)}\lambda\right)(-(\gamma+\mu+\omega_2)\lambda)-\left(\frac{\beta_1\phi_2\Lambda\epsilon(\tau_2(\pi+\mu)+\tau_3\pi)}{\mu(\pi+\mu)}\right)\right]=0.$$

Then the eigenvalues are $\lambda_1=-(\pi+\mu)<0$ or $\lambda_2=-\mu<0$ or $\lambda_3=-(\delta\gamma+\mu)<0$ or $a_0\lambda^2+a_1\lambda+a_2=0$.

where,

$$a_0=1,$$
$$a_1=(\gamma+\mu+\omega_2)+(\epsilon+\mu)+\frac{\beta_1\Lambda(\tau_2(\pi+\mu)+\tau_3\pi)}{\mu(\pi+\mu)},$$
$$a_2=(\epsilon+\mu)(\gamma+\mu+\omega_2)(1-\mathscr{R}_0^s).$$

Applying Routh–Hurwitz criteria stated in [33], each eigenvalue of the matrix is negative whenever $\mathscr{R}_0^s<1$; thus, the syphilis infection-free equilibrium point has local asymptotic stability if $\mathscr{R}_0^s<1$.

Theorem 9: Syphilis infection-free equilibrium point E_s^0 of the model (6) has global stability if $\mathscr{R}_0^s<1$; otherwise, it is unstable.

Proof: Let the Lyapunov representative function be given as $l(I_{as},I_{ss})=aI_{as}+bI_{ss}$, where $=\frac{[(\gamma+\mu)+\phi_2\epsilon]}{(\epsilon+\mu)(\gamma+\mu+\omega_2)}$, $b=\frac{\phi_2}{(\gamma+\mu+\omega_2)}$.

$$\Longrightarrow l(I_{as},I_{ss})=\frac{[(\gamma+\mu+\omega_2)+\phi_2\epsilon]}{(\epsilon+\mu)(\gamma+\mu+\omega_2)}I_{as}+\frac{\phi_2}{(\gamma+\mu+\omega_2)}I_{ss}.$$
$$\Longrightarrow\frac{dl}{dt}=\frac{[(\gamma+\mu+\omega_2)+\phi_2\epsilon]}{(\epsilon+\mu)(\gamma+\mu+\omega_2)}(\lambda_sS-I_{as}(\epsilon+\mu))+\frac{\phi_2}{(\gamma+\mu)}(\epsilon I_{as}-I_{ss}(\gamma+\mu+\omega_2)),$$
$$\leq\frac{[(\gamma+\mu+\omega_2)+\phi_2\epsilon]}{(\epsilon+\mu)(\gamma+\mu+\omega_2)}(\beta_1(I_{as}+\phi_2I_{ss})S^*-I_{as}(\epsilon+\mu))+\frac{\phi_2}{(\gamma+\mu)}(\epsilon I_{as}-I_{ss}(\gamma+\mu+\omega_2)),$$
$$\leq\frac{[(\gamma+\mu+\omega_2)+\phi_2\epsilon]}{(\epsilon+\mu)(\gamma+\mu+\omega_2)}(\beta_1I_{as}S^*+\beta_1\phi_2I_{ss}S^*-I_{as}(\epsilon+\mu))+\frac{\phi_2}{(\gamma+\mu)}(\epsilon I_{as}-I_{ss}(\gamma+\mu+\omega_2)),$$
$$\leq([\beta_1S^*-(\epsilon+\mu)]\frac{[(\gamma+\mu+\omega_2)+\phi_2\epsilon]}{(\epsilon+\mu)(\gamma+\mu+\omega_2)}+\frac{\phi_2\epsilon}{(\gamma+\mu+\omega_2)})I_{as}+(\frac{\beta_1\phi_2[(\gamma+\mu+\omega_2)+\phi_2\epsilon]S^*}{(\epsilon+\mu)(\gamma+\mu+\omega_2)}-\phi_2)I_{ss},$$
$$\leq([\frac{[(\gamma+\mu)+\phi_2\epsilon]\beta_1S^*}{(\epsilon+\mu)(\gamma+\mu+\omega_2)}-\frac{[(\gamma+\mu+\omega_2)+\phi_2\epsilon]}{(\gamma+\mu+\omega_2)}])I_{as}+(\frac{\beta_1\phi_2[(\gamma+\mu+\omega_2)+\phi_2\epsilon]S^*}{(\epsilon+\mu)(\gamma+\mu+\omega_2)}-\phi_2)I_{ss},$$
$$\leq\frac{[(\gamma+\mu+\omega_2)+\phi_2\epsilon]\beta_1\Lambda(\tau_2(\pi+\mu)+\tau_3\pi)}{\mu(\pi+\mu)(\epsilon+\mu)(\gamma+\mu+\omega_2)}I_{as}-\frac{[(\gamma+\mu+\omega_2)+\phi_2\epsilon]}{(\gamma+\mu+\omega_2)}I_{as}+(\frac{\beta_1\phi_2[(\gamma+\mu+\omega_2)+\phi_2\epsilon]\Lambda(\tau_2(\pi+\mu)+\tau_3\pi)}{\mu(\pi+\mu)(\epsilon+\mu)(\gamma+\mu+\omega_2)}-\phi_2)I_{ss}.$$
$$\leq([\frac{[(\gamma+\mu+\omega_2)+\phi_2\epsilon]\beta_1\Lambda(\tau_2(\pi+\mu)+\tau_3\pi)}{\mu(\pi+\mu)(\epsilon+\mu)(\gamma+\mu+\omega_2)}-m])I_{as}+(\frac{\beta_1\phi_2[(\gamma+\mu+\omega_2)+\phi_2\epsilon]\Lambda(\tau_2(\pi+\mu)+\tau_3\pi)}{\mu(\pi+\mu)(\epsilon+\mu)(\gamma+\mu+\omega_2)}-\phi_2),\ where$$
$$m=\frac{[(\gamma+\mu+\omega_2)+\phi_2\epsilon]}{(\gamma+\mu+\omega_2)}>1.$$
$$\leq m([\frac{\mathscr{R}_0^s}{m}-1])I_{as}+\phi_2(\frac{\mathscr{R}_0^s}{\phi_2}-1)I_{ss},$$
$$\frac{\mathscr{R}_0^s}{m}<1,\frac{\mathscr{R}_s^0}{\phi_2}<1,$$
$$\frac{\mathscr{R}_0^s}{m}<1,\frac{\mathscr{R}_0^s}{\phi_2}<1\ \text{implies}\ \mathscr{R}_0^s<1\ \text{since m}$$
$$=\frac{[(\gamma+\mu+\omega_2)+\phi_2\epsilon]}{(\gamma+\mu+\omega_2)}>1,\ \text{and}\ \phi_2>1.$$

Hence, the syphilis-free equilibrium point is globally stable if $\mathscr{R}_0^s<1$.

3.3. COVID-19 and syphilis co-infection model analysis

3.3.1. The model (3) disease-free equilibrium

Making all the equations of (3) zero with $I_c=I_{as}=I_{ss}=I_{cs}=0$, the disease-free equilibrium point of (3) is given by $E^0=\left(P_c^0,P_s^0,S^0,I_c^0,Q_c^0,I_{as}^0,I_{ss}^0,T_s^0,T_{cs}^0,T^0\right)=\left(\frac{\tau_1\Lambda}{(\beta+\mu)},\frac{\tau_3\Lambda}{(\pi+\mu)},\frac{\Lambda(\tau_2(\beta+\mu)(\pi+\mu)+\tau_1\beta(\pi+\mu)+\tau_3\pi(\beta+\mu))}{\mu(\beta+\mu)(\pi+\mu)},0,0,0,0,0,0\right)$.

3.3.2. The model (3) reproduction number

The COVID-19 and syphilis co-infection model (3) reproduction number denoted by $\mathfrak{R}_0^{cs}$ is calculated using next-generation matrix criteria, as stated in [44]. Since we have four infectious groups, those are I_c, I_{as}, I_{ss}, and I_{cs}, and we have

$$f_i=\begin{bmatrix}\beta_2(I_c+\phi_1I_{cs})(S+P_s)\\ \beta_1(I_{as}+\phi_2I_{ss}+\phi_3I_{cs})(S+P_c)\\ 0\\ \beta_2(\theta_2I_{as}+\theta_3I_{ss})(I_c+\phi_1I_{cs})+\theta_1\beta_1(I_{as}+\phi_2I_{ss}+\phi_3I_{cs})I_c\end{bmatrix}.$$
$$\Longrightarrow f=\begin{bmatrix}\beta_2(S^0+P_s^0) & 0 & 0 & \phi_1(S^0+P_s^0)\\ 0 & \beta_1(S^0+P_c^0) & \beta_1\phi_2(S^0+P_c^0) & \beta_1\phi_3(S^0+P_c^0)\\ 0 & 0 & 0 & 0\\ 0 & 0 & 0 & 0\end{bmatrix},$$

and

$$v_i = v_i^-(x) - v_i^+(x) = \begin{bmatrix} I_c\left(\theta_1\beta_1(I_{as}+\phi_2 I_{ss}+\phi_3 I_{cs})+\rho+\mu+\omega_1\right) \\ I_{as}\left(\theta_2\beta_2(I_c+\phi_1 I_{cs})+\epsilon+\mu\right) \\ I_{ss}\left(\theta_3\beta_2(I_c+\phi_1 I_{cs})+\gamma+\mu+\omega_2\right)-\epsilon I_{as} \\ I_{cs}(\varepsilon+\mu+\omega_3) \end{bmatrix}.$$

$$\Longrightarrow v = \begin{bmatrix} (\rho+\mu+\omega_1) & 0 & 0 & 0 \\ 0 & (\epsilon+\mu) & 0 & 0 \\ 0 & -\epsilon & (\gamma+\mu+\omega_2) & 0 \\ 0 & 0 & 0 & (\varepsilon+\mu+\omega_3) \end{bmatrix}.$$

Then applying Mathematica, we have got

$$v^{-1} = \begin{bmatrix} \frac{1}{(\rho+\mu+\omega_1)} & 0 & 0 & 0 \\ 0 & \frac{1}{(\varepsilon+\mu)} & 0 & 0 \\ 0 & 0 & \frac{1}{(\gamma+\mu+\omega_2)} & 0 \\ 0 & 0 & 0 & \frac{1}{(\varepsilon+\mu+\omega_3)} \end{bmatrix},$$

and

$$fv^{-1} = \begin{bmatrix} \frac{\beta_2(S^0+P^0{}_s)}{(\rho+\mu+\omega_1)} & 0 & 0 & \frac{\phi_1(S^0+P^0{}_s)}{(\varepsilon+\mu+\omega_3)} \\ 0 & \frac{\beta_1(S^0+P^0{}_c)}{(\varepsilon+\mu)} & \frac{\beta_1\phi_2(S^0+P^0{}_c)}{(\gamma+\mu+\omega_2)} & \frac{\beta_1\phi_3(S^0+P^0{}_c)}{(\varepsilon+\mu+\omega_3)} \\ 0 & 0 & 0 & 0 \\ 0 & 0 & 0 & 0 \end{bmatrix}.$$

$$\Longrightarrow \begin{vmatrix} \frac{\beta_2(S^0+P^0{}_s)}{(\rho+\mu+\omega_1)}-\lambda & 0 & 0 & \frac{\phi_1(S^0+P^0{}_s)}{(\varepsilon+\mu+\omega_3)} \\ 0 & \frac{\beta_1(S^0+P^0{}_c)}{(\varepsilon+\mu)}-\lambda & \frac{\beta_1\phi_2(S^0+P^0{}_c)}{(\gamma+\mu+\omega_2)} & \frac{\beta_1\phi_3(S^0+P^0{}_c)}{(\varepsilon+\mu+\omega_3)} \\ 0 & 0 & 0-\lambda & 0 \\ 0 & 0 & 0 & 0-\lambda \end{vmatrix} = 0.$$

Then, the corresponding eigenvalues are $\lambda_1 = 0$ or $\lambda_2 = 0$ or $\lambda_3 = \frac{\beta_2(S^0+P^0{}_s)}{(\rho+\mu+\omega_1)} = \frac{\beta_2\Lambda\tau_2}{\mu(\rho+\mu+\omega_1)} + \frac{\beta_2\Lambda\tau_1\beta}{\mu(\beta+\mu)(\rho+\mu+\omega_1)} + \frac{\beta_2\Lambda\tau_3}{\mu(\rho+\mu+\omega_1)} = \Re_0^c + n$ or $\lambda_4 = \beta_1(\frac{\tau_2\Lambda(\beta+\mu)(\pi+\mu)+\tau_1\beta\Lambda(\pi+\mu)+\tau_3\pi\Lambda(\beta+\mu)+\tau_1\Lambda\mu(\pi+\mu)}{\mu(\beta+\mu)(\pi+\mu)(\varepsilon+\mu)}) = \Re_0^s - m$ where, $n = \frac{\beta_2\Lambda\tau_3}{\mu(\rho+\mu+\omega_1)}$, $m = \frac{\beta_1\Lambda[\epsilon\phi_2(\tau_2(\pi+\mu)+\tau_3\pi)-\tau_1((\pi+\mu)\gamma+\mu+\omega_2)]}{\mu(\pi+\mu)(\gamma+\mu+\omega_2)(\epsilon+\mu)}$.

Therefore, the COVID-19–syphilis complete model (3) reproduction number denoted by $\Re_0^{cs}$ is given by $\Re_0^{cs} = \max\left\{\Re_0^c + n, \Re_0^s - m\right\}$.

3.3.3. Model (3) disease-free equilibrium local stability

Theorem 10: The full-model (3) disease-free equilibrium point has local asymptotic stability if $\Re_0^{cs} < 1$; otherwise, it is unstable.

Proof: The Jacobian of the COVID-19 and syphilis co-infection model (3) at E^0 is as follows:

$$J(E^0) = \begin{pmatrix} a & 0 & 0 & 0 & 0 & b & c & 0 & d & 0 \\ 0 & e & 0 & f & 0 & 0 & 0 & 0 & g & 0 \\ \beta & \pi & h & i & 0 & j & k & l & m & 0 \\ 0 & 0 & 0 & n & 0 & 0 & 0 & 0 & o & 0 \\ 0 & 0 & 0 & \rho & h & 0 & 0 & 0 & 0 & 0 \\ 0 & 0 & 0 & 0 & 0 & p & q & 0 & r & 0 \\ 0 & 0 & 0 & 0 & 0 & \epsilon & s & 0 & 0 & 0 \\ 0 & 0 & 0 & 0 & 0 & 0 & \gamma & t & 0 & 0 \\ 0 & 0 & 0 & 0 & 0 & 0 & 0 & 0 & u & 0 \\ 0 & 0 & 0 & 0 & 0 & 0 & 0 & 0 & \varepsilon & h \end{pmatrix},$$

where $a = -(\beta+\mu), b = -\beta_1 P_c{}^0, c = -\beta_1\phi_2 P_c{}^0, d = -\beta_1\phi_3 P_c{}^0, e = -(\pi+\mu), f = -\beta_2 P_s{}^0, g = -\beta_2\phi_1 P_s{}^0, h = -\mu, i = -\beta_2 S^0, j = -\beta_1 S^0, k = -\beta_1\phi_2 S^0, l = \delta\gamma, m = -(\beta_1\phi_3+\beta_2\phi_1) S^0, n = \beta_2(S+P_s) - (\rho+\mu+\omega_1), o = \beta_2\phi_1(S+P_s), p = \beta_1(S+P_c)-(\epsilon+\mu), q = \beta_1\phi_2(S+P_c), r = \beta_1\phi_3(S^0+P_c{}^0), s = -(\gamma+\mu+\omega_2), t = -(\delta\gamma+\mu), u = -(\varepsilon+\mu+\omega_3)$.

$$\Longrightarrow \begin{vmatrix} a-\lambda & 0 & 0 & 0 & 0 & b & c & 0 & d & 0 \\ 0 & e-\lambda & 0 & f & 0 & 0 & 0 & 0 & g & 0 \\ \beta & \pi & h-\lambda & i & 0 & j & k & l & m & 0 \\ 0 & 0 & 0 & n-\lambda & 0 & 0 & 0 & 0 & o & 0 \\ 0 & 0 & 0 & \rho & h-\lambda & 0 & 0 & 0 & 0 & 0 \\ 0 & 0 & 0 & 0 & 0 & p-\lambda & q & 0 & r & 0 \\ 0 & 0 & 0 & 0 & 0 & \epsilon & s-\lambda & 0 & 0 & 0 \\ 0 & 0 & 0 & 0 & 0 & 0 & \gamma & t-\lambda & 0 & 0 \\ 0 & 0 & 0 & 0 & 0 & 0 & 0 & 0 & u-\lambda & 0 \\ 0 & 0 & 0 & 0 & 0 & 0 & 0 & 0 & \varepsilon & h-\lambda \end{vmatrix} = 0.$$

By using square block matrix properties, we rewrite the above determinant as follows:

$$\begin{vmatrix} A & B \\ 0 & C \end{vmatrix} = 0, \text{ where}$$

$$A = \begin{bmatrix} a-\lambda & 0 & 0 & 0 & 0 \\ 0 & e-\lambda & 0 & f & 0 \\ \beta & \pi & h-\lambda & i & 0 \\ 0 & 0 & 0 & n-\lambda & 0 \\ 0 & 0 & 0 & \rho & h-\lambda \end{bmatrix}, B = \begin{bmatrix} b & c & 0 & d & 0 \\ 0 & 0 & 0 & g & 0 \\ j & k & l & m & 0 \\ 0 & 0 & 0 & 0 & 0 \\ 0 & 0 & 0 & 0 & 0 \end{bmatrix},$$

$$C = \begin{bmatrix} p-\lambda & q & 0 & r & 0 \\ \epsilon & s-\lambda & 0 & 0 & 0 \\ 0 & \gamma & t-\lambda & 0 & 0 \\ 0 & 0 & 0 & u-\lambda & 0 \\ 0 & 0 & 0 & \varepsilon & h-\lambda \end{bmatrix}, O = \begin{bmatrix} 0 & 0 & 0 & 0 & 0 \\ 0 & 0 & 0 & 0 & 0 \\ 0 & 0 & 0 & 0 & 0 \\ 0 & 0 & 0 & 0 & 0 \\ 0 & 0 & 0 & 0 & 0 \end{bmatrix}.$$

$$\begin{vmatrix} a-\lambda & 0 & 0 & 0 & 0 & b & c & 0 & d & 0 \\ 0 & e-\lambda & 0 & f & 0 & 0 & 0 & 0 & g & 0 \\ \beta & \pi & h-\lambda & i & 0 & j & k & l & m & 0 \\ 0 & 0 & 0 & n-\lambda & 0 & 0 & 0 & 0 & o & 0 \\ 0 & 0 & 0 & \rho & h-\lambda & 0 & 0 & 0 & 0 & 0 \\ 0 & 0 & 0 & 0 & 0 & p-\lambda & q & 0 & r & 0 \\ 0 & 0 & 0 & 0 & 0 & \epsilon & s-\lambda & 0 & 0 & 0 \\ 0 & 0 & 0 & 0 & 0 & 0 & \gamma & t-\lambda & 0 & 0 \\ 0 & 0 & 0 & 0 & 0 & 0 & 0 & 0 & u-\lambda & 0 \\ 0 & 0 & 0 & 0 & 0 & 0 & 0 & 0 & \varepsilon & h-\lambda \end{vmatrix} = |A|\,|C| = 0.$$

From this, we do have

$$|A| = (a-\lambda)(e-\lambda)(h-\lambda)(n-\lambda)(h-\lambda),$$
$$|C| = (t-\lambda)(u-\lambda)(h-\lambda)(\left(p-\lambda\right)(s-\lambda)-q\epsilon), |A|$$
$$|C| = \left[(a-\lambda)(e-\lambda)(h-\lambda)(n-\lambda)(h-\lambda)\right] \left[(t-\lambda)(u-\lambda)(h-\lambda)(\left(p-\lambda\right)(s-\lambda)-q\epsilon)\right] = 0.$$

Then, the eigenvalue of the full model is as follows:

$$\lambda_1 = a \text{ or } \lambda_2 = e \text{ or } \lambda_3 = h \text{ or } \lambda_4 = n \text{ or } \lambda_5 = h \text{ or } \lambda_6 = t \text{ or}$$
$$\lambda_7 = u \text{ or } \lambda_8 = h \text{ or } a_0\lambda^2 + a_1\lambda + a_2 = 0, \text{ where,}$$
$$a_0 = 1,$$
$$a_1 = (\rho+\mu+\omega_1)(\epsilon+\mu)\left(1-\Re_0^{cs}\right) > 0,$$

$$a_2 = (\epsilon + \mu)\,\phi_2\epsilon\left[1 - \Re_0^{cs}\right] > 0, if \Re_0^{cs} < 1.$$

Therefore, the co-infection model disease-free equilibrium point has local asymptotic stability if $\Re_0^{cs} < 1$.

3.3.4. The full-model endemic equilibrium and stabilities

The COVID-19 and syphilis co-infection model endemic equilibrium point is denoted by $E_{cs}^* = \left(P_c^*, P_s^*, S^*, I_c^*, Q_c^*, I_{as}^*, I_{ss}^*, I_{cs}^*, T_s^*, T^*\right)$. The analysis of the COVID-19-only mono-infection system (5) and the syphilis-only sub-model (6) shows that there is no endemic equilibrium point whenever $\Re_0^c < 1$ and $\Re_0^s < 1$, respectively, which means there is no endemic equilibrium point if $\Re_0^{cs} < 1$ for the co-infection model (3). In other words, the COVID-19 and syphilis co-infection disease-free equilibrium point have global stability if $\Re_0^{cs} < 1$.

The explicit calculation of the co-infection model endemic equilibrium in terms of model parameters is tedious analytically; however, the model (3) endemic equilibriums correspond to

1. $E_1^* = \left(P_c^*, 0, S^*, I_c^*, Q_c^*, 0, 0, 0, 0, 0\right)$, if $\Re_0^c > 1$ is the syphilis-free (COVID-19 persistence) equilibrium point.

   The analysis of the equilibrium E_1^* is similar to the endemic equilibrium E_c^* in the model (5).
2. $E_2^* = \left(0, P_s^*, S^*, 0, 0, I_{as}^*, I_{ss}^*, 0, 0, T_s^*, 0\right)$, if $\Re_0^s > 1$ is the COVID-19-free (syphilis persistence) equilibrium point. The analysis of the equilibrium E_2^* is similar to the endemic equilibrium E_s^* in Equation (6).
3. $E_{cs}^* = \left(P_c^*, P_s^*, S^*, I_c^*, Q_c^*, I_{as}^*, I_{ss}^*, I_{cs}^*, T_s^*, T^*\right)$ is the COVID-19 and syphilis co-existence persistence equilibrium point. It exists when each component of E_{cs}^* is positive whenever $\Re_0^{cs} > 1$ for this case, we have shown its stability in the numerical simulation part given in Section 4.

4. Sensitivity analysis and numerical simulations

In this section, we carried out the sensitivity analysis to examine the most sensitive parameters in the disease spreading and numerical simulations to verify the qualitative results of the mathematical model (3). Particularly, some numerical verification is considered to illustrate the qualitative analysis and results of the preceding sections. Here, we have taken some parameter values from literature and assumed some of the parameter values that are not from real data since there is a lack of mathematical modeling analysis literature which have studied the COVID-19 and syphilis co-infection transmission dynamics in the community. The fundamental problem of numerical analysis of a mathematical model is how to estimate parameters. Randomly choosing the values of parameters in the model in plausible intervals followed by sensitivity to the parameters is possible partially to overcome the limitations of parameters [41].

Here, the numerical simulation is used for checking the behaviors of the full-model (3) solutions and the effects of parameters in the transmission as well as the controlling of COVID-19 infection, syphilis infection, and co-infection of COVID-19 and syphilis. For numerical simulation purposes, we have applied MATLAB ode45 code with parameter values given in Table 3.

TABLE 3 Parameter values for numerical simulations.

Parameter	Value	References
μ	0.0000559 $year^{-1}$	[17]
Λ	500 day^{-1}	[45]
β	0.30 day^{-1}	Assumed
π	0.21 day^{-1}	Assumed
ρ	0.5 day^{-1}	[45]
ϵ	0.40 $year^{-1}$	[12]
ε	0.3 $year^{-1}$	Assumed
γ	0.021 $year^{-1}$	[38]
δ	0.2482 $year^{-1}$	[34]
β_1	8 $year^{-1}$	[38]
β_2	0.6 day^{-1}	[45]
θ_1	1.1 dimensionless	Assumed
θ_2	1.1 dimensionless	Assumed
θ_3	1.1 dimensionless	Assumed
τ_1	0.27 dimensionless	Assumed
τ_2	0.41 dimensionless	Assumed
τ_3	0.32 dimensionless	Assumed
ω_1	0.023 day^{-1}	[45]
ω_2	0.06849 $year^{-1}$	[17]
ω_3	0.07 $year^{-1}$	Assumed

4.1. Analysis of sensitivity

Definition: The syphilis and COVID-19 co-infection model (3) normalized forward sensitivity index for its variable reproduction number is denoted by $\mathscr{R}_0^{cs}$ its derivative depends on a parameter ζ is defined by $\mathrm{SEI}(p) = \frac{\partial \mathscr{R}_0^{cs}}{\partial \zeta} * \frac{\zeta}{\mathscr{R}_0^{cs}}$ [20, 21, 42].

The syphilis and COVID-19 co-infection model sensitivity index values justify the significance of different parameters in the single infections and co-infection spreading in the community. The parameter which has the highest magnitude of the sensitivity index value compared to other parameter index values is the most sensitive. Here, we have calculated the sensitivity index values in terms of the basic reproduction number $\mathscr{R}_0^{cs} = \max\left\{\mathscr{R}_0^s, \mathscr{R}_0^c\right\}$. Using parameter values stated in Table 3, the sensitivity index values of the model (3) are calculated in Tables 4, 5.

Using parameter values in Table 3, we have computed $\Re_0^{cs} = \max\left\{\Re_0^c, \Re_0^s\right\} = \max\{2.7, 3.2\} = 3.2$ and biologically, it means that syphilis infection, COVID-19 infection, and their co-infection are spreading in the population. The sensitivity index values stated in Table 4 explain that the recruitment rate Λ and the COVID-19 spreading rate β_2 have a high direct impact on the COVID-19 basic reproduction $\Re_0^c$. That means the recruitment rate and the COVID-19 transmission rates are the most sensitive parameters where stakeholders can control the transmission rate by applying prevention and control measures. Similarly, the COVID-19 protection portion τ_1 and the quarantine with treatment rate ρ also have an indirect impact on the COVID-19 reproduction number $\Re_0^c$.

TABLE 4 Sensitivity indexes of $\mathscr{R}_0^{cs} = \mathscr{R}_0^c$.

Sensitivity index	Values
SEI(β_2)	1
SEI(Λ)	1
SEI(τ_2)	0.50
SEI(β)	0.09
SEI(τ_1)	−0.56
SEI(μ)	−0.13
SEI(ρ)	−0.65
SEI(ω_1)	−0.07

TABLE 5 Sensitivity indexes of $\mathscr{R}_0^{cs} = \mathscr{R}_0^s$.

Sensitivity index	Values
SEI(β_1)	1
SEI(Λ)	1
SEI(γ)	−0.65
SEI(ω_2)	−0.32
SEI(π)	0.12
SEI(τ_2)	0.56
SEI(τ_3)	−0.64
SEI(ϕ_2)	0.41
SEI(ϵ)	0.46

Sensitivity indices stated in Table 5 explain that the recruitment rate Λ and syphilis spreading rate β_1 have a high direct impact on the syphilis basic reproduction $\mathfrak{R}_0^s$. That means the recruitment rate and syphilis transmission rates are the most sensitive parameters where stakeholders can control the transmission rate by applying prevention and control measures. Similarly, the syphilis protection portion τ_3 and syphilis treatment rate γ have a high indirect effect on the syphilis reproduction number $\mathfrak{R}_0^s$.

4.2. Results of numerical simulations

4.2.1. Behaviors of solutions of model (3) whenever $\mathfrak{R}_0^{cs} < 1$

In the numerical simulation given in Figure 2, we observed that all the COVID-19 and syphilis co-infection model (3) solutions converge toward the disease-free equilibrium point whenever $\mathfrak{R}_0^c = 0.71$ and $\mathfrak{R}_0^s = 0.34$ with $\beta_1 = 0.3$ and $\beta_2 = 0.08$, respectively. At the co-infection disease-free equilibrium point, each solution curve of the model converges to zero while the susceptible group increases and then becomes constant, implying that the disease-free equilibrium point of the COVID-19 and syphilis co-infection model has global asymptotic stability if $\mathfrak{R}_0^{cs} < 1$. Biologically it means the COVID-19 and syphilis co-infection diseases have been eradicated from the community through time whenever $\mathfrak{R}_0^{cs} = \max\{\mathfrak{R}_0^c, \mathfrak{R}_0^s\} = 0.71 < 1$.

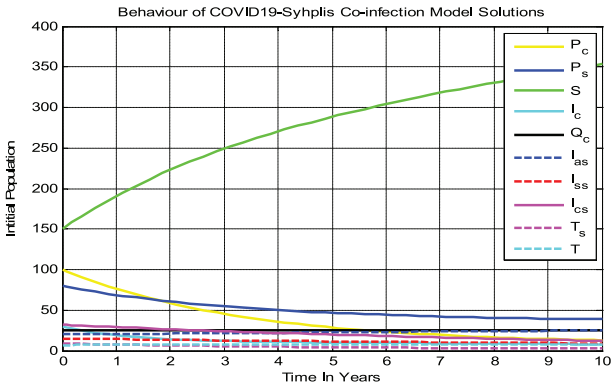

FIGURE 2
The complete model solutions behavior if $\mathfrak{R}_0^{cs} < 1$ at $\beta_1 = 0.3$ and $\beta_2 = 0.08$.

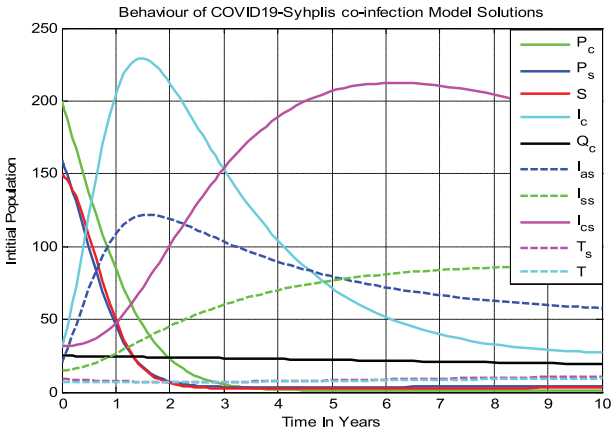

FIGURE 3
Behaviors of the full model solutions whenever $\mathfrak{R}_0^{cs} > 1$ at $\beta_1 = 8$ and $\beta_2 = 11$.

4.2.2. Behaviors of the model solutions whenever $\mathfrak{R}_0^{cs} > 1$

Figure 3 shows that all the COVID-19 and syphilis co-infection model (3) solutions converge toward the endemic equilibrium point whenever $\mathfrak{R}_0^c = 3.2$ and $\mathfrak{R}_0^s = 2.1$ with $\beta_1 = 8$ and $\beta_2 = 11$, respectively. After 10 years, the full-model solutions converge to the endemic equilibrium, while the susceptible population decreases and then remains constant means the COVID-19 and syphilis co-infection model endemic equilibrium point has local asymptotic stability if $\mathfrak{R}_0^{cs} = \max\{\mathfrak{R}_0^c, \mathfrak{R}_0^s\} = 3.2 > 1$. Biologically, it means that COVID-19 and syphilis co-infection disease spreads throughout the community under consideration.

4.2.3. Effects of protection measures on reproduction numbers

The numerical simulation represented by Figure 4 shows that when we maximize the COVID-19 rate of protection τ_1, the reproduction number $\mathfrak{R}_0^c$ decreases, implying that the COVID-19 spreading rate decreases. Its biological meaning is that whenever the COVID-19 rate of protection $\tau_1 > 0.7$ the reproduction

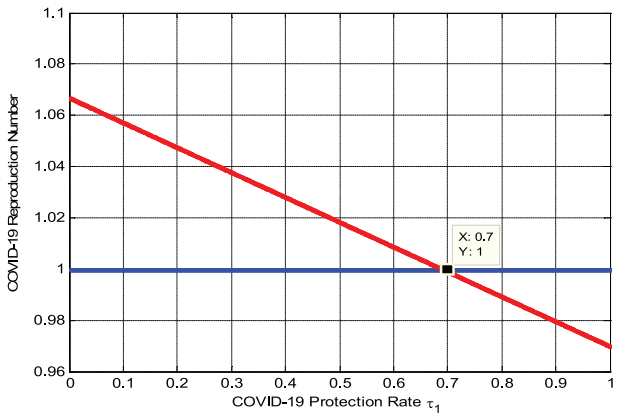

FIGURE 4
Effect of COVID-19 protection rate on $\Re_0^c$.

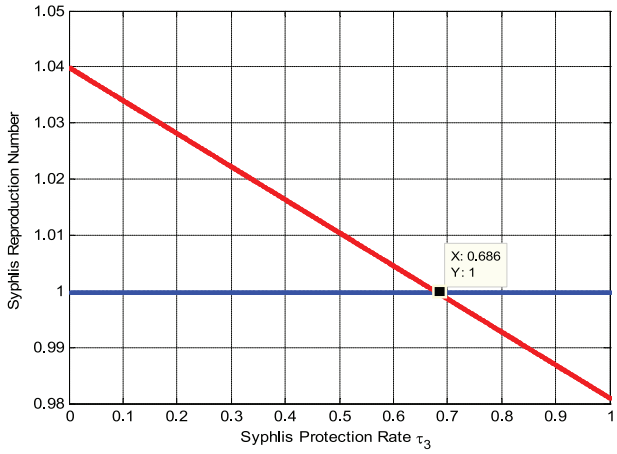

FIGURE 5
Effect of syphilis protection rate τ_3 on $\Re_0^s$.

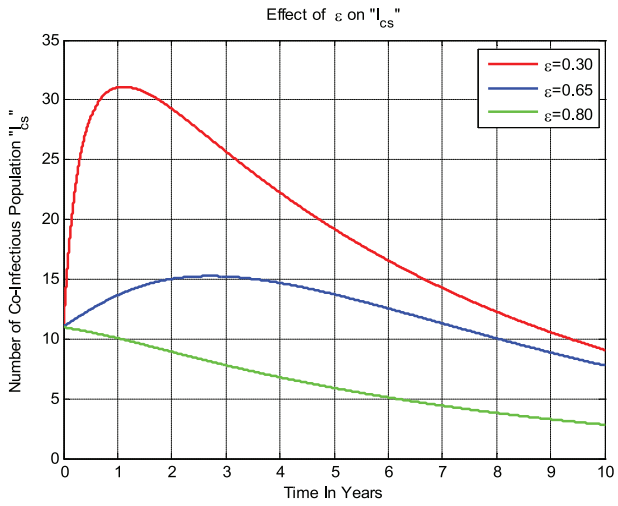

FIGURE 6
Impact of treatment rate ε on I_{cs}.

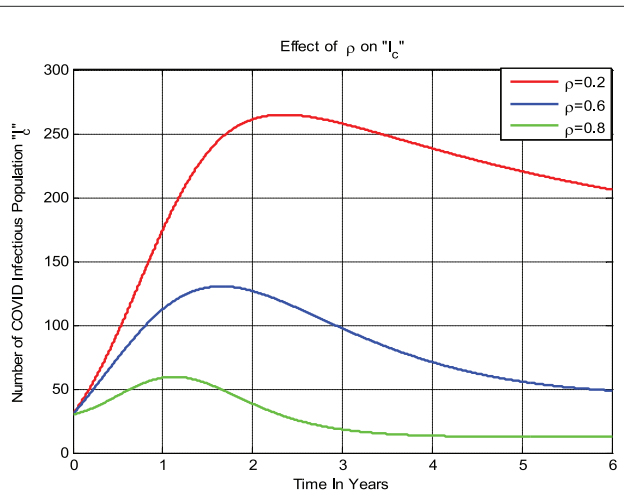

FIGURE 7
Impact of treatment rate ρ on I_c.

number $\Re_0^c < 1$, that is, the COVID-19 infection will be eradicated throughout the community.

Here, the numerical simulation represented by Figure 5 shows that whenever we maximize the syphilis protection rate τ_3, the syphilis reproduction number $\Re_0^s$ decreases, implying that the syphilis spreading rate decreases. Whenever $\tau_3 > 0.686$ then $\Re_0^s < 1$, biologically, it means the syphilis infection eradicate from the community.

4.2.4. Impact of treatment on co-infected population

The numerical simulation given in Figure 6 shows that whenever the combined treatment rate ε of the COVID-19 virus and syphilis microorganism Treponema pallidum bacterium co-infected individuals I_{cs} increases, the number of co-infected individuals decreases; that is, whenever the value of ε increases from 0.3 to 0.8, then the co-infected group I_{cs} going down.

The numerical simulation given in Figure 7 shows that if the treatment rate ρ of COVID-19 increases, then the number of infections in the population decreases; that is, whenever ρ value increases from 0.2 to 0.8 then the infected group I_c decreases.

5. Discussions and conclusion

In this study, we have formulated and analyzed a new deterministic mathematical model for gaining insight into the effects of protections and treatments on the transmission dynamics of COVID-19 and syphilis co-infection. Both the positivity and boundedness of the complete model solutions have been discussed to show that the model is both mathematically and biologically meaningful. COVID-19 infection-free equilibrium point, COVID-19 incidence equilibrium point, and local and global stabilities of COVID-19 infection-free and COVID-19 incidence equilibrium points have been examined. Syphilis infection-free equilibrium point, syphilis incidence equilibrium point, and local and global stabilities of syphilis-free and syphilis incidence equilibrium points have been

carried out. Using data stated in Table 3, we have carried out and discussed both sensitivity and numerical analyses of the full COVID-19 and syphilis co-infection model. From the analytical and numerical results, we observed that the model disease-free equilibrium points have global asymptotic stability when the basic reproduction numbers are less than unity. Biologically, this means that diseases die out in the community, with the full-model solutions converging to their endemic equilibrium point whenever their basic reproduction number is greater than unity, the reproduction numbers of both the COVID-19 infection and syphilis infection sub-models decreasing when the corresponding protection and treatment rates are maximized, and the numbers of co-infected individuals decreasing when the co-infection treatment rate is increased.

Based on the findings of this study, we recommend public health stakeholders concentrate on increasing both the COVID-19 and syphilis protection rates, as well as the syphilis treatment rate, the COVID-19 isolation with treatment rate, and the co-infection treatment rate, in order to reduce and possibly eradicate syphilis and COVID-19 co-infection transmission in the community. Finally, since no other COVID-19 and syphilis mathematical modeling approach literature has been formulated and analyzed, this study is not exhaustive. Interested researchers can extend this study in different manners, such as including syphilis mother-to-child transmission, COVID-19 vaccination as a new compartment, two-strain COVID-19 co-infection with syphilis, age structure for both infections, the four infection stages of syphilis (primary, secondary, latent, and tertiary), optimal control approach, stochastic method, fractional order method, and applying appropriate real population data.

Data availability statement

All relevant data is contained within the article: The original contributions presented in the study are included in the article/supplementary material, further inquiries can be directed to the corresponding author/s.

Ethics statement

Ethical review and approval was not required for the study on human participants in accordance with the local legislation and institutional requirements. The patients/participants provided their written informed consent to participate in this study.

Author contributions

Both authors listed have made a substantial, direct, and intellectual contribution to the work and approved it for publication.

Acknowledgments

The authors thank Mr. Sitotaw Eshete for his great Wi-Fi contribution that we have used in the study.

Conflict of interest

The authors declare that the research was conducted in the absence of any commercial or financial relationships that could be construed as a potential conflict of interest.

Publisher's note

All claims expressed in this article are solely those of the authors and do not necessarily represent those of their affiliated organizations, or those of the publisher, the editors and the reviewers. Any product that may be evaluated in this article, or claim that may be made by its manufacturer, is not guaranteed or endorsed by the publisher.

References

1. Panovska-Griffiths J. Can mathematical modelling solve the current COVID-19 crisis? *BMC Public Health.* (2020) 20:1–3. doi: 10.1186/s12889-020-08671-z

2. Adiga A, Dubhashi D, Lewis B, Marathe M, Venkatramanan S, Vullikanti A. Mathematical models for COVID-19 pandemic: a comparative analysis. *J Indian Inst Sci.* (2020) 100:793–807. doi: 10.1007/s41745-020-00200-6

3. Musuuza JS, Watson L, Parmasad V, Putman-Buehler N, Christensen L, Safdar N. Prevalence and outcomes of co-infection and superinfection with SARS-CoV-2 and other pathogens: a systematic review and meta-analysis. *PLoS ONE.* (2021) 16:e0251170. doi: 10.1371/journal.pone.0251170

4. Kumar P, Erturk VS, Murillo-Arcila M. A new fractional mathematical modelling of COVID-19 with the availability of vaccine. *Results Phys.* (2021) 24:104213. doi: 10.1016/j.rinp.2021.104213

5. Omame A, Sene N, Nometa I, Nwakanma CI, Nwafor EU, Iheonu NO, et al. Analysis of COVID-19 and comorbidity co-infection model with optimal control. *Optimal Control Appl Methods.* (2021) 42:1568–90. doi: 10.1002/oca.2748

6. Tuite AR, Fisman DN, Greer AL. Mathematical modelling of COVID-19 transmission and mitigation strategies in the population of Ontario, Canada. *CMAJ.* (2020) 192:E497–505. doi: 10.1503/cmaj.200476

7. Boukanjime B, Caraballo T, El Fatini M, El Khalifi M. Dynamics of a stochastic coronavirus (COVID-19) epidemic model with Markovian switching. *Chaos Solitons Fractals.* (2020) 141:110361. doi: 10.1016/j.chaos.2020.110361

8. Din A, Khan A, Baleanu D. Stationary distribution and extinction of stochastic coronavirus (COVID-19) epidemic model. *Chaos Solitons Fractals.* (2020) 139:110036. doi: 10.1016/j.chaos.2020.110036

9. Abdela SG, Berhanu AB, Ferede LM, van Griensven J. Essential healthcare services in the face of COVID-19 prevention: experiences from a referral hospital in Ethiopia. *Am J Trop Med Hyg.* (2020) 103:1198. doi: 10.4269/ajtmh.20-0464

10. Gumel AB, Lubuma J, Sharomi O, Terefe YA. Mathematics of a sex-structured model for syphilis transmission dynamics. *Math Methods Appl Sci.* (2018) 41:8488–513. doi: 10.1002/mma.4734

11. Momoh AA, Bala Y, Washachi DJ, Déthié D. Mathematical analysis and optimal control interventions for sex structured syphilis model with three stages of infection and loss of immunity. *Adv Diff Equ.* (2021) 2021:1–26. doi: 10.1186/s13662-021-03432-7

12. Peeling RW, Mabey D, Kamb ML, Chen XS, Radolf JD. "Benzaken." AS Syphilis. *Nat Rev Dis Prim.* (2017) 3:17073. doi: 10.1038/nrdp.2017.73

13. Peeling RW, Hook III EW. The pathogenesis of syphilis: the Great Mimicker, revisited. *J Pathol.* (2006) 208:224–32. doi: 10.1002/path.1903

14. Saad-Roy CM, Shuai Z, Van den Driessche P. A mathematical model of syphilis transmission in an MSM population. *Math Biosci.* (2016) 277:59–70. doi: 10.1016/j.mbs.2016.03.017

15. Tessema B, Yismaw G, Kassu A, Amsalu A, Mulu A, Emmrich F, et al. Seroprevalence of HIV, HBV, HCV and syphilis infections among blood donors at Gondar

University Teaching Hospital, Northwest Ethiopia: declining trends over a period of five years. *BMC Infect Dis.* (2010) 10:1–7. doi: 10.1186/1471-2334-10-111

16. World Health Organization. *WHO Guidelines for the Treatment of Treponema pallidum (Syphilis)*. Geneva: WHO (2016).

17. Iboi E, Okuonghae D. Population dynamics of a mathematical model for syphilis. *Appl Math Model.* (2016) 40:3573–90. doi: 10.1016/j.apm.2015.09.090

18. Milner FA, Zhao R. A new mathematical model of syphilis. *Math Model Nat Phenom.* (2010) 5:96–108. doi: 10.1051/mmnp/20105605

19. Tuite AR, Fisman DN, Mishra S. Screen more or screen more often? Using mathematical models to inform syphilis control strategies. *BMC Public Health.* (2013) 13:1–9. doi: 10.1186/1471-2458-13-606

20. Teklu SW, Rao KP. HIV/AIDS-Pneumonia codynamics model analysis with vaccination and treatment. *Comput Math Methods Med.* (2022) 2022:3105734. doi: 10.1155/2022/3105734

21. Teklu SW, Mekonnen TT. HIV/AIDS-pneumonia coinfection model with treatment at each infection stage: mathematical analysis and numerical simulation. *J Appl Math.* (2021) 2021:5444605. doi: 10.1155/2021/5444605

22. Danane J, Allali K, Hammouch Z, Nisar KS. Mathematical analysis and simulation of a stochastic COVID-19 Lévy jump model with isolation strategy. *Results Phys.* (2021) 23:103994. doi: 10.1016/j.rinp.2021.103994

23. Bonyah E, Chukwu CW, Juga ML. Modeling fractional order dynamics of syphilis via Mittag-Leffler law. *medRxiv.* (2021). doi: 10.3934/math.2021485

24. Nabi KN, Abboubakar H, Kumar P. Forecasting of COVID-19 pandemic: from integer derivatives to fractional derivatives. *Chaos Solitons Fractals.* (2020) 141:110283. doi: 10.1016/j.chaos.2020.110283

25. Nabi KN, Kumar P, Erturk VS. Projections and fractional dynamics of COVID-19 with optimal control strategies. *Chaos Solitons Fractals.* (2021) 145:110689. doi: 10.1016/j.chaos.2021.110689

26. Kumar P, Erturk VS, Murillo-Arcila M, Banerjee R, Manickam A. A case study of 2019-nCOV cases in Argentina with the real data based on daily cases from March 03, 2020 to March 29, 2021 using classical and fractional derivatives. *Adv Diff Equ.* (2021) 2021:1–21. doi: 10.1186/s13662-021-03499-2

27. Etemad S, Avci I, Kumar P, Baleanu D, Rezapour S. Some novel mathematical analysis on the fractal-fractional model of the AH1N1/09 virus and its generalized Caputo-type version. *Chaos Solitons Fractals.* (2022) 162:112511. doi: 10.1016/j.chaos.2022.112511

28. Zarin R, Khan A, Kumar P. Fractional-order dynamics of Chagas-HIV epidemic model with different fractional operators. *AIMS Math.* (2022) 7:18897–924. doi: 10.3934/math.20221041

29. Gao W, Veeresha P, Baskonus HM, Prakasha DG, Kumar P. A new study of unreported cases of 2019-nCOV epidemic outbreaks. *Chaos Solitons Fractals.* (2020) 138:109929. doi: 10.1016/j.chaos.2020.109929

30. Kumar P, Erturk VS, Abboubakar H, Nisar KS. Prediction studies of the epidemic peak of coronavirus disease in Brazil via new generalised Caputo type fractional derivatives. *Alexandr Eng J.* (2021) 60:3189–204. doi: 10.1016/j.aej.2021.01.032

31. Vellappandi M, Kumar P, Govindaraj V. Role of fractional derivatives in the mathematical modeling of the transmission of Chlamydia in the United States from 1989 to 2019. *Nonlinear Dyn.* (2022) 2022:1–15. doi: 10.1007/s11071-022-08073-3

32. Abbas S, Tyagi S, Kumar P, Ertürk VS, Momani S. Stability and bifurcation analysis of a fractional-order model of cell-to-cell spread of HIV-1 with a discrete time delay. *Math Methods Appl Sci.* (2022) 45:7081–95. doi: 10.1002/mma.8226

33. Teklu SW, Terefe BB. Mathematical modeling analysis on the dynamics of university students animosity towards mathematics with optimal control theory. *Sci Rep.* (2022) 12:1–19. doi: 10.1038/s41598-022-15376-3

34. Babaei A, Ahmadi M, Jafari H, Liya A. A mathematical model to examine the effect of quarantine on the spread of coronavirus. *Chaos Solitons Fractals.* (2021) 142:110418. doi: 10.1016/j.chaos.2020.110418

35. Basnarkov L. SEAIR. Epidemic spreading model of COVID-19. *Chaos Solitons Fractals.* (2021) 142:110394.

36. Mohamadou Y, Halidou A, Kapen PT. A review of mathematical modeling, artificial intelligence and datasets used in the study, prediction and management of COVID-19. *Appl Intell.* (2020) 50:3913–25. doi: 10.1007/s10489-020-01770-9

37. Ndaïrou F, Area I, Nieto JJ, Torres DF. Mathematical modeling of COVID-19 transmission dynamics with a case study of Wuhan. *Chaos Solitons Fractals.* (2020) 135:109846. doi: 10.1016/j.chaos.2020.109846

38. Nwankwo A, Okuonghae D. Mathematical analysis of the transmission dynamics of HIV syphilis co-infection in the presence of treatment for syphilis. *Bull Math Biol.* (2018) 80:437–92. doi: 10.1007/s11538-017-0384-0

39. Teklu SW, Kotola BS. The impact of protection measures and treatment on pneumonia infection: a mathematical model analysis supported by numerical simulation. *bioRxiv.* (2022). doi: 10.1101/2022.02.21.481255

40. Vellappandi M, Kumar P, Govindaraj V. Role of vaccination, the release of competitor snails, chlorination of water, and treatment controls on the transmission of bovine schistosomiasis disease: a mathematical study. *Phys Script.* (2022) 97:074006. doi: 10.1088/1402-4896/ac7421

41. Oshinubi K, Buhamra SS, Al-Kandari NM, Waku J, Rachdi M, Demongeot J. Age dependent epidemic modeling of COVID-19 outbreak in Kuwait, France, and Cameroon. In: Send P, editor. *Healthcare* (Vol. 10, No. 3). MDPI (2022), p. 482.

42. Teklu SW. Mathematical analysis of the transmission dynamics of COVID-19 infection in the presence of intervention strategies. *J Biol Dyn.* (2022) 16:640–64. doi: 10.1080/17513758.2022.2111469

43. Castillo-Chavez C, Feng Z, Huang W. On the computation of ro and its role on. In: Castillo-Chavez PC, Blower S, Driessche P, Kirschner D, Yakubu A-A, editors. *Mathematical Approaches for Emerging and Reemerging Infectious Diseases: An Introduction.* vol 1, 229 (2002). doi: 10.1007/978-1-4757-3667-0_13

44. Van den Driessche P, Watmough J. Reproduction numbers and sub-threshold endemic equilibria for compartmental models of disease transmission. *Math Biosci.* (2002) 180:29–48. doi: 10.1016/S0025-5564(02)00108-6

45. Mekonen KG, Balcha SF, Obsu LL, Hassen A. Mathematical modeling and analysis of TB and COVID-19 coinfection. *J Appl Math.* (2022) 2022:1–20. doi: 10.1155/2022/2449710

frontiers | Frontiers in Applied Mathematics and Statistics

TYPE Original Research
PUBLISHED 16 March 2023
DOI 10.3389/fams.2023.1122330

OPEN ACCESS

EDITED BY
Salih Djilali,
University of Chlef, Algeria

REVIEWED BY
Yubin Yan,
University of Chester, United Kingdom
Soufiane Bentout,
Centre Universitaire Ain Temouchent, Algeria

*CORRESPONDENCE
Maya Rayungsari
maya.rayungsari@gmail.com

†PRESENT ADDRESS
Maya Rayungsari,
Department of Mathematics Education, Faculty of Pedagogy and Psychology, PGRI Wiranegara University, Pasuruan, Indonesia

SPECIALTY SECTION
This article was submitted to Mathematical Biology, a section of the journal Frontiers in Applied Mathematics and Statistics

RECEIVED 12 December 2022
ACCEPTED 14 February 2023
PUBLISHED 16 March 2023

CITATION
Rayungsari M, Suryanto A, Kusumawinahyu WM and Darti I (2023) Dynamics analysis of a predator–prey fractional-order model incorporating predator cannibalism and refuge. *Front. Appl. Math. Stat.* 9:1122330. doi: 10.3389/fams.2023.1122330

Dynamics analysis of a predator–prey fractional-order model incorporating predator cannibalism and refuge

Maya Rayungsari*†, Agus Suryanto, Wuryansari Muharini Kusumawinahyu and Isnani Darti

Department of Mathematics, Faculty of Mathematics and Natural Sciences, University of Brawijaya, Malang, Indonesia

In this article, we consider a predator–prey interaction incorporating cannibalism, refuge, and memory effect. To involve the memory effect, we apply Caputo fractional-order derivative operator. We verify the non-negativity, existence, uniqueness, and boundedness of the model solution. We then analyze the local and global stability of the equilibrium points. We also investigate the existence of Hopf bifurcation. The model has four equilibrium points, i.e., the origin point, prey extinction point, predator extinction point, and coexistence point. The origin point is always unstable, while the other equilibrium points are conditionally locally asymptotically stable. The stability of the coexistence point depends on the order of the Caputo derivative, α. The prey extinction point, predator extinction point, and coexistence point are conditionally globally and asymptotically stable. There exists Hopf bifurcation of coexistence point with parameter α. The analytic results of stability properties and Hopf bifurcations are confirmed by numerical simulations.

KEYWORDS

predator-prey system, cannibalism, refuge, Caputo fractional-order derivative, local and global stability analyzes, Hopf bifurcation (critical) value

1. Introduction

Predator–prey interaction, as the basis of the food chain, is among the most essential ecological issues. In numerous published research, mathematical models have been developed to explain the dynamics of Predator–prey interaction, such as by incorporating social behavior [1, 2], age structure [3, 4], ratio-dependent functional response [5, 6], harvesting [7, 8], and so on. The Predator–prey model is still being developed by considering many factors that occur in nature. Cannibalism, the consuming of the same species in whole or in part, is one of its most intriguing aspects since many animals in nature exhibit cannibalistic behaviors, such as carnivore mammals [9–11], fish [12, 13], and spiders [14–16]. Cannibalism may provide adaptive advantages such as exploiting conspecifics as a food source or eliminating possible competitors [17].

Some researchers have investigated the mathematical model involving cannibalism [18–21]. Kang et al. [18] studied a single-species cannibalism model with stage structure. The model studied is a dynamic system of one population such an age structure that divides the population into two classes, i.e., eggs and an adult class consisting of larvae, pupae, queen insects, worker insects, and other types. Zhang et al. [19] analyzed predator–prey

models with cannibalism and stage structure in predators so that the model studied was a three-dimensional dynamical model. In Zhang's model, the predator population is divided into two subpopulations, i.e., juvenile and adult predators. The birth rate of juvenile predators is assumed to be proportional to the number of adult predators and follows the Malthus growth model. Predation of prey and juvenile predators by adult predators follows the type-I Holling functional response. Meanwhile, Deng et al. [20] studied a two-dimensional predator–prey model with predator cannibalism.

Aside from cannibalism, another interesting Predator–prey phenomenon to investigate is prey hiding behavior from predator captures and attacks. This is known as refuge behavior in the context of ecology. The mathematical model of Predator–prey interaction with prey refuge has also piqued the interest of researchers [21–25]. Rayungsari et al. [21] modified model proposed by Deng et al. [20] by adding the assumption that there is a refuge in the cannibalized predator population, as much as mP. Moreover, it is also assumed that predators need time to catch and handle the prey, so that the rate of prey predation follows the Holling type-II functional response. The Predator–prey model incorporating predator cannibalism and refuge proposed by Rayungsari et al. [21] is as follows:

$$\begin{aligned}\frac{dN}{dt} &= rN\left(1-\frac{N}{K}\right)-\frac{b_1NP}{k_1+N},\\ \frac{dP}{dt} &= \frac{c_1NP}{k_1+N}+c_2P-eP-\frac{b_2(1-m)P^2}{k_2+(1-m)P},\end{aligned} \tag{1}$$

where $N \geq 0$ and $P \geq 0$ represent prey density and predator density, respectively. The parameters of system (Equation 1) are positive constants described in Table 1. Predator cannibalism is represented by the last term of the second equation in system (Equation 1). The model can be interpreted as follows: In the absence of predator, prey grows logistically with the intrinsic growth rate r and the environmental carrying capacity K. With the presence of the predator, the prey population density decreases by $\frac{b_1NP}{k_1+N}$, where b_1 is the maximum predation rate and k_1 is the half-saturation constant. The predation rate follows Holling type-II functional response with the assumption that predators need time to catch and handle the prey. With the prey predation by predator, the predator population density increases by $\frac{c_1NP}{k_1+N}$, where c_1 is the conversion rate of predation of prey into predator births and $c_1 \leq b_1$. Predators die naturally with the death rate e. The term $\frac{b_2(1-m)P^2}{k_2+(1-m)P}$ depicts the decrease in predator population density caused by cannibalism with saturated a cannibalism rate, which follows Holling type-II functional response,

$$\frac{b_2(1-m)P}{k_2+(1-m)P}. \tag{2}$$

The value of Equation (2) monotonically increases with the supremum b_2. $(1-m)P$ is the amount of the available predator to be cannibalized, as m is the coefficient of refuge. The conversion rate of cannibalism into predator birth (c_2) is assumed to be less than the maximum predator cannibalism rate (b_2).

TABLE 1 Description of parameters.

Parameter	Description
r	Intrinsic growth rate of prey
K	Environmental carrying capacity for prey
b_1	Maximum prey predation rate
k_1	Half-saturation constant of predation
c_1	Conversion rate of prey biomass into predator birth
c_2	Conversion rate of cannibalism into predator birth
e	Predator natural death rate
b_2	Maximum predator cannibalism rate
m	Coefficient of refuge
k_2	Half-saturation constant of predator cannibalism

The model proposed by Rayungsari et al. [21] was constructed in a system of nonlinear differential equations with the first-order derivative, where the change of population density at any time depends on the current population density instantaneously. Whereas in reality, the current condition is also affected by the history of all previous conditions, which is called the memory effect [26]. The phenomenon or systems that have memory and genetic characteristics can be described by a fractional differential system [27]. The definition of fractional-order derivative was first introduced by Liouville [28] motivated by L'Hôpital and Leibniz's critical thinking on derivatives of order $\frac{1}{2}$. Liouville's definition was modified by Riemann by applying a direct generalization of the Cauchy formula and named Riemann–Liouville fractional derivative operator [29]. The fractional-order derivative concept by Liouville and Riemann utilizes Euler's study of fractional integration, which led him to construct the Gamma function as generalization of the factorial concept for fractional numbers [30]. In 1967, Michele Caputo modified the Riemann–Liouville operator so that when solving differential equations, no initial conditions are required. The definition of the modified operator is named by Caputo fractional-order derivative operator. Predator–prey models using Caputo-type fractional derivatives have been widely studied recently [24, 31–33]. Hence, in this article, we modify and analyze the Predator–prey model incorporating predator cannibalism and refuge in Rayungsari et al. [21] by applying the Caputo fractional-order derivative operator.

This article is organized as follows. In Section 2, model development and basic properties are described. The basic properties consist of verification of the non-negativity, existence, uniqueness, and boundedness of solutions of the model. In Section 3, the results of dynamical analysis are presented. The results consist of the existence and stability of equilibrium points. Both local and global stability are investigated, while the analyzed bifurcation is the Hopf bifurcation. In Section 4, the numerical simulations and intrepretations are carried out to confirm the analytical results. Finally, in Section 5, we draw some concluding remarks.

2. Model development and basic properties

By applying the Caputo fractional-order derivative operator to the left-hand side of system (Equation 1), the model becomes

$$\begin{aligned} D_*^\alpha N &= rN\left(1-\frac{N}{K}\right)-\frac{b_1NP}{k_1+N} \\ D_*^\alpha P &= \frac{c_1NP}{k_1+N}+c_2P-eP-\frac{b_2(1-m)P^2}{k_2+(1-m)P} \end{aligned}, \tag{3}$$

with $\alpha \in \mathbb{R}, 0 < \alpha \leq 1$, and D_*^α is the α-order of Caputo fractional derivative operator defined by $D_*^\alpha x(t) = \frac{1}{\Gamma(1-\alpha)}\int_0^t (t-s)^{-\alpha}x(s)\,ds$.

Since the variables in the system (Equation 3) represent the population densities, the solution of the system must be non-negative. The solution of system (Equation 3) is guaranteed to be non-negative by the following theorem.

THEOREM 1. All solutions of Equation (3) are non-negative for any initial values $(N(0), P(0)) \in \mathbb{R}_+^2$.

Proof. Since $D_*^\alpha = N\left(r\left(1-\frac{N}{K}\right)-\frac{b_1P}{k_1+N}\right)$, then $D_*^\alpha N(0) = 0$ if $N(0) = 0$. $D_*^\alpha N = 0$ means there is no change of prey population density. Consequently, $N(t) = 0, \forall t > 0$. Then, we prove that if $N(0) > 0$ then $N(t) \geq 0$ for every $t > 0$. Suppose that the statement is wrong, so there is $t^* > 0$ such as

$$\begin{aligned} &N(t) > 0,\ 0 \leq t < t^*, \\ &N(t) = 0,\ t = t^*, \\ &N(t) < 0,\ t \geq t^*, \end{aligned} \tag{4}$$

From Equations (3), (4), we get that $D_*^\alpha N = 0, t = t^*$. Thus, there is no change in the population density of N when $t = t^*$. From the prior statement, $N(t) = 0, t = t^*$, so that $N(t) = 0, t > t^*$. This contradicts the statement that $N(t) < 0$ for $t > t^*$. Therefore, $N(t) \geq 0$ for all $t > 0$ is correct. In the same way, it can be proved that $P(t) \geq 0$ for every $t > 0$.

Next, we show the existence and uniqueness of solution of the system (Equation 3) using Theorem 3.7 in Li et al. [34]. Consider a region $[0, \infty) \times \Omega$, where $\Omega = \{X = (N, P) \in \mathbb{R}_+^2 : c_2 < e\}$. Then, we denote a mapping $F(X) = (F_1(X), F_2(X))$, where

$$\begin{aligned} F_1(X) &= rN\left(1-\frac{N}{K}\right)-\frac{b_1NP}{k_1+N}, \\ F_2(X) &= \frac{c_1NP}{k_1+N}+c_2P-eP-\frac{b_2(1-m)P^2}{k_2+(1-m)P}. \end{aligned} \tag{5}$$

For all $X = (N, P), \bar{X} = (\bar{N}, \bar{P}) \in \Omega$,

$$\begin{aligned} ||F(X)-F(\bar{X})|| &\leq \left|F_1(X)-F_1(\bar{X})\right| + \left|F_2(X)-F_2(\bar{X})\right| \\ &= \left|\left[rN\left(1-\frac{N}{K}\right)-\frac{b_1NP}{k_1+N}\right]-\left[r\bar{N}\left(1-\frac{\bar{N}}{K}\right)-\frac{b_1\bar{N}\bar{P}}{k_1+\bar{N}}\right]\right| \\ &\quad+\left|\left[\frac{c_1NP}{k_1+N}+c_2P-eP-\frac{b_2(1-m)P^2}{k_2+(1-m)P}\right]\right. \\ &\quad\left.-\left[\frac{c_1\bar{N}\bar{P}}{k+\bar{N}}+c_2\bar{P}-e\bar{P}-\frac{b_2(1-m)\bar{P}^2}{k_2+(1-m)\bar{P}}\right]\right| \\ &\leq |rN-\bar{N}| + \left|\frac{N^2-\bar{N}^2}{K}\right| + \left|\frac{b_1NP(k_1+\bar{N})-b_1\bar{N}\bar{P}(k_1+N)}{(k_1+N)(k_1+\bar{N})}\right| \\ &\quad+\left|\frac{c_1NP(k_1+\bar{N})-c_1\bar{N}\bar{P}(k_1+N)}{(k_1+N)(k_1+\bar{N})}\right| + |(c_2-e)(P-\bar{P})| \\ &\quad+\left|\frac{b_2(1-m)(P^2(k_2+(1-m)\bar{P})-(\bar{P}^2(k_2+(1-m)P)}{(k_2+(1-m)P)(k_2+(1-m)\bar{P})}\right| \\ &\leq \left[r+\frac{r(N+\bar{N})}{K}+\frac{(b_1+c_1)k_1P}{(k_1+N)(k_1+\bar{N})}\right]|N-\bar{N}| \\ &\quad+\left[\frac{(b_1+c_1)\bar{N}}{k_1+\bar{N}}+e-c_2\right. \\ &\quad\left.+\frac{b_2(1-m)\left[k_2(P+\bar{P})+P\bar{P}(1-m)\right]}{(k_2+(1-m)P)(k_2+(1-m)\bar{P})}\right]|P-\bar{P}|. \end{aligned}$$

Since in the following discussion, it can be proved that the system solution (Equation 3) is bounded in Ω, there is a positive constant $M = \max\{N, P\}, \forall t \geq 0$. Hence, we have

$$\begin{aligned} ||F(X)-F(\bar{X})|| &\leq \left[r+\frac{2M}{K}+\frac{(b_1+c_1)k_1M}{k_1^2}\right]|N-\bar{N}| \\ &\quad+\left[\frac{(b_1+c_1)M}{k_1}+e-c_2+\frac{b_2(1-m)\left[2k_2M+(1-m)M^2\right]}{k_2^2}\right] \\ &\quad|P-\bar{P}| \\ &= L_1|N-\bar{N}| + L_2|P-\bar{P}|, \end{aligned}$$

with

$$\begin{aligned} L_1 &= r+\frac{2M}{K}+\frac{(b_1+c_1)k_1M}{k_1^2}, \\ L_2 &= \frac{(b_1+c_1)M}{k_1}+e-c_2+\frac{b_2(1-m)\left[2k_2M+(1-m)M^2\right]}{k_2^2}. \end{aligned}$$

By choosing a positive constant $L = \max\{L_1, L_2\}$, we get

$$||F(X)-F(\bar{X})|| \leq L||X-\bar{X}||. \tag{6}$$

Based on Equation (6), the function $F(X)$ satisfies the Lipschitz condition so that there exist a unique solution $X(t)$ of the system (Equation 3) with any initial value of $X(0) = (N(0), P(0))$. Thus, we derive the following theorem.

THEOREM 2. For the system (Equation 3) with any non-negative initial condition $(N(0), P(0)) \in \Omega$, there exist a unique solution $X(t) \in \Omega$.

Next, due to the limited carrying capacity of the prey and predator resources, the size of both populations in the system (Equation 3) must be limited. Consider a function defined by

$$V(t) = N(t) + \frac{b_1}{c_1}P(t).$$

The Caputo derivative α-order of V satisfies,

$$\begin{aligned} D_*^\alpha V &\leq D_*^\alpha N + \frac{b_1}{c_1} D_*^\alpha P \\ &= \left[rN\left(1-\frac{N}{K}\right) - \frac{b_1 NP}{k_1+N} \right] \\ &+ \tfrac{b_1}{c_1}\left[\tfrac{c_1 NP}{k_1+N} + c_2 P - eP - \tfrac{b_2(1-m)P^2}{k_2+(1-m)P} \right] \\ &= rN - \frac{r}{K}N^2 + \frac{b_1}{c_1}\left(c_2 - e - \frac{b_2(1-m)P}{k_2+(1-m)P} \right) P \\ &\leq rN - \tfrac{r}{K}N^2 + \tfrac{b_1}{c_1}(c_2-e)\,P. \end{aligned}$$

For any positive constant φ,

$$\begin{aligned} D_*^\alpha V + \varphi V &\leq rN - \frac{r}{K}N^2 + \frac{b_1}{c_1}(c_2-e)P + \varphi\left(N + \frac{b_1}{c_1}P\right) \\ &= (r+\varphi)N - \frac{r}{K}N^2 + \frac{b_1}{c_1}(c_2 - e + \varphi)P. \end{aligned}$$

If $c_2 < e$ and by choosing $0 < \varphi < e - c_2$, we get

$$\begin{aligned} D_*^\alpha V + \varphi V &< (r+\varphi)N - \frac{r}{K}N^2 \\ &= -\frac{r}{K}\left[\left(N - \frac{(r+\varphi)K}{2r} \right)^2 - \left(\frac{(r+\varphi)K}{2r} \right)^2 \right] \\ &\leq \frac{r}{K}\left(\frac{(r+\varphi)K}{2r} \right)^2. \end{aligned} \tag{7}$$

Based on Equation (7), Generalized Mean Value Theorem in Odibat and Shawagfeh [35], and Lemma 6.1 (Fractional Comparison Principle) in Li et al. [34], we get that,

$$\begin{aligned} V(t) &\leq \left(V(0) - \frac{r}{\varphi K}\left(\frac{(r+\varphi)K}{2r} \right)^2 \right) E_\alpha[-\varphi(t)^\alpha] \\ &+ \frac{r}{\varphi K}\left(\frac{(r+\varphi)K}{2r} \right)^2. \end{aligned} \tag{8}$$

$E_\alpha[-\varphi(t)^\alpha] \to 0 as \to +\infty$, so that,

$$V(t) \to \frac{r}{\varphi K}\left(\frac{(r+\varphi)K}{2r} \right)^2, t \to +\infty.$$

Hence, we establish the following theorem.

THEOREM 3. All solutions of Equation (2) with initial values $(N(0), P(0)) \in \{(x,y) \in R_+^2 : c_2 < e\}$ are uniformly bounded

3. Dynamical analysis

3.1. Existence of equilibrium points

In the similar way as in Rayungsari et al. [21], the system (Equation 3) has four equilibrium points, namely $E_0 = (0,0)$, $E_1 = (0, P_1)$, $E_2 = (K, 0)$, and $E_3 = (N_3, P_3)$, where $P_1 = \frac{k_2(e-c_2)}{(c_2-e-b_2)(1-m)}$. If $b_2 + e \neq c_1 + c_2$, then N_3 and P_3 in E_3 is obtained from the solution of a cubic equation using the Cardano's formula [36, 37], i.e.,

$$\begin{aligned} N_3 &= \frac{\sqrt[3]{q_2 \pm \sqrt{q_2^2 + \frac{4}{27}q_1^3}}}{\sqrt[3]{2}} - \frac{q_1\sqrt[3]{2}}{3\sqrt[3]{q_2 \pm \sqrt{q_2^2 + \frac{4}{27}q_1^3}}} - \frac{B}{3A}, \\ P_3 &= \frac{r}{b_1}\left(1 - \frac{N_3}{K}\right)(k_1 + N_3), \end{aligned} \tag{9}$$

with

$$\begin{aligned} q_1 &= \frac{3AC - B^2}{3A^2}, \\ q_2 &= \frac{9ABC - 2B^3 - 27A^2D}{27A^3}, \\ A &= \frac{r}{b_1 K}(1-m)(b_2 - c_1 - c_2 + e), \\ B &= \frac{r}{b_1}(1-m)\left[(c_1 + c_2 - e - b_2) - \frac{k_1}{K}(c_1 + 2(c_2 - e - b_2)) \right], \\ C &= (c_1 + c_2 - e)k_2 \\ &+ \tfrac{rk_1}{b_1}(1-m)\left[c_1 + (2-k_1)(c_2-e) - 2b_2 + \tfrac{b_2 k_1}{K} \right], \\ D &= k_1\left[k_2(c_2 - e) + \frac{rk_1}{b_1}(1-m)(c_2 - e - b_2) \right]. \end{aligned}$$

Whereas, if $b_2 + e = c_1 + c_2$, we have the value of N_3 and P_3 as follows:

$$N_3 = \frac{-R \pm \sqrt{R^2 - 4QS}}{2Q}, P_3 = \frac{r}{b_1}\left(1 - \frac{N_3}{K}\right)(k_1 + N_3),$$

with

$$\begin{aligned} Q &= \frac{c_1 r k_1}{b_1 K}(1-m), \\ R &= b_2 k_2 + \frac{rk_1}{b_1}(1-m)\left(k_1(c_1 - b_2) - c_1 + \frac{b_2 k_1}{K} \right), \\ S &= k_1\left[k_2(b_2 - c_1) - \frac{r c_1 k_1}{b_1}(1-m) \right]. \end{aligned}$$

Two of the equilibrium points need existence conditions. E_1 exists in $\mathbb{R}_+^2$ if $0 < c_2 - e < b_2$. The coexistence point E_3 exists in $\mathbb{R}_+^2$ if $q_2^2 + \frac{4}{27}q_1^3 \geq 0$ and $0 < N_3 < K$ for $b_2 + e \neq c_1 + c_2$. Meanwhile, for $b_2 + e = c_1 + c_2$, E_3 exists in $\mathbb{R}_+^2$ if $R^2 - 4QS \geq 0$ and $0 < N_3 < K$.

3.2. Local stability

Local stability of the equilibrium points of Equation (3) are determined by the arguments of the eigenvalues of Jacobian matrix and applying Matignon Local Stability Theorem in Petras [38]. Suppose that E^* is an equilibrium point of system (Equation 3). Based on Matignon Local Stability Theorem, E^* is local asymptotically stable if all of the eigenvalues λ_j of the Jacobian matrix,

$$J(E^*) = \begin{bmatrix} r\left(1 - \frac{2N}{K}\right) - \frac{b_1 k_1 P}{(k_1+N)^2} & -\frac{b_1 N}{k_1+N} \\ \frac{c_1 k_1 P}{(k_1+N)^2} & \frac{c_1 N}{k_1+N} + c_2 - e \\ & -\frac{b_2(1-m)P\left[2k_2 + (1-m)P\right]}{(k_2+(1-m)P)^2} \end{bmatrix} \tag{10}$$

that satisfies $|\arg(\lambda_j)| > \frac{\alpha\pi}{2}$.

THEOREM 4. The origin point $E_0(0,0)$ is always unstable.

Proof. The Jacobian matrix for $E_0 = (0,0)$ is

$$J(E_0) = \begin{bmatrix} r & 0 \\ 0 & c_2 - e \end{bmatrix}, \tag{11}$$

so the eigenvalues are $\lambda_1 = r$ and $\lambda_2 = c_2 - e$. The argument of the first eigenvalue is $|\arg(\lambda_1)| = 0 < \frac{\alpha\pi}{2}$. If $c_2 > e$ then $|\arg(\lambda_2)| = 0 < \frac{\alpha\pi}{2}$ (E_0 is an unstable source), while if $c_2 > e$ then $|\arg(\lambda_2)| = \pi > \frac{\alpha\pi}{2}$ (E_0 is an unstable saddle node).

THEOREM 5. Prey extinction point $E_1(0, P_1)$ is local asymptotically stable if $r < \frac{b_1 P_1}{k_1}$ and unstable saddle node if $r > \frac{b_1 P_1}{k_1}$.

Proof. By substituting $E_1 = (0, P_1)$ to Equation (10), we get the Jacobian matrix for E_1,

$$J(E_1) = \begin{bmatrix} r - \frac{b_1 P_1}{k_1} & 0 \\ \frac{c_1 P_1}{k_1} & \frac{(c_2 - e)(c_2 - e - b_2)}{b_2} \end{bmatrix}. \tag{12}$$

The eigenvalues are $\lambda_1 = r - \frac{b_1 P_1}{k_1}$ and $\lambda_2 = \frac{(c_2 - e)(c_2 - e - b_2)}{b_2}$. Based on the existence condition of E_1, then λ_2 is the negative real number and $|\arg(\lambda_2)| = \pi > \frac{\alpha\pi}{2}$. Hence, the local stability of E_1 depends on λ_1. If $r < \frac{b_1 P_1}{k_1}$, $\lambda_1 < 0$, and $|\arg(\lambda_1)| = \pi > \frac{\alpha\pi}{2}$ so that E_1 is local asymptotically stable. Otherwise, if $r > \frac{b_1 P_1}{k_1}$ then $\lambda_1 > 0$, $|\arg(\lambda_1)| = \pi > \frac{\alpha\pi}{2}$, and E_1 is an unstable saddle node.

THEOREM 6. The predator extinction point $E_2(K, 0)$ is local asymptotically stable if $e > \frac{c_1 K}{k_1 + K} + c_2$ and unstable saddle node if $e < \frac{c_1 K}{k_1 + K} + c_2$.

Proof. With the same way, we get the Jacobian matrix for E_2 as follows:

$$J(E_2) = \begin{bmatrix} -r & -\frac{b_1 K}{k_1 + K} \\ 0 & \frac{c_1 K}{k_1 + K} + c_2 - e \end{bmatrix}. \tag{13}$$

The eigenvalues are $\lambda_1 = -r$ and $\lambda_2 = \frac{c_1 K}{k_1 + K} + c_2 - e$. It is clear that $|\arg(\lambda_1)| = \pi > \frac{\alpha\pi}{2}$. E_2 is local asymptotically stable if $|\arg(\lambda_2)| > \frac{\alpha\pi}{2}$, i.e., for $e > \frac{c_1 K}{k_1 + K} + c_2$. If $e < \frac{c_1 K}{k_1 + K} + c_2$, $|\arg(\lambda_2)| = 0 < \frac{\alpha\pi}{2}$, and E_2 is an unstable saddle node.

For existence point $E_3(N_3, P_3)$, the Jacobian matrix is as follows:

$$J(E_3) = \begin{bmatrix} J_{11} & J_{12} \\ J_{21} & J_{22} \end{bmatrix}, \tag{14}$$

where

$$\begin{aligned} J_{11} &= \frac{rN_3}{k_1 + N_3}\left(1 - \frac{k_1 + 2N_3}{K}\right), \\ J_{12} &= -\frac{b_1 N_3}{k_1 + N_3}, \\ J_{21} &= \frac{c_1 k_1 r}{b_1(k_1 + N_3)}\left(1 - \frac{N_3}{K}\right), \\ J_{22} &= -\frac{b_1 b_2 k_2 r(1-m)\left(1 - \frac{N_3}{K}\right)(k_1 + N_3)}{\left(b_1 k_2 + r(1-m)\left(1 - \frac{N_3}{K}\right)(k_1 + N_3)\right)^2}. \end{aligned} \tag{15}$$

Thus, the eigenvalues are obtained from the following quadratic equation.

$$\lambda^2 - trace(J(E_3)) + \det(J(E_3)) = 0, \tag{16}$$

where

$$\begin{aligned} \det(J(E_3)) &= J_{11}J_{22} - J_{12}J_{21} \\ &= -\frac{r^2 b_1 b_2 k_2 (1-m) N_3 \left(1 - \frac{N_3}{K}\right)}{\left(b_1 k_2 + r(1-m)\left(1 - \frac{N_3}{K}\right)(k_1 + N_3)\right)^2}\left(1 - \frac{k_1 + 2N_3}{K}\right) \\ &\quad + \frac{c_1 k_1 r N_3}{(k_1 + N_3)^2}\left(1 - \frac{N_3}{K}\right) \end{aligned} \tag{17}$$

and

$$\begin{aligned} trace(J(E_3)) &= J_{11} + J_{22} \\ &= \frac{rN_3}{k_1 + N_3}\left(1 - \frac{k_1 + 2N_3}{K}\right) \\ &\quad - \frac{b_1 b_2 k_2 r(1-m)\left(1 - \frac{N_3}{K}\right)(k_1 + N_3)}{\left(b_1 k_2 + r(1-m)\left(1 - \frac{N_3}{K}\right)(k_1 + N_3)\right)^2}. \end{aligned} \tag{18}$$

Suppose that

$$a = \frac{b_1 b_2 k_2 (1-m)\left(1 - \frac{N_3}{K}\right)(k_1 + N_3)^2}{N_3\left(b_1 k_2 + r(1-m)\left(1 - \frac{N_3}{K}\right)(k_1 + N_3)\right)^2} > 0, \tag{19}$$

then

$$\begin{aligned} trace(J(E_3)) &= \frac{rN_3}{k_1 + N_3}\left(1 - \frac{k_1 + 2N_3}{K}\right) - \frac{arN_3}{k_1 + N_3} \\ &= \frac{rN_3}{k_1 + N_3}\left(1 - a - \frac{k_1 + 2N_3}{K}\right) \\ &= \frac{rN_3}{k_1 + N_3}\left(\frac{K - aK - k_1 - 2N_3}{K}\right). \end{aligned} \tag{20}$$

Suppose that d is the discriminant of Equation (16), i.e.,

$$d = trace(J(E_3))^2 - 4\det(J(E_3)). \tag{21}$$

The cases are divided into two parts, those are for $d \geq 0$ and for $d < 0$.

1. Case 1 ($d \geq 0$)
   For this case, if $k_1 > K - 2N_3$, we have $\det(J) > 0$ and $trace(J) < 0$. Therefore, the eigenvalues (solutions of Equation 16) are real and negative. Consequently, $|\arg(\lambda_j)| = \pi > \frac{\alpha\pi}{2}$ for $j = 1, 2$ and E_3 is local asymptotically stable.

2. Case 2 ($d < 0$)
   In case ($d < 0$), the eigenvalues are complex number with non-zero imaginary part $\lambda = \frac{trace(J(E_3)) + \sqrt{d}}{2}$ and $\bar{\lambda} = \frac{trace(J(E_3)) - \sqrt{d}}{2}$. Suppose that
   (a) If $k_1 > K - 2N_3 - aK$, then $trace(J) < 0$ so that $Re(\lambda) < 0$ and E_3 is local asymptotically stable since $|\arg(\lambda)| = |\arg(\bar{\lambda})| = \pi > \frac{\alpha\pi}{2}$.
   (b) If $k_1 < K - 2N_3 - aK$, then $trace(J) > 0$ so that $Re(\lambda) > 0$ and E_3 is local asymptotically stable if $|\arg(\lambda)| > \frac{\alpha\pi}{2}$.

   Hence, we establish the following theorem.

THEOREM 7. Suppose that $d = trace(J(E_3))^2 - 4\det(J(E_3))$ with $trace(J(E_3))$ and $\det(J(E_3))$ are the trace and determinant of matrix $J(E_3)$ in Equation (14). $E_3 = (N_3, P_3)$ is locally asymptotically stable if one of the following conditions are satisfied.

1. $d \geq 0$ and $k_1 > K - 2N_3$,
2. $d < 0$ and $k_1 > K - 2N_3 - aK$,
3. $d < 0$, $k_1 < K - 2N_3 - aK$, and $|\arg(\lambda)| = \left|\frac{Im(\lambda)}{Re(\lambda)}\right| = \left|\frac{\lambda - \bar{\lambda}}{\lambda + \bar{\lambda}}\right| > \frac{\alpha\pi}{2}$,

with a is as in Equation (19).

3.3. Global stability

Next, we investigate the global stability of E_1, E_2, and E_3. For this aim, we use the help of Lemma 3.1 in Vargas-De-Leon [39] and Generalized Lasalle Invariance Principle in Huo et al. [40].

For prey extinction point $E_1(0, P_1)$, we consider a Lyapunov function,

$$V_1(N,P) = N + \frac{b_1}{c_1}\left(P - P_1 - P_1 \ln \frac{P}{P_1}\right).$$

The Caputo derivative α-order of V_1 is as follows:

$$\begin{aligned}
D_*^\alpha V_1 &\leq D_*^\alpha N + \frac{b_1}{c_1}\left(\frac{P-P_1}{P}\right) D_*^\alpha P \\
&= rN\left(1 - \frac{N}{K}\right) - \frac{b_1 NP}{k_1 + N} \\
&+ \frac{b_1}{c_1}\left(\frac{P-P_1}{P}\right)\left(\frac{c_1 NP}{k_1+N} + c_2 P - eP - \frac{b_2(1-m)P^2}{k_2 + (1-m)P}\right) \\
&= rN\left(1 - \frac{N}{K}\right) - \frac{b_1 NP_1}{k_1 + N} \\
&+ \frac{b_1}{c_1 P_1}(P - P_1)\left(\frac{k_2(c_2 - e)P_1 + k_2(e - c_2)P}{k_2 + (1-m)P}\right) \\
&= rN\left(1 - \frac{N}{K}\right) - \frac{b_1 NP_1}{k_1 + N} \\
&- \frac{b_1}{c_1 P_1}(P - P_1)^2\left(\frac{k_2(c_2 - e)}{k_2 + (1-m)P}\right) \\
&\leq rN\left(1 - \frac{N}{K}\right) - \frac{b_1 NP_1}{k_1 + N}.
\end{aligned}$$

If $r < \frac{b_1 P_1}{k_1}$, then we have,

$$\begin{aligned}
D_*^\alpha V_1 &\leq rN\left(1 - \frac{N}{K}\right) - \frac{rk_1 N}{k_1 + N} \\
&= \frac{rN}{K(k_1 + N)}\left(KN - k_1 N - N^2\right).
\end{aligned}$$

$D_*^\alpha V_1 = 0$ only if $N = 0$. For $N > 0$, if $K \leq k_1$, then $D_*^\alpha V_1 \leq 0$ and according to Generalized Lasalle Invariance Principle [40], E_1 is globally asymptotically stable. We write the global stability conditions of E_1 in the following theorem.

THEOREM 8. If $E_1 = (0, P_1)$ exists, then E_1 is globally asymtotically stable if $r < \frac{b_1 P_1}{k_1}$ and $K \leq k_1$.

Then, we construct a Lyapunov function as follows:

$$V_2(N,P) = \frac{c_1}{b_1}\left(N - K - K\ln\frac{N}{K}\right) + P,$$

for $E_2(K, 0)$. We have,

$$\begin{aligned}
D_*^\alpha V_2 &\leq \frac{c_1}{b_1}\left(\frac{N-K}{N}\right) D_*^\alpha N + D_*^\alpha P \\
&= \frac{c_1}{b_1}\left(\frac{N-K}{N}\right)\left(rN\left(1 - \frac{N}{K}\right) - \frac{b_1 NP}{k_1 + N}\right) + \frac{c_1 NP}{k_1 + N} \\
&\quad + c_2 P - eP - \frac{b_2(1-m)P^2}{k_2 + (1-m)P} \\
&= -\frac{c_1 r}{b_1 K}(N - K)^2 \\
&+ P\left(\frac{c_1 K}{k_1 + N} + c_2 - e - \frac{b_2(1-m)P}{k_2 + (1-m)P}\right) \\
&\leq P\left(\frac{c_1 K}{k_1 + N} + c_2 - e - \frac{b_2(1-m)P}{k_2 + (1-m)P}\right) \\
&\leq P\left(\frac{c_1 K}{k_1 + N} + c_2 - e\right).
\end{aligned}$$

Suppose that $e > \frac{c_1 K}{k_1} + c_2$. Thus, we have,

$$\begin{aligned}
D_*^\alpha V_2 &\leq P\left(\frac{c_1 K}{k_1 + N} + c_2 - \left(\frac{c_1 K}{k_1} + c_2\right)\right) \\
&= P\left(\frac{c_1 K}{k_1 + N} - \frac{c_1 K}{k_1}\right) \leq 0.
\end{aligned}$$

We get that $D_*^\alpha V_2 \leq 0, \forall (N,P) \in \mathbb{R}_+^2$. Hence, E_2 is globally asymptotically stable with the condition as in the following theorem.

THEOREM 9. E_2 is globally asymtotically stable if $e > \frac{c_1 K}{k_1} + c_2$.

To investigate the global stability of coexistence point, we consider a Lyapunov function

$$V_3(N,P) = N - N_3 - N_3 \ln\frac{N}{N_3} + \frac{b_1}{c_1}\left(P - P_3 - P_3 \ln\frac{P}{P_3}\right),$$

where N_3 and P_3 as in Equation (9). The α-order derivative of V_3 satisfies

$$\begin{aligned} D_*^{\alpha} V_3 \leq & \left(1-\frac{N_3}{N}\right)\left(rN\left(1-\frac{N}{K}\right)-\frac{b_1 NP}{k_1+N}\right) \\ & + \frac{b_1}{c_1}\left(1-\frac{P_3}{P}\right)\left(\frac{c_1 NP}{k_1+N}+c_2 P-eP-\frac{b_2(1-m)P^2}{k_2+(1-m)P}\right) \\ & = (N-N_3)\left[r\left(\frac{N_3-N}{K}\right)-\frac{b_1 k_1(P-P_3)}{(k_1+N)(k_1+N_3)}\right] \\ & + \frac{b_1}{c_1}(P-P_3)\left[\frac{c_1 k_1(N-N_3)}{(k_1+N)(k_1+N_3)}\right. \\ & \left. - \frac{b_2 k_2(1-m)(P-P_3)}{(k_2+(1-m)P)(k_2+(1-m)P_3)}\right] \\ & = -\frac{r}{K}(N-N_3)^2-\frac{b_1(N-N_3)(N_3P-NP_3)}{(k_1+N)(k_1+N_3)} \\ & - \frac{b_1 b_2 k_2(1-m)(P-P_3)^2}{c_1(k_2+(1-m)P)(k_2+(1-m)P_3)}. \end{aligned}$$

Consider a domain $\Omega^* = \left\{(N,P)\middle|\frac{P}{P_3}>\frac{N}{N_3}>1\right\}$. Then, $D_*^{\alpha}V_3 < 0$ and E_3 is globally asymptotically stable in Ω^*. Hence, we derive the following theorem.

THEOREM 10. E_3 is globally asymptotically stable in the domain $\Omega^* = \left\{(N,P)\middle|\frac{P}{P_3}>\frac{N}{N_3}>1\right\}$.

3.4. Existence of Hopf bifurcation

THEOREM 11. If $d<0$ and $k_1 < K-2N_3-aK$ with a is given in Equation (19), then E_3 undergoes Hopf bifurcation when the order of Caputo derivative, α, pass α^* with

$$\alpha^* = \tan^{-1}\left|\frac{Im(\lambda^*)}{Re(\lambda^*)}\right| \tag{22}$$

and λ^* is an eigenvalue of E_3.

Proof. Suppose that $d<0$ and $k_1 < K-2N_3-aK$. Then, the eigenvalues of $J(E_3)$ are a pair of complex number $\lambda_1 = \lambda^*$ and $\lambda_2 = \bar{\lambda^*}$ with positive real part. Suppose that

$$f(\alpha) = \frac{\alpha\pi}{2} - \min|\arg(\lambda_i)_{i=1,2}|.$$

For $\alpha = \alpha^*$ with

$$\alpha^* = \tan^{-1}\left|\frac{Im(\lambda^*)}{Re(\lambda^*)}\right|,$$

we have $f(\alpha^*) = 0$ and $\left.\frac{df(\alpha)}{d\alpha}\right|_{\alpha=\alpha_*} = \frac{\pi}{2} \neq 0$. According to Theorem 3 in Li and Wu [41], E_3 undergoes Hopf bifurcation at $\alpha = \alpha^*$.

4. Numerical simulations

In this section, numerical simulations of the model (Equation 3) are carried out using Matlab software and the predictor–corrector scheme, which is introduced by Diethelm et al. [42]. The purposes of the numerical simulations are to confirm the dynamics analysis results and the existence of Hopf bifurcation. Since there are no available data related to our proposed model yet, the parameter values are chosen hypothetically in Table 2.

TABLE 2 Parameter values.

Parameter	Simulation 1	Simulation 2	Simulation 3
r	1	1	1
K	1	1	1
b_1	0.5	0.5	0.3
k_1	0.3	0.3	0.3
c_1	0.2	0.1	0.2
c_2	0.2	0.2	0.12
e	0.1	0.3	0.02
b_2	0.3	0.3	0.35
m	0.3	0.3	0.3
k_2	1	1	1

For parameter values in Simulation 1, E_1 exists, i.e., $E_1 = (0, 0.7143)$ and the local stability condition in Theorem 5 is satisfied. We conduct numerical simulations with several values of α. The results in Figure 1 show that the solutions tend to the prey extinction point for all α values chosen. This is consistent with the analytical results since the Jacobi matrix eigenvalues are negative real numbers, which involve E_1 always asymptotically stable with the selected parameter values for any order derivative of the $\alpha \in (0,1]$. However, we can see a difference in the solution's behavior for each α. The lower the α value, the slower the solution reaches E_1.

For the second simulation, we use the same parameter values but c_1 and e (see Table 2). As a result, the existence condition for E_1 is not satisfied, so the point does not exist. It means that the prey can survive from extinction. For the predator extinction point $E_2(1,0)$, the stability condition in Theorem 6 is satisfied and E_2 is asymptotically stable for any fractional order of $\alpha \in (0,1]$. It fits the numerial simulation results in Figure 2. Represented by some values of α, we can see that the solutions with initial value close to E_2 go to E_2. With a greater α value, the solution will reach the predator extinction point faster.

Next, we demonstrate the effect of the derivative order on the behavior of the solution, with $0.8 \leq \alpha \leq 1$. The parameter values in the last column of Table 2 were chosen. With those parameter values, the coexistence point exists, i.e., $E_3(0.1423, 1.2645)$, which has the eigenvalues $\lambda^* = 0.0232 + 0.1589i$ and $\bar{\lambda^*} = 0.0232 - 0.1589i$. The parameter values satisfy $k_1 < K-2N_3-aK$ and the discriminant of the quadratic equation of the eigenvalues is negative, i.e., $d = -0.1010$. Based on the Theorem 7, the stability of E_3 is determined by the argument of the order derivative α. The threshold is $\alpha^* = 0.9077$, which satisfies $\alpha^* < \frac{2}{\pi}\left|\frac{\lambda^*-\bar{\lambda^*}}{\lambda^*+\bar{\lambda^*}}\right|$.

From the bifurcation diagram in Figure 3, we can see that for $\alpha < \alpha^*$, the solutions tend to E_3. Meanwhile, for $\alpha > \alpha^*$, the

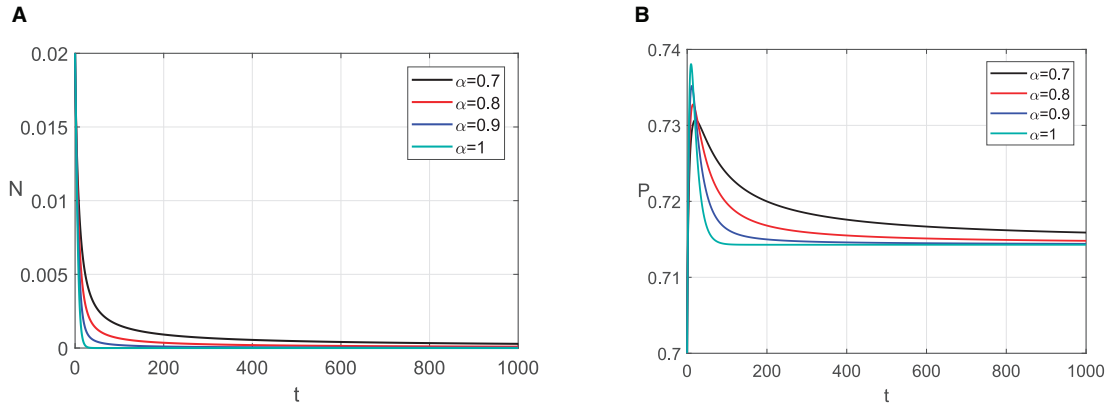

FIGURE 1
Graphic solutions of Simulation 1. **(A)** Solutions of N with respect to time t. **(B)** Solutions of P with respect to time t.

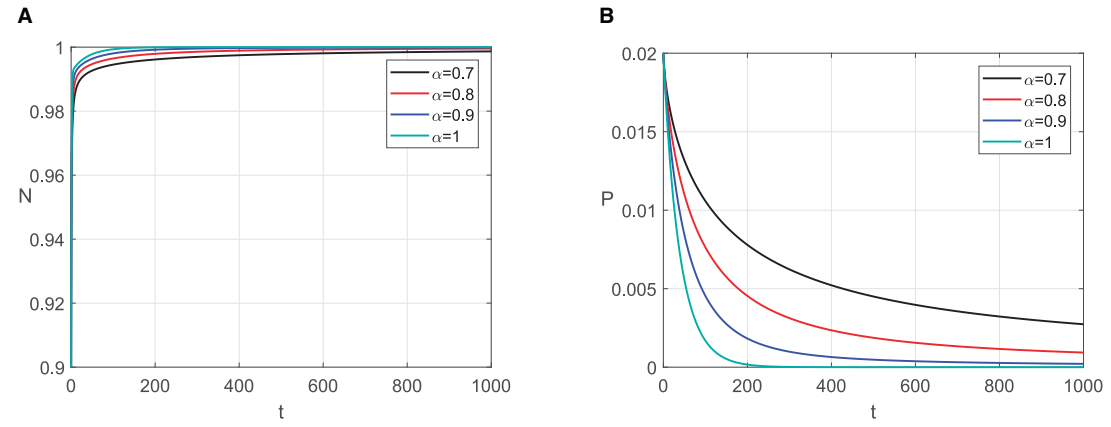

FIGURE 2
Graphic solutions of Simulation 2. **(A)** Solutions of N with respect to time t. **(B)** Solutions of P with respect to time t.

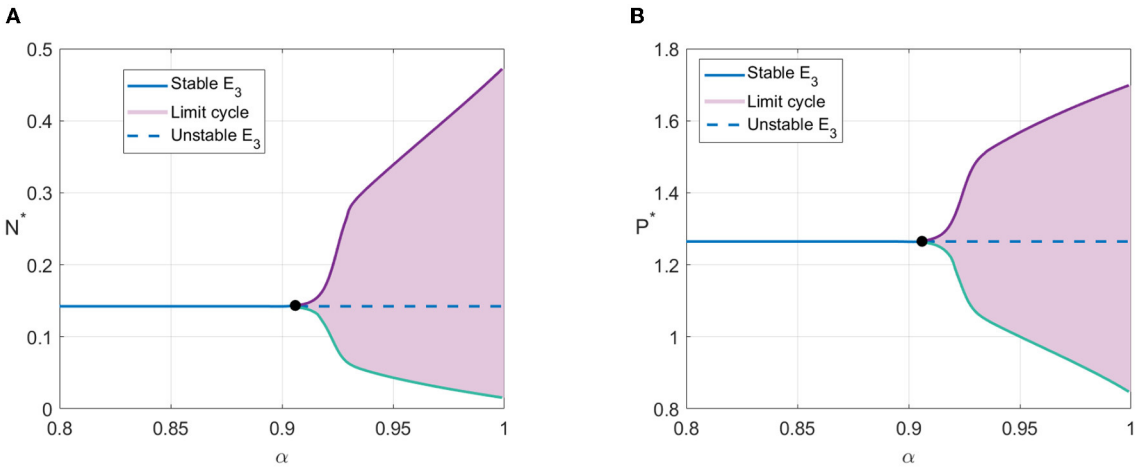

FIGURE 3
Bifurcation diagram with α as bifurcation parameter. **(A)** Value of N^* with respect to derivative order α. **(B)** Value of P^* with respect to derivative order α.

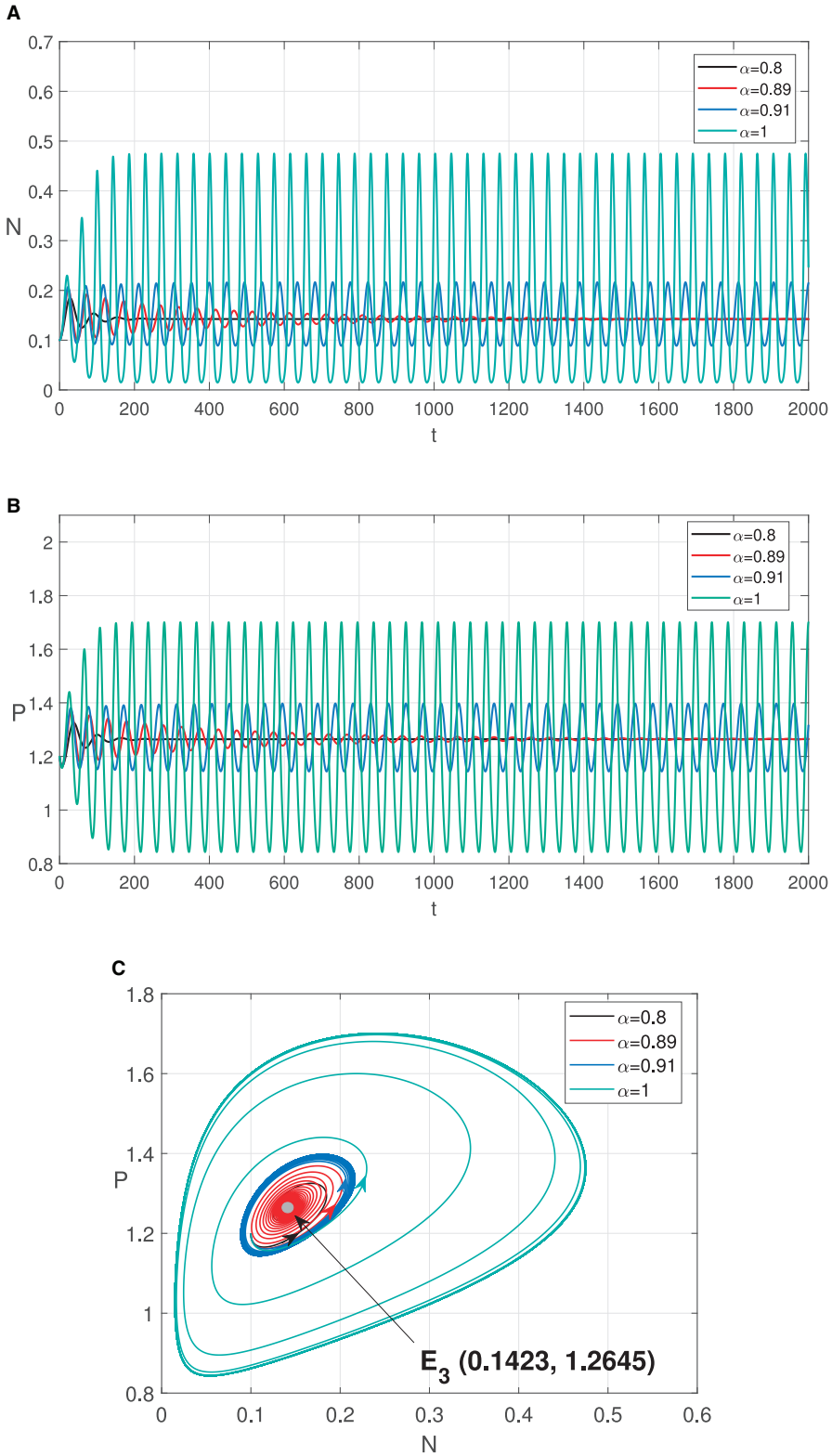

FIGURE 4
Graphic solutions of Simulation 3. **(A)** Solutions of N with respect to time t. **(B)** Solutions of P with respect to time t. **(C)** Phase portraits.

solutions tend to limit cycle around E_3. As confirmation of the bifurcation diagram, two α values satisfying $\alpha < \alpha^*$, i.e., $\alpha = 0.8$ and $\alpha = 0.89$, and two α values satisfying $\alpha.\alpha^*$, i.e., $\alpha = 0.91$ and $\alpha = 1$, are selected to simulate the solutions of N and P with respect to time. For $\alpha = 0.8$ and $\alpha = 0.89$, the solutions tend to E_3. The solution with $\alpha = 0.89$ oscillates longer than $\alpha = 0.8$ before

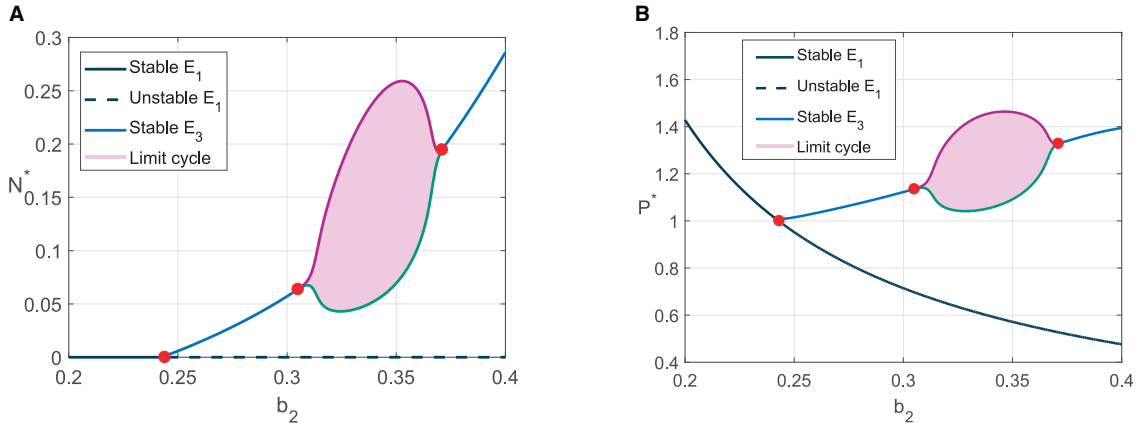

FIGURE 5
Bifurcation diagram with b_2 as bifurcation parameter. **(A)** The value of N^* for $0.2 \leq b_2 \leq 0.4$. **(B)** The value of P^* for $0.2 \leq b_2 \leq 0.4$.

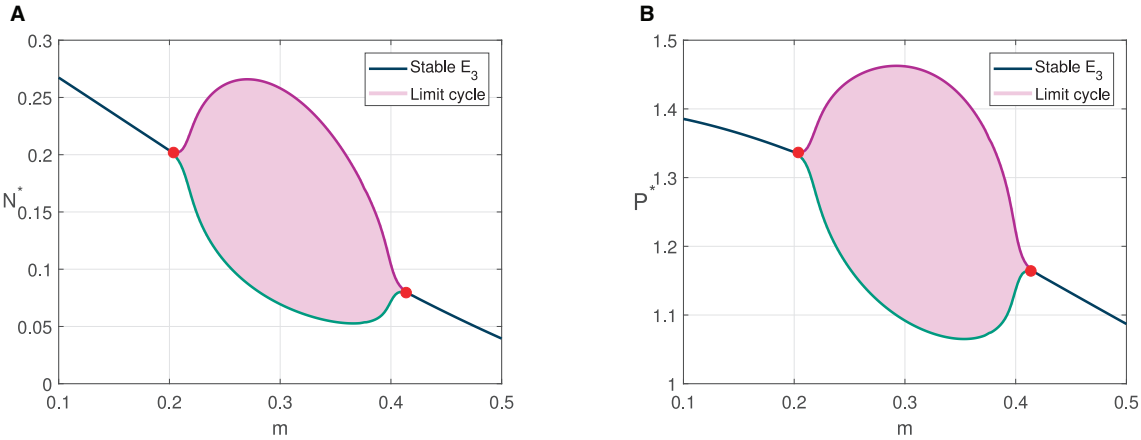

FIGURE 6
Bifurcation diagram with m as bifurcation parameter. **(A)** The value of N^* for $0.1 \leq m \leq 0.5$. **(B)** The value of P^* for $0.1 \leq m \leq 0.5$.

finally convergent to E_3. Meanwhile, for $\alpha = 0.91$ and $\alpha = 1$, each solution convergent to a limit cycle. The amplitude of the limit cycle solution with $\alpha = 1$ is greater than $\alpha = 0.91$.

Numerical simulations in Figures 3, 4 show the existence of Hopf bifurcation in system (3) with α as bifurcation parameter. In addition, the system also undergoes one-parameter Hopf bifurcation with other bifurcation parameters such as cannibalism rate (b_2) and refuge coefficient (m). The bifurcation diagrams are shown in Figures 5, 6, respectively.

For bifurcation diagram with parameter b_2, we have three bifurcation points, i.e., $b_2^* = 0.2429$, $b_2^{**} = 0.306$, and $b_2^{***} = 0.372$. For $b_2 < b_2^*$, the solutions convergent to prey extinction point E_1. It is in accordance with the analytical result since the stability condition of E_1 is satisfied. When the predator cannibalism rate is increased pass b_2^*, E_1 is unstable, and the solutions convergent to the coexistence point, which means the predator survive from extinction. The solutions tend to limit cycle when $b_2^{**} < b_2 < b_2^{***}$. For bifurcation diagram with parameter m, we have two bifurcation points, i.e., m^*, m^{**}. For $m < m^*$, the solutions convergent to coexistence point. The solutions tend to limit cycle in the refuge coefficient range $m^* < m < m^{**}$.

5. Conclusion

A first-order system of Predator–prey interaction incorporating predator cannibalism and refuge is modified by applying Caputo fractional-order derivative operator. We verify the non-negativity, existence, uniqueness, and boundedness of the model solution. The local and global stability of equilibrium points are then examined. In addition, the existence of Hopf bifurcation is investigated. There are four equilibrium points in the model: the origin point, the prey extinction point, the predator extinction point, and the coexistence point. Since the eigenvalues are real numbers, the first three equilibrium points have the same local stability as the first-order system. However, the local stability of the coexistence point differs from that of the first-order system. The coexistence point with positive real-part eigenvalues is locally

asymptotically stable in the modified system as long as the absolute of the eigenvalue arguments are bigger than $\frac{\alpha\pi}{2}$. Even though it is based on different theories, the global stability properties of all equilibrium points are identical to those in the first-order system. Under certain conditions, the Hopf bifurcation exists for the coexistence point. Numerical simulations confirmed the analytical results of stability properties and the existence of Hopf bifurcation.

Data availability statement

The original contributions presented in the study are included in the article/supplementary material, further inquiries can be directed to the corresponding author.

Author contributions

AS and WMK: conceptualization. MR, AS, and ID: methodology. MR: software, data curation, writing—original draft preparation, and visualization. AS, WMK, and ID: validation, writing—reviewing and editing, and supervision. MR and AS: formal analysis. MR, AS, WMK, and ID: investigation. AS: resources and project administration. All authors have read and agreed to the published version of the manuscript.

Conflict of interest

The authors declare that the research was conducted in the absence of any commercial or financial relationships that could be construed as a potential conflict of interest.

Publisher's note

All claims expressed in this article are solely those of the authors and do not necessarily represent those of their affiliated organizations, or those of the publisher, the editors and the reviewers. Any product that may be evaluated in this article, or claim that may be made by its manufacturer, is not guaranteed or endorsed by the publisher.

References

1. Djilali S, Bentout S. Spatiotemporal patterns in a diffusive predator-prey model with prey social behavior. *Acta Appl Math*. (2020) 169:125–43. doi: 10.1007/s10440-019-00291-z

2. Mezouaghi A, Djilali S, Bentout S, Biroud K. Bifurcation analysis of a diffusive predator-prey model with prey social behavior and predator harvesting. *Math Methods Appl Sci*. (2022) 45:718–31. doi: 10.1002/mma.7807

3. Beay LK, Suryanto A, Darti I, et al. Hopf bifurcation and stability analysis of the Rosenzweig-MacArthur predator-prey model with stage-structure in prey. *Math Biosci Eng*. (2020) 17:4080–97. doi: 10.3934/mbe.2020226

4. Bentout S, Djilali S, Atangana A. Bifurcation analysis of an age-structured prey-predator model with infection developed in prey. *Math Methods Appl Sci*. (2022) 45:1189–208. doi: 10.1002/mma.7846

5. Rayungsari M, Kusumawinahyu WM, Marsudi M. Dynamical analysis of predator-prey model with ratio-dependent functional response. *Appl Math Sci*. (2014) 8:1401–10. doi: 10.12988/ams.2014.4111

6. Blyuss KB, Kyrychko YN, Blyuss OB. Complex dynamics near extinction in a predator-prey model with ratio dependence and Holling type III functional response. *Front Appl Math Stat*. (2022) 2022:123. doi: 10.3389/fams.2022.1083815

7. Suryanto A, Darti I, S Panigoro H, Kilicman A. A fractional-order predator-prey model with ratio-dependent functional response and linear harvesting. *Mathematics*. (2019) 7:1100. doi: 10.3390/math7111100

8. Panigoro HS, Rahmi E, Resmawan R. Bifurcation analysis of a predator-prey model involving age structure, intraspecific competition, Michaelis-Menten type harvesting, and memory effect. *Front Appl Mathand Statistics*. (2023) 2023:124. doi: 10.3389/fams.2022.1077831

9. Trapanese C, Bey M, Tonachella G, Meunier H, Masi S. Prolonged care and cannibalism of infant corpse by relatives in semi-free-ranging capuchin monkeys. *Primates*. (2020) 61:41–47. doi: 10.1007/s10329-019-00747-8

10. Oliva-Vidal P, Tobajas J, Margalida A. Cannibalistic necrophagy in red foxes: do the nutritional benefits offset the potential costs of disease transmission? *Mammalian Biol*. (2021) 101:1115–20. doi: 10.1007/s42991-021-00184-5

11. Allen ML, Krofel M, Yamazaki K, Alexander EP, Koike S. Cannibalism in bears. *Ursus*. (2022) 2022:1–9. doi: 10.2192/URSUS-D-20-00031.2

12. Cunha-Saraiva F, Balshine S, Wagner RH, Schaedelin FC. From cannibal to caregiver: tracking the transition in a cichlid fish. *Animal Behaviour*. (2018) 139:9–17. doi: 10.1016/j.anbehav.2018.03.003

13. Canales TM, Delius GW, Law R. Regulation of fish stocks without stock-recruitment relationships: the case of small pelagic fish. *Fish Fish*. (2020) 21:857–71. doi: 10.1111/faf.12465

14. Koltz AM, Wright JP. Impacts of female body size on cannibalism and juvenile abundance in a dominant arctic spider. *J Animal Ecol*. (2020) 89:1788–98. doi: 10.1111/1365-2656.13230

15. Marchetti MF, Persons MH. Egg sac damage and previous egg sac production influence truncated parental investment in the wolf spider, Pardosa milvina. *Ethology*. (2020) 126:1111–21. doi: 10.1111/eth.13091

16. Zhang S, Yu L, Tan M, Tan NY, Wong XX, Kuntner M, et al. Male mating strategies to counter sexual conflict in spiders. *Commun Biol*. (2022) 5:1–12. doi: 10.1038/s42003-022-03512-8

17. Bose APH. Parent-offspring cannibalism throughout the animal kingdom: a review of adaptive hypotheses. *Biol Rev*. (2022) 97:1868–85. doi: 10.1111/brv.12868

18. Kang Y, Rodriguez-Rodriguez M, Evilsizor S. Ecological and evolutionary dynamics of two-stage models of social insects with egg cannibalism. *J Math Anal Appl*. (2015) 430:324–53. doi: 10.1016/j.jmaa.2015.04.079

19. Zhang F, Chen Y, Li J. Dynamical analysis of a stage-structured predator-prey model with cannibalism. *Math Biosci*. (2019) 307:33–41. doi: 10.1016/j.mbs.2018.11.004

20. Deng H, Chen F, Zhu Z, Li Z. Dynamic behaviors of Lotka-Volterra predator-prey model incorporating predator cannibalism. *Adv Diff Equat*. (2019) 1:359. doi: 10.1186/s13662-019-2289-8

21. Rayungsari M, Suryanto A, Kusumawinahyu WM, Darti I. Dynamical analysis of a predator-prey model incorporating predator cannibalism and refuge. *Axioms*. (2022) 11:116. doi: 10.3390/axioms11030116

22. Mondal S, Samanta G. Dynamics of an additional food provided predator-prey system with prey refuge dependent on both species and constant harvest in predator. *Physica A*. (2019) 534:122301. doi: 10.1016/j.physa.2019.122301

23. Saha S, Samanta G. Analysis of a predator-prey model with herd behavior and disease in prey incorporating prey refuge. *Int J Biomath*. (2019) 12:1950007. doi: 10.1142/S1793524519500074

24. Panigoro HS, Rahmi E, Achmad N, Mahmud SL. The influence of additive Allee effect and periodic harvesting to the dynamics of Leslie-Gower predator-prey model. *Jambura J Math*. (2020) 2:87–96. doi: 10.34312/jjom.v2i2.4566

25. Qi H, Meng X. Threshold behavior of a stochastic predator-prey system with prey refuge and fear effect. *Appl Math Lett*. (2021) 113:106846. doi: 10.1016/j.aml.2020.106846

26. Suryanto A, Darti I, Anam S. Stability analysis of a fractional order modified Leslie-Gower model with additive Allee effect. *Int J Math Math Sci*. (2017) 2017:1–9. doi: 10.1155/2017/8273430

27. Li Z, Liu L, Dehghan S, Chen Y, Xue D. A review and evaluation of numerical tools for fractional calculus and fractional order controls. *Int J Control*. (2017) 90:1165–81. doi: 10.1080/00207179.2015.1124290

28. Liouville J. *Memoire Sur Le Calcul Des Differentielles a Indices Quelconques*. (1832). Available online at: https://books.google.com/books?id=6jfBtwAACAAJ

29. Samko SG, Kilbas AA, Marichev OI. *Fractional Integrals and Derivatives: Theory and Applications*. Switzerland; Philadelphia, PA: Gordon and Breach Science Publishers (1993).

30. Farid G. A unified integral operator and further its consequences. *Open J Math Anal*. (2020) 4:1–7. doi: 10.30538/psrp-oma2020.0047

31. Panigoro HS, Suryanto A, Kusumawinahyu WM, Darti I. Dynamics of an eco-epidemic predator-prey model involving fractional derivatives with power-law and Mittag-Leffler kernel. *Symmetry*. (2021) 13:785. doi: 10.3390/sym13050785

32. Rahmi E, Darti I, Suryanto A. A modified leslie-gower model incorporating beddington-deangelis functional response, double allee effect and memory effect. *Fractal Fract*. (2021) 5:84. doi: 10.3390/fractalfract5030084

33. Alqhtani M, Owolabi KM, Saad KM. Spatiotemporal (target) patterns in sub-diffusive predator-prey system with the Caputo operator. *Chaos Solitons Fractals*. (2022) 160:112267. doi: 10.1016/j.chaos.2022.112267

34. Li Y, Chen Y, Podlubny I. Stability of fractional-order nonlinear dynamic systems: lyapunov direct method and generalized Mittag-Leffler stability. *Comput Math Appl*. (2010) 59:1810–21. doi: 10.1016/j.camwa.2009.08.019

35. Odibat ZM, Shawagfeh NT. Generalized Taylor's formula. *Appl Math Comput*. (2007) 186:286–93. doi: 10.1016/j.amc.2006.07.102

36. Ganti S, Gopinathan S. A note on the solutions of cubic equations of state in low temperature region. *J Mol Liquids*. (2020) 315:113808. doi: 10.1016/j.molliq.2020.113808

37. Hafsi Z. Accurate explicit analytical solution for Colebrook-White equation. *Mech Res Commun*. (2021) 111:103646. doi: 10.1016/j.mechrescom.2020.103646

38. Petras I. *Fractional-order Nonlinear Systems: Modeling, Analysis, and Simulation*. Beijing: Springer London (2011).

39. Vargas-De-Leon C. Volterra-type Lyapunov functions for fractional-order epidemic systems. *Commun Nonlinear Sci Numer Simulat*. (2015) 24:75–85. doi: 10.1016/j.cnsns.2014.12.013

40. Huo J, Zhao H, Zhu L. The effect of vaccines on backward bifurcation in a fractional order HIV model. *Nonlinear Anal Real World Appl*. (2015) 26:289–305. doi: 10.1016/j.nonrwa.2015.05.014

41. Li X, Wu R. Hopf bifurcation analysis of a new commensurate fractional-order hyperchaotic system. *Nonlinear Dyn*. (2014) 78:279–88. doi: 10.1007/s11071-014-1439-5

42. Diethelm K, Ford NJ, Freed AD. A predictor-corrector approach for the numerical solution of fractional differential equations. *Nonlinear Dyn*. (2002) 29:3–22. doi: 10.1023/A:1016592219341

frontiers | Frontiers in Applied Mathematics and Statistics

TYPE Original Research
PUBLISHED 23 March 2023
DOI 10.3389/fams.2023.1096167

OPEN ACCESS

EDITED BY
Dumitru Trucu,
University of Dundee, United Kingdom

REVIEWED BY
Cyrille Bertelle,
University of Le Havre, France
Shariful Alam,
Indian Institute of Engineering Science and Technology, Shibpur, India

*CORRESPONDENCE
I. Sukarsih
✉ icih21002@mail.unpad.ac.id

SPECIALTY SECTION
This article was submitted to Mathematical Biology, a section of the journal Frontiers in Applied Mathematics and Statistics

RECEIVED 11 November 2022
ACCEPTED 27 February 2023
PUBLISHED 23 March 2023

CITATION
Sukarsih I, Supriatna AK, Carnia E and Anggriani N (2023) A Runge-Kutta numerical scheme applied in solving predator-prey fuzzy model with Holling type II functional response. *Front. Appl. Math. Stat.* 9:1096167. doi: 10.3389/fams.2023.1096167

A Runge-Kutta numerical scheme applied in solving predator-prey fuzzy model with Holling type II functional response

I. Sukarsih[1]*, A. K. Supriatna[2], E. Carnia[2] and N. Anggriani[2]

[1]Doctoral Program of Mathematics, Faculty of Mathematics and Natural Sciences, Universitas Padjadjaran, Sumedang, Indonesia, [2]Department of Mathematics, Faculty of Mathematics and Natural Sciences, Universitas Padjadjaran, Sumedang, Indonesia

The predator-prey model has been extensively studied, but only studies models in a certain environment, where all parameters and initial values involved in the model are assumed to be certain. In real practice, some parameters and initial values are often uncertain. To overcome this uncertainty problem, a model can be made by using a fuzzy theoretical approach. In this paper, we develop a numerical scheme for solving two predator-prey models with a Holling type II functional response by considering fuzzy parameters and initial populations. The behavior of the model was studied qualitatively using the 5th order Runge-Kutta method of which was modified for the fuzzy system using the Zadeh extension principle. The numerical simulation results show that, when the initial populations of prey and predators are fuzzy, the behavior of the fuzzy model would be qualitatively the same as the crisp model. Finally, we conclude that the resulting fuzzy behavior represents a generalization of crisp behavior. This gives more realistic results since the solution is obtained by explicitly considering the problem of uncertainty.

KEYWORDS

predator-prey fuzzy model, Holling type II functional response, fuzzy parameter, fuzzy initial population, Zadeh extension principle, 5th order Runge-Kutta method

1. Introduction

The predator-prey model is a model of the interaction between two species expressed in the form of a system of differential equations that describes the dynamic relationship between prey and predators [1]. This model was first introduced by Lotka and Volterra, so it is known as the Lotka-Volterra predator-prey model. In this model, the dynamic behavior of a simple predator-prey model is studied. Various applications of the predator-prey system, such as those in Supriatna and Possingham [2, 3] and several other modifications of the predator-prey model have been made by incorporating additional biological processes into the classic Lotka-Volterra predator-prey equation, including functional response modifications [4].

In ecological systems, the degree of predation depends on the functional response. A functional response considers the number of prey that the predator has successfully consumed per unit time. It is also introduced to describe changes in the rate of prey

consumption by predators when prey density varies [4]. The most common and well-known functional response is the type-II Holling functional response. The Holling type II functional response describes the increasing rate of predator's consumption when the density of prey is low. Meanwhile, when the prey density is high, the predator's consumption is constant. In this case, it represents a phenomenon that the predator takes very little time to find the prey, and when the prey consumption rate reaches the highest level, the predator becomes easily full.

In recent years, various studies on predator-prey models with type-II Holling functional responses have been carried out, including in in Dawes and Souze [4], Jana and Kar [5], Ma et al. [6]. Those studies consider a predator-prey model in a definite environment, where all parameters affecting population size and initial values involved in the model are assumed to be crisp. However, in reality, each parameter and initial value is uncertain, unclear, or incomplete. This uncertainty is caused by inaccuracies made during the process of observation, measurement, experimentation, and so on. To overcome this problem, a model can be made using different approaches such as the stochastic approach, the fuzzy approach and the fuzzy-stochastic approach. A crisp ODE system could be more suitable to be converted into a fuzzy differential equation system whenever the parameters or the initial values are uncertain and have a degree of perseptional values.

In recent decades, the application of fuzzy theory has been widely used as a very effective tool in mathematical modeling to solve real problems that take into account uncertainty. In this approach, uncertain variables and parameters are represented by intervals and fuzzy numbers. In the study of fuzzy differential equations, the term fuzzy differential equations can be in the form of differential equations with fuzzy coefficients, differential equations with fuzzy initial values or fuzzy boundary values [7–12]. The stability of the fuzzy dynamic system in a dynamic population is studied through fuzzy differential equation and fuzzy initial value problem [13]. Various numerical solutions for systems of fuzzy equations have also been introduced in Ahmad and Hasan [10], Jayakumar et al. [14], Nayak and Chakraverty [15], Behroozpoor et al. [16], Tapaswini and Chakraverty [17], and Tapaswini and Chakraverty [18].

The fuzzy predator-prey model was first introduced in da Silva Peixoto et al. [19], where a classic deterministic predator-prey model was formulated using a fuzzy rule-based system. The development of fuzzy differential equations has resulted in new discoveries of fuzzy predator-prey models, including those made by Ahmad and Hasan [10], Pandit and Singh [20], Ak and Oru [21], Ahmad and De Baets [22], Narayanamoorthy et al. [23], Omar et al. [24], and Pal et al. [25]. The authors in Ahmad and Hasan [10], Ahmad and De Baets [22], and Omar et al. [24] used the Euler and 4th order Runge-Kutta method through the principles of Zadeh extension. While the authors in Ak and Oru [21], used the concept of generalized fuzzy derivatives. Other authors in Pandit and Singh [20], used Hukuhara derivative. Moreover, the authors in Narayanamoorthy et al. [23], used the fractional modified Euler method. On the biological perspective, there are some authors who have studied fuzzy predator-prey models with functional responses such as [20, 23, 24, 26]. They all studied a predator-prey model with fuzzy initial conditions. Fuzzy predator-prey models with functional responses have also been studied by Pal et al. [27], Yu et al. [28], Pal et al. [29], Meng and Wu [30], Mahata et al. [31], and Pal et al. [32], who presented fuzzy predator-prey harvesting models. Their work studied two species of predator-prey harvesting models by considering fuzzy parameters. Among those work, the authors in Mallak et al. [26], studied a fuzzy predator-prey model with an arctan functional response using the Hukuhara derivative approach, to describe the satiation predator's consumption.

Our research discusses predator-prey models with Holling type II functional responses by considering fuzzy parameters and fuzzy initial populations. The motivation is that we would like to see how different is the dynamics of the sytems compared to their counterpart crisp predator-prey systems. To proceed we will present some preliminaries regarding the fuzzy number theory and fuzzy differential equation background in Sections 2 and 3 followed by the 5th order Runge-Kutta numerical scheme for fuzzy differential Section 4. In Section 5, we discuss the equilibria and their stabilities condition for two predator-prey models with fuzzy parameters and fuzzy initial values followed by the applications of the 5th order Runge-Kutta numerical scheme to those predator prey models in Section 6. Finally some discussion and conclusion are presented in Sections 7 and 8, respectivelly.

2. Preliminaries

Some of the basic concepts used in this paper, such as fuzzy number, the α-level of the fuzzy number, and the Zadeh extension principle, will be introduced in this section.

2.1. Fuzzy theory

Definition 2.1 [33]. *Let U be a non-empty set, and A is a subset of U. The characteristic function of A is given by*

$$\chi_A(x) = \begin{cases} 1, & \text{if } x \in A \\ 0, & \text{if } x \notin A \end{cases}$$

for each $x \in U$.

Definition 2.2 [33]. *A fuzzy subset F of the non-empty set U is defined by a function $\varphi_F : U \to [0,1]$, which is called the membership function of F.*

Definition 2.3 (α-level) [33]**.** *α-level of the fuzzy subset A of U is the classical set $[A]^\alpha$ defined by*

$$[A]^\alpha = \left\{ x \in U : \varphi_A(x) \geq \alpha, \alpha \in (0,\ 1] \right\}.$$

Support of A is $supp\ A = \{x \in U : \varphi_A(x) > 0\} = [A]^0$.
Core of A is $core\ A = \{x \in U : \varphi_A(x) = 1\} = [A]^1$.

Definition 2.4 (Fuzzy Number) [7]**.** *A fuzzy subset A is called a fuzzy number if the defined universal set is the set of all real numbers $\mathbb{R}$ and satisfies the following conditions:*

(i) *All α-level A is not empty for $0 \leq \alpha \leq 1$*
(ii) *All α-levels of A are open intervals of $\mathbb{R}$*

(iii) *supp* $A = \{x \in \mathbb{R} : \varphi_A(x) > 0\}$ *is bounded.*

The set of all fuzzy numbers is denoted by $\mathcal{F}(\mathbb{R})$, and the α-level of the fuzzy number A is denoted by $[A]^\alpha = [a_1^\alpha, a_2^\alpha]$.

Definition 2.5 [33]. *A fuzzy number A is called a triangular fuzzy number if its membership function has the following equation:*

$$\mu_{A(x)} = \begin{cases} 0, & \text{if } x < a, \\ \frac{x-a}{b-a}, & \text{if } a \le x \le b, \\ \frac{c-x}{c-b}, & \text{if } b \le x \le c, \\ 0, & \text{if } x > c \end{cases}$$

and α*-level of A is,* $[A]^\alpha = \left[a + \alpha\left(b-a\right),\ c - \alpha(c-b)\right]$, *for one* $\alpha \in [0, 1]$.

2.2. Zadeh extension principle

Zadeh's extension principle is one of the basic ideas that encourage the expansion of non-fuzzy mathematical concepts to become fuzzy. This method was proposed by Zadeh to extend the concept from classical set theory to fuzzy set theory.

Definition 2.6 (Zadeh Extension Principle) [7]. *Let X and Y being two universal sets and* $f : X \to Z$ *are classical functions. The extension of f is a function* $\hat{f}(A) \in \mathcal{F}(Z)$, $A \in \mathcal{F}(X)$ *such that*

$$\varphi_{\hat{f}(A)}(z) = \begin{cases} \varphi_A(x), & \text{if } f^{-1}(z) \neq \varnothing \\ 0, & \text{iff}^{-1}(z) = \varnothing \end{cases}$$

where $f^{-1}(z) = \left\{x | f(x) = z\right\}$.

Theorem 2.1 [7]. *if* $f : \mathbb{R}^n \to \mathbb{R}^n$ *is a continuous function, then* $\hat{f} : \mathcal{F}(\mathbb{R}^n) \to \mathcal{F}(\mathbb{R}^n)$ *is well-defined, continuous, and*

$$\left[\hat{f}(A)\right]^\alpha = f([A]^\alpha)$$

for each $\alpha \in [0, 1]$.

Definition 2.7 [33]. *Suppose* $f : \mathbb{R} \times \mathbb{R} \to \mathbb{R}$ *is a continuous function. If A and B are two fuzzy numbers, then the extension* $\hat{f}$ *via A and B, is a fuzzy subset* $\hat{f}(A, B)$ *of* $\mathbb{R}$ *with the membership function given by*:

$$\varphi_{\hat{f}(A,B)}(z) = \begin{cases} sup\ \min\left[\varphi_A(x), \varphi_B(y)\right], & \text{if } f^{-1}(z) \neq \varnothing \\ f^{-1}(z) & \\ 0, & \text{if } f^{-1}(z) = \varnothing \end{cases}$$

where $f^{-1}(z) = \left\{(x, y) | f(x, y) = z\right\}$
and $\left[\hat{f}(A, B)\right]^\alpha = f([A]^\alpha, [B]^\alpha) = \left\{f(x, y) | x \in \left[a_1^\alpha, a_2^\alpha\right], y \in [b_1^\alpha, b_2^\alpha]\right\}$.

3. Fuzzy differential equation

The initial value problem is given to be

$$\begin{cases} x'(t) = f(t, x(t)), \\ x(t_0) = x_0, \end{cases} \tag{1}$$

where f is continuous and $x_0 \in \mathbb{R}^n$. Suppose the initial condition x_0 is uncertain and is modeled by a fuzzy set, then the problem (1) converted into a fuzzy differential equation

$$\begin{cases} x'(t) = f(t, x(t)), \\ x(t_0) \in X_0, \end{cases} \tag{2}$$

where $f : [t_0, T] \times \mathcal{F}(\mathbb{R}^n) \to \mathcal{F}(\mathbb{R}^n)$, $X_0 \in \mathcal{F}(\mathbb{R}^n)$.

Suppose also $L_t(x_0) = x(t, x_0)$ is the solution to the problem (1), then by applying extension principle for $L_t(x_0) = x(t, x_0)$ obtained $\hat{L}_t(X_0) = X(t, X_0)$, which is the solution of the fuzzy problem (2).

Definition 3.1 (Equilibrium Point) [13]. *A fuzzy number* $\overline{X} \in \mathcal{F}(\mathbb{R}^n)$ *is the equilibrium point of* (2) *if*

$$\hat{L}_t\left(\overline{X}\right) = \overline{X}, \text{ for each } t \ge 0$$

or equivalent to

$$[\hat{L}_t\left(\overline{X}\right)]^\alpha = [\overline{X}]^\alpha, \forall \alpha \in [0, 1].$$

Theorem 3.1 [13]. *If* $\overline{x}$ *is the equilibrium point of the classical system* (1), *then* $\chi_{[\overline{x}]}$ *is the equilibrium point of the fuzzy system* (2) *where* $\chi_{[\overline{x}]}$ *is a characteristic function of* $\overline{x}$.

Theorem 3.2 [13]. *Suppose* $\overline{x}$ *is the equilibrium point of the deterministic initial value problem* (2), *then*

(a) $\overline{x}$ *stable if and only if* $\chi_{[\overline{x}]}$ *is stable for the fuzzy initial value problem* (2).
(b) $\overline{x}$ *is asymptotic table, if and only if* $\chi_{[\overline{x}]}$ *is stable asymptotically for the fuzzy initial value problem* (2).

In many cases, a deterministic solution to problem (2) is often difficult to obtain, therefore the author considers the method introduced in [10] which modifies the 5th order Runge-Kutta method for the fuzzy model as follows.

4. Runge-Kutta 5th order numerical scheme

In this section, we will study a two-dimensional fuzzy differential equation system with the form:

$$\begin{cases} X'(t) = f(X, Y), & X(t_0) = X_0 \\ Y'(t) = g(X, Y), & Y(t_0) = Y_0 \end{cases} \tag{3}$$

where $f, g : \mathbb{R}^2 \to \mathbb{R}$ is continuous function, and $X_0, Y_0 \in \mathcal{F}(\mathbb{R})$

By modifying the 5th order Runge-Kutta method, the solution to the fuzzy initial value problem (3) would be:

$$\begin{cases} X_{i+1} = X_i + \frac{1}{6}(K_1 + 4K_4 + K_5) \\ Y_{i+1} = Y_i + \frac{1}{6}(L_1 + 4L_4 + L_5) \end{cases} \tag{4}$$

where

$$
\begin{aligned}
K_1 &= h \cdot f(X_i, Y_i) \\
L_1 &= h \cdot g(X_i, Y_i) \\
K_2 &= h \cdot f\left(X_i + \frac{1}{3}K_1, Y_i + \frac{1}{3}L_1\right) \\
L_2 &= h \cdot g\left(X_i + \frac{1}{3}K_1, Y_i + \frac{1}{3}L_1\right) \\
K_3 &= h \cdot f\left(X_i + \frac{1}{3}K_2, Y_i + \frac{1}{3}L_2\right) \\
L_3 &= h \cdot g\left(X_i + \frac{1}{3}K_2, Y_i + \frac{1}{3}L_2\right) \\
K_4 &= h \cdot f\left(X_i + \frac{1}{2}K_3, Y_i + \frac{1}{2}L_3\right) \\
L_4 &= h \cdot g\left(X_i + \frac{1}{2}K_3, Y_i + \frac{1}{2}L_3\right) \\
K_5 &= h \cdot f\left(X_i + K_4, Y_i + L_4\right) \\
L_5 &= h \cdot g\left(X_i + K_4, Y_i + L_4\right).
\end{aligned}
$$

Since the arguments X_i and Y_i on the right-hand side are iterative, we can define a new function as follows:

$$
\begin{cases}
F_h(X_i, Y_i) = X_i + \frac{1}{6}\left(K_1 + 4K_4 + K_5\right) \\
G_h(X_i, Y_i) = Y_i + \frac{1}{6}\left(L_1 + 4L_4 + L_5\right)
\end{cases} \tag{5}
$$

so that (4) becomes

$$
\begin{cases}
X_{i+1} = F_h(X_i, Y_i) \\
Y_{i+1} = G_h(X_i, Y_i)
\end{cases} \tag{6}
$$

F_h and $G_h$are fuzzy number-valued functions, then

$$
\begin{aligned}
F_h\left([X_i]^\alpha, [Y_i]^\alpha\right) = \big[&\min\left\{F_h(u,v) \middle| u\epsilon\left[x_{i,1}^\alpha, x_{i,2}^\alpha\right], v\epsilon\left[y_{i,1}^\alpha, y_{i,2}^\alpha\right]\right\}, \\
&max\{F_h(u,v) | u\epsilon\left[x_{i,1}^\alpha, x_{i,2}^\alpha\right], v\epsilon[y_{i,1}^\alpha, y_{i,2}^\alpha]\}\big]
\end{aligned}
$$

and

$$
\begin{aligned}
G_h\left([X_i]^\alpha, [Y_i]^\alpha\right) = \big[&\min\left\{G_h(u,v) \middle| u\epsilon\left[x_{i,1}^\alpha, x_{i,2}^\alpha\right], v\epsilon\left[y_{i,1}^\alpha, y_{i,2}^\alpha\right]\right\}, \\
&max\{G_h(u,v) | u\epsilon\left[x_{i,1}^\alpha, x_{i,2}^\alpha\right], v\epsilon[y_{i,1}^\alpha, y_{i,2}^\alpha]\}\big]
\end{aligned}
$$

Let $[X_{i+1}]^\alpha = \left[x_{i+1,1}^\alpha, x_{i+1,2}^\alpha\right]$ and $[Y_{i+1}]^\alpha = \left[y_{i+1,1}^\alpha, y_{i+1,2}^\alpha\right]$, then we get

$$
\begin{cases}
x_{i+1,1}^\alpha = F_h\left(x_{i,1}^\alpha, y_{i,1}^\alpha\right) = min\{F_h(u,v) | u\epsilon\left[x_{i,1}^\alpha, x_{i,2}^\alpha\right], v\epsilon[y_{i,1}^\alpha, y_{i,2}^\alpha]\} \\
x_{i+1,2}^\alpha = F_h\left(x_{i,2}^\alpha, y_{i,2}^\alpha\right) = \max\left\{F_h(u,v) \middle| u\epsilon\left[x_{i,1}^\alpha, x_{i,2}^\alpha\right], v\epsilon\left[y_{i,1}^\alpha, y_{i,2}^\alpha\right]\right\} \\
y_{i+1,1}^\alpha = G_h\left(x_{i,1}^\alpha, y_{i,1}^\alpha\right) = min\{G_h(u,v) | u\epsilon\left[x_{i,1}^\alpha, x_{i,2}^\alpha\right], v\epsilon[y_{i,1}^\alpha, y_{i,2}^\alpha]\} \\
y_{i+1,2}^\alpha = G_h\left(x_{i,2}^\alpha, y_{i,2}^\alpha\right) = max\{G_h(u,v) | u\epsilon\left[x_{i,1}^\alpha, x_{i,2}^\alpha\right], v\epsilon[y_{i,1}^\alpha, y_{i,2}^\alpha]\}
\end{cases} \tag{7}
$$

To approximate the solution (3) at each α-level, the partition $t_0 < t_1 < t_2 < \cdots < t_{N-1} < t_N = T$ is created on the interval $[t_0, T]$, with $t_i = t_0 + ih$, $i = 0, 1, 2, \ldots, N$ and the length of the partition $h = \frac{T - t_0}{N} > 0$.

5. Predator-prey fuzzy model with type II Holling functional response

In this section, two predator-prey models with type II Holling functional response will be studied to construct a fuzzy model. The first model was built from the deterministic model introduced by Jha et al. [34]. In this model, all parameters and the initial population are assumed to be certain, whereas in reality the parameter values and the initial population number cannot be known with certainty. In the next section, the model is expressed in a fuzzy model, where the initial population and uncertain parameters are expressed in fuzzy numbers. This model is expressed in Equations (4.1), (4.2), and (4.3) which is called model I. The second model is a modification of model I by considering harvesting. First of all, the deterministic model of model I is modified by adding a harvesting factor for both predator and prey. This model is then expressed in a fuzzy model, where the initial population and parameters are considered uncertain. This model is expressed in Equations (4.4), (4.5), and (4.6) which is called model II.

Model I: A predator-prey model with a type II Holling functional response introduced in Jha et al. [34] is given as:

$$
\begin{cases}
x'(t) = ax\left(1 - \frac{x}{K}\right) - \frac{bxy}{(A+x)}, & x(t_0) = x_0 \\
y'(t) = -cy + \frac{dxy}{(A+x)}, & y(t_0) = y_0
\end{cases} \tag{8}
$$

where x and y are prey and predator population density at time t, K is environmental carrying capacity, a is prey intrinsic growth rate, b is prey predation rate, c is the predator mortality rate, d is the predator conversion, and A is the constant saturation factor of the predator. All model parameters are assumed to be positive.

If $(\overline{x,y})$ is an equilibrium points of (8), by setting the derivatives equal to zero, we get the equilibrium points are $(0,\ 0)$, $(K,\ 0)$, and $(\overline{x}, \overline{y})$, where $\overline{x} = \frac{Ac}{d-c}$, $\overline{y} = \frac{a}{b}(A + \overline{x})\left(1 - \frac{\overline{x}}{K}\right)$, and $(\overline{x,y})$ is positive when $d > c$. The stability at these points is

(i) The system unstable at (0,0)
(ii) The system is asymptotically stable at (K,0), if $K < \frac{Ac}{d-c}$ (or $K > \frac{Ac}{d-c}$ if $d < c$)
(iii) The system is asymptotically stable at $(\overline{x}, \overline{y})$, if $K < \frac{a(A+\overline{x})^2}{b\overline{y}}$.

Suppose the initial population of prey and predators are uncertain, i.e., X_0 and Y_0 become fuzzy initial populations of prey and predators, respectively, at t_0. Then by applying the fuzzy initial value problem, where the initial population is a fuzzy number, the fuzzy predator-prey model of the system (8) becomes

$$
\begin{cases}
x'(t) = ax\left(1 - \frac{x}{K}\right) - \frac{bxy}{(A+X)}, & x(t_0) = X_0 \\
y'(t) = -cy + \frac{dxy}{(A+x)}, & y(t_0) = Y_0
\end{cases} \tag{9}
$$

where $X_0, Y_0 \in \mathcal{F}(\mathbb{R}^2)$.

Based on Theorems (3.1) and (3.2), the fuzzy equilibrium point of the system (9) is $\chi_{\{0,0\}}$, $\chi_{\{K,0\}}$, and $\chi_{\left\{\frac{Ac}{d-c},\ \frac{a}{b}(A+\overline{x})\left(1-\frac{\overline{x}}{K}\right)\right\}}$ exists if $d > c$. The stability at these points is:

(i) The equilibrium point $\chi_{\{0,0\}}$ is unstable
(ii) The equilibrium point $\chi_{\{K,0\}}$ is asymptotically stable if $K < \frac{Ac}{d-c}$ (or $K > \frac{Ac}{d-c}$ if $d < c$)
(iii) The equilibrium point $\chi_{\left\{\frac{Ac}{d-c},\ \frac{a}{b}(A+\overline{x})\left(1-\frac{\overline{x}}{K}\right)\right\}}$ asymptotically stable if $K < \frac{a(A+\overline{x})^2}{b\overline{y}}$

Suppose it is assumed that the parameter a is also uncertain. By changing the variable X in (9) into $X = (X_1, X_2) = (X, a)$, then the fuzzy model (9) becomes

$$\begin{cases} X_1^{'}(t) = X_1X_2\left(1-\frac{X_1}{K}\right) - \frac{bX_1Y}{(A+X_1)}, & X_1(t_0) = X_{10} \\ X_2^{'}(t) = 0, & X_2(t_0) = a \\ Y^{'}(t) = -cY + \frac{dX_1Y}{(A+X_1)}, & Y(t_0) = Y_0 \end{cases} \quad (10)$$

where $X_0, Y_0, a \in \mathcal{F}(\mathbb{R})$.

Model II. If it is assumed that both prey and predator populations in system (8) are the target of harvesting efforts, then system (8) becomes

$$\begin{cases} x^{'}(t) = ax\left(1-\frac{x}{K}\right) - \frac{bxy}{(A+x)} - p_1Ex, & x(t_0) = x_0 \\ y^{'}(t) = -cy + \frac{\delta xy}{(A+x)} - p_2Ey, & y(t_0) = y \end{cases} \quad (11)$$

where E denotes the catch effort, and p_1, p_2, respectively, shows the coefficient catching power of prey and predator, where the function p_iEx adoption from Das et al. [35].

If $(\overline{x,y})$ is an equilibrium points of (11), by setting the derivatives equal to zero, we get the equilibrium points are $(0,\ 0)$, $\left(-\frac{K(p_1E-a)}{a},\ 0\right)$, and $(\bar{x}, \bar{y})$ where $\bar{x} = -\frac{A(p_2E+c)}{p_2E-d+c}$, $\bar{y} = \frac{Ad\left(E^2Kp_1p_2 - EKap_2 - EKp_1d + EKp_1c - EAap_2 + Kad - Kac - Aac\right)}{Kb(p_2E-d+c)^2}$ exists if $E < \frac{d-c}{p_2}$ and $E\left(EKp_1p_2 - Kap_2 - Kp_1d + Kp_1c - Aap_2\right) > Kac + Aac - Kad$. The stability at these points is

(i) The system is stable at (0,0) if $E > \frac{a}{p_1}$

(ii) The system is asymptotically stable at $\left(-\frac{K(p_1E-a)}{a},\ 0\right)$, if $E < \frac{a}{p_1}$

Suppose the initial population of prey and predators are uncertain, i.e., X_0 and Y_0 becomes the initial fuzzy population of prey and predators, respectively, at t_0, then the fuzzy predator-prey model obtained from the system (11) would be

$$\begin{cases} X^{'}(t) = aX\left(1-\frac{X}{K}\right) - \frac{bXY}{(A+X)} - p_1EX, & X(t_0) = X_0 \\ Y^{'}(t) = -cY + \frac{dXY}{(A+X)} - p_2EY, & Y(t_0) = Y_0 \end{cases} \quad (12)$$

where $X_0, Y_0 \in \mathcal{F}(\mathbb{R})$.

Based on Theorems (3.1) and (3.2), the fuzzy equilibrium points of the system (12) are $\chi_{\{0,0\}}$, $\chi_{\left\{-\frac{K(p_1E-a)}{a},0\right\}}$, and $\chi_{\left\{-\frac{A(p_2E+c)}{p_2E-d+c},\ \frac{Ad\left(E^2Kp_1p_2 - EKap_2 - EKp_1d + EKp_1c - EAap_2 + Kad - Kac - Aac\right)}{Kb(p_2E-d+c)^2}\right\}}$ exists if $E < \frac{d-c}{p_2}$, and $E\left(EKp_1p_2 - Kap_2 - Kp_1d + Kp_1c - Aap_2\right) > Kac + Aac - Kad$. The stability at these points is:

(i) The equilibrium point $\chi_{\{0,0\}}$ is stable *if* $E > \frac{a}{p_1}$

(ii) The equilibrium point $\chi_{\left\{-\frac{K(p_1E-a)}{a},0\right\}}$ is asymptotically stable if $E < \frac{a}{p_1}$.

6. Numerical simulation

In this section, we will explore the solution both of the above model for some case different according to the conditions of stability at each point of equilibrium using the 5th order Runge-Kutta method. Numerical simulations were carried out to compare the behavior of the crisp system and the fuzzy system.

Model I: For model I, Numerical simulation is divided into two cases. It is assumed for both cases the values of the parameters $a = 0.5$, $b = 0.254$, $K = 1,000$, and $A = 500$. Parameters c and d in this model are assumed as follows:

(i) $c = 0.125$ and $d = 0.325$
(ii) $c = 0.325$ and $d = 0.125$

Suppose the initial population of prey and predators is $X_0 = 1,100$ and $Y_0 = 900$.

Case (i):

For the case (i) where $d > c$ and $K < \frac{a(A+\bar{x})^2}{b\bar{y}}$ obtained three equilibrium points: (0.0), (1,000, 0), and (312.5, 1099.594). Equilibrium points (0, 0) and (1,000, 0) are unstable, and at points (312.5, 1099.594) are asymptotically stable. The results of the numerical simulation of case (i) are presented in Figures 1, 2A. Figure 1A shows a stable system toward the equilibrium point (312.5, 1099.594). The phase plane graph for case (i) is presented in Figure 2A.

Let the initial population X_0 and Y_0 uncertain be defined as a triangular fuzzy number with $[X_0]^\alpha = [1,050 + 50\alpha,\ 1,150 - 50\alpha]$ and $[Y_0]^\alpha = [850 + 50\alpha,\ 950 - 50\alpha]$. Based on theorems 3.1 and 3.2, the fuzzy equilibrium points are obtained: $\chi_{\{0,0\}}$, $\chi_{\{1,000,\ 0\}}$, and $\chi_{\{312.5,\ 1099.594\}}$, where the equilibrium point $\chi_{\{0,0\}}$ and $\chi_{\{1,000,\ 0\}}$ is unstable, and the equilibrium point $\chi_{\{312.5,\ 1099.594\}}$ is asymptotically stable. The numerical simulation results for the fuzzy model in case (i) are presented in Figures 1, 2B. Figure 1B shows the fuzzy system is stable toward the equilibrium point $\chi_{\{312.5,\ 1099.594\}}$. The fuzzy phase plane graph for case (i) is presented in Figure 2B.

Let other than X_0 and Y_0, parameter a is also uncertain and is expressed in triangular fuzzy numbers with $[a]^\alpha = [0.4 + 0.1\alpha,\ 0.6 - 0.1\alpha]$, then the behavior of the system shown in Figure 3.

The simulation results can be seen that by adding a parameter as a fuzzy number, the dynamic behavior of the fuzzy system qualitatively shows the same results when only the initial populations of prey and predators are fuzzy, and this is in accordance with the behavior of the crisp system.

Case (ii):

For the case (ii) where $d < c$ and $K > \frac{Ac}{d-c}$, three equilibrium points are obtained: (0.0), (1,000, 0), and $(-812.5, -1114.973)$. The point $(-812.5, -1114,973)$ is ignored because it has a negative value, the stability of the equilibrium point is: at point (0,0) is unstable and at point (1,000, 0) is asymptotically stable. The results of the numerical simulation of case (ii) are presented in Figures 4, 5A. Figure 4A shows the system is stable toward the equilibrium point (1,000, 0). The phase plane graph for case (ii) is presented in Figure 5A.

Suppose the initial population is uncertain and defined as a triangular fuzzy number as in case (i). Based on theorems 3.1 and 3.2, the fuzzy equilibrium points are obtained: $\chi_{\{0,0\}}$, and $\chi_{\{1,000,\ 0\}}$, where at the equilibrium point $\chi_{\{0,0\}}$ is unstable and at the point $\chi_{\{1,000,\ 0\}}$ asymptotically stable.

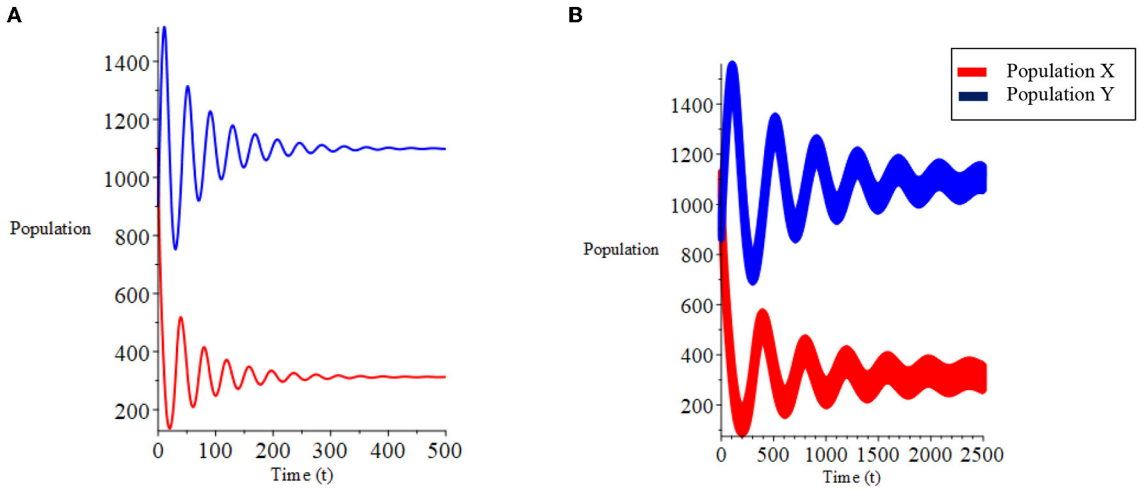

FIGURE 1
Population growth over time from case (i) of model I. **(A)** Crisp. **(B)** Fuzzy.

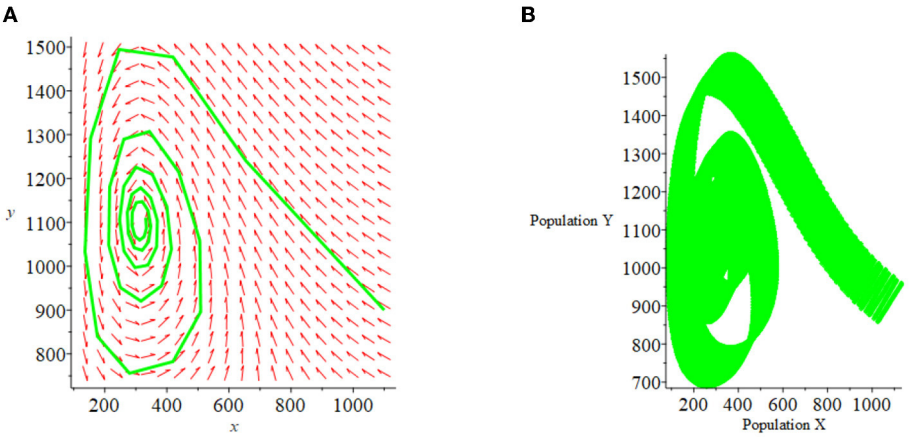

FIGURE 2
Phase Plane of case (i) of model I. **(A)** Crisp. **(B)** Fuzzy.

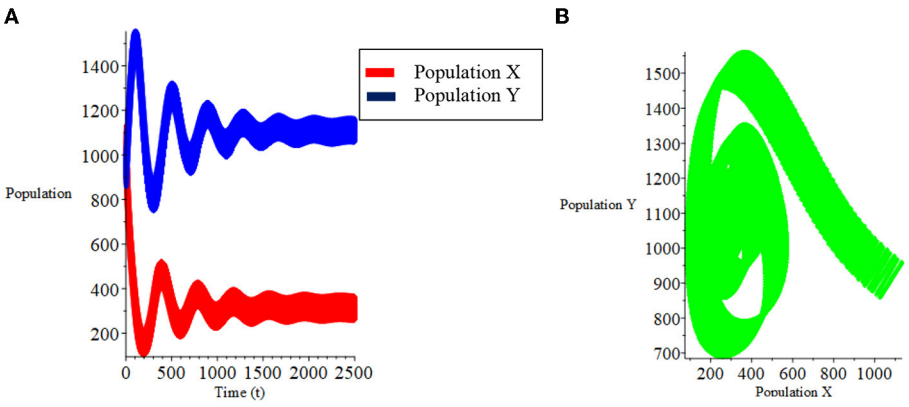

FIGURE 3
(A) Population growth over time. **(B)** Phase plane fuzzy for case (i) of model I with parameter a and population X_0, Y_0 is fuzzy.

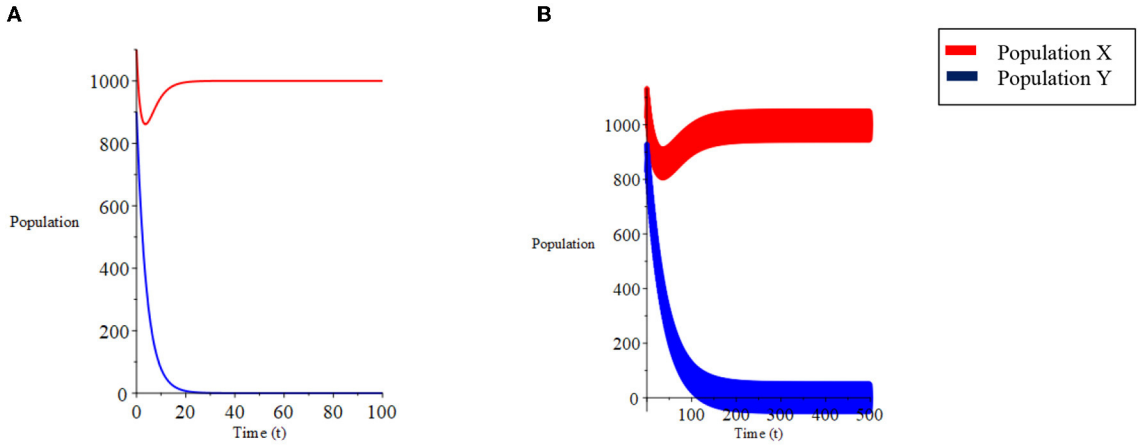

FIGURE 4
Population growth over time for case (ii) of model I. **(A)** Crisp. **(B)** Fuzzy.

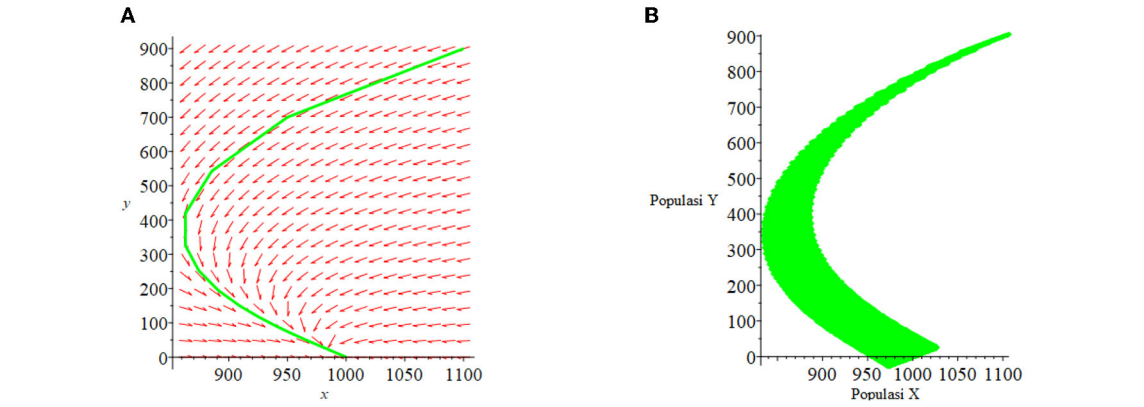

FIGURE 5
Phase Plane for case (ii) of model I. **(A)** Crisp. **(B)** Fuzzy.

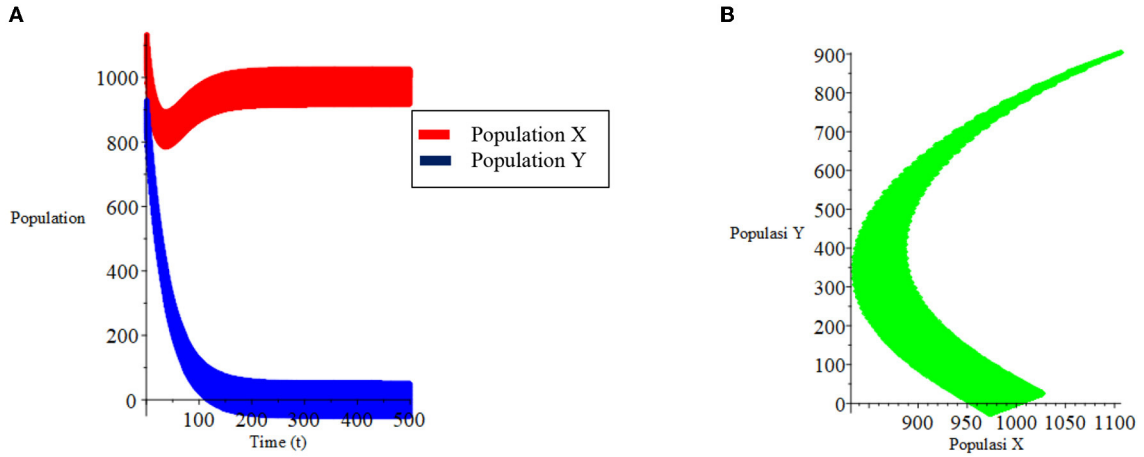

FIGURE 6
(A) Population growth over time. **(B)** Phase plane fuzzy for case (ii) of model I with parameter a and population X_0, Y_0 are fuzzy.

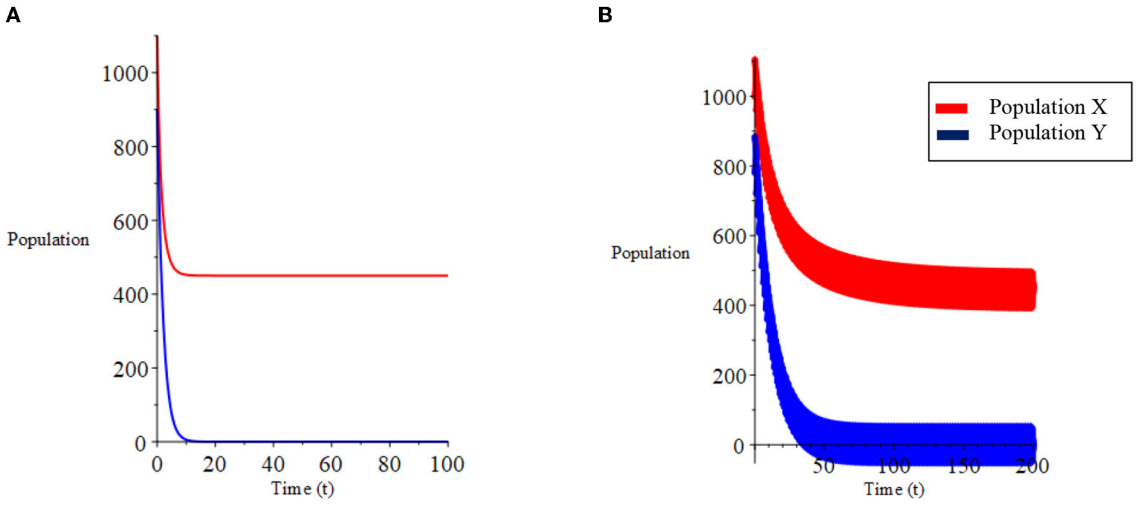

FIGURE 7
Population growth over time for case (i) of model II. **(A)** Crisp. **(B)** Fuzzy.

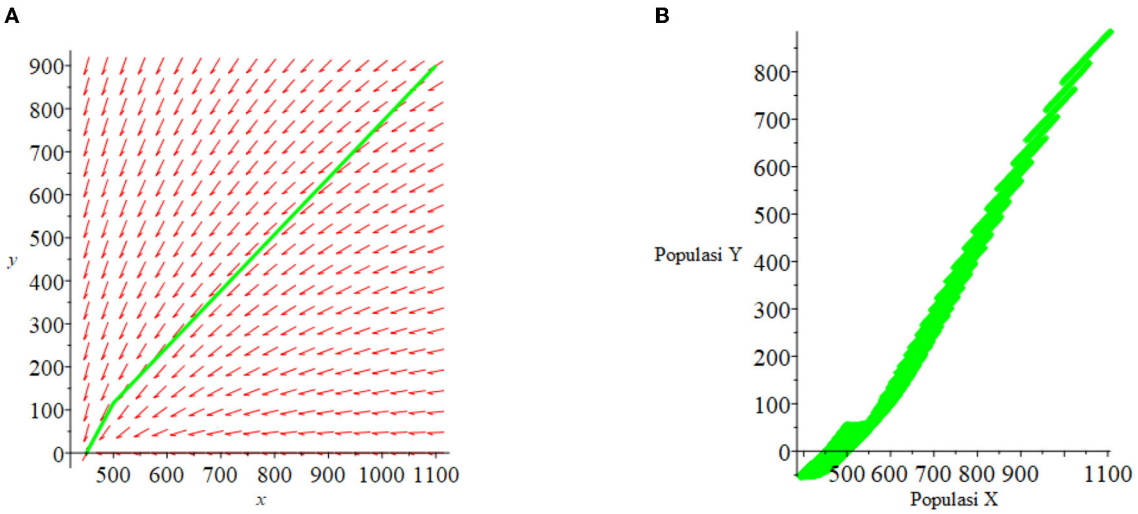

FIGURE 8
Phase Plane for case (i) of model II. **(A)** Crisp. **(B)** Fuzzy.

The numerical simulation results for the fuzzy model in case (ii) are presented in Figures 4, 5B. Figure 4B shows the fuzzy system is stable toward the equilibrium point $\chi_{\{1{,}000,\ 0\}}$. The fuzzy phase plane graph for case (ii) is presented in Figure 5B.

Let other than X_0 and Y_0, parameter a is also uncertain and is expressed in triangular fuzzy numbers as in case (i), then the behavior of the system is shown in Figure 6.

The results of the numerical simulation are presented in Figures 1–6 shows that for both cases of model I, the solution graph with the fuzzy approach differs quantitatively, but qualitatively gives the same results as the graph from the crisp system when only the initial population is fuzzy, but slightly different when one of the parameters and the initial population is fuzzy.

Model II: For model II, Numerical simulation is divided into two cases. It is assumed for both cases the values of the parameters and the initial population are the same as for model I: $a = 0.5$, $b = 0.254$, $K = 1,000$, and $A = 500$. And other parameters in this model are assumed as follows:

(i) $c = 0.325$, $d = 0.125$, $p_1 = 1$, $p_2 = 2$, and $E = 0.275$
(ii) $c = 0.125$, $d = 0.325$, $p_1 = 1$, $p_2 = 1$, and $E = 0.6$

Suppose the initial population of prey and predators is $X_0 = 1,100$ and $Y_0 = 900$.

Case (i):

For case (i) where $E < \frac{a}{p_1}$ obtained three equilibrium points: (0.0), (450,0), and (−583.3, −169.51). The point (−583.3, −169.51) is ignored because it is negative. The stability at equilibrium point

(0, 0) is unstable and at (450,0) is asymptotically stable. The numerical simulation results of case (i) are presented in Figures 7, 8A. Figure 7A shows the system is stable toward the point of equilibrium (450.0). The phase plane graph for case (i) is presented in Figure 8A.

Suppose the initial population X_0 and Y_0 uncertain is defined as a triangular fuzzy number as in model I, then the fuzzy equilibrium point $\chi_{\{0,0\}}$ is unstable, and the fuzzy equilibrium point $\chi_{\{450,0\}}$ is asymptotically stable. The numerical simulation results for the fuzzy model in case (i) are presented in Figures 7, 8B. Figure 7B shows a stable fuzzy system toward the equilibrium point $\chi_{\{450,0\}}$.The fuzzy phase plane graph for case (i) is presented in Figure 8B.

Case **(ii):**

For the case (ii) where $E > \frac{a}{p_1}$ obtained three equilibrium points: (0.0), (−200,0), and (−906.25, −564.792). The points (−200,0) and (−906.25, −564.792) are ignored because they are negative. The numerical simulation results of case (ii) are presented in Figures 9, 10A. Figure 9A shows the system is stable toward the equilibrium point (0,0). The phase plane graph for case (ii) is presented in Figure 10A.

Suppose the initial population is uncertain and defined as a triangular fuzzy number as in model I, then the fuzzy equilibrium point $\chi_{\{0,0\}}$ is stable. The numerical simulation results for the fuzzy model in case (ii) are presented in Figures 9, 10B. Figure 9B shows the fuzzy system is stable toward the equilibrium point $\chi_{\{0,0\}}$. The fuzzy phase plane graph for case (ii) is presented in Figure 10B.

7. Discussion

The research presented in this paper is an extension of the predator-prey model with a type II Holling functional response discussed by Jha et al. [34] taking into account the uncertainty in the parameters and the initial population expressed in fuzzy numbers. This model is further expanded by adding harvesting factors to both populations. In this study, the behavior of the system is only studied qualitatively by performing numerical simulations to explore the behavior of the fuzzy system and compare it with the crisp system. In conducting the simulation, we use triangular fuzzy numbers to express uncertainty in the initial population and parameters. Of the two models studied, we found the same results. In both models,

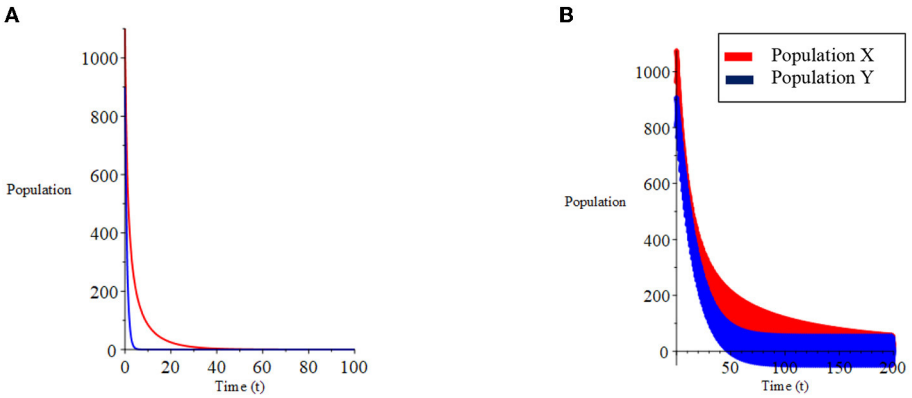

FIGURE 9
Population growth over time for case (ii) of model II. **(A)** Crisp. **(B)** Fuzzy.

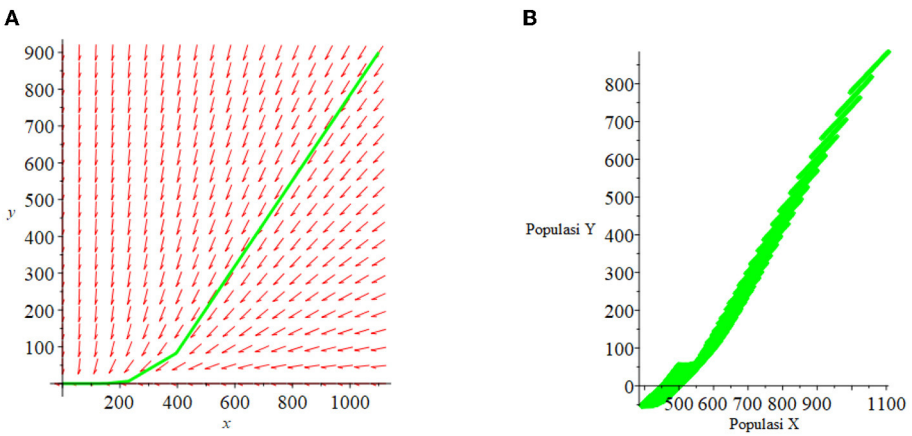

FIGURE 10
Phase plane for case (ii) of model II. **(A)** Crisp. **(B)** Fuzzy.

the fuzzy system shows the same behavior as the crisp system when only the initial population of prey and predators is fuzzy or when one parameter is added as a fuzzy parameter. Another result obtained is, for the fuzzy model, the time required for the system to reach equilibrium is longer than the crisp model. This is due to the uncertainty in the initial value expressed in the fuzzy interval. This research only studied the behavior of the system qualitatively through numerical simulation. In this numerical simulation, all the figures of the phase planes for the fuzzy systems above are plotted for the value of the α-level equals zero. It seems that the phase planes for the crisp systems can be extracted from the fuzzy system's phase planes with the α-level equals zero. This is an interesting result that can be interpreted crisp model can be used as a special case of fuzzy model whenever the degree of uncertainty is relatively low.

8. Conclusion

In this paper, we have developed a numerical scheme to find the solution of two predator-prey models with a Holling type II functional response by considering fuzzy parameters and fuzzy initial populations. The first model was developed from the model studied by Jha et al. [34] by replacing the initial population and one of the parameters with a fuzzy number. While the second model was developed from the first model by adding harvesting factors to both prey and predator populations. The behavior of the model was studied qualitatively using the Runge-Kutta method of order-5 which was modified for the fuzzy system using the Zadeh extension principle. The numerical simulation results show that, when the initial population prey and predators that have fuzzy values, then both fuzzy models have the same behavior as the crisp model, but the fuzzy model takes a longer time to achieve stability than the crisp model. This is due to the uncertainty in the initial population which is indicated by fuzzy intervals. Likewise, when one parameter is added with a fuzzy value, the fuzzy model has the same behavior as the crisp model. Finally, we can conclude that fuzzy behavior represents a generalization of crisp behavior, and this gives more realistic results that represent the problem of uncertainty. However, there are still much work to be done in the future, including studying the stability of the system analytically, bifurcation problems, and others. As pointed by one of the reviewer, it "would have been more interesting to place the choice of parameters on the crisp model exibiting marked sensitivity behavior to initial conditions" and this is currently under investigation by the authors.

Data availability statement

The original contributions presented in the study are included in the article/supplementary material, further inquiries can be directed to the corresponding author.

Author contributions

AS designed and supervised the research. IS developed the scheme and numerical simulations. EC and NA conducted the literature review. All authors contributed to the articles and approved the submitted versions.

Funding

This research was published with funding from Universitas Padjadjaran through the Article Processing Charge (APC) Replacement Scheme.

Conflict of interest

The authors declare that the research was conducted in the absence of any commercial or financial relationships that could be construed as a potential conflict of interest.

Publisher's note

All claims expressed in this article are solely those of the authors and do not necessarily represent those of their affiliated organizations, or those of the publisher, the editors and the reviewers. Any product that may be evaluated in this article, or claim that may be made by its manufacturer, is not guaranteed or endorsed by the publisher.

References

1. Wang Q, Zhai S, Liu Q, Liu Z. Stability and optimal harvesting of a predator-prey system combining prey refuge with fuzzy biological parameters. *Math Biosci. Eng.* (2021) 18:9094–120. doi: 10.3934/mbe.2021448

2. Supriatna AK, Possingham HP. Optimal harvesting for a predator-prey metapopulation. *Bull Math Biol.* (1998) 60:49–65. doi: 10.1006/bulm.1997.0005

3. Supriatna AK, Possingham HP. Harvesting a two-patch predator-prey metapopulation. *Nat Resour Model.* (1999) 12:481–98. doi: 10.1111/j.1939-7445.1999.tb00023.x

4. Dawes JHP, Souza MO. A derivation of Holling's type I, II and III functional responses in predator-prey systems. *J Theor Biol.* (2013) 327:11–22. doi: 10.1016/j.jtbi.2013.02.017

5. Jana S, Kar TK. Modeling and analysis of a prey-predator system with disease in the prey. *Chaos Solitons Fract.* (2013) 47:42–53. doi: 10.1016/j.chaos.2012.12.002

6. Ma Z, Wang S, Wang T, Tang H. Stability analysis of prey-predator system with Holling type functional response and prey refuge. *Adv Differ Equat.* (2017) 2017:243. doi: 10.1186/s13662-017-1301-4

7. Gomes LT, de Barros LC, Bede B. Fuzzy differential equations in various approaches (2015). doi: 10.1007/978-3-319-22575-3

8. Mizukoshi MT, Barros LC, Chalco-Cano Y, Román-Flores H, Bassanezi RC. Fuzzy differential equations and the extension principle. *Inf Sci.* (2007) 177:3627–35. doi: 10.1016/j.ins.2007.02.039

9. Bandyopadhyay A, Kar S. *System of Type-2 Fuzzy Differential Equations and Its Applications.* Vol. 31. London: Springer (2019).

10. Ahmad MZ, Hasan MK. Modeling of biological populations using fuzzy differential equations. *Int J Mod Phys Conf Ser.* (2012) 9:354–63. doi: 10.1142/S2010194512005429

11. Barros LC, Gomes LT, Tonelli PA. *Fuzzy Differential Equations: An Approach via Fuzzification of the Derivative Operator*. Vol. 230. Elsevier (2013). doi: 10.1016/j.fss.2013.03.004

12. Alamin A, Mondal SP, Alam S, Goswami A. Solution and stability analysis of non-homogeneous difference equation followed by real life application in fuzzy environment. *Sadhana Acad Proc Eng Sci*. (2020) 45:185. doi: 10.1007/s12046-020-01422-1

13. Mizukoshi MT, Barros LC, Bassanezi RC. Stability of fuzzy dynamic systems. *Int Uncertain J Fuzziness Knowl Based Syst*. (2009) 17:69–83. doi: 10.1142/S0218488509005747

14. Jayakumar T, Maheskumar D, Kanagarajan K. Numerical solution of fuzzy differential equations by Runge Kutta method of order five. *Appl Math Sci*. (2012) 6:2989–3002. doi: 10.17654/FS021020135

15. Nayak S, Chakraverty S. Numerical solution of fuzzy stochastic differential equation. *J Intell Fuzzy Syst*. (2016) 31:555–63. doi: 10.3233/IFS-162168

16. Behroozpoor AA, Vahidian Kamyad A, Mazarei MM. Numerical solution of fuzzy initial value problem (FIVP) using optimization. *Int J Adv Appl Sci*. (2016) 3:36–42. doi: 10.21833/ijaas.2016.08.007

17. Tapaswini S, Chakraverty S. Numerical solution of Fuzzy arbitrary order predator-prey equations. *Appl Appl Math Int J*. (2013) 8:647–72.

18. Tapaswini S, Chakraverty S. A New approach to fuzzy initial value problem by improved euler method. *Fuzzy Inf Eng*. (2012) 4:293–312. doi: 10.1007/s12543-012-0117-x

19. da Silva Peixoto M, de Barros LC, Bassanezi RC. Predator-prey fuzzy model. *Ecol Model*. (2008) 214:39–44. doi: 10.1016/j.ecolmodel.2008.01.009

20. Pandit P, Singh P. *Prey Predator Model With Fuzzy Initial Conditions*. International Journal of Web Engineering and Technology (IJEIT). Vol. 3. (2014). p. 65–8.

21. Ak O, Oru O. *A Prey Predator Model With Fuzzy Initial Values*. Hacettepe Journal of Mathematics and Statistics. Vol. 41. (2012). p. 387–95.

22. Ahmad MZ, De Baets B. A predator-prey model with fuzzy initial populations. In: *2009 International Fuzzy Systems Association world congress and 2009 European Society of Fuzzy Logic and Technology*. (2009). p. 1311–4. Available online at: https://www.researchgate.net/publication/221399560_A_Predator-Prey_Model_with_Fuzzy_Initial_Populations

23. Narayanamoorthy S, Baleanu D, Thangapandi K, Perera SSN. Analysis for fractional-order predator–prey model with uncertainty. *IET Syst Biol*. (2019) 13:277–89. doi: 10.1049/iet-syb.2019.0055

24. Omar AHA, Ahmed IAA, Hasan YA. The fuzzy ratio prey-predator model. *Int J Comput Sci Electron Eng*. (2015) 3:101–6.

25. Pal D, Mahapatra GS, Samanta GP. Parameter uncertainty in biomathematical model described by one-prey two-predator system with mutualism. *Int J Biomath*. (2017) 10:1750082. doi: 10.1142/S1793524517500826

26. Mallak S, Farekh D, Attili B. Numerical investigation of fuzzy predator-prey model with a functional response of the form arctan(ax). *Mathematics*. (2021) 9:17–9. doi: 10.3390/math9161919

27. Pal D, Mahapatra GS, Samanta GP. Stability and bionomic analysis of fuzzy prey–predator harvesting model in presence of toxicity: a dynamic approach. *Bull Math Biol*. (2016) 78:1493–519. doi: 10.1007/s11538-016-0192-y

28. Yu X, Yuan S, Zhang T. About the optimal harvesting of a fuzzy predator–prey system: a bioeconomic model incorporating prey refuge and predator mutual interference. *Nonlinear Dyn*. (2018) 94:2143–60. doi: 10.1007/s11071-018-4480-y

29. Pal D, Mahapatra GS, Samanta GP. Stability and bionomic analysis of fuzzy parameter based prey–predator harvesting model using UFM. *Nonlinear Dyn*. (2015) 79:1939–55. doi: 10.1007/s11071-014-1784-4

30. Meng XY, Wu YQ. Dynamical analysis of a fuzzy phytoplankton–zooplankton model with refuge, fishery protection and harvesting. *J Appl Math Comput*. (2020) 63:361–89. doi: 10.1007/s12190-020-01321-y

31. Mahata A, Mondal SP, Roy B, Alam S. Study of two species prey-predator model in imprecise environment with MSY policy under different harvesting scenario. *Environ Dev Sustain*. (2021) 23:14908–32. doi: 10.1007/s10668-021-01279-2

32. Pal D, Mahapatra GS, Samanta GP. A study of bifurcation of prey-predator model with time delay and harvesting using fuzzy parameters. *J Biol Syst*. (2018) 26:339–72. doi: 10.1142/S021833901850016X

33. de Barros LC, Bassanezi RC, Lodwick WA. *Studies in Fuzziness and Soft Computing A First Course in Fuzzy Logic, Fuzzy Dynamical Systems, and Biomathematics Theory and Applications* Berlin: Springer (2017).

34. Jha P, Ghorai S. Stability of prey-predator model with Holling type response function and selective harvesting. *J Appl Comput Math*. (2017) 6:3. doi: 10.4172/2168-9679.1000358

35. Das T, Mukherjee RN, Chaudhuri KS. Bioeconomic harvesting of a prey–predator fishery. *J Biol Dyn*. (2009) 3:447–62. doi: 10.1080/17513750802560346

frontiers | Frontiers in Applied Mathematics and Statistics

TYPE Original Research
PUBLISHED 06 April 2023
DOI 10.3389/fams.2023.1064130

OPEN ACCESS

EDITED BY
Salih Djilali,
University of Chlef, Algeria

REVIEWED BY
Soufiane Bentout,
Centre Universitaire Ain Temouchent, Algeria
Fethi Souna,
University of Sidi-Bel-Abbès, Algeria

*CORRESPONDENCE
Md. Haider Ali Biswas
✉ mhabiswas@yahoo.com

SPECIALTY SECTION
This article was submitted to Mathematical Biology, a section of the journal Frontiers in Applied Mathematics and Statistics

RECEIVED 07 October 2022
ACCEPTED 07 March 2023
PUBLISHED 06 April 2023

CITATION
Mulk M, Islam KN and Biswas MHA (2023) Modeling and numerical analysis for mechanical characterization of soft tissue mechanism applying inverse finite element technique. *Front. Appl. Math. Stat.* 9:1064130. doi: 10.3389/fams.2023.1064130

Modeling and numerical analysis for mechanical characterization of soft tissue mechanism applying inverse finite element technique

Md. Mulk[1], Kazi Nusrat Islam[2] and Md. Haider Ali Biswas[2]*

[1]School of Biomedical Engineering, Western University Canada, London, ON, Canada, [2]Mathematics Discipline, Science Engineering, and Technology School, Khulna University, Khulna, Bangladesh

Tissue-mimicking materials [e.g., polyvinyl alcohol cryogel (PVA-C)] are extensively used in clinical applications such as tissue repair and tissue engineering. Various mechanical testing techniques have been used to assess the biomechanical compatibility of tissue-mimicking materials. This article presents the development of inverse finite element (FE) techniques that are solved using numerical optimization to characterize the mechanical properties of PVA-C specimens. In this study, a numerical analysis where the displacement influence factor was employed in conjunction with a linear elastic model of finite thickness was performed. In the analysis, the effects of Poisson's ratio, specimen aspect ratio, and relative indentation depth were investigated, and a novel mathematical term was introduced to Sneddon's equation. In addition, a robust optimization algorithm was developed in MATLAB that utilized FE modeling for parameter estimation before it was rigorously validated.

KEYWORDS

indentation, soft tissue, non-destructive, PVA-C, construct, isotropy, optimization, finite element modeling

1. Introduction

Inverse finite element analysis is a numerical method used to characterize the material properties of soft tissues for biomedical engineering applications [1, 2]. Many techniques have been implemented previously to characterize tissue *in vivo*, *ex vivo*, or tissue-mimicking materials [3]. During the characterization process, the first-order Ogden hyperelastic model is used for estimating material properties. Many previous studies have indicated that the indentation test is an effective technique for characterizing the compressive behavior of tissue under small and large deformation loading conditions [4]. Samani et al. [5] considered tissue hyperelasticity in their indentation-based measurement technique and reported hyperelastic parameters of breast tissues. Soft tissues or tissue-mimicking materials are typically modeled as non-linear, homogeneous, isotropic, and nearly incompressible. The Ogden hyperelastic model is commonly used to capture biological tissue non-linearity. Isvilanonda et al. used the first-order Ogden constitutive model in the material characterization process, and after using an inverse problem analysis of experimental data, they obtained very good results [6–8]. A similar approach is followed in this article whereby indentation testing data are processed through an inverse FE framework to estimate tissue hyperelastic parameters. For solving the inverse problem in this article, an optimization algorithm developed in MATLAB was used where the tissue FE model was used to calculate the cost function to be minimized [9]. For the first step, FE modeling

is a good candidate and has been used extensively in this article. For the second step, a cost or objective function that measures the difference between measured and model-based mechanical response is developed. With these two essential elements, the hyperelastic parameters can be calculated and optimized by iteratively refining the sought parameters with initial estimates until the cost function reaches its minimum value [10–12].

The main motivation of the article as well as the novelty of this study can be highlighted clearly in the following paragraph.

A variety of clinical procedures for assessing structural and functional damage of tissues and treating the effectiveness of tissue therapeutics are under active investigation. Therapeutics of soft tissues depend on the mechanical response of the organs and neighboring tissues. Indentation techniques can be used to probe the local mechanical properties of soft tissues and tissue mimics. The effect of relative indentation depth, aspect ratio, Poisson's ratio, and dimensionless k on the indentation response of soft tissue mimics needs to be further investigated for an improved understanding of material characterization. One way to solve this problem is mesh refinement which also verifies the convergence of stresses, but most of the mesh sensitivity cases showed divergence. Even with increasing load sharp edges form crack that makes the cylindrical indenter very unpopular. To overcome this problem, a novel approach displacement influence factor (IF) is used with Boussinesq's equation to calculate stress at any point underneath the indenter. Non-linear, hyperelastic models have been used previously to characterize sources of non-linearities (i.e., material and geometrical) in this type of problem but have presented some problems. In this study, indentation responses from cylindrical indenters are investigated using numerical methods to develop and optimize new techniques for characterizing non-linear material properties using Ogden and Mooney Rivlin's hyperelastic models.

In this article, we develop a comprehensive understanding of soft tissue characterization based on a hyperelastic model using inverse analysis. Moreover, we conduct a parametric analysis with varying material properties and examine the effectiveness of an optimization method. Sensitivity analysis was conducted for cylindrical and spherical indentation tests. Our analysis shows the effect of specimen thickness, PVA-C concentration, and freeze–thaw cycle on (μ, α).

1.1. Hyperelastic model

A hyperelastic or green-type elastic material [13–15] is a type of material that follows constitutive models where the stress–strain behavior is defined by a strain energy density function [16]. They are considered to be truly elastic as they store energy during loading and dissipate equal amounts of energy during the unloading process. These materials experience large strains that are mostly recoverable [17–19]. To define hyperelasticity, many mathematical models have been developed and different aspects of non-linear elastic material behavior have been explained [20, 21]. These types of models have been very successfully applied to soft materials and tissues.

Polyvinyl alcohol cryogel (PVA-C) samples of 5%, 10%, and 15% concentrations are modeled as soft tissue mimics to examine their non-linear material properties. Experimental force–displacement (F–D) data were used as an input parameter for the Ogden hyperelastic model.

A hyperelastic material is a type of constitutive model where the presence of a strain energy density function is assumed, and the stress–strain relationship is derived from a strain energy density function. The Ogden hyperelastic model for isotropic material can be obtained from strain as follows:

$$W=\sum_{i=1}^{\infty}\frac{\mu_i}{\alpha_i}\left(\lambda_1^{\alpha_i}+\lambda_2^{\alpha_i}+\lambda_3^{\alpha_i}-3\right)+\sum_{i=1}^{\infty}k_i(J^{el}-1)^{2i}, \quad (1)$$

where μ, α, and K are presented as constitutive parameters, J is the determinant of the strain tensor, and λ is known as the principle stretch. For incompressible material deformation, $J = 1$ leads the second term in the aforementioned equation to vanish. For the first-order Ogden model, $n = 1$. Thus, the model will have only two unknown parameters of shear modulus (μ) and strain hardening exponent (α).

For a uniaxial compression test, the nominal stress (σ) is represented as a function of the stretch ratio λ. The first-order Ogden material model can be presented in the form as given in equation (2):

$$\sigma=\frac{2\mu}{\alpha}\left(\lambda^{(\alpha-1)}-\lambda^{(-\alpha/2-1)}\right). \quad (2)$$

The aforementioned two equations can take only positive values. The experimental force–displacement (F–d) data are used as an input parameter for the hyperelastic model. By applying curve fitting to the experimental (σ – λ) data, the first-order Ogden parameter is extracted.

1.2. Numerical analysis

Commercial FE software package Abaqus was used to create an axisymmetric model for examining indentation. PVA-C was used as a soft tissue mimic, and a flat-ended cylindrical indenter was modeled in this simulation. The contact surface between the indenter and the soft tissue was set as frictionless. Soft biological tissue is generally considered to be incompressible [22]. For optimal numerical accuracy, high mesh density was adapted underneath the indenter, and convergence criteria were verified. Indentation tests were simulated under linear and non-linear hyperelastic model assumptions. Numerical analysis was performed by FEM using Abaqus version 6:13–4 (2013). Cylindrical indenters and rigid flat-ended cylindrical indenters were used for numerical analysis. An indenter of radius 4 mm was indented on a soft tissue-mimicking sample of PVA-C with 5%, 10%, and 15% (w/w) concentrations. The sample size was $L = 19$ mm and $B = 12$ mm. The soft tissue sample was modeled as homogeneous, isotropic, and nearly incompressible.

TABLE 1 FE generated variable for cylindrical indentation.

Cylindrical indentation			
Hyperelastic model—ogden strain energy function with $N = 1$			
	μ	α	D
	0.0003	11.77	0.00000000
Problem size			
Number of elements			3,864
Number of elements defined by the user			3,783
Number of internal elements generated for contact			80
Number of nodes			7,818
Number of nodes defined by the user			3,875
Number of internal nodes generated by the program			3,943
Total number of variables in the model			11,694

The Ogden hyperelastic material model used in simulation of soft tissue mimics 5% PVA-C and 15% 2FTC.

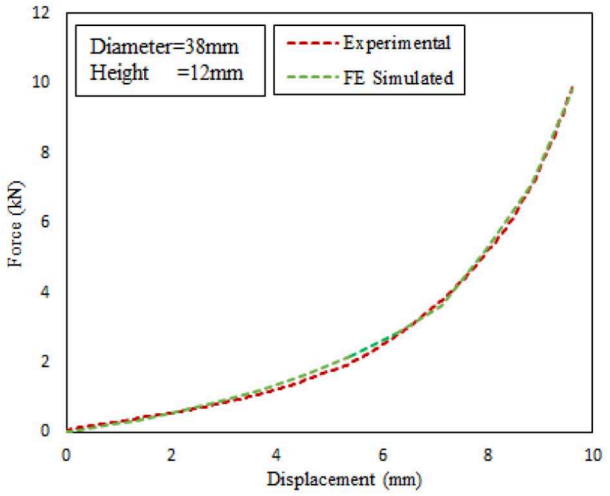

FIGURE 1
Load vs. displacement graph for PVA-C model with 5% concentration.

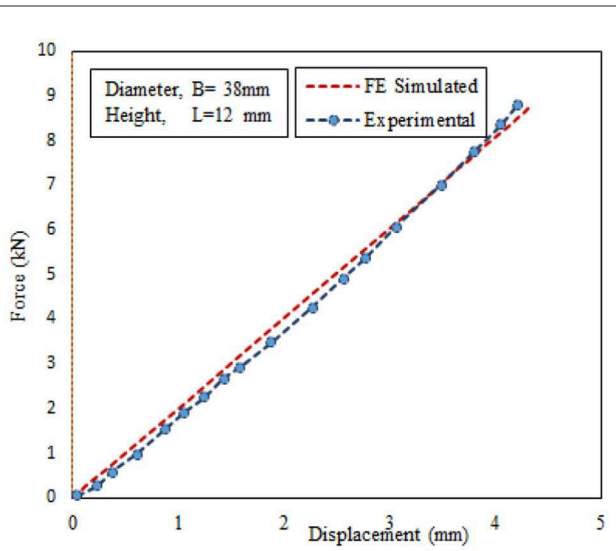

FIGURE 2
Load vs. displacement graph for PVA-C model with 15% concentration.

An axisymmetric model was developed and meshed with (CAX4RH) and (CAX3H) linear quadrilateral elements. A very fine mesh was made at the contact zone and comparatively, the coarse mesh was utilized outside the contact zone. The boundary conditions for the three sides of the sample were fixed ($U1 = U2 = U3 = UR1 = UR2 = UR3 = 0$), and one side is variable ($U1 = U3 = UR2 = 0$). During the indentation test, a 4N vertical load was applied, and the contact between the indenter and the sample was considered frictionless. The Ogden hyperelastic material model was considered for PVA-C samples undergoing the indentation test, the data of which are provided in Ref. [23]. The simulation was completed in 13 steps with a step size of 0.01. To observe the indentation responses, the hyperelastic FE model was analyzed including a sample with finite thick and infinite thickness made of PVA-C with 5% and 15% concentrations.

1.3. Numerical model setting

A two-dimensional axisymmetric cylindrical indentation model was developed by using Abaqus version 6:13–4 (2013). The Ogden first-order strain energy density function was used in the numerical simulation. In total, 7818 (CAX4RH) nodes were generated in the meshing process, as shown in Table 1.

An axisymmetric FE model was developed by using Abaqus, and PVA-C 5% and 15% 2FTC experimental data obtained from Ref. [23] were used as an input parameter for the first-order Ogden hyperelastic model. The load–displacement graph for both PVA concentrations is shown in Figures 1, 2.

1.4. Parametric studies

Based on previous research, it has been found that the hyperelastic parameters determined using cylindrical or spherical indentation testing are not always the same as those obtained from experimental uniaxial compression tests [4, 6, 10, 20]. To investigate the sources of such disagreement, a parametric study was conducted to examine the influence of (μ, α) on the shape of the simulated data. An optimization algorithm combined with MATLAB was used to minimize the sum of the squared difference between the experimental measurements and the FE-simulated Ogden hyperelastic model. This allowed for the unknown parameters (μ, α) to be determined. A sensitivity analysis was then conducted to verify the accuracy and robustness of the parameters. For cylindrical uniaxial indentation obtained from inverse analysis shown in Table 2.

TABLE 2 For cylindrical and uniaxial indentation (μ, α) obtained from the inverse analysis.

Method	Material	Radius (B/2)	Depth (L)	Experimental	Inverse	Experimental	Inverse
	PVA (%) 2FTC	(mm)	(mm)	Mu (kPa)	Alpha	Mu (kPa)	Alpha
UCS	5	19	12	0.0025	10.749	0.0026	10.965
Cylindrical	5	19	12	0.00249	10.76	0.0025	11.8
Cylindrical	10	19	12	0.004	4.67	0.004	4.84
UCS	15	19	12	0.01	25	0.011	24.93
Cylindrical	15	19	12	0.011	25	0.016	25.43
Cylindrical	20	19	12	0.0213	25	0.02	25.4

For 5%, 10%, 15%, and 20% PVA-C, 2FTC specimens.

1.5. Inverse finite element analysis

The inverse FE method was used to determine the hyperelastic material parameters of soft tissue specimens from indentation responses [24, 25]. Based on Hadamard's definition, an inverse problem is posed if one of the three conditions is violated: (i) existence, (ii) uniqueness, and (iii) stability. Many optimization algorithms are commonly used as such least square fitting power low, Levenberg–Marquardt (LM) Trust Region Algorithm, and Kalman Filter to solve the inverse problems.

The inverse analysis is introduced to minimize an objective function with respect to unknown constitutive material parameters (μ, α) that match the experimental data [10, 26]. The Levenberg–Marquardt (LM) method was used in this dissertation to extract the unknown parameters based on the inverse analysis. The LM method is defined as the minimization of the error function Φ with respect to a vector $\hat{P}$. The error function is represented as follows:

$$\Phi\left(\hat{P}\right) = \frac{1}{2}\sum_{i=1}^{n}\left[r_i\left(\hat{P}\right)\right]^2 = \frac{1}{2}r^T r \tag{3}$$

Here, $P\acute{L}$ is a vector that contains unknown constitutive parameters $\hat{P}^T = \{\mu, \alpha\}$, and n is the number of measurements. The vector $\hat{r}$ is defined as follows:

$$\hat{r} = t^* - \hat{t}, \tag{4}$$

where t^* and $\hat{t}$ are the model-predicted and experimental data.

1.6. Optimization algorithm: Using ogden model

A detailed flowchart of the inverse optimization process to characterize the tissue hyperelastic parameters used in the current study is shown in Figure 3.

First, experimental (F–D) data were used as an input parameter for the numerical model (Abaqus). Simulated (F–D) data were then used as an input parameter for inverse analysis (MATLAB). An object junction was introduced to minimize the quadratic difference between simulated- and model-predicted data. Through the optimization process, a numerical convergence was achieved, and an optimized unknown parameter was obtained. These parameters were used as an input parameter of Abaqus for numerical validation.

1.7. Mesh optimization with μ and α

Although the implicit method with Newton–Raphson iterative solver is enough to obtain the converged solution, mesh optimization through adaptive meshing was adopted for numerical accuracy. Optimized μ and α through mesh convergence are shown in Figures 4, 5.

1.8. Identification for estimating material properties

The Ogden model is used to identify the hyperelastic material properties. The Levenburg–Marquardt (LM) algorithm was used to minimize the difference between experimental- and model-predicted data. Here, a novel approach is introduced to determine and validate material hyperelasticity. This method includes the following steps:

- Experimental data are used as input for the Ogden hyperelasticity model.
- Numerical analysis is carried out with FEM (Abaqus), and the output of the load–displacement curve is recorded.
- This load–displacement data are used as input for the Levenburg–Marquardt (LM) optimization algorithm in MATLAB.
- Initial estimate values (μ, α) are used for initializing the optimization algorithm.
- *MATLABR* Simulink: *R*2015*a* used @ *fminsearch* algorithm was used to fit the Ogden first-order hyperelastic model as shown in Equation (2). Moreover, the Levenburg–Marqardt (LM) optimization algorithm was used as shown in Equation (3). The optimized parameters (μ, α) are recorded as shown in Equation (4).

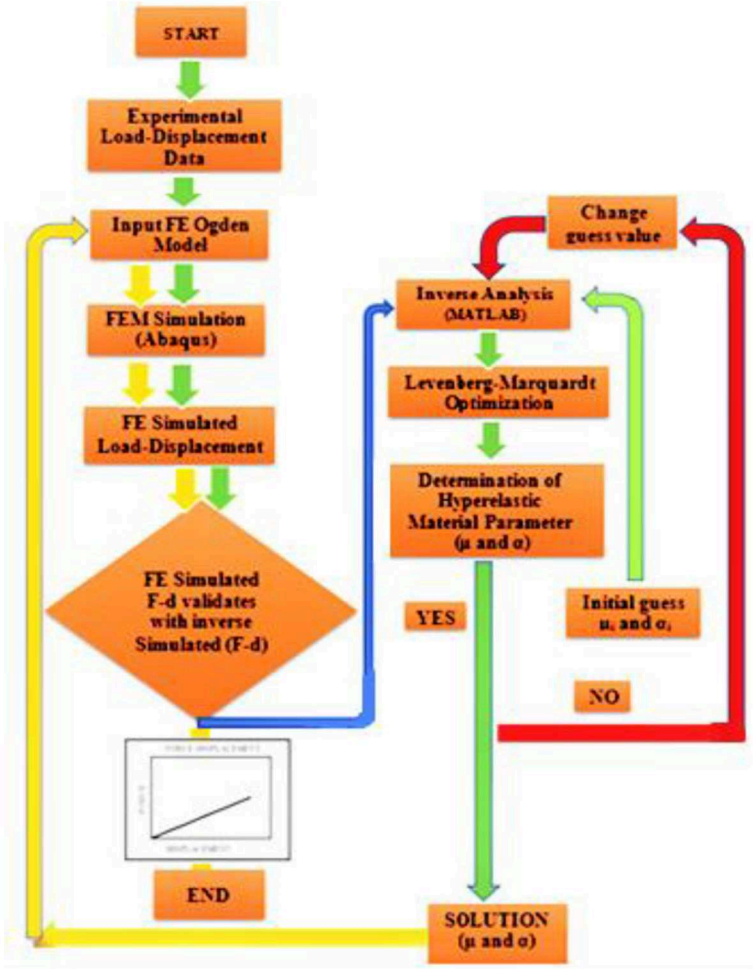

FIGURE 3
Flowchart of the inverse optimization process to characterize the unknown tissue hyperelastic parameters—Ogden parameter.

- These optimized parameters (μ, α) are inserted in FEA (Abaqus) for validation and verification of the inverse problem.

Through inverse analysis, extracted Ogden parameters are readily available to use in simulation and also to verify the stability of the solution. The detailed process is shown in the flowchart of Figure 3.

A new technique has been developed to characterize the biomechanical properties of nonlinear material using Ogden and hyperelastic models. Experimental results are compared with the novel inverse technique that can be further investigated to develop patient-specific artificial organs.

1.9. Validation exercise

FE-simulated cylindrical load–displacement data were used in the robust optimization algorithm through inverse analysis. The entire procedure is shown as a flowchart in Figure 3. A validation exercise was conducted using Ogden parameters (μ), which were varied while α was kept constant and vice versa as shown in Figures 6, 7 [10].

The results obtained from the load–displacement curve indicated that there is a significant effect of (μ), as this parameter explains the strength of the material and α is the strain hardening coefficient. In the process of validation, μ and α values were compared with that of Ref. [10] and found good agreement.

2. Results

Before conducting any surgical procedures, planning for biomaterial research, or any other fields where applicable, unique identification of material properties is essential. The accuracy, effectiveness, and robustness of such procedures need verification [3] with FE-simulated data. The performances of the novel model are illustrated in this section. In general, 5% and 15% (w/w) soft tissue mimic data [23] were used in the hyperelastic model. During the simulation, cylindrical, spherical, and uniaxial indentation tests were conducted.

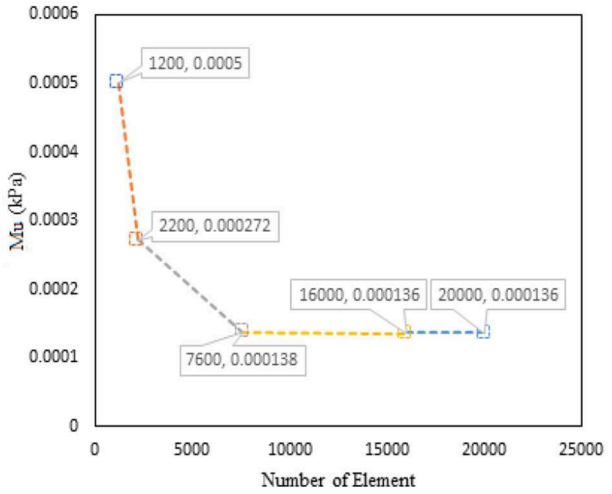

FIGURE 4
Graph of μ vs. number of elements for PVA-C modeled with 5% concentration and finite thickness.

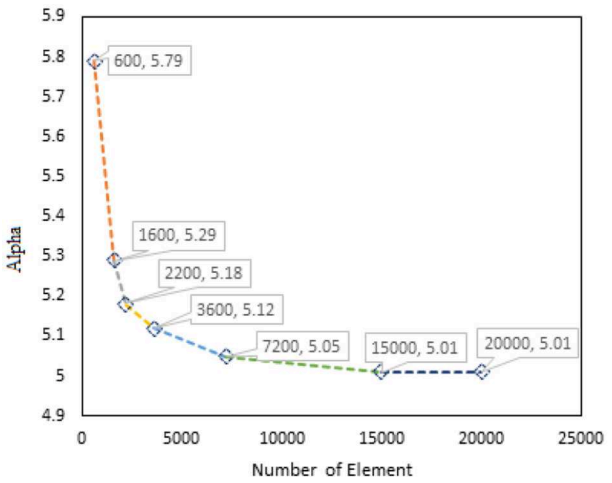

FIGURE 5
Graph of α vs. number of elements for PVA-C modeled with 15% concentration and finite thickness.

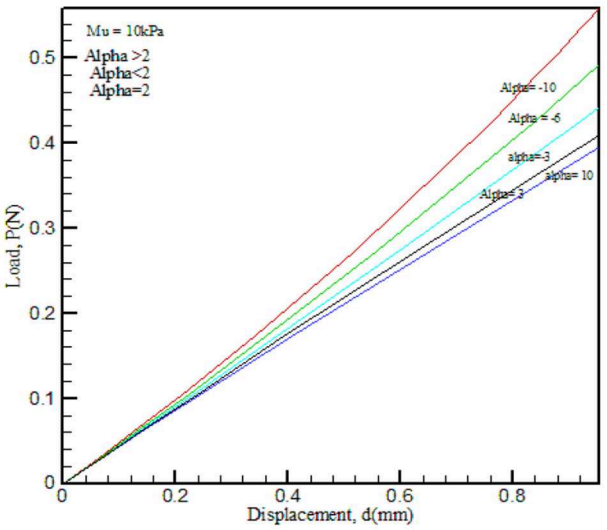

FIGURE 6
FE-simulated load–displacement graph for the Ogden hyperelastic model. Material property α was kept constant and μ was varied.

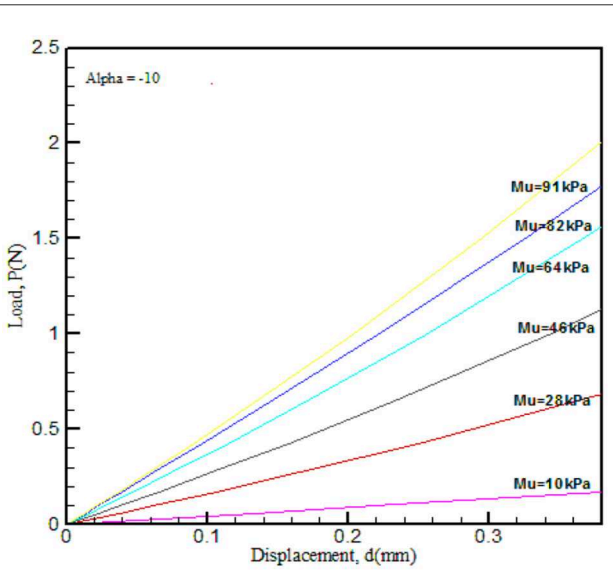

FIGURE 7
FE-simulated load–displacement graph for the Ogden hyperelastic model. Material property α was varied and μ was kept constant.

The hyperelastic model was simulated in the Abaqus environment, where Ogden first-order constitutive model was used, and experimental data were fitted for parameter optimization. The indentation response from cylindrical indentation for 5% and 15% soft tissue mimics are shown in Figures 8, 9 along with optimized (μ and α) values.

Experimental data obtained from Ref [7, 23, 27] were used as an input parameter for the FE-simulated Ogden model. FE-simulated and model-predicted load vs. displacement curve for PVA-C, 2FTC5%, and 15% specimens are shown earlier. This process is used as an optimization algorithm for the determination of material properties (μ and α).

Figure 10 shows a residual–stretch graph. It is defined by the proportion of variance (R-square) between the observed and the predicted data. The FE-simulated Ogden model was used in the optimization algorithm to gain the residual–stretch results. Experimental data at a concentration of (i) PVA-C 5%, 2FTC and (ii) PVA-C 15%, 2FTC were used from cylindrical indentation.

2.1. Optimization algorithm

A detailed flowchart of the inverse optimization process to characterize the tissue hyperelastic parameters used in the current study is shown in Figure 11.

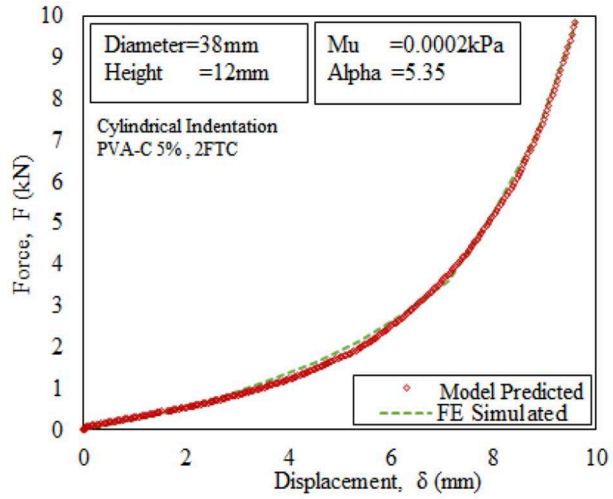

FIGURE 8
Load vs. displacement graph for PVA-C sample with finite thickness and 5% concentration.

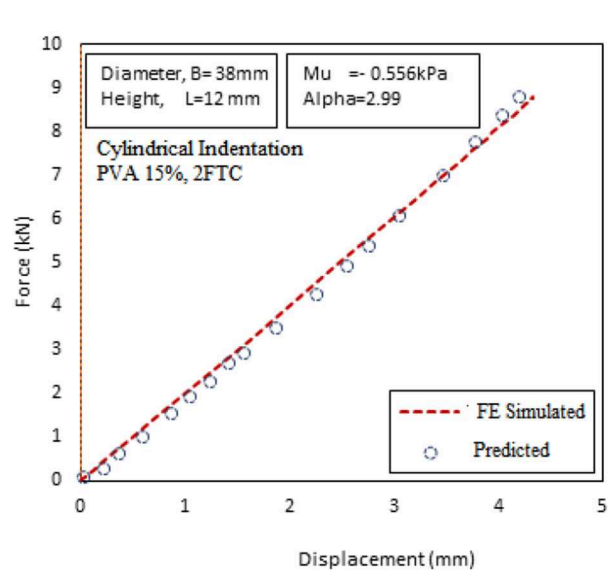

FIGURE 9
Load vs. displacement graph for PVA-C sample with finite thickness and 15% concentration.

First, experimental (F–D) data are used as an input parameter for the numerical model (Abaqus). Simulated (F–D) data were then used as an input parameter for inverse analysis (MATLAB). An object junction was introduced to minimize the quadratic difference between simulated and model-predicted data. Through the optimization process, a numerical convergence was achieved and an optimized unknown parameter was obtained. These parameters were used as an input parameter of Abaqus for numerical validation.

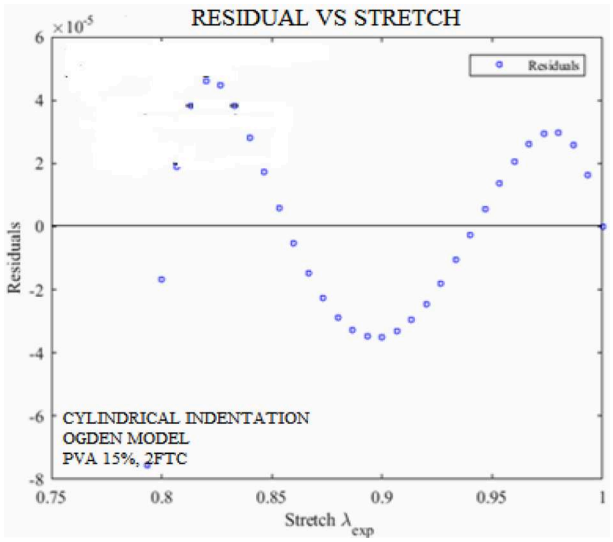

FIGURE 10
Residual vs. stretch graph for PVA-C samples with 15% concentration, where fitness coefficient is $R^2 = 0.9998$.

2.2. Effect of μ and α on thickness

The extracted Ogden parameters from the inverse optimization algorithm are plotted against various concentrations of PVA-C 5%, 2FTC and PVA-C 15%, 2FTC as shown in Figures 12, 13.

It can be hypothesized that (μ, α) values have a greater dependency on thickness. As the thickness increases, both μ and α increase.

2.3. Effect of concentration

The freeze and thaw technique is a part of the stability testing that determines whether any formulation will remain stable under various conditions. The extracted Ogden parameters from the inverse optimization algorithm are plotted against concentration and freeze–thaw cycles are shown in Figures 14, 15.

This led us to conclude that there is a proportional relationship between (μ, α) values and PVA-C concentration and freeze-thaw cycles. With the increase in PVA-C concentration, (μ, α) values increase. With the increase of the freeze–thaw cycle time (FTC), the values of (μ, α) also increase.

2.4. Sensitivity analysis: Cylindrical indentation

To overcome the stability problem, sensitivity analysis was conducted by adding noise (±1% and ±2 %) to the solutions. This noise modulation with the input data will enable us to investigate whether there is any extraneous influence on material and equipment. Fellay et al. [6, 13] considered this problem as another minimization approach.

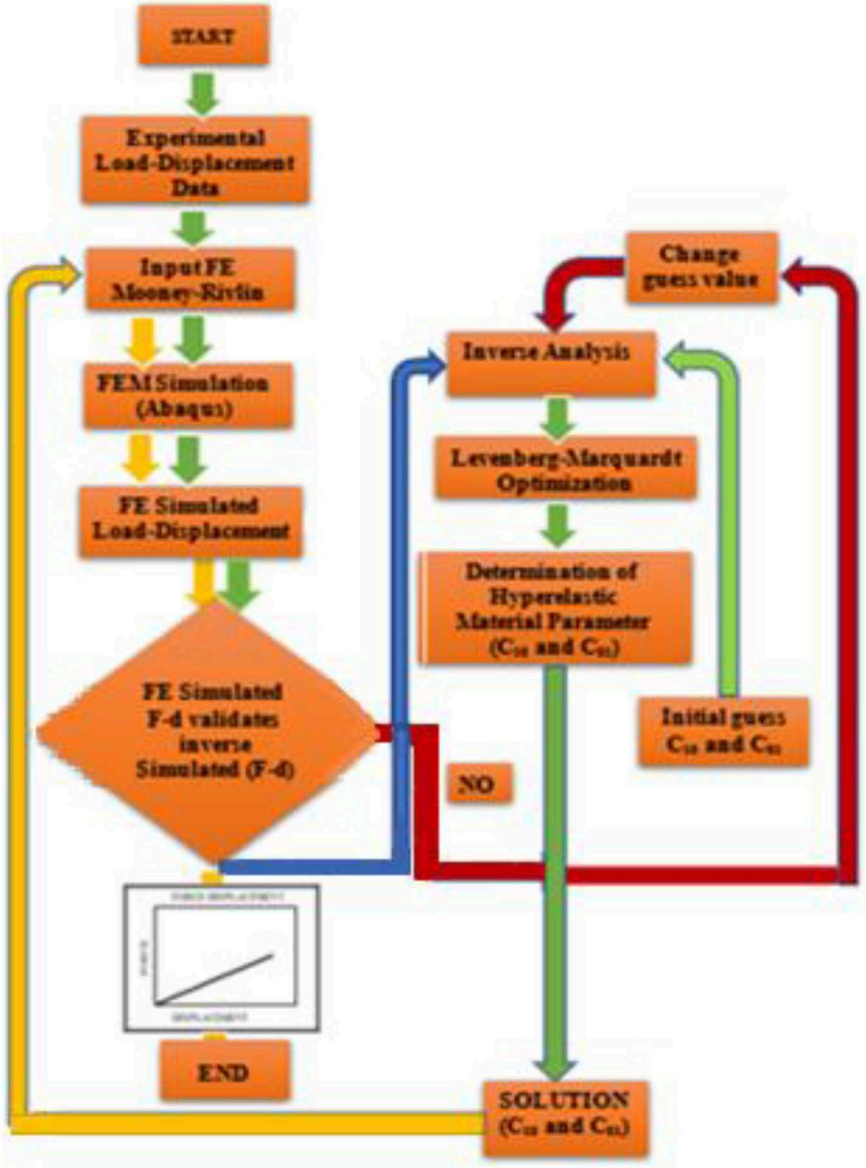

FIGURE 11
Flowchart of the inverse optimization process to characterize the unknown tissue hyperelastic parameters Mooney–Rivlin parameters.

After determining optimal material parameters, the sensitivity analysis of the solution was analyzed by adding noise (±1% and ±2%) to the iterative solutions. Based on Hadamard's [9] article, a solution to any inverse problem continuously depends on the stability of the data [28]. The sensitivity of the solution indicates that there was no external influence in the solution. This again proved the uniqueness of the solution.

The objective of the study was to characterize the nonlinear behavior of soft tissue phantom. The combination of the inverse method in conjunction with the FE method enables the identification of unknown material parameters. The LM optimization algorithm was used to optimize material properties by minimizing the sum of squared differences between the model-predicted and experimentally measured load–displacement data, which provided benchmarks for accurate Ogden parameters (μ, α). The accuracy, effectiveness, and robustness of such procedures were validated through FE-simulated data, which is cross-checked by the LM optimization technique and finally, compared with published results.

First, the simulated data were used as an input parameter for the MATLAB optimization algorithm. The robust optimization technique was performed as expected, which confirmed the uniqueness of the solution. Second, the Ogden parameters were plotted at various thicknesses. This proved that μ and α have a significant effect on specimen thickness. Moreover, μ and α were plotted against concentration and freeze–thaw cycles. The simulated result confirmed the dependency of μ and α on PVA concentration and freeze–thaw cycles. This means that the

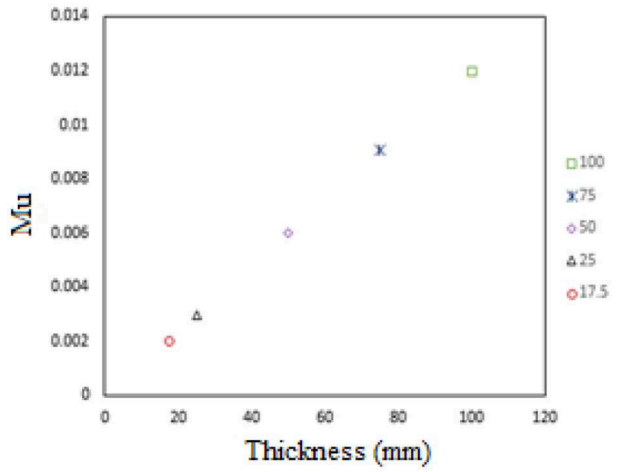

FIGURE 12
Graph of μ vs. various thicknesses for PVA-C 5%.

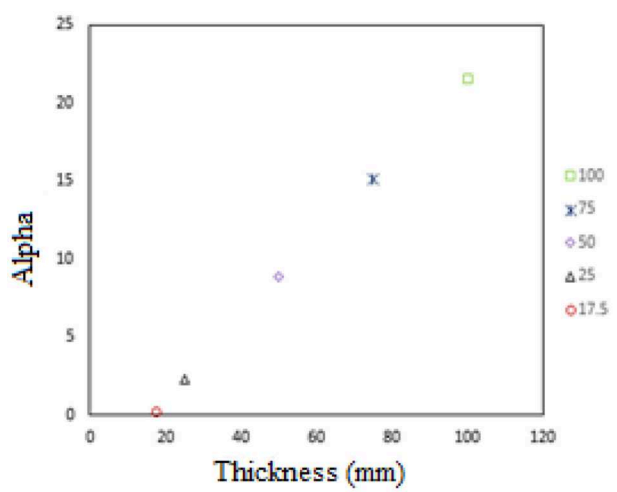

FIGURE 13
Graph of α vs. various thicknesses for PVA-C 5%.

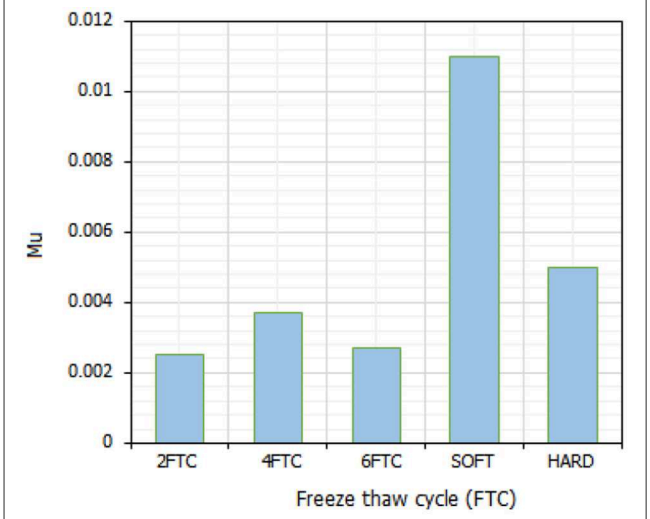

FIGURE 14
Graph of μ vs. various PVA-C concentrations.

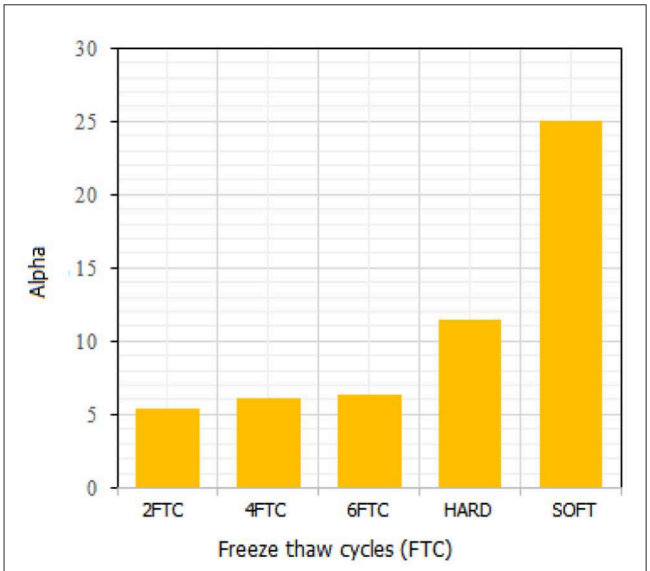

FIGURE 15
Graph of α vs. various PVA-C concentrations.

value of μ and α increases with the increase in concentration and freeze–thaw cycles with the little exception of PVA at higher concentrations.

R-squared values for 5% and 15% PVA-C, 2FTC were obtained through the parameter estimation techniques, and their fitness coefficients were 0.99999 and 0.9998, respectively. This led us to conclude that the optimization algorithm provided accurate results in the determination of the Ogden parameter. Finally, PVA-C 5% and PVA-C 15% have undergone a sensitivity test by adding $y \pm 2\%$ noise to the solution. No extraneous effect was observed. Thus, supporting the uniqueness of the solution. This robust technique will be proposed as a "gold standard" for future biomedical research.

Finally, some perspectives and future works of this study have been summarized in the **Conclusion** section.

3. Conclusion

A numerical study was conducted to characterize the nonlinear mechanical properties of PVA-C. A range of PVA-C phantom data was analyzed in the numerical study. The force–displacement data were recorded and used in FEA studies for experimental data validations and material characterizations.

1. The developed finite element model (FE) can be utilized to determine the distribution of resulting stresses of linear and nonlinear elastic thin-structured materials for a given load. Since this FE model incorporates an influence factor (IF), the stress

distribution could be computed up to 36% (with IF = 1, and IF = 0.637) more reliably.
2. Introduction of friction coefficient (Ω) in the developed analytical model provides up to 23% difference in magnitude of the functional parameter k used in different standard models such as Zhang's, Cao's, and Hayes' models. Thus, the proposed analytical solution can potentially provide an improved understanding of the indentation response of soft tissues.
3. The developed inverse algorithm is suitable to identify a few biomechanical properties (e.g., Ogden and Mooney–Rivlin parameters) for a new development of artificial materials (e.g., scaffolding, tissue generation, and phantoms for surgical training).
4. Overall, the finite element model, the analytical model, and the inverse algorithm developed in this study would provide an important tool in the design and characterization of soft tissue materials. In future research, this technique can be further explored to help develop patient-specific artificial organs, which can replace the need for human organ transplantations.

Data availability statement

The original contributions presented in the study are included in the article/Supplementary material, further inquiries can be directed to the corresponding author.

Author contributions

Conceptualization, methodology, and writing—original draft preparation: MM. Software and validation: MB. Writing—review and editing: MB and KI. All authors have read and agreed to the published version of the manuscript.

Acknowledgments

The authors would like to thank Rayyan Syed Kamal, Master of Science candidate in Interdisciplinary Medical Sciences at Western University, London ON, Canada, for taking the time to edit and consult the clarification of the concept mentioned in this manuscript. Kamal's knowledge of science communication proved to be an asset in this manuscript. The authors would also like to thank Maryium Mansur, Bachelor of Science in Nursing at Western University, London ON, Canada, for editing this manuscript.

Conflict of interest

The authors declare that the research was conducted in the absence of any commercial or financial relationships that could be construed as a potential conflict of interest.

Publisher's note

All claims expressed in this article are solely those of the authors and do not necessarily represent those of their affiliated organizations, or those of the publisher, the editors and the reviewers. Any product that may be evaluated in this article, or claim that may be made by its manufacturer, is not guaranteed or endorsed by the publisher.

Supplementary material

The Supplementary Material for this article can be found online at: https://www.frontiersin.org/articles/10.3389/fams.2023.1064130/full#supplementary-material

References

1. Costa KD, Yin FC. Analysis of indentation: implications for measuring mechanical properties with atomic force microscopy. *J Biomech Eng.* (1999) 121:462–71.

2. Di Silvestro MR, Suh JKF. A cross-validation of the biphasic poro-viscoelastic model of articular cartilage in unconfined compression, indentation, and confined compression. *J Biomech.* (2001) 34:519–25. doi: 10.1016/S0021-9290(00)00224-4

3. Rivlin RS, Saunders DW. Large elastic deformations of isotropic materials. VII. Experiments on the deformation of rubber. *Philos Trans R Soc Lond Ser A Math Phys Sci.* (1951) 243:251–88.

4. Cox MA, Driessen NJ, Boerboom RA, Bouten CVC, Baaijens FPT. Mechanical characterization of anisotropic planar biological soft tissues using finite indentation: experimental feasibility. *J Biomech.* (2008) 41:422–9. doi: 10.1016/j.jbiomech.2007.08.006

5. Samani A, Plewes D, A. method to measure the hyperelastic parameters of *ex vivo* breast tissue samples. *Phys Med Biol.* (2004) 49:4395–405. doi: 10.1088/0031-9155/49/18/014

6. Isvilanonda V, Iaquinto JM, Pai S, Mackenzie-Helnwein P, Ledoux WR. Hyperelastic compressive mechanical properties of the subcalcaneal soft tissue: an inverse finite element analysis. *J Biomech.* (2016) 49:1186–91. doi: 10.1016/j.jbiomech.2016.03.003

7. Bentout S, Chekroun A, Kuniya T. Parameter estimation and prediction for coronavirus disease outbreak 2019 (COVID-19) in Algeria. *AIMS Public Health.* (2020) 7:306. doi: 10.3934/publichealth.2020026

8. Sheldon MR, Fillyaw MJ, Thompson WD. The use and interpretation of the Friedman test in the analysis of ordinal-scale data in repeated measures designs. *Physiother Res Int.* (1996) 1:221–8.

9. Hadamard J. Lectures on Cauchy's problem in linear partial differential equations. *Physiology.* (1923) 14:334.

10. Fellay LS, Fasce LA, Czerner M, Pardo E, Frontini PM. On the feasibility of identifying first order ogden constitutive parameters of gelatin gels from flat punch indentation tests. *Soft Mater.* (2015) 13:188–200. doi: 10.1080/1539445X.2015.1059346

11. Ogden RW. Volume changes associated with the deformation of rubber-like solids. *J Mech Phys Solids.* (1976) 24:323–38.

12. Kauer M, Vuskovic V, Dual J, Szekely G, Bajka M. Inverse finite element characterization of soft tissues. *Med Image Anal.* (2002) 6:275–87. doi: 10.1016/S1361-8415(02)00085-3

13. Narayanan B, Olender ML, Marlevi D. An inverse method for mechanical characterization of heterogeneous diseased arteries using intravascular imaging. *Sci Rep.* (2021) 11:22540. doi: 10.1038/s41598-021-01874-3

14. Djilali S, Bentout S, Kumar S, Touaoula TM. Approximating the asymptomatic infectious cases of the COVID-19 disease in Algeria and India using a mathematical model. *Int J Model Simul Sci Comput.* (2022) 13:2250028. doi: 10.1142/S1793962322500283

15. Fereidoonnezhad B, Naghdabadi R, Arghavani J. A hyperelastic constitutive model for fiber-reinforcedrubber-like materials. *Int J Eng Sci.* (2013) 71:36–44. doi: 10.1016/j.ijengsci.2013.06.001

16. Lin YY, Hu BW. Load relaxation of a flat rigid circular indenter on a gel half space. *J Non-Cryst Solids.* (2006) 352:4034–40. doi: 10.1016/j.jnoncrysol.2006.07.007

17. Valero C, Navarro B, Navajas D, García-Aznar JM. Finite element simulation for the mechanical characterization of soft biological materials

by atomic force microscopy. *J Mech Behav Biomed Mater.* (2016) 62:222–35. doi: 10.1016/j.jmbbm.2016.05.006

18. Li WH, Zhang XZ. The effect of friction on magnetorheological fluids. *Korea Aust Rheol J.* (2008) 20:45–50. Available online at: https://ro.uow.edu.au/engpapers/3910

19. Ali A, Hosseini M, Sahari BB. A review of constitutive models for rubber-like materials. *Am J Eng Appl Sci.* (2010) 3:232–9. doi: 10.3844/ajeassp.2010.232.239

20. Myers A, Chen P, Albert YL, Seki Y. Biological materials: structure and mechanical properties. *Prog Mater Sci.* (2008) 53:1–206. doi: 10.1016/j.pmatsci.2007.05.002

21. Holzapfel GA. Biomechanics of soft tissue. *Handbook Mater Behav.* (2000) 7:1–15. Available online at: https://biomechanics.stanford.edu/me338/me338_project02.pdf

22. Hirabayashi S, Iwamoto M. Finite element analysis of biological soft tissue surrounded by a deformable membrane that controls transmembrane flow. *Theor Biol Med Model.* (2018) 15:21. doi: 10.1186/s12976-018-0094-9

23. Zakeri M. *Assessment of the Non-linear Stress–strain Characteristics of Poly(vinyl alcohol) Cryogel*. Ontario: The University of Western Ontario (2017).

24. Kyriacou SK, Shah AD, Humphrey JD. Inverse finite element characterization of nonlinear hyperelastic membranes. *ASME J Appl Mech.* (1997) 64:257–62.

25. Soufiane B, Touaoula TM. Global analysis of an infection age model with a class of nonlinear incidence rates. *J Math Anal Appl.* (2016) 434:1211–39. doi: 10.1016/j.jmaa.2015.09.066

26. Gamonpilas C, Charalambides MN, Williams JG, Dooling PJ, Gibbon SR. Predicting the mechanical behavior of starch gels through inverse analysis of indentation data. *Appl Rheol.* (2010) 20:1–9. doi: 10.3933/ApplRheol-20-33283

27. Bentout S, Tridane A, Djilali S, Touaoula TM. Age-structured modeling of COVID-19 epidemic in the USA, UAE and Algeria. *Alexand Eng J.* (2021) 60:401–11. doi: 10.1016/j.aej.2020.08.053

28. Munera EM. *Characterization of Brain Tissue Phantom Musinganindentation Device and Inverse Finite Element Parameter Estimation Algorithm* (2011). p. 99.

frontiers | Frontiers in Applied Mathematics and Statistics

TYPE Original Research
PUBLISHED 26 April 2023
DOI 10.3389/fams.2023.1094971

OPEN ACCESS

EDITED BY
Bapan Ghosh,
Indian Institute of Technology Indore, India

REVIEWED BY
Mohd Hafiz Mohd,
University of Science Malaysia (USM), Malaysia
Anuj Kumar,
Thapar Institute of Engineering & Technology, India

*CORRESPONDENCE
Dipo Aldila
✉ aldiladipo@sci.ui.ac.id

RECEIVED 10 November 2022
ACCEPTED 29 March 2023
PUBLISHED 26 April 2023

CITATION
Aldila D, Aulia Puspadani C and Rusin R (2023) Mathematical analysis of the impact of community ignorance on the population dynamics of dengue.
Front. Appl. Math. Stat. 9:1094971.
doi: 10.3389/fams.2023.1094971

Mathematical analysis of the impact of community ignorance on the population dynamics of dengue

Dipo Aldila*, Chita Aulia Puspadani and Rahmi Rusin

Department of Mathematics, Faculty of Mathematics and Natural Sciences, Universitas Indonesia, Depok, Indonesia

This study proposes a dengue spread model that considers the nonlinear transmission rate to address the level of human ignorance of dengue in their environment. The $SIR - UV$ model has been proposed, where SIR denotes the classification of the human population and UV denotes the classification of the mosquito population. Assuming that the total human population is constant, and the mosquito population is already in its steady-state condition, using the *Quasi-Steady State Approximation* (QSSA) method, we reduce our $SIR - UV$ model into a more simple IR-model. Our analytical result shows that a stable disease-free equilibrium exists when the basic reproduction number is <1. Furthermore, our model also shows the possibility of a backward bifurcation. The more ignorant the society is about dengue, the higher the possibility that backward bifurcation phenomena may appear. As a result, the condition of the basic reproduction number being <1 is insufficient to guarantee the extinction of dengue in a population. Furthermore, we found that increasing the recovery rate, reducing the waning immunity rate, and mosquito life expectancy can reduce the possibility of backward bifurcation phenomena. We use dengue incidence data from Jakarta to calibrate the parameters in our model. Through the fast Fourier transform analysis, it was found that dengue incidence in Jakarta has a periodicity of 52.4, 73.4, and 146.8 weeks. This result indicates that dengue will periodically appear at least every year in Jakarta. Parameter estimation for our model parameters was carried out by assuming the infection rate of humans as a sinusoidal function by determining the three most dominant frequencies. Numerical and sensitivity analyses were conducted to observe the impact of community ignorance on dengue endemicity. From the sensitivity analysis, we found that, although a larger community ignorance can trigger a backward bifurcation, this threshold can be minimized by increasing the recovery rate, prolonging the temporal immunity, or reducing the mosquito population. Therefore, to control dengue transmission more effectively, media campaigns undertaken by the government to reduce community ignorance should be accompanied by other interventions, such as a good treatment in the hospital or vector control programs. With this combination of interventions, it will be easier to achieve a condition of dengue-free population when the basic reproduction number is less than one.

KEYWORDS

dengue, community ignorance, quasi-steady state approximation, basic reproduction number, fast Fourier transform

1. Introduction

Dengue is an infectious disease that is caused by the dengue virus (DEN virus or DENV). This virus is transmitted through the bite of an infected female *Aedes aegypti* or *Aedes albopictus* [1, 2]. It is estimated that ∼50% of the world population is at risk of dengue every year [3]. Dengue has been the subject of main concern in many tropical and subtropical countries, including Indonesia. Since the first case of dengue in Indonesia was reported in Jakarta and Surabaya way back in 1968, the incidence of dengue in Indonesia continues to spread to this day [4]. Based on a new report from the Ministry of Health Indonesia, from early 2022 until 20 February 2022, the cumulative number of dengue cases was recorded as 13,776 cases. Meanwhile, the number of deaths due to dengue was recorded as 145 cases [5].

There are four different serotypes of DENV, namely, DENV-1, DENV-2, DENV-3, and DENV-4 [6, 7]. In many cases, the primary infection of dengue is often asymptomatic. In contrast, the secondary infection with different serotypes from the primary infection may develop more severe symptoms, such as bone pain and headache, up to more occasionally fatal symptoms [8, 9]. Individuals who have already recovered from the primary infection will maintain a lifelong immunity to the first DENV that had caused the primary infection, but only temporal to the other three serotypes [10]. When the short-term immunity to other serotypes wanes, the recovered individuals may acquire a secondary infection that can be even more severe than the primary infection. This phenomenon is called the ADE process [11, 12].

There is no specific treatment to cure dengue-infected individuals of the disease. The main action plan to treat dengue-infected individuals is rendered feasible by giving them supportive care, or if the case is severe, then the patient requires hospitalization which becomes an obligation to be done. Recently, several candidates for dengue vaccines have been in the process of development [13, 14]. An affordable and effective dengue vaccine will give importance to the control of dengue spread around the world. The main control program adopted by many governments worldwide to control the spread of dengue is the vector control program and steps are taken to reduce the probability of a successful infection through a mosquito repellent. Another option to prevent the spread of dengue (and other diseases) is by developing community awareness on the danger of the disease [15–18]. Community participation in eliminating or at least suppressing the spread of dengue can be done through several activities, such as through media campaigns to disseminate knowledge about how to prevent acquiring infection from mosquitoes from individual levels up to community levels. The author in [15] implies that the risk of dengue may be increased when there is a lack of community awareness due to misunderstanding between the community and the government. Therefore, maintaining community awareness by reducing the ignorance of dengue is essential to guarantee intervention success in controlling the spread of dengue.

Mathematical models have been used widely by researchers to understand how vector-borne diseases spread among the population [19–23]. For the dengue transmission model, many authors have used mathematical modeling to guide public health strategies to control the spread of dengue. The mathematical modeling process is very challenging due to the complexity of the dengue transmission mechanism. A more complex model may bring in a more realistic modeling, but finding the analytical results and conclusion often entails difficulty. Hence, the researcher needs to develop a realistic but simple model with realistic assumptions. The use of real incidence data is also needed to calibrate the performance of the model. There are many approaches that can be used to construct the dengue transmission model, such as with ordinary differential equations [24, 25], partial differential equations [26, 27], fractional-order differential equations [28, 29], stochastic differential equations [30–32], and other approaches.

Many mathematical models for dengue transmission use a deterministic approach. Although the transmission process of dengue involves a vector animal (*Aedes* mosquito) as the prime spreader, some authors use a host-to-host modeling approach [30, 33, 34]. This approach does not involve the dynamics of mosquitoes in their model since it can be argued that the mosquitoes' life expectancy is very short compared to the human life expectancy. Hence, the dynamic of mosquitoes is much faster compared to that of the human. The authors in [35] find that the only essential dynamics are coming from the human population, and mosquito dynamics only slightly perturb them. The other approach is adopted by considering the dynamic of mosquitoes [24, 25]. With this approach, the mosquito population is explicitly involved in the model. With the involvement of mosquito dynamics, such implementation of vector control can be modeled into the equation. When the vector control is involved in the model, an optimal control approach can be used to understand the short-term impact of the intervention and determine the most effective strategy [36–38]. Modeling dengue transmission is not only for the macro scale (population scale). Some of the authors also construct the model to understand the dynamic within the host [39, 40]. This modeling is conducted to understand the interaction between the free virus with susceptible targeted cells. Some interesting factors are involved in this modeling approach, such as the infectivity of the virus and immune response.

From the aspect of the impact of community awareness on the dengue transmission model, there are some models which have been introduced by authors. The authors in [41] introduced a mathematical model of dengue where the effect of media awareness was included. Mathematical analysis on the equilibrium points and the basic reproduction number was included in it. The author in [42] introduced a multistrain dengue model that combined mosquito control programs and human awareness. They found that the control of a large number of mosquitoes and human awareness was required to control dengue effectively. The author introduced an optimal control problem of dengue with human awareness and vector control in [43]. The authors used Pontryagin's maximum principle to characterize the necessary conditions for the optimal control problem. The author in [44] introduced a modified host–vector model by considering low- and high-risk susceptible populations. The author analyzed global stability on all equilibrium points. The author in [45] introduced an optimal control model of dengue transmission. The author developed the

model by considering five control variables: information spread, bed nets, treatment, screening, and insecticide. The impact of a media campaign that can reduce the rate of infection was developed by the author in [24]. The author conducted a cost-effectiveness analysis to understand the most cost-effective strategy that can be employed to control dengue transmission. Recently, the authors in [25] combined vaccination, vector control, and media campaign in their model where the seasonality was accommodated. All the mentioned references consider the same assumption that (1) aware individuals have a smaller probability of being infected due to their awareness and (2) more prominent infected individuals will reduce the infection rate more. The second assumption is reasonable when we wish to model the spread of dengue among a population where awareness of dengue could increase the participation of the population in the dengue control programs.

To calibrate the proposed dengue model, many authors use incidence data to estimate their parameters. The idea behind this development is to find the best-fit parameters, such that the model simulation output can fit the time series of the data. Please see the following references for the use of incidence data in their dengue research: Aguiar and Stollenwerk [30], ten Bosch et al. [31], Aguiar et al. [34], and Aldila et al. [46]. With this parameter estimation, the researcher can make a short time prediction on their model. Some interventions can be included in their model and the possible outcomes predicted in the near future.

Motivated by the above discussion, no authors had discussed the impact of community ignorance on the spread of dengue. In this circumstance, more infected individuals will increase the probability of infection in the human and mosquito populations. In some countries where dengue fever continues to emerge throughout the year, the level of public ignorance of the spread of dengue fever is no longer as high as for several newly discovered diseases and it is quite a concern, such as Zika in 2018 or COVID-19 in the late 2019. Hence, it is important to consider the community's ignorance of our proposed model. Based on this background, here in this article, we introduce our SIR-UV mathematical model to describe the spread of dengue under the impact of community ignorance. The Quasi-Steady State Approximation method was used to simplify the model. We used the weekly incidence data of dengue from Jakarta during the period from January 2008 to December 2021 to estimate the parameter values in our model. We used the fast Fourier transform to extract the most significant frequency from our data. With this dominant frequency, we fit our model output with the data by assuming the infection rate as a sinusoidal function that depends on time. Some mathematical and numerical analyses were conducted to understand the qualitative behavior of our model and how it was related to the basic reproduction number. Furthermore, we also analyzed how community ignorance can trigger the appearance of a backward bifurcation, which can cause dengue to exist, even though the basic reproduction number is already <1. The layout of this article is as follows: In Section 2, we construct our model. In the same section, we perform our data assimilation to find out the best-fit parameters of our model. The model analysis is given in Section 3, which is followed by some sensitivity analyses and numerical experiments in Section 4. The concluding remarks are given in Section 5.

2. Mathematical model and data assimilation

2.1. Model formulation

To develop our dengue transmission model, we introduce N and M as the total human and female *Aedes* sp. populations. Let the total human population be classified into Susceptible, Infected, and Recovered compartments, which are denoted by S, I, and R, respectively. On the other hand, the mosquito population is only classified into Susceptible and Infected compartments, which are denoted by U and V, respectively. Due to the short life expectancy of mosquitoes, we do not consider the recovery process in the mosquito population. Since dengue does not transmit vertically to newborns, we assume that the recruitment rates of a human and mosquitoes are going to be susceptible. The rates of a newborn human and mosquitoes are given by Λ_h and Λ_v, respectively. Susceptible humans can get infected by dengue only if infected mosquitoes bite them. In many countries where dengue become can be found all-year round, for instance in Indonesia, public awareness of dengue fever is not as high as that of new disease incidents such as COVID-19. Cases of dengue fever only received attention when the cases were already very high and made the hospital unable to accommodate the increasing number of patients. Due to these phenomena, the authors feel that it is important to discuss the factors of public neglect of news on dengue fever. Based on this assumption, we notice that the infection rate will increase when the number of infected individuals increases. Therefore, the incidence of infection will occur at a much faster pace compared to the standard mass action infection function ($\beta_h SV$), where β_h is the infection rate in the human population. Hence, we assume that the infection rate is nonlinear and depends on the number of infected individuals. In this case, we choose $\beta_h(I) = \beta_h(1+\alpha I)$, where $\alpha > 0$ represents the incidence increasing factor due to community ignorance against dengue. For a further discussion on this type of function, please see [47]. Based on this assumption, we have $\beta_h(1+\alpha I)SV$ as the total number of new infections of susceptible individuals due to contact with infected mosquitoes with a probability of infection β_h. Based on similar arguments, we derived that the rate of new infected mosquitoes is given by $\beta_v(1+\alpha I)UI$, where β_v is the infection rate of dengue in the mosquito population. Let γ be the recovery rate, δ the waning rate of temporal immunity, μ_h the natural death rate of a human, and μ_v the natural death rate of mosquitoes, we have the dynamic of dengue transmission under a nonlinear infection rate as given in system (1).

$$\begin{aligned}
\frac{dS}{dt} &= \Lambda_h - \beta_h(1+\alpha I)SV + \delta R - \mu_h S,\\
\frac{dI}{dt} &= \beta_h(1+\alpha I)SV - \gamma I - \mu_h I,\\
\frac{dR}{dt} &= \gamma I - \delta R - \mu_h R.\\
\frac{dU}{dt} &= \Lambda_v - \beta_v(1+\alpha I)UI - \mu_v U,\\
\frac{dV}{dt} &= \beta_v(1+\alpha I)UI - \mu_v V,
\end{aligned} \tag{1}$$

with an initial condition $S(0) > 0, I(0) \geq 0, R(0) \geq 0, U(0) > 0, V(0) \geq 0$. Our model is well defined both mathematically and biologically. Please see Theorem 1 for the non-negative solution property of each variable of system (1) and the feasible region of the solution in Theorem 2.

THEOREM 1. Model (1) with initial condition $S(0) > 0, I(0) \geq 0, R(0) \geq 0, U(0) > 0, V(0) \geq 0$ always has a non-negative solution for all times $t \geq 0$.

PROOF. We use an integrating factor to solve this theorem. Under the given initial conditions, from $\frac{dS}{dt}$ in system (1), we have

$$\frac{dS}{dt} = \Lambda_h - \beta_h(1+\alpha I)SV + \delta R - \mu_h S.$$

It can be written as

$$\frac{dS}{dt} + A(t)S = B(t) \tag{2}$$

where

$$A(t) = \beta_h(1+\alpha I)V + \mu_h,$$
$$B(t) = \Lambda_h + \delta R,$$

Define an integrating factor $C(t) = e^{\int_0^T A(t)dt}$ and multiply (2) with the integrating factor. Hence, we have

$$e^{\int_0^T A(t)dt}\frac{dS}{dt} + e^{\int_0^T A(t)dt}A(t)S = e^{\int_0^T A(t)dt}B(t).$$

It can be written as

$$D_t[S(t)e^{\int_0^T A(t)dt}] = e^{\int_0^T A(t)dt}B(t).$$

By integrating both sides of the above equation, we obtain

$$\int_0^T D_t[S(t)e^{\int_0^T A(t)dt}]dt = \int_0^T e^{\int_0^T A(t)dt}B(t)dt.$$

Therefore,

$$S(T) = e^{-\int_0^T A(t)dt}\left(\int_0^T e^{\int_0^T A(t)dt}B(t)dt + S_0\right) > 0.$$

In a similar way, it can be shown that $I(t) \geq 0, R(t) \geq 0, U(t) > 0$, and $V(0) \geq 0$, under the given initial condition $I_0 \geq 0, R_0 \geq 0, U_0 > 0$, and $V_0 \geq 0$. Thus, the solutions of $S(t), I(t), R(t), U(t)$, and $V(t)$ are non-negative for all times $t > 0$.t

THEOREM 2. Model (1) with initial condition $S(0) > 0, I(0) \geq 0, R(0) \geq 0, U(0) > 0, V(0) \geq 0$ is bounded in the region

$$\Omega = \left\{(S,I,R,U,V) \in \mathbb{R}_5^+ \cup \mathbf{0}_5 : N = S+I+R = \frac{\Lambda_h}{\mu_h}, M = U+V = \frac{\Lambda_v}{\mu_v}\right\}. \tag{3}$$

PROOF. From model (1), we obtain

$$\frac{dN}{dt} = \Lambda_h - \mu_h N.$$
$$\frac{dM}{dt} = \Lambda_v - \mu_v.$$

We assume that the total population of human and mosquito is constant, so we obtain the system bounded in $N = \frac{\Lambda_h}{\mu_h}$ and $M = \frac{\Lambda_v}{\mu_v}$. Hence, all feasible solutions of model (1) enter the region

$$\Omega = \left\{(S,I,R,U,V) \in \mathbb{R}_5^+ \cup \mathbf{0}_5 : N = S+I+R = \frac{\Lambda_h}{\mu_h}, M = U+V = \frac{\Lambda_v}{\mu_v}\right\}.$$

2.2. A quasi-steady state approximation

It is approximated that the life expectation of a mosquito is 30 days [48]. Considering human life expectation, which is around 70 years [49], a mosquito population can reach its equilibrium in a much shorter duration compared to a human population. It indicates that the mosquito population has a fast dynamics, while the human population has a slow dynamics. Based on this assumption, we may assume that the mosquito populations have already reached their equilibrium condition in our simulation time interval. Hence, using the quasi-steady state approximation, taking $\frac{dU}{dt} = 0$ and $\frac{dV}{dt} = 0$, gives us

$$U^* = \frac{\Lambda_v}{\beta_v(1+\alpha I)I + \mu_v},$$
$$V^* = \frac{\beta_v(1+\alpha I)\Lambda_v}{(\beta_v(1+\alpha I)I + \mu_v)\mu_v}.$$

Substituting the above quasi-steady state approximation of (U^*, V^*) in model (1), we have

$$\begin{aligned}\frac{dS}{dt} &= \Lambda_h - \beta_h(1+\alpha I) + \delta R - \mu_h S,\\ \frac{dI}{dt} &= \frac{\beta_h(1+\alpha I)^2 S I \beta_v \Lambda_v}{((1+\alpha I)I\beta_v + \mu_v)\mu_v} - (\gamma + \mu_h)I,\\ \frac{dR}{dt} &= \gamma I - \delta R - \mu_h R.\end{aligned} \tag{4}$$

Assuming that the total human population is constant. Then, we have $S = N - I - R$. Hence, the system (4) now reads as

$$\begin{aligned}\frac{dI}{dt} &= \frac{\beta_h(1+\alpha I)^2(N-I-R)IM}{((1+\alpha I)I + \kappa_v)} - (\gamma + \mu_h)I,\\ \frac{dR}{dt} &= \gamma I - \delta R - \mu_h R.\end{aligned} \tag{5}$$

where $\kappa_v = \frac{\mu_v}{\beta_v}$ and $M = \frac{\Lambda_v}{\mu_v}$. The simple IR -model in system (5) has an advantage compared to the original $SIRUV$ -model in system (1) from the perspective of data assimilation, which will be described in the next section. Furthermore, we will analyze the IR -model in system (5) to understand the long time behavior of the $SIRUV$-model.

2.3. Data assimilation

Jakarta is the capital of Indonesia with a total population of more than 10 million people based on the census data of 2022. The temperature in Jakarta is relatively stable throughout the year, between 24 and 33°C. The highest temperatures are recorded between August and early November. The rainy season in Jakarta falls between October and May every year with more than a 47% chance of a rainy day. The highest rainfall occurs in January with the average rainfall of 22.6 days [50].

Dengue fever has become an annual problem in Indonesia, including Jakarta. The number of dengue fever cases in Jakarta during 2008 to December 2021 can be seen in Figure 1A. High cases of dengue fever are always associated with a high rainfall in Jakarta. The existing literature indicates that the high cases of dengue fever follow a seasonal (periodic) pattern. Based on this observation, it is necessary to analyze the existence of periodicity in the data of dengue fever cases in Jakarta city. Therefore, we apply a fast Fourier transform to our data, and the result can be seen in Figure 1B. From Figure 1B, we show that the three dominant frequencies are 0.019,

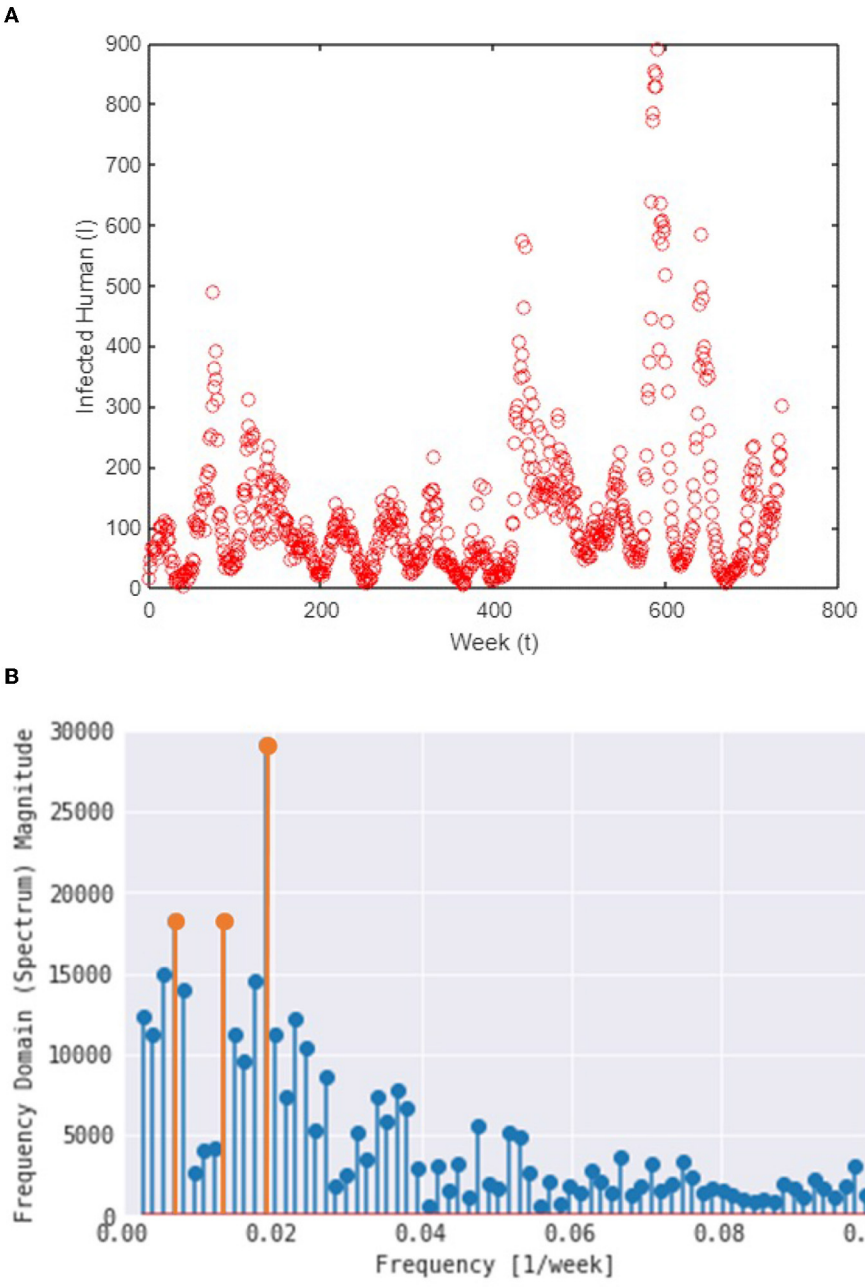

FIGURE 1
(A) The number of weekly infected dengue individuals in Jakarta from January 2008 to December 2021. **(B)** The result of fast Fourier transform analysis from dengue data in Jakarta.

0.013, and 0.006. These frequencies are correlated to a periodicity of 52.43, 73.4, and 146.8 weeks, respectively.

Our aim in this section is to calibrate our proposed mathematical models with the real situation in the field. To do this, we construct a model fitting that involves parameter estimation, which includes the identification of the parameter values that can fit between the model solution [variable I in system (5)] with the incidence data in Figure 1A. For the purpose of parameter estimation, we used the "fmincon" toolbox in Matlab. Fmincon can be used to find the minimum of constrained nonlinear multivariable functions.

As we mentioned earlier, our incidence data indicate a periodic solution. To capture this phenomenon, we treat the infection rate β_h as a sinusoidal parameter, which is given by

$$\beta_h(t) = a + \sum_{i=1}^{3} b_i \cos(2\pi d_i t) + c_i \sin(2\pi d_i t), \tag{6}$$

where a is the median value of $\beta_h(t)$, b_i, and c_i are the amplitudes of $\beta_h(t)$, while d_i refers to the frequencies of $\beta_h(t)$. Our problem lies in minimizing the Euclidean distance between our model solution $[I(t)]$ and the time series data in Figure 1A using the best-fit parameter $\beta_h(t)$ with model in (5) as the constraint. This task reads as minimizing the following cost function

$$\mathcal{J} = \frac{1}{2\omega} \sum_{t=1}^{734} (I^{\text{solution}} - I^{\text{data}})^2, \tag{7}$$

where ω is the variance of the data and I^{solution} is the solution of $I(t)$ from

$$\begin{aligned} \frac{dI}{dt} &= \frac{\left(a + \sum_{i=1}^{3} b_i \cos(2\pi d_i t) + c_i \sin(2\pi d_i t)\right)(1+\alpha I)^2 (N - I - R) IM}{((1+\alpha I) I + \kappa_v)} \\ &\quad - (\gamma + \mu_h) I, \\ \frac{dR}{dt} &= \gamma I - \delta R - \mu_h R. \end{aligned} \tag{8}$$

Our task is to find the best-fit parameter $\Gamma_1 = \{a, b_i, c_i, d_i, \alpha, \kappa_v\}$ and the best initial condition $\Gamma_2 = \{I(t=0), R(t=0)\}$. We choose other parameter values as follows:

$$N = 10\,000\,000 [51], \quad M = 2N \text{ (assumption)}, \quad \gamma = \frac{1}{4} [52],$$

$$\mu_h = \frac{1}{70 \times 52} [49], \quad \delta = \frac{1}{9 \times 4} [52].$$

The result of the parameter estimation is given in Figure 2, while the parameter values and the initial condition are given in Table 1. We can see that our model can fit the qualitative behavior of the data such as the time when the outbreak appears and also when it decreases. However, our model cannot fit the data in all simulation times. We extend our simulation time for the next 2 years until December 2023. We can see that the peak of dengue cases in Jakarta is expected to still appear around April 2022 and March 2023.

3. Model analysis

3.1. Equilibrium points and the basic reproduction number

The dengue-free equilibrium of system (5) is given by

$$(I, R) = (0, 0). \tag{9}$$

In this case, since $S = N - I - R$, then the complete model gives the dengue-free equilibrium as given by $(S, I, R) = (N, 0, 0)$. Next, we calculate the respected basic reproduction number of system (5). The basic reproduction number ($\mathcal{R}_0$) in the context of dengue is the expected number of secondary cases (in human/mosquitoes) due to one bite of infected/susceptible mosquito to susceptible/infected human, respectively, during its infection period in a fully susceptible population. To calculate the respected basic reproduction number of system (5), we use the next-generation matrix approach introduced by the authors in [53]. First, we calculate the Jacobian matrix of the infected subcompartment of system (5) evaluated in the dengue-free equilibrium in (9). This matrix is given by:

$$\mathcal{J} = \left[\frac{\beta_h NM}{\kappa_v} - \gamma - \mu_h \right].$$

Next, we can decompose $\mathcal{J}$ as $\mathcal{F} + \mathcal{V}$, where $\mathcal{F}$ is the transmission matrix and $\mathcal{V}$ is the transition matrix. Hence, we have $\mathcal{F} = \left[\frac{\beta_h NM}{\kappa_v}\right]$ and $\mathcal{V} = [-\gamma - \mu_h$. Therefore, the next-generation matrix of system (5) is given by:

$$\mathcal{K} = \mathcal{F}\mathcal{V}^{-1} = \left[\frac{\beta_h NM}{\kappa_v(\gamma + \mu_h)} \right].$$

Therefore, the basic reproduction number of system (5), which is taken by the spectral radius of $\mathcal{K}$, is given by:

$$\mathcal{R}_0 = \frac{\beta_h NM}{\kappa_v(\gamma + \mu_h)}. \tag{10}$$

In many epidemiological models [], many authors can find the relation between the disease extinction with a condition of $\mathcal{R}_0 > 1$. In our proposed dengue model, we find this relation in the following theorem.

THEOREM 3. *The dengue-free equilibrium of system (5) is locally asymptotically stable if $\mathcal{R}_0 < 1$, and unstable if $\mathcal{R}_0 > 1$.*

PROOF. We use standard linearization to prove the theorem. Linearization around the dengue-free equilibrium is given by

$$\mathbf{J}|_{DFE} = \begin{bmatrix} \frac{\beta_h NM}{\kappa_v} - \gamma - \mu_h & 0 \\ \gamma & -\delta - \mu_h \end{bmatrix}.$$

Eigenvalues of the above linearization matrix are given by

$$\lambda_1 = \frac{\beta_h NM}{\kappa_v} - \gamma - \mu_h, \qquad \lambda_2 = -\delta - \mu_h.$$

Equilibrium is asymptotically stable if all the real parts of its eigenvalues are negative. All of our parameters are positive,

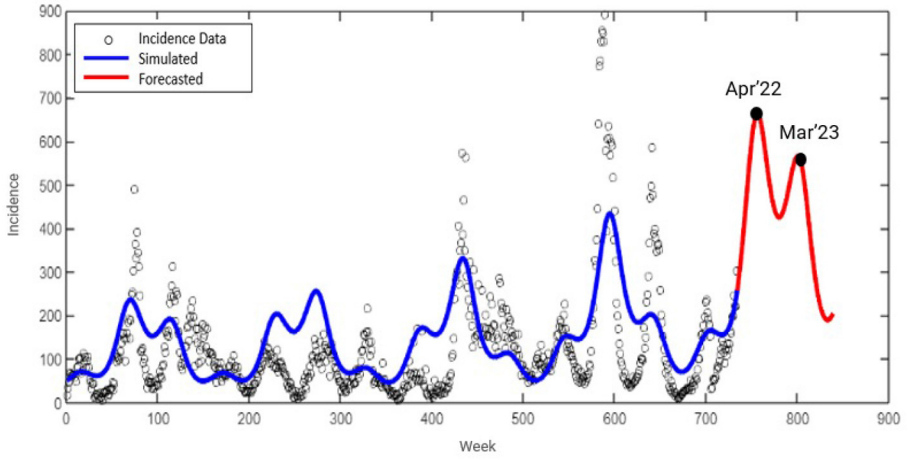

FIGURE 2
Fitted dengue cases $I(t)$, for the model (8), using data from Jakarta from 2008 to 2021.

therefore the second eigenvalue has negative real parts. To prove that the first eigenvalue has a negative real part, it must be assumed that $\frac{\beta_h NM}{\kappa_v(\gamma+\mu_h)} < 1 \iff \mathcal{R}_0 < 1$. □

The second equilibrium point is the endemic equilibrium point, which is given by:

$$(I, R) = \left(I^*, \frac{\gamma I}{\delta + \mu_h}\right). \tag{11}$$

where I^* is taken from the positive roots of the following third-degree polynomial

$$F(I, \tau) = a_3 I^3 + a_2 I^2 + a_1 I + a_0 = 0, \tag{12}$$

where $\tau = \{\beta_h, M, N, \alpha, \gamma, \delta, \kappa_v, \mu_h\}$, and

$$\begin{aligned}
a_3 &= \beta_h M\alpha^2(\gamma + \mu_h + \delta),\\
a_2 &= M\beta_h\left(N\alpha(\delta+\mu_h) - 2(\delta+\gamma+\mu_h)\right) - (\delta+\mu_h)(\gamma+\mu_h),\\
a_1 &= (M\beta_h + \mu_h)(\delta+\gamma+\mu_h) + \delta\gamma - MN\alpha\beta_h(\delta+\mu_h),\\
a_0 &= -(\delta+\mu_h)(\gamma+\mu_h)\kappa_v(\mathcal{R}_0 - 1).
\end{aligned}$$

Since $a_0 < 0 \iff \mathcal{R}_0 > 1$ and $a_3 > 0$, then we have the following theorem.

THEOREM 4. The dengue IR-model in system (5) always has at least one dengue-endemic equilibrium point if $\mathcal{R}_0 > 1$.

PROOF. Since $a_3 > 0$, then $\lim_{I\to-\infty} F(I,\tau) = -\infty$ and $\lim_{I\to\infty} F(I,\tau) = \infty$. For special cases when $\mathcal{R}_0 = 1$, we have one zero root of $F(I,\tau)$. Hence, when $a_0 < 0$ which is equivalent to $\mathcal{R}_0 > 1$, then the graphic of $F(I,\tau)$ will be shifted downward as far as a_0 is concerned. Hence, we have at least one new positive root I of $F(I,\tau)$ when $\mathcal{R}_0 > 1$. □

Since the sign of a_1 is not always positive or negative, it is possible to have another dengue endemic equilibrium when $\mathcal{R}_0 < 1$. Furthermore, since the existence of the dengue-endemic equilibrium point depends on a third-degree polynomial, it is possible to have more than one dengue-endemic equilibrium point.

TABLE 1 Best-fit parameter of system (8) for Figure 2.

Parameter	Value	Parameter	Value
a	1.3965×10^{-8}	α	5.1021×10^{-5}
b_1	1.9395×10^{-9}	c_1	0
b_2	0	c_2	6.1745×10^{-14}
b_3	0	c_1	1.4867×10^{-9}
d_1	0.019	d_2	0.0104
d_3	0.0059	κ_v	2.8192×10^{6}
$I(0)$	50	$R(0)$	109.64

THEOREM 5. There exists a dengue-endemic equilibrium when $\mathcal{R}_0 < 1$ if $\alpha > \alpha^*$, where $\alpha^* = \frac{(\gamma+\mu_h+\delta)\kappa_v + N(\delta+\mu_h)}{2(\delta+\mu_h)N\kappa_v}$.

PROOF. Let us choose β_h as the bifurcation parameter. To conduct the gradient analysis of I at $\mathcal{R}_0 = 1$ and $I = 0$ using polynomial (12), we need to rewrite each a_i for $i = 0, 1, 2, 3$ as a function of $\mathcal{R}_0$. First rewriting β_h as a function of $\mathcal{R}_0$ using the expression on (10), we have

$$\beta_h^* = \frac{(\gamma+\mu_h)\kappa_v\mathcal{R}_0}{MN}. \tag{13}$$

Substitute $\beta_h = \beta_h^*$ into $F(I,\tau)$, differentiate I respect to $\mathcal{R}_0$, and evaluate it at $\mathcal{R}_0 = 1, I = 0$. We obtain

$$\frac{\partial I}{\partial \mathcal{R}_0} = -\frac{\kappa_v(\delta+\mu_h)N}{(2\alpha(\delta+\mu_h)N - \delta - \gamma - \mu_h)\kappa_v - N(\delta+\mu_h)}. \tag{14}$$

Hence, we have that $\frac{\partial I}{\partial \mathcal{R}_0} < 0$ if and only if $\alpha > \alpha^*$ where

$$\alpha^* = \frac{(\gamma+\mu_h+\delta)\kappa_v + N(\delta+\mu_h)}{2(\delta+\mu_h)N\kappa_v}. \tag{15}$$

Since the condition of $\frac{\partial I}{\partial \mathcal{R}_0} < 0$ indicates the existence of a positive root of $F(I,\tau) = 0$ when $\mathcal{R}_0 < 1$, we conclude that there

TABLE 2 The possible number of dengue-endemic equilibria of model (5) depends on whether $\mathcal{R}_0$ is lesser or larger than 1.

Case	a_3	a_2	a_1	a_0	$\mathcal{R}_0$	Possible positive roots
1	+	+	+	+	$\mathcal{R}_0 < 1$	0
2	+	+	+	−	$\mathcal{R}_0 > 1$	1
3	+	+	−	+	$\mathcal{R}_0 < 1$	0 or 2
4	+	+	−	−	$\mathcal{R}_0 > 1$	1
5	+	−	+	+	$\mathcal{R}_0 < 1$	0 or 2
6	+	−	+	−	$\mathcal{R}_0 > 1$	1 or 3
7	+	−	−	+	$\mathcal{R}_0 < 1$	0 or 2
8	+	−	−	−	$\mathcal{R}_0 > 1$	1

exists a dengue-endemic equilibrium when $\mathcal{R}_0 < 1$ if $\alpha > \alpha^*$. Hence, the proof is completed. □

To analyze the possible number of dengue-endemic equilibria of model (5), we use the well-known Descartes' rule of signs. The number of possible positive roots of $F(I,\tau)$ is calculated by how many times the sign of a_i changed. The number of possible positive roots $F(I,\tau)$ is the same or slightly lower by an even/odd number as the number of changes in the sign of the coefficients. The result is given in Table 2.

3.2. Backward bifurcation analysis

In the previous section, we found that the dengue-endemic equilibrium is always locally asymptotically stable if $\mathcal{R}_0 < 1$, and unstable when $\mathcal{R}_0 > 1$. Furthermore, we also found that our simplified *IR*-model does not always have a unique dengue-endemic equilibrium point. It is possible to have multiple dengue-endemic equilibria when $\mathcal{R}_0 < 1$. Hence, it is important to analyze its local stability criteria. Furthermore, we analyze the bifurcation type of our *IR*-model using the well-known Castillo–Song bifurcation theorem [54]. The theorem is given as follows.

THEOREM 6 (**Castillo–Song Bifurcation Theorem**, [54]). Consider a general system of ODEs with parameter ϕ:

$$\frac{dx}{dt} = f(x,\phi), \quad f:\mathbb{R}^n \times \mathbb{R} \to \mathbb{R}^n \quad \text{and} \quad f \in \mathbb{C}^2(\mathbb{R}^n \times \mathbb{R}). \tag{16}$$

Without loss of generality, it is assumed that 0 is an equilibrium of system (16) for all values of the parameter ϕ, that is

$$f(0,\phi) \equiv 0 \ \text{ for all } \phi. \tag{17}$$

Assume

1. $A = D_x f(0,0) = \left(\frac{\partial f_i}{\partial x_j}(0,0)\right)$ is the linearization matrix of system (16) around the equilibrium 0 with ϕ evaluated at 0. Zero is a simple eigenvalue of A and all other eigenvalues of A have negative real parts.
2. Matrix A has a non-negative right eigenvector w and a left eigenvector v corresponding to the zero eigenvalue.

Let f_k be the kth component of f and

$$a = \sum_{k,i,j=1}^{n} v_k q_i w_j \frac{\partial^2 f_k}{\partial x_i \partial x_j}(0,0), \tag{18}$$

$$b = \sum_{k,i=1}^{n} v_k w_i \frac{\partial^2 f_k}{\partial x_i \partial \phi}(0,0). \tag{19}$$

The local dynamics of (16) around 0 are totally determined by a and b.

1. $a > 0, b > 0$. When $\phi < 0$ with $|\phi| \ll 1$, 0 is locally asymptotically stable, and there exists a positive unstable equilibrium; when $0 < \phi \ll 1$, 0 is unstable, and there exists a negative and locally asymptotically stable equilibrium;
2. $a < 0, b < 0$. When $\phi < 0$ with $|\phi| \ll 1$, 0 is unstable; when $0 < \phi \ll 1$, 0 is locally asymptotically stable, and there exists a positive unstable equilibrium;
3. $a > 0, b < 0$. When $\phi < 0$ with $|\phi| \ll 1$, 0 is unstable, and there exists a locally asymptotically stable negative equilibrium; when $0 < \phi \ll 1$, 0 is stable, and there exists a positive unstable equilibrium;
4. $a < 0, b > 0$. When ϕ changes from negative to positive, 0 changes its stability from stable to unstable. Correspondingly a negative unstable equilibrium becomes positive and locally asymptotically stable.

Now, we are ready to prove the existence of the backward bifurcation phenomena of our simplified *IR*-model. Let us assume

$$x_1 = I, x_2 = R,$$
$$g_1 = \frac{dI}{dt}, g_2 = \frac{dR}{dt}.$$

Therefore, the *IR*-model can be written as

$$g_1 = \frac{\beta_h(1+\alpha x_1)^2(N - x_1 - x_2)x_1 M}{(1+\alpha x_1)x_1 + \kappa_v} - (\gamma + \mu_h)x_1,$$
$$g_2 = \gamma x_1 - (\delta + \mu_h)x_2.$$

Next, we linearize the above system around the dengue-free equilibrium which yields

$$\boldsymbol{M} = \mathbf{J}|_{DFE,\mathcal{R}_0=1} = \begin{bmatrix} 0 & 0 \\ \gamma & -\delta - \mu_h \end{bmatrix},$$

which has two eigenvalues

$$\lambda_1 = 0, \quad \lambda_2 = -\delta - \mu_h.$$

Please note that we have a simple zero eigenvalue, and one other eigenvalue is negative, which fulfills the first assumption of the Castillo–Song bifurcation theorem.

Next, we determine the right eigenvectors of $\boldsymbol{M}$ by solving $\boldsymbol{M}\boldsymbol{w} = \boldsymbol{0}$, where $\boldsymbol{w} = (w_1, w_2)$ is a column vector. We obtained

$$w_1 = \frac{(\delta + \mu_h)w_2}{\gamma}, \quad w_2 = w_2.$$

Next, we determine the left eigenvectors of M by solving $\boldsymbol{vM} = \mathbf{0}$, where $\boldsymbol{v} = (v_1, v_2)$ is a row vector. We obtained

$$v_1 = 1, \quad v_2 = 0.$$

Hence, we have also shown that our preliminary result fulfills two assumptions, such that we can use the Castillo–Song bifurcation theorem.

Next, we calculate a and b using the formula in the Castillo–Song bifurcation theorem. In our case, 0 is the dengue-free equilibrium. We assumed β_h as the bifurcation parameter, such that the critical value of β_h makes $\mathcal{R}_0 = 1$. Since we have that $v_2 = 0$, there is no need to determine the partial derivatives of g_2. Thus, we had the non-zero derivatives of g_1 as follows:

$$\begin{aligned}
\frac{\partial^2 g_1}{\partial x_1^2}(\mathbf{0},0) &= \frac{2(\gamma+\mu_h)(2N\alpha\kappa_v - N - \kappa_v)}{N\kappa_v},\\
\frac{\partial^2 g_1}{\partial x_1 \partial x_2}(\mathbf{0},0) &= -\frac{\gamma+\mu_h}{N},\\
\frac{\partial^2 g_1}{\partial x_2 \partial x_1}(\mathbf{0},0) &= -\frac{\gamma+\mu_h}{N},\\
\frac{\partial^2 g_1}{\partial x_1 \partial \beta_h}(\mathbf{0},0) &= \frac{NM}{\kappa_v}.
\end{aligned}$$

Using the above derivatives, we can obtain the values of a and b as follows:

$$\begin{aligned}
a &= \sum_{k,i,j=1}^{2} \boldsymbol{v}_k \boldsymbol{w}_i \boldsymbol{w}_j \frac{\partial^2 g_k}{\partial x_i \partial x_j}(\mathbf{0},0),\\
&= \frac{2(\delta+\mu_h)^2(\gamma+\mu_h)(2N\alpha\kappa_v - N - \kappa_v)}{N\kappa_v\gamma^2} - \frac{2(\delta+\mu_h)(\gamma+\mu_h)}{\gamma N},\\
b &= \sum_{k,i=1}^{2} \boldsymbol{v}_k \boldsymbol{w}_i \frac{\partial^2 g_k}{\partial x_i \partial \beta_h}(\mathbf{0},0),\\
&= \frac{(\delta+\mu_h)NM}{\gamma\kappa_v}.
\end{aligned}$$

From these calculations, we always obtain b with a positive value, whereas a could be positive or negative. To make a positive, we need to satisfy

$$\alpha > \frac{(\gamma+\mu_h+\delta)\kappa_v + N(\delta+\mu_h)}{2(\delta+\mu_h)N\kappa_v} = \alpha^*.$$

Hence, we obtained that a is positive when $\alpha > \alpha^*$ and a is negative when $\alpha < \alpha^*$. Based on the Castillo–Song Theorem, we would have that our *IR*-model undergoes a forward bifurcation when a is negative and b is positive. On the other hand, we would have that our IR-model undergoes a backward bifurcation when a is positive and b is positive. Hence, our model could undergo backward and forward bifurcation depending on the value of α.

THEOREM 7. Model (5) undergoes a backward bifurcation at $\mathcal{R}_0 = 1$ if $\alpha > \alpha^*$ where

$$\alpha^* = \frac{(\gamma+\mu_h+\delta)\kappa_v + N(\delta+\mu_h)}{2(\delta+\mu_h)N\kappa_v}.$$

Otherwise, model (5) undergoes a forward bifurcation when $\alpha < \alpha^*$.

Please note that α^* in Theorem 7 is the same as with α^* in Theorem 5. The results in this section enumerate some important information from our proposed model.

1. The *IR*-model in system (5) has a dengue-free equilibrium point. This equilibrium point always exists, and is locally stable if $\mathcal{R}_0 < 1$. These results indicate that we can expect a dengue-free condition in the community as long as we can reduce the basic reproduction number to be <1.
2. The dengue-endemic equilibrium of the *IR*-model always exists and is locally stable if $\mathcal{R}_0 > 1$. Hence, whenever the dengue-free equilibrium is unstable, we always have a stable endemic equilibrium.
3. It is possible to have a stable endemic equilibrium when $\mathcal{R}_0 < 1$. Hence, a condition $\mathcal{R}_0 < 1$ does not always guarantee the disappearance of dengue from the community.

4. Numerical experiments

In this section, we conduct several numerical experiments to understand the behavior of our model with respect to the level of community ignorance (α). The first simulation will be the bifurcation diagram, followed by numerical simulation on the dynamic of the model with respect to time.

As previously mentioned in Theorem 7, a backward bifurcation occurs when $\alpha > \alpha^*$, where α presents the ignorance level of the community. Larger α means more ignorance in the community about the spread of dengue. To present the situation, we conduct numerical experiments to show a possible type of bifurcation that could appear from our model. At first, we set up all coefficients on the polynomial (12) as a function of $\mathcal{R}_0$. By solving $\mathcal{R}_0$ with respect to β_h, we have $\beta_h = \frac{(\gamma+\mu_h)\kappa_v\mathcal{R}_0}{MN}$, and substituting it in (12), yields:

$$a_3(\mathcal{R}_0)I^3 + a_2(\mathcal{R}_0)I^2 + a_1(\mathcal{R}_0)I + a_0 = 0, \tag{20}$$

where

$$\begin{aligned}
a_3(\mathcal{R}_0) &= \mathcal{R}_0\frac{\kappa_v(\gamma+\mu_h)\alpha^2(\gamma+\mu_h+\delta)}{N},\\
a_2(\mathcal{R}_0) &= -(\alpha(\gamma+\mu_h))\\
&\quad \frac{\kappa_v(N\alpha(\delta+\mu_h) - 2(\gamma+\mu_h+\delta))\mathcal{R}_0 - N(\delta+\mu_h)}{N},\\
a_1(\mathcal{R}_0) &= -(\gamma+\mu_h)\\
&\quad \frac{\kappa_v(2N\alpha(\mu_h+\delta) - (\delta+\gamma+\mu_h))\mathcal{R}_0 - N(\delta+\mu_h)}{N},\\
a_0(\mathcal{R}_0) &= -(\delta+\mu_h)(\gamma+\mu_h)\kappa_v(\mathcal{R}_0 - 1).
\end{aligned}$$

Next, we substitute the parameter values as given in Section 2.3 which gives us

$$\begin{aligned}
&0.0196\mathcal{R}_0\alpha^2 I^3 - \left(19793\alpha^2\mathcal{R}_0 + (0.039\mathcal{R}_0 + 0.007)\alpha\right)I^2 \ldots\\
&+ \left(0.007 + (0.019 - 39586\alpha)\mathcal{R}_0\right)I + \left(19793(1-\mathcal{R}_0)\right) = 0. \quad (21)
\end{aligned}$$

Using these parameter values, we have the value of α^* as 6.729×10^{-7}. Therefore, we choose $\alpha = 5 \times 10^{-8} < \alpha^*$ to find the forward bifurcation as shown in Figure 3A and $\alpha = 5 \times 10^{-6} > \alpha^*$ to find the backward bifurcation as shown in Figure 3B.

Backward bifurcation phenomena imply that a condition $\mathcal{R}_0 < 1$ will not be enough to guarantee the disappearance of dengue

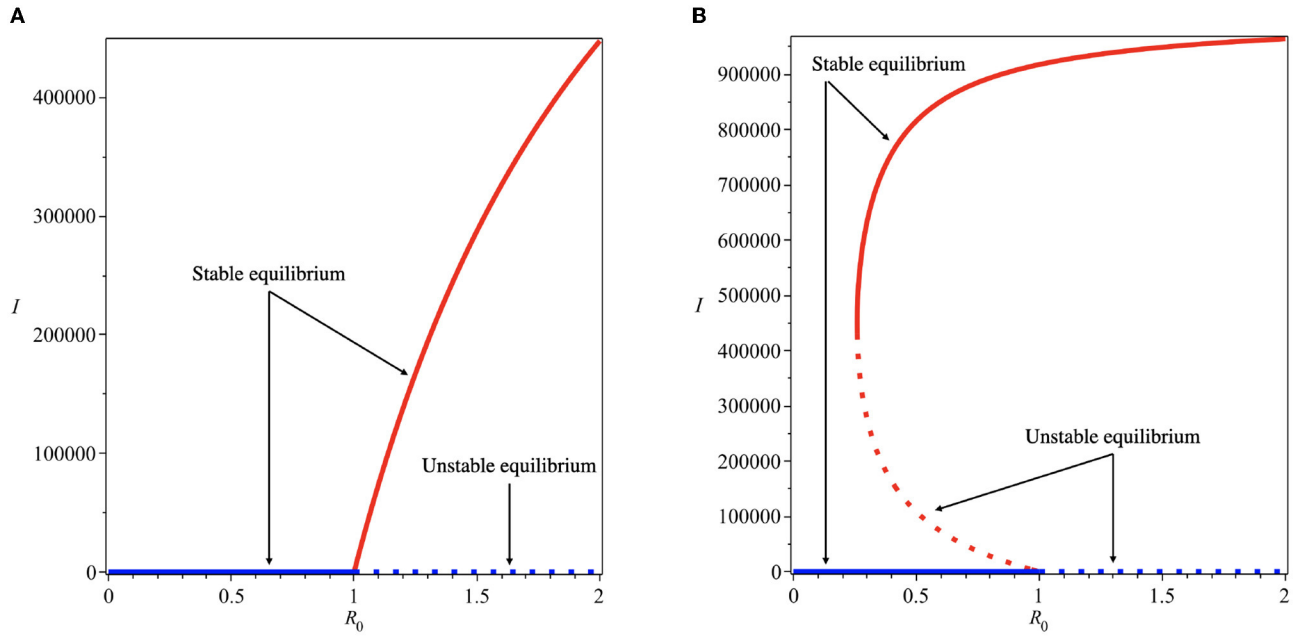

FIGURE 3
Forward **(A)** and backward **(B)** bifurcation diagrams of system (5) for different values of α^*. Red and blue curves present the dengue-free equilibrium and dengue-endemic equilibrium points, respectively.

from the community. We can see that for some parameter value when $\mathcal{R}_0 < 1$, we can have multiple stable equilibrium points, i.e., the dengue-free equilibrium and the endemic equilibrium point (please see Figure 3B). When the ignorance level of the community is small enough (at least smaller than α^*, a condition $\mathcal{R}_0 < 1$ is enough to guarantee the disappearance of dengue from the community (please see Figure 3A). To illustrate the bistability phenomenon when a backward bifurcation appears, we show the phase portrait of system (5) with some initial conditions. The results are given in Figure 4, where we have a stable node dengue-free equilibrium and a stable-spiral endemic equilibrium point. It can be seen that different initial conditions may lead to a different final state condition. To see further impact of α on the bifurcation phenomena of our model, we conduct numerical experiments as shown in Figure 5. These numerical experiments confirm our previous results on the impact of α on the appearance of backward bifurcation phenomena at $\mathcal{R}_0 = 1$. Smaller the level of ignorance of the community, higher the chance to have a free endemic equilibrium when $\mathcal{R}_0 < 1$.

The public health implication of backward bifurcation is that it is not enough to only reduce the basic reproduction number to eliminate dengue. Another factor, which in our case is the community ignorance level of dengue, should also be considered for further intervention in the field. Therefore, it is necessary to find the impact of model parameters on the critical level of community ignorance. To determine this, we calculate the normalized sensitivity of α^* with respect to γ, μ_h, δ, and κ_v. Using the formula given by [55], we have:

$$\Gamma^{\gamma}_{\alpha^*} = \frac{\gamma\kappa_v}{N(\delta+\mu_h)+\kappa_v(\delta+\gamma+\mu_h)},$$

$$\Gamma^{\mu_h}_{\alpha^*} = -\frac{\mu_h\kappa_v\gamma}{(\delta+\mu_h)\left(N(\delta+\mu_h)+\kappa_v(\delta+\gamma+\mu_h)\right)}$$

$$\Gamma^{\delta}_{\alpha^*} = -\frac{\delta\kappa_v\gamma}{(\delta+\mu_h)\left(N(\delta+\mu_h)+\kappa_v(\delta+\gamma+\mu_h)\right)}$$

$$\Gamma^{\kappa_v}_{\alpha^*} = -\frac{N(\delta+\mu_h)}{N(\delta+\mu_h)+\kappa_v(\delta+\gamma+\mu_h)}.$$

From a previous analysis, we know that a backward bifurcation will appear when $\alpha > \alpha^*$ and a forward bifurcation if $\alpha < \alpha^*$. We can see from the expression of Γ_{α^*}, we have that $\Gamma^{\gamma}_{\alpha^*} > 0$, which indicates that increasing γ will increase α^*. Hence, a larger recovery rate will increase the chance of non-appearance of backward bifurcation phenomena at $\mathcal{R}_0 = 1$, since we have a larger interval of $\alpha \in [0, \alpha^*]$. On the other hand, we can see that $\Gamma^{\mu_h}_{\alpha^*}, \Gamma^{\delta}_{\alpha^*}$, and $\Gamma^{\kappa_v}_{\alpha^*}$ are negative, which indicates that increasing natural death rate of human (μ_h), waning immunity (δ), and mosquito dynamic parameters (κ_v) will reduce α^*. Hence, different with the effect of recovery rate, increasing μ_h, δ, and κ_v will increase the chance of appearance of backward bifurcation phenomena, since the interval of $\alpha \in [0, \alpha^*]$ is getting smaller. Therefore, we can conclude that longer the temporal immunity of human (smaller δ^{-1}) will increase the chance of finding the only possible condition that dengue disappears when $\mathcal{R}_0 < 1$. Furthermore, we also find that when κ_v increases (larger life expectation of mosquitoes or a smaller infection rate in mosquitoes) will increase the possible existence of dengue-endemic situation in the field, even though $\mathcal{R}_0$ is already <1.

Next, we carry out numerical simulation in Figure 6 using MatLab to understand the impact of the human level of ignorance on the spread of dengue. We use the same parameter values that we used to produce Figure 2. We can see that less ignorance of the community (smaller α) to the

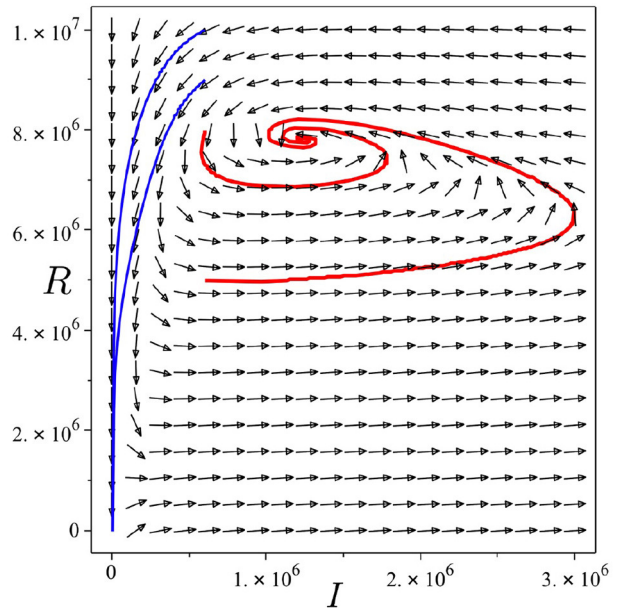

FIGURE 4
Trajectories of system (5) in $I - R$ plane show bistability phenomena when $\mathcal{R}_0 = 0.5$. Parameter values used are the same as they have been used for Figure 3B. Red curve tends to the endemic equilibrium point, while blue curve tends to the dengue-free equilibrium point.

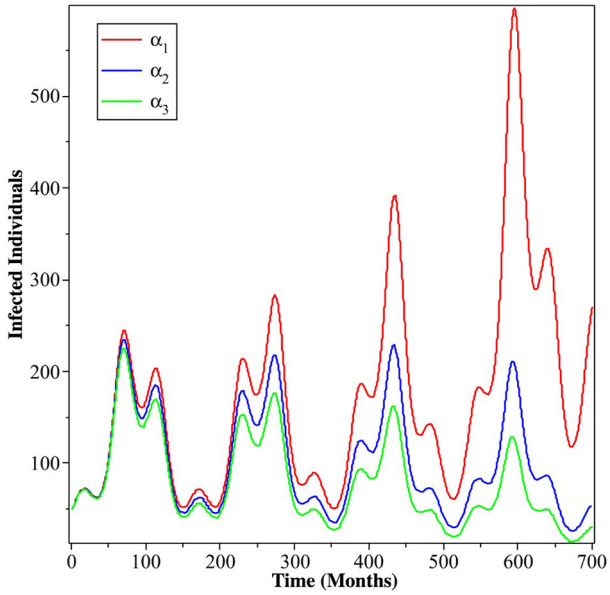

FIGURE 6
Simulation results showing the impact of the level of ignorance of the community on the dynamics of infected individuals. The red, blue, and green curves present $\alpha = 5.1021 \times 10^{-5}$, $\alpha = 4.1021 \times 10^{-5}$, and $\alpha = 3.1021 \times 10^{-5}$, respectively.

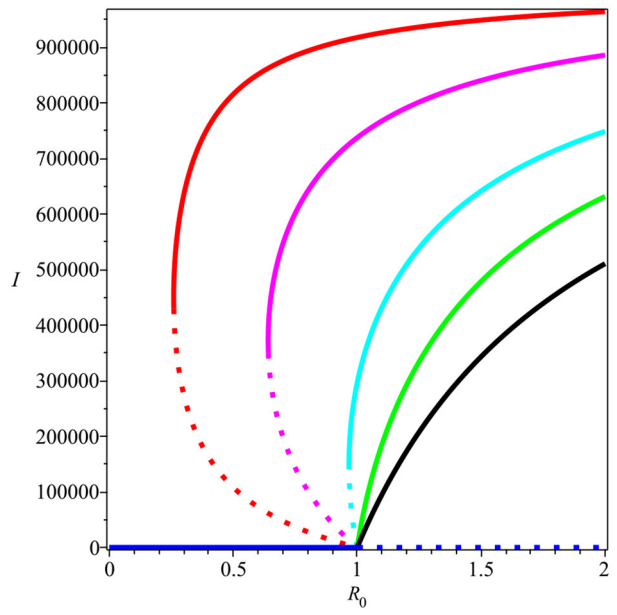

FIGURE 5
The impact of α on the type of bifurcation phenomena at $\mathcal{R}_0 = 1$. Red, magenta, cyan, green, and black curves present the condition of α being equal to 5, 2, 0.9, 0.5, and 0.2×10^{-6}, respectively.

dynamics of infected individuals will reduce the number of infected individuals. The impact will be more significant as time increases.

5. Summary and concluding remarks

A mathematical model was presented and studied in this article to assess the impact of the level of human ignorance on the spread of dengue. At the beginning of the study, we introduced our SIR-UV model. Using the QSSA approach, we simplified the model to an IR-model. With this approach, we converted our host–vector dengue model to a host-to-host dengue model. A host-to-host dengue model is a common approach adopted by several researchers to reduce the complexity of their model, by considering the fact that the dynamic of mosquitoes is very fast compared to that of human dynamics [30, 33, 34]. Two types of equilibria emerged from the model, namely the dengue-free equilibrium and the endemic equilibrium point. The basic reproduction number, denoted by $\mathcal{R}_0$, was calculated. We found that the dengue-free equilibrium point was always locally asymptotically stable when $\mathcal{R}_0 < 1$. The center manifold theory was used to establish the stability of the endemic equilibrium point, and it showed that the existence of backward bifurcation appears when the level of community ignorance increases. In this situation, we conclude that ensuring the size of the basic reproduction number to be <1 does not always guarantee the disappearance of dengue. Several authors have shown the appearance of a backward bifurcation in the dengue transmission model in their models [56–59]. Their analysis showed that some crucial aspects were not included in the calculation of the basic reproduction number. This aspect may trigger the backward bifurcation phenomena, making the dengue control program more difficult to achieve. In our model, we show that, even though the level of community ignorance does not appear in the basic

reproduction number, it does trigger the backward bifurcation. More ignorant the population about dengue, the more difficult it is for dengue to be controlled since the condition of basic reproduction number <1 no longer guarantees the disappearance of dengue.

To test our model, we fit our model output with dengue incidence data in Jakarta, Indonesia. Our preliminary analysis of the time series dengue data reveals the existence of periodicity of dengue incidence data in Jakarta from 2008 to 2021. Three dominant frequencies of the data related to a periodicity of 53, 74, and 147 weeks. These results indicate that dengue cases in Jakarta always recur every year. A numerical experiment on the bifurcation diagram has shown that reducing community ignorance can significantly change the endemic situation. The chance of the existence of dengue-endemic equilibrium when the basic reproduction number is <1 can be avoided when the community ignorance is relatively small. To reduce community ignorance, a media campaign to increase people's awareness of dengue could be an alternative intervention. On the other hand, we find that we can increase the chance of the non-existence of backward bifurcation by increasing the recovery rate of a human, prolonging the temporal immunity, or reducing the life expectancy of a mosquito. Our non-autonomous simulation was conducted by assuming the infection parameter as a sinusoidal function with three dominant frequencies. It has been shown that reducing community ignorance of dengue could suppress the incidence of dengue in Jakarta. Although the outbreak still appears, the outbreak can be reduced significantly. The longer period of intervention of media campaigns to reduce community ignorance will give a more significant reduction in dengue outbreaks.

Data availability statement

The data analyzed in this study is subject to the following licenses/restrictions: It can be available due to personal request to the corresponding author. Requests to access these datasets should be directed to aldiladipo@sci.ui.ac.id.

Author contributions

DA, CA, and RR contributed to the concept and design of the study and wrote the original version of the article. CA organized the data used in the article. DA wrote the final version of the manuscript. All authors contributed to the article and approved the submitted version.

Funding

This research was funded by the Ministry of Education and Culture of Indonesia in collaboration with the Education Fund Management Institution (LPDP) of the Republic of Indonesia through the UKICIS Research Grant Scheme (ID number 4345/E4/AL.04/2022).

Acknowledgments

The authors thank all reviewers for their constructive suggestions.

Conflict of interest

The authors declare that the research was conducted in the absence of any commercial or financial relationships that could be construed as a potential conflict of interest.

Publisher's note

References

1. World Health Organization (WHO). *Dengue and Severe Dengue.* (2022). Available online at: https://www.who.int/news-room/fact-sheets/detail/dengue-and-severe-dengue (accessed February 22, 2022).

2. Kraemer MU, Sinka ME, Duda KA, Mylne AQ, Shearer FM, Barker CM, et al. The global distribution of the arbovirus vectors *Aedes aegypti* and *Ae. albopictus. Elife.* (2015) 4:e08347. doi: 10.7554/eLife.08347

3. Messina JP, Brady OJ, Golding N, Kraemer M, Wint G, Ray SE, et al. The current and future global distribution and population at risk of dengue. *Nat Microbiol.* (2019) 4:1508–15. doi: 10.1038/s41564-019-0476-8

4. Kementerian Kesehatan. *Buletin Jendela Epidemiologi, Vol. 2, Agustus 2010.* (2010). Available online at: https://www.kemkes.go.id/folder/view/01/structure-publikasi-pusdatin-buletin.html (accessed February 1, 2022).

5. Databox. *Musim Penghujan, Terjadi 13.776 Kasus DBD Pada Awal 2022.* (2022). Available online at: https://databoks.katadata.co.id (accessed June 15, 2022).

6. Tuiskunen Back A, Lundkvist A. Dengue viruses—an overview. *Infect Ecol Epidemiol.* (2013) 3:19839. doi: 10.3402/iee.v3i0.19839

7. Wang E, Ni H, Xu R, Barrett ADT, Watowich SJ, Gubler DJ, et al. Evolutionary relationships of endemic/epidemic and sylvatic dengue viruses. *J Virol.* (2000) 74:3227–34. doi: 10.1128/jvi.74.7.3227-3234.2000

8. Sierra B, Perez AB, Vogt K, Garcia G, Schmolke K, Aguirre E, et al. Secondary heterologous dengue infection risk: disequilibrium between immune regulation and inflammation? *Cell Immunol.* (2010) 262:134–40. doi: 10.1016/j.cellimm.2010.02.005

9. John ALSt, Rathore APS. Adaptive immune responses to primary and secondary dengue virus infections. *Nat Rev Immunol.* (2019) 19:218–30. doi: 10.1038/s41577-019-0123-x

10. Weiskopf D, Sette A. T-cell immunity to infection with dengue virus in humans. *Front Immunol.* (2014) 5:93. doi: 10.3389/fimmu.2014.00093

11. Rothman AL. Cellular immunology of sequential dengue virus infection and its role in disease pathogenesis. In: Ahmed R, Akira S, Casadevall A, Galan JE, Garcia-Sastre A, Mailissen B, Rappuoli R, editors. *Dengue Virus*. Berlin; Heidelberg: Springer (2009). p. 83–98.

12. Guzman MG, Halstead SB, Artsob H, Buchy P, Farrar J, Gubler DJ, et al. Dengue: a continuing global threat. *Nat Rev Microbiol.* (2010) 8:S7–16. doi: 10.1038/nrmicro2460

13. Wilder-Smith A. Dengue vaccine development by the year 2020: challenges and prospects. *Curr Opin Virol.* (2020) 43:71–8. doi: 10.1016/j.coviro.2020.09.004

14. Deng S-Q, Yang X, Wei Y, Chen J-T, Wang X-J, Peng H-J. A review on dengue vaccine development. *Vaccines.* (2020) 8:63. doi: 10.3390/vaccines8010063

15. Zahir A, Ullah A, Shah M, Mussawar A. Community participation, dengue fever prevention and control practices in Swat, Pakistan. *Int J MCH AIDS.* (2016) 5:39–45. doi: 10.21106/ijma.68

16. Kumar N, Verma S, Shiba, Choudhary P, Singhania K, Kumar M. Dengue awareness and its determinants among urban adults of Rohtak, Haryana. *J Fam Med Primary Care.* 9:2040–4. doi: 10.4103/jfmpc.jfmpc_1203_19

17. Rizki LP, Anggreni SN. Community awareness to prevent and control of Dengue fever after Sunda Strait Tsunami in Labuhan, Banten, Indonesia. *J Community Med.* (2020) 3:1016.

18. Phuyal P, Kramer IM, Kuch U, Magdeburg A, Groneberg DA, Lamichhane Dhimal M, et al. The knowledge, attitude and practice of community people on dengue fever in Central Nepal: a cross-sectional study. *BMC Infect Dis.* (2022) 22:454. doi: 10.1186/s12879-022-07404-4

19. Aldila D. Dynamical analysis on a malaria model with relapse preventive treatment and saturated fumigation. *Comput Math Methods Med.* (2022) 2022:1135452. doi: 10.1155/2022/1135452

20. Handari BD, Ramadhani RA, Chukwu CW, Khoshnaw SHA, Aldila D. An optimal control model to understand the potential impact of the new vaccine and transmission-blocking drugs for malaria: a case study in Papua and West Papua, Indonesia. *Vaccines.* (2022) 10:1174. doi: 10.3390/vaccines10081174

21. Tasman H, Aldila D, Dumbela PA, Ndii MZ, Herdicho FF, Chukwu CW. Assessing the impact of relapse, reinfection and recrudescence on malaria eradication policy: a bifurcation and optimal control analysis. *Trop Med Infect Dis.* (2022) 7:263. doi: 10.3390/tropicalmed7100263

22. Handari BD, Aldila D, Dewi BO, Rosuliyana H, Khosnaw SHA. Analysis of yellow fever prevention strategy from the perspective of mathematical model and cost-effectiveness analysis. *Math Biosci Eng.* (2022) 19:1786–824. doi: 10.3934/mbe.2022084

23. Aldila D, Rasyiqah K, Ardaneswari G, Tasman H. A mathematical model of Zika disease by considering transition from the asymptomatic to symptomatic phase. *J Phys.* (2021) 1821:012001. doi: 10.1088/1742-6596/1821/1/012001

24. Aldila D. Optimal control for dengue eradication program under the media awareness effect. *Int J Nonlin Sci Numer Simul.* (2021) 24:95–122. doi: 10.1515/ijnsns-2020-0142

25. Ndii MZ. The effects of vaccination, vector controls and media on dengue transmission dynamics with a seasonally varying mosquito population. *Results Phys.* (2022) 34:105298. doi: 10.1016/j.rinp.2022.105298

26. Falcón-Lezama JA, Martínez-Vega RA, Kuri-Morales PA, Ramos-Castañeda J, Adams B. Day-to-day population movement and the management of dengue epidemics. *Bull Math Biol.* (2016) 78:2011–33. doi: 10.1007/s11538-016-0209-6

27. Lourenço J, Recker M. Natural, persistent oscillations in a spatial multi-strain disease system with application to dengue. *PLoS Comput Biol.* (2013) 9:e1003308. doi: 10.1371/journal.pcbi.1003308

28. Gu Y, Khan M, Zarin R, Khan A, Yusuf A, Humphries UW. Mathematical analysis of a new nonlinear dengue epidemic model via deterministic and fractional approach. *Alexand Eng J.* 67:1–21. doi: 10.1016/j.aej.2022.10.057

29. Pandey HR, Phaijoo GR, Gurung DB. Vaccination effect on the dynamics of dengue disease transmission models in Nepal: a fractional derivative approach. *Part Differ Equat Appl Math.* (2023) 7:100476. doi: 10.1016/j.padiff.2022.100476

30. Aguiar M, Stollenwerk N. Mathematical models of dengue fever epidemiology: multi-strain dynamics, immunological aspects associated to disease severity and vaccines. *Commun Biomath Sci.* (2017) 1:1. doi: 10.5614/cbms.2017.1.1.1

31. ten Bosch QA, Singh BK, Hassan MRA, Chadee DD, Michael E. The role of serotype interactions and seasonality in dengue model selection and control: insights from a pattern matching approach. *PLoS Negl Trop Dis.* (2016) 10:e0004680. doi: 10.1371/journal.pntd.0004680

32. Din A, Khan T, Li Y, Tahir H, Khan A, Ali-Khan W. Mathematical analysis of dengue stochastic epidemic model. *Results Phys.* (2021) 20:103719. doi: 10.1016/j.rinp.2020.103719

33. Kabir KA, Tanimoto J. Cost-efficiency analysis of voluntary vaccination against n-serovar diseases using antibody-dependent enhancement: a game approach. *J Theor Biol.* (2020) 503:110379. doi: 10.1016/j.jtbi.2020.110379

34. Aguiar M, Stollenwerk N, Halstead SB. The impact of the newly licensed dengue vaccine in endemic countries. *PLoS Negl Trop Dis.* (2016) 10:e0005179. doi: 10.1371/journal.pntd.0005179

35. Rocha F, Aguiar M, Souza M, Stollenwerk N. Understanding the effect of vector dynamics in epidemic models using center manifold analysis. *AIP Conf Proc.* (2012) 1479:1319. doi: 10.1063/1.4756398

36. Xue L, Zhang H, Sun W, Scoglio C. Transmission dynamics of multi-strain dengue virus with cross-immunity. *Appl Math Comput.* (2021) 392:125742. doi: 10.1016/j.amc.2020.125742

37. Ghosh JK, Ghosh U, Sarkar S. Qualitative analysis and optimal control of a two-strain dengue model with its co-infections. *Int J Appl Comput Math.* (2020) 6:161. doi: 10.1007/s40819-020-00905-3

38. Bock W, Jayathunga Y. Optimal control of a multi-patch Dengue model under the influence of Wolbachia bacterium. *Math Biosci.* (2019) 315:108219. doi: 10.1016/j.mbs.2019.108219

39. Ben-Shachar R, Koelle K. Minimal within-host dengue models highlight the specific roles of the immune response in primary and secondary dengue infections. *J R Soc Interface.* (2015) 12:20140886. doi: 10.1098/rsif.2014.0886

40. Clapham HE, Tricou V, Van Vinh Chau N, Simmons CP, Ferguson NM. Within-host viral dynamics of dengue serotype 1 infection. *J R Soc Interface.* (2014) 11:20140094. doi: 10.1098/rsif.2014.0094

41. Misra AK, Sharma A, Li J. A mathematical model for control of vector borne diseases through media campaigns. *Discr Contin Dyn Syst B* (2013) 18:1909–27. doi: 10.3934/dcdsb.2013.18.1909

42. Mishra A, Gakkhar S. The effects of awareness and vector control on two strains dengue dynamics. *Appl Math Comput.* (2014) 246:159–67. doi: 10.1016/j.amc.2014.07.115

43. Zheng T, Nie L. Modelling the transmission dynamics of two-strain Dengue in the presence awareness and vector control. *J Theor Biol.* (2018) 443:82–91. doi: 10.1016/j.jtbi.2018.01.017

44. Dwivedi A, Keval R. Analysis for transmission of dengue disease with different class of human population. *Epidemiol Methods.* (2021) 10:20200046. doi: 10.1515/em-2020-0046

45. Srivastav AK, Kumar A, Srivastava PK, Ghosh M. Modeling and optimal control of dengue disease with screening and information. *Eur Phys J Plus.* (2021) 136:1187. doi: 10.1140/epjp/s13360-021-02164-7

46. Aldila D, Ndii MZ, Anggriani N, Tasman H, Handari BD. Impact of social awareness, case detection, and hospital capacity on dengue eradication in Jakarta: a mathematical model approach. *Alexand Eng J.* (2023) 64:691–707. doi: 10.1016/j.aej.2022.11.032

47. Alexander ME, Moghadas SM. Bifurcation analysis of an SIRS epidemic model with generalized incidence. *SIAM J Appl Math.* (2005) 65:1794–816. doi: 10.1137/040604947

48. Aldila D, Goetz T, Soewono E. An optimal control problem arising from a dengue disease transmission model. *Math Biosci.* (2013) 242:9–16. doi: 10.1016/j.mbs.2012.11.014

49. Badan Pusat Statistik. *Angka Harapan Hidup (AHH) Menurut Provinsi dan Jenis Kelamin Tahun 2018-2020.* (2020). Available online at: https://www.bps.go.id/indicator/40/501/1/angka-harapan-hidup-ahh-menurut-provinsi-dan-jenis-kelamin.html (accessed February 18, 2022).

50. *Iklim Dan Cuaca Rata-Rata Sepanjang Tahun d Jakarta*. Available online at: https://id.weatherspark.com/y/116847/Cuaca-Rata-rata-pada-bulan-in-Jakarta-Indonesia-Sepanjang-Tahun (accessed November 18, 2022).

51. Badan Pusat Statistik. *Jumlah Penduduk Provinsi DKI Jakarta Menurut Kelompok Umur dan Jenis Kelamin (Tahun 2018-2020).* (2020). Available online at: https://jakarta.bps.go.id/indicator/12/111/1/jumlah-penduduk-provinsi-dki-jakarta-menurut-kelompok-umur-dan-jenis-kelamin.html (accessed February 18, 2022).

52. Wijaya KP, Aldila D, Schafer LE. Learning the seasonality of disease incidences from empirical data. *Ecol Complex.* (2019) 38:83–97. doi: 10.1016/j.ecocom.2019.03.006

53. Diekmann O, Heesterbeek JAP, Roberts MG. The construction of next-generation matrices for compartmental epidemic models. *J R Soc Interface.* (2010) 7:873–85. doi: 10.1098/rsif.2009.0386

54. Castillo-Chavez C, Song B. Dynamical models of tuberculosis and their applications. *Math Biosci Eng.* (2014) 1:361–404. doi: 10.3934/mbe.2004.1.361

55. Chitnis N, Hyman J, Cushing J. Determining important parameters in the spread of malaria through the sensitivity analysis of a mathematical model. *Bull Math Biol.* (2008) 70:1272–96. doi: 10.1007/s11538-008-9299-0

56. Garba SM, Gumel AB, Abu Bakar MR. Backward bifurcations in dengue transmission dynamics. *Math Biosci.* (2008) 215:11–25. doi: 10.1016/j.mbs.2008.05.002

57. Hamdan NI, Kilicman A. The development of a deterministic dengue epidemic model with the influence of temperature: a case study in Malaysia. *Appl Math Model.* (2021) 90:547–67. doi: 10.1016/j.apm.2020.08.069

58. Taghikhani R, Sharomi O, Gumel AB. Dynamics of a two-sex model for the population ecology of dengue mosquitoes in the presence of Wolbachia. *Math Biosci.* (2020) 328:108426. doi: 10.1016/j.mbs.2020.108426

59. Abidemi A, Ackora-Prah J, Fotoyinbo HO, Asamoah JKK. Lyapunov stability analysis and optimization measures for a dengue disease transmission model. *Phys A.* (2022) 602:127646. doi: 10.1016/j.physa.2022.127646

frontiers | Frontiers in Applied Mathematics and Statistics

TYPE Original Research
PUBLISHED 04 July 2023
DOI 10.3389/fams.2023.1122107

OPEN ACCESS

EDITED BY
Asep K. Supriatna,
Padjadjaran University, Indonesia

REVIEWED BY
Nuning Nuraini,
Bandung Institute of Technology, Indonesia
Athithan Singaram,
SRM Institute of Science and Technology, India
Muhamad Deni Johansyah,
Padjadjaran University, Indonesia

*CORRESPONDENCE
D. K. K. Vamsi
✉ dkkvamsi@sssihl.edu.in

RECEIVED 12 December 2022
ACCEPTED 14 June 2023
PUBLISHED 04 July 2023

CITATION
Prakash DB and Vamsi DKK (2023) Stochastic time-optimal control and sensitivity studies for additional food provided prey-predator systems involving Holling type-IV functional response. *Front. Appl. Math. Stat.* 9:1122107. doi: 10.3389/fams.2023.1122107

Stochastic time-optimal control and sensitivity studies for additional food provided prey-predator systems involving Holling type-IV functional response

D. Bhanu Prakash and D. K. K. Vamsi*

Department of Mathematics and Computer Science, Sri Sathya Sai Institute of Higher Learning, Prasanthi Nilayam, India

In this study we consider an additional food provided prey-predator model exhibiting Holling type-IV functional response incorporating the combined effects of both the continuous white noise and discontinuous Lévy noise. We prove the existence and uniqueness of global positive solutions for the proposed model. We perform the stochastic sensitivity analysis for each of the parameters in a chosen range. Later we do the time optimal control studies with respect quality and quantity of additional food as control variables. Making use of the arrow condition of the sufficient stochastic maximum principle, we characterize the optimal quality of additional food and optimal quantity of additional food. We then perform the sensitivity of these control variables with respect to each of the model parameters. Numerical results are given to illustrate the theoretical findings with applications in biological conservation and pest management. At the end we briefly study the influence of the noise on the dynamics of the model.

KEYWORDS

stochastic optimal control, time-optimal control, Holling type-IV response, biological conservation, pest management, Brownian motion, Lévy noise

MSC 2020 codes: 37A50; 60H10; 60J65; 60J70; 60J76; 49K45

1. Introduction

The complex natural ecosystems present around us kindled great attention of many ecologists and mathematicians to the mathematical modeling of ecological systems in the last few decades. The interaction among species in these ecosystems can be of several forms like competition, mutual interference, prey-predator interactions and so on. The very first ecological models are framed from the pioneering works of Lotka [1] and Volterra [2] in 1925. Various complex models are framed and studied ever since.

The basic component of these prey-predator systems is a functional response, which is defined as the rate at which each predator captures prey [3]. These functional response can be majorly classified into two types the first being Density-dependent and the second Ratio-dependent. Density-dependent functional responses are usually preferred as they capture the saturation effect, incorporate handling time, and exhibit an asymptotic approach, which are limited in the case of ratio-dependent responses. Some of the functional responses include Holling functional responses [4], Beddington-DeAngelis functional responses [5], Arditi-Ginzburg functional responses [6], Hassell-Varley functional responses [7], and Crowley and Martin functional response [8].

Among the density-dependent functional responses, the Holling type functional responses are the first ones to be proposed. Among the Holling responses, Holling type-IV response is best suited to capture the group defense mechanism of prey especially in high densities. This is also called as inhibitory effect of the prey. Some examples in real life include, Musk ox are more successful at fending off wolves when in herds than when alone [9] and some other organisms that display this kind of response in nature can be found in [10, 11]. The Holling type-IV functional response also exhibits a saturation effect, meaning that the rate of prey consumption by predators increases at a decreasing rate as prey density increases. This saturation effect aligns with empirical observations that predators have limited capacity and cannot consume an unlimited number of prey items. The Holling type-IV functional response contributes to stable equilibrium or oscillations in predator-prey dynamics, which is consistent with observed patterns in many predator-prey systems. This stability is essential for maintaining ecological balance and preventing population crashes or outbreaks.

In recent decades, many pioneering dynamical modeling works [12–17] reveal that the provision of additional food to predators both in the complimentary and supplementary sense, plays a vital role in controlling the dynamics of the system. Additional food can be provided by establishing artificial feeding stations, organizing supplementary feeding programs or by the provision of nest boxes or artificial structures. By providing the specific conceptual information about the system to be studied and also the empirical data, one should be able to define the sense of the provided additional food for a particular mathematical model.

The availability of these additional food resources can play a significant role in predator populations and their ecological dynamics. Some of the significant findings of these works include the following:

- In some instances it is observed that the additional food can dampen predator-prey cycles by reducing the intensity of predation on natural prey during periods of prey scarcity.
- Access to additional food can increase the chances of survival for predator individuals, especially during periods of food scarcity or low prey availability.
- By having access to a variety of food sources, predators may be able to exploit niche opportunities and develop specialized feeding strategies. This specialization can lead to a more efficient utilization of resources and reduce competition among predators within a community.

The authors in Srinivasu et al. and Srinivasu and Prasad [12, 13] studied the prey-predator systems involving Holling type-II functional response and the authors in Srinivasu et al. [15] studied the prey-predator systems involving Holling type-III functional response. Also, the authors in Sabelis and Van Rijn [18] explicitly studied the impact of the additional food provided to predator, both in supplementary and complementary sense. The authors in Srinivasu et al. [14] have studied an additional food provided deterministic prey-predator systems involving Holling type-IV functional response. In Ananth and Vamsi and May [17, 19], the authors studied the optimal control problems of deterministic prey-predator systems involving Holling type-IV functional response with the quality of additional food and the quantity of additional food as the control parameters respectively. As in earlier mentioned works the authors in the works [15, 17, 19] also considered the provision of additional food to predators both in the complimentary and supplementary sense.

Specifically in the context of Holling type-IV prey-predator models, additional food can have several influences on the dynamics of the system. The Holling type-IV functional response is characterized by a saturating feeding rate that increases with prey density but eventually levels off. When additional food is introduced into the model, it can enhance predator fitness, buffer the prey population against high predation pressures, and potentially reduce the predation pressure on primary prey. Also, the provision of additional food can cascade down the food web, affecting lower trophic levels. For example, reduced predation pressure on natural prey can lead to increased herbivore populations, which may then impact plant communities and ecosystem structure. The availability of additional food can contribute to the stability and resilience of predator-prey systems and aid as a tool for the conservation and management of the ecosystem. The authors in Srinivasu et al. [14] have studied an additional food provided deterministic prey-predator systems involving Holling type-IV functional response. In Ananth and Vamsi and May [17, 19], the authors studied the optimal control problems of deterministic prey-predator systems involving Holling type-IV functional response with the quality of additional food and the quantity of additional food as the control parameters respectively. It is important to note that the specific influence of additional food in a Holling type-IV prey-predator model depends on various factors, including the parameters of the model, the relative availability of primary prey and additional food, and the ecological context. The dynamics and outcomes can vary depending on the specific assumptions and interactions incorporated into the model.

Often it is observed that the parameters in an ecosystem are effected by the environmental fluctuations [20]. For instance, authors in Elton [21] observed that the main cause of animal number fluctuations is the instability of the environment. In recent years, many researchers have drawn their attention to stochastic models which captures these fluctuations. Most stochastic prey-predator models are driven by the Brownian motion, which captures the continuous noise.

White noise is a type of random signal that has equal intensity at all frequencies. White noise reflects the inherent unpredictability and stochasticity of ecological systems. White noise can represent natural environmental fluctuations such as temperature changes, wind patterns, or random disturbances in resource availability that are experienced by organisms [20]. It can also describe the random variation observed in biological processes. For example, individual behaviors, reproductive events, or physiological responses may exhibit stochastic fluctuations resembling white noise. In mathematical and computational models, white noise is often used as a simplifying assumption to capture the inherent randomness in ecological processes. It can be employed to simulate the unpredictable nature of ecological phenomena or to represent random perturbations in system

dynamics. Authors in Li and Zhao and Xu et al. [22, 23] studied the deterministic and stochastic dynamics of a modified Leslie-Gower prey-predator system with simplified Holling type-IV functional response.

However, the sudden changes in environment like toxic pollutants, floods, earthquakes and so on, cannot be captured by the Brownian motion as it is a continuous noise. Hence, addition of a discontinuous noise, like Lévy noise, to the prey-predator system with Brownian motion makes the models more realistic [24].

Discontinuous Lévy noise refers to a type of stochastic process characterized by intermittent and unpredictable jumps or bursts of activity. It is based on the Lévy distribution, which describes the probability of large, rare events occurring. In a biological and ecological context, discontinuous Lévy noise captures the occurrence of rare events that can have significant ecological consequences. These events can include extreme weather events, catastrophic disturbances, or sudden changes in resource availability. Discontinuous Lévy noise reflects the non-Gaussian and heavy-tailed nature of these rare events [24]. The use of discontinuous Lévy noise in ecological modeling allows for the incorporation of rare events, abrupt shifts, long-range correlations, and non-Markovian dynamics. It provides a way to capture the non-linearity, complexity, and unpredictability observed in ecological systems and can help elucidate the role of rare events in shaping ecosystem dynamics.

Jia et al. [25] uses the stochastic averaging method to analyze the modified stochastic Lotka-Volterra models under combined Gaussian and Poisson noise. Ma et al. [24] studies the dynamics and dynamics of a Stochastic One-Predator-Two-Prey time delay system with jumps. Recently, authors in Prakash and Vamsi [26] studied the optimal and time-optimal control studies for additional food provided prey-predator systems involving Holling type-III functional response in the presence of the continuous white noise.

To the best of our knowledge, there is no study of additional food provided stochastic prey-predator system with jumps. Secondly, the optimal control studies of Stochastic Differential Equations with Jumps (SDEJ) were not performed on prey-predator systems. Lastly, very few works involved Holling type-IV response which incorporates the most important group defense property. Motivated by these observations, in this work, we study the optimal control problems for additional food provided stochastic Holling type-IV prey-predator systems under combined Gaussian and Lévy noise. We consider the provision of additional food to predators both in the complimentary and substitutable sense to the prey and also assume that the predators are generalists in nature.

The article is structured as follows: In Section 2 we present the basic analysis of the stochastic prey-predator model with Holling type-IV functional response and additional food with intra-specific competition among predators. In Subsection 2.1 we introduce the stochastic prey-predator model followed by the existence of global positive solution for this model in Subsection 2.2. We perform the stochastic sensitivity analysis in Subsection 2.3. The time-optimal control problem is formulated and the optimal quality and quantity of additional food is characterized in Subsections 3.1–3.3. Sensitivity of stochastic controls are discussed in Subsection 3.5. Section 3.4 illustrates the key findings of the analysis through numerical simulations in the context of both biological conservation and pest management. Section 4 studies the effect of noise on the dynamics of the model. Finally, we present the discussions and conclusions in Section 5.

2. Stochastic analysis

2.1. The stochastic model formulation

Let N and P denote the biomass of prey and predator population densities respectively. In the absence of predator, the prey growth is modeled using logistic equation. Further, we assume that the prey species exhibit Holling type-IV functional response toward predators. We also assume that the predators are supplemented with an additional food of biomass A, which is uniformly distributed in the habitat. Incorporating these assumptions, the prey-predator dynamics with Holling type-IV functional response along with additional food for predators can be described as:

$$\begin{aligned}\frac{\mathrm{d}N(t)}{\mathrm{d}t} &= rN(t)\left(1-\frac{N(t)}{K}\right)\\ &\quad -\left(\frac{cN(t)}{(A\eta\alpha+a)(bN^2(t)+1)+N(t)}\right)P(t)\\ \frac{\mathrm{d}P(t)}{\mathrm{d}t} &= e\left(\frac{N(t)+\eta A(bN^2(t)+1)}{(A\eta\alpha+a)(bN^2(t)+1)+N(t)}\right)P(t)-m_1P(t)\end{aligned} \tag{1}$$

In addition, we also assume that the predators exhibit intra-specific competition. We capture this competition in similar lines with [27, 28]. Accordingly, the system (1) gets transformed to the following system.

$$\begin{aligned}\frac{\mathrm{d}N(t)}{\mathrm{d}t} &= rN(t)\left(1-\frac{N(t)}{K}\right)\\ &\quad -\left(\frac{cN(t)}{(A\eta\alpha+a)(bN^2(t)+1)+N(t)}\right)P(t)\\ \frac{\mathrm{d}P(t)}{\mathrm{d}t} &= e\left(\frac{N(t)+\eta A(bN^2(t)+1)}{(A\eta\alpha+a)(bN^2(t)+1)+N(t)}\right)P(t)\\ &\quad -m_1P(t)-\delta P(t)^2\end{aligned} \tag{2}$$

Here the term η represents the ratio between the search rate of the predator for additional food and prey respectively. The term $-\delta P^2(t)$ accounts for the intra-specific competition among the predators in order to avoid their unbounded growth in the absence of target prey [14, 15]. Here the term α denotes the ratio between the maximum growth rates of the predator when it consumes the prey and additional food respectively. This term can be seen to be an equivalent of quality of additional food. For a complete analysis of model (1), the reader is referred to Vamsi et al. [16].

The biological descriptions of the various parameters involved in the systems (1) and (2) are described in Table 1.

In order to reduce the complexity of the model, we non-dimensionalize the system (2) using the following non-dimensional parameters.

$$N=ax,\ P=\frac{ay}{c},\ \gamma=\frac{K}{a},\ \xi=\frac{\eta A}{a},\ \omega=ba^2,\ m_2=\frac{c}{a\delta}.$$

TABLE 1 Description of variables and parameters present in the systems (1), (2).

Parameter	Definition	Dimension
T	Time	time
N	Prey density	biomass
P	Predator density	biomass
A	Additional food	biomass
r	Prey intrinsic growth rate	$time^{-1}$
K	Prey carrying capacity	biomass
c	Maximum rate of predation	$time^{-1}$
e	Maximum growth rate of predator	$time^{-1}$
m_1	Predator mortality rate	$time^{-1}$
δ	Death rate of predators due to intra-specific competition	$biomass^{-1}\ time^{-1}$
α	Quality of additional food for predators	Dimensionless
b	Group defense in prey	$biomass^{-2}$

Accordingly, system (2) gets reduced to the following system.

$$\begin{aligned}\frac{dx}{dt} &= rx\left(1-\frac{x}{\gamma}\right)-\left(\frac{xy}{(1+\alpha\xi)(\omega x^2+1)+x}\right)\\ \frac{dy}{dt} &= e\left(\frac{x+\xi(\omega x^2+1)}{(\alpha\xi+1)(\omega x^2+1)+x}\right)y-m_1y-m_2y^2\end{aligned} \tag{3}$$

Here the term $\frac{\eta A^2}{N}$ denotes the quantity of additional food perceptible to the predator with respect to the prey relative to the nutritional value of prey to the additional food. Hence the term $\xi = \frac{\eta A}{a}$ can be seen to be an equivalent of quantity of additional food.

In real world scenarios, environmental fluctuations affect the dynamics of the system. In order to capture these fluctuations, we introduce the multiplicative white noise terms into (3). As in Sengupta et al., Bodine and Yust, and Srinivasu et al. [27, 29, 30], we now suppose that the intrinsic growth rate of prey and the death rate of predator are mainly affected by environmental noise such that

$$r \to r+\sigma_1 dW_1(t),\ m_1 \to m_1+\sigma_2 dW_2(t)$$

where $W_i(t)$ $(i = 1,2)$ are the mutually independent standard Brownian motions with $W_i(0) = 0$ and σ_1 and σ_2 are positive constants and they represent the intensities of the white noise.

Also, the system can go through huge, occasionally catastrophic disturbances. Since white noise is a continuous noise, it cannot capture sudden environmental changes. To cater to these, we also apply a discontinuous stochastic process as Lévy jumps to model these abrupt natural phenomenon as in Ma et al. and La Cognata et al. [24, 31].

We now perturb r and m_1 with discontinuous Lévy noise in addition to the continuous white noise. So, we have

$$\begin{aligned}r &\to r+\sigma_1 dW_1(t)+\int_{\mathbb{Y}}\gamma_1(v)\,\widetilde{N}(dt,dv),\ -m_1\\ &\to -m_1+\sigma_2 dW_2(t)+\int_{\mathbb{Y}}\gamma_2(v)\,\widetilde{N}(dt,dv)\end{aligned} \tag{4}$$

According to the Lévy decomposition theorem [32], we have $\widetilde{N}(t,dv) = N(t,dv)-\lambda(dv)t$, where $\widetilde{N}(t,dv)$ is a compensated Poisson process and N is a Poisson counting measure with characteristic measure λ on a measurable subset $\mathbb{Y}$ of $(0,+\infty)$ with $\lambda(\mathbb{Y}) < \infty$. The distribution of Lévy jumps $L_i(t)$ can be completely parameterized by (a_i,σ_i,λ) and satisfies the property of infinite divisibility.

Now, by incorporating noise induced parameters (4) into the reduced deterministic system of Equation (3), we get the following additional food provided stochastic prey-predator system exhibiting Holling type-IV functional response along with the environmental fluctuations captured using the white noise and Lévy noise.

$$\begin{aligned}dx(t) &= x(t)\left[r\left(1-\frac{x(t)}{\gamma}\right)-\left(\frac{y(t)}{(1+\alpha\xi)(\omega x^2(t)+1)+x(t)}\right)\right]dt\\ &\quad+\sigma_1 x(t)dW_1(t)+x(t)\int_{\mathbb{Y}}\gamma_1(v)\,\widetilde{N}(dt,dv)\\ dy(t) &= y(t)\left[e\left(\frac{x(t)+\xi(\omega x^2(t)+1)}{(1+\alpha\xi)(\omega x^2(t)+1)+x(t)}\right)-m_1-m_2y(t)\right]dt\\ &\quad+\sigma_2 y(t)dW_2(t)+y(t)\int_{\mathbb{Y}}\gamma_2(v)\,\widetilde{N}(dt,dv)\end{aligned} \tag{5}$$

2.2. Existence of global positive solution

In order to do the stochastic time optimal control studies for the system (5), we first prove that the system (5) has a unique global positive solution.

Theorem 1. For any given initial value $X(\theta) = (x(\theta),y(\theta)) \in C([-\tau_0,0],\mathbb{R}^{+^2})$, there exists a unique positive global solution $((x(t),y(t))$ of system (5) on $t \geq 0$.

Note: The above theorem for existence of solutions of (5) can be proved in similar lines to the proof in Ma et al. [24] using the Lyapunov method.

Proof. For any given initial value $(x(\theta),y(\theta)) \in C([-\tau_0,0],\mathbb{R}^{+^2})$, there is a unique positive $(x(t),y(t)) \in \mathbb{R}^{+^2}$ for $t \in [0,\tau_e]$, where τ_e is the explosion time. Subsequently, we will show that $\tau_e = \infty$, which yields that $(x(t),y(t))$ is the global solution.

Let $m_0 \geq 0$ be sufficiently large so $x(t)$ and $y(t)$ lie within the interval $[1/m_0,m_0]$. For each $m \geq m_0$, we define the stopping time:

$$\tau_e = \inf\left\{t \in [-\omega,\tau_e) : x \notin \left(\frac{1}{m_0},m_0\right), y \notin \left(\frac{1}{m_0},m_0\right)\right\} \tag{6}$$

Evidently, τ_e is strictly increasing when $m \longrightarrow \infty$. Let $\tau_\infty = \lim_{m\longrightarrow\infty}\tau_m$; thus $\tau_\infty \leq \tau_m$ a.s. Else there exist pairs of constants $T > 0, m_1 \geq m_0$ and $0 < \epsilon < 1$ such that $P(\tau_\infty \leq T) \geq \epsilon, m \geq m_1$.

Let $V(x, y) = x - 1 - \ln x + y - 1 - \ln y$ be a C^2-function.

Using Itô's formula, we get

$$dV = LV dt + \sigma_1(x-1)dW_1 + \sigma_2(y-1)dW_2$$

where

$$\begin{aligned}
LV &= (x-1)\left[r\left(1-\frac{x(t)}{\gamma}\right) - \left(\frac{y(t)}{(1+\alpha\xi)(\omega x^2(t)+1)+x(t)}\right)\right] \\
&\quad +(y-1)\left[e\left(\frac{x(t)+\xi(\omega x^2(t)+1)}{(1+\alpha\xi)(\omega x^2(t)+1)+x(t)}\right)\right. \\
&\quad \left. -m_1 - m_2 y(t)\right] + \frac{\sigma_1^2}{2} + \frac{\sigma_2^2}{2} \\
&= rx - r - \frac{r}{\gamma}x^2 + \frac{r}{\gamma}x - \frac{xy}{(1+\alpha\xi)(\omega x^2+1)+x} \\
&\quad + \frac{y}{(1+\alpha\xi)(\omega x^2+1)+x} + \frac{exy}{(1+\alpha\xi)(\omega x^2+1)+x} \\
&\quad + \frac{e\xi\omega x^2 y}{(1+\alpha\xi)(\omega x^2+1)+x} + \frac{e\xi y}{(1+\alpha\xi)(\omega x^2+1)+x} \\
&\quad - \frac{ex}{(1+\alpha\xi)(\omega x^2+1)+x} - \frac{e\xi\omega x^2}{(1+\alpha\xi)(\omega x^2+1)+x} \\
&\quad - \frac{e\xi}{(1+\alpha\xi)(\omega x^2+1)+x} - m_1 y + m_1 - m_2 y^2 + m_2 y \\
&\quad + \frac{\sigma_1^2}{2} + \frac{\sigma_2^2}{2} \\
&\leq rx - \frac{r}{\gamma}x^2 + \frac{r}{\gamma}x + y \\
&\quad + ey + \frac{\xi e\omega}{\omega(1+\alpha\xi)}y + e\xi y \\
&\quad + m_1 - m_2 y^2 + m_2 y + \frac{\sigma_1^2}{2} + \frac{\sigma_2^2}{2} \\
&= \left[\left(r+\frac{r}{\gamma}\right)x - \frac{r}{\gamma}x^2\right] \\
&\quad + \left[\left(e + e\xi + m_2 + \frac{\xi e}{1+\alpha\xi}\right)y - m_2 y^2\right] \\
&\quad + \left(m_1 + \frac{\sigma_1^2}{2} + \frac{\sigma_2^2}{2}\right),
\end{aligned}$$

From derivative test, we can see that $Ax - Bx^2 \leq \frac{A^2}{4B}$, where A and B are constants. Therefore,

$$\begin{aligned}
LV &\leq \frac{(r+\frac{r}{\gamma})^2}{4\frac{r}{\gamma}} + \frac{1}{4m_2}\left(e + e\xi + m_2 + \frac{\xi e}{1+\alpha\xi}\right)^2 \\
&\quad + \left(m_1 + \frac{\sigma_1^2}{2} + \frac{\sigma_2^2}{2}\right) \leq K,
\end{aligned}$$

where K is a positive constant.

Thus,

$$dV \leq K dt + \sigma_1(x-a)dW_1 + \sigma_2(y-b)dW_2$$

Taking expectation, yields

$$EV(x(\tau_m \wedge T), y(\tau_m \wedge T)) \leq V(x(0), y(0)) + E\int_0^{\tau_m \wedge T} K dt.$$

Setting $\Omega_m = \{\tau_m \wedge T, m \geq m_0\}$, we obtain $P(\Omega_m) \geq \epsilon$. For each $\omega \in \Omega_m$, there are $x(\tau_m, \omega)$, $y(\tau_m, \omega)$ equaling either m or $1/m$ such that

$$\begin{aligned}
V(x(0), y(0)) + KT &\geq E[1_{\Omega_k(\omega)} V(x(\tau_m, \omega), y(\tau_m, \omega))] \\
&\geq \epsilon[(\frac{1}{m} - 1 - \ln\frac{1}{m}) \wedge (m - 1 - \ln m)],
\end{aligned}$$

where $1_{\Omega_k(\omega)}$ denotes the indicator function of $\Omega_k(\omega)$.

For $m \longrightarrow \infty$, we have

$$\infty > V(x(0), y(0)) + KT = \infty$$

which is a contradiction. So, we have that $\tau_\infty = \infty$. This completes the proof. □

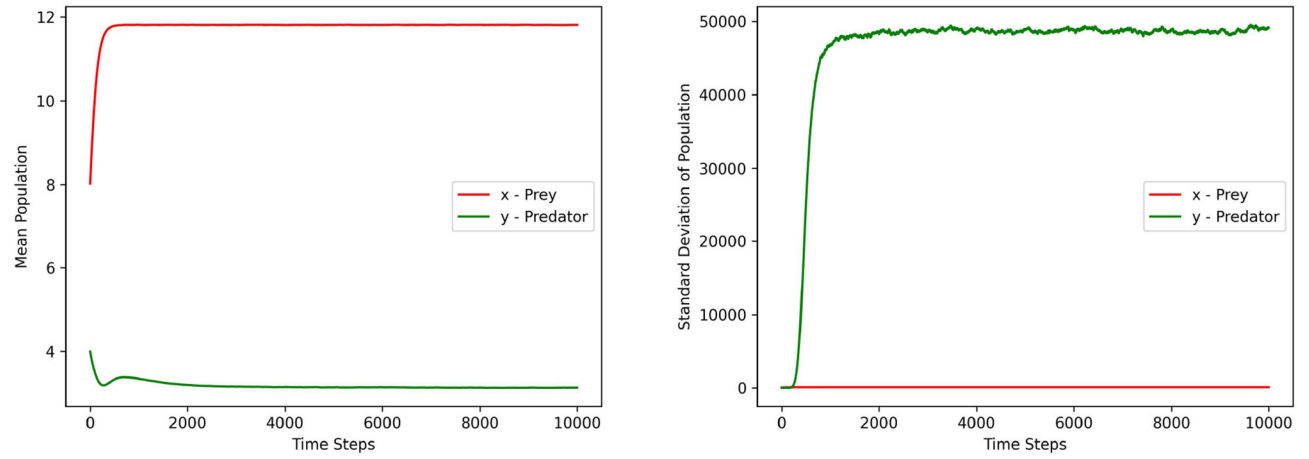

FIGURE 1
This figure depicts the mean and standard deviation of the predator, prey populations for the system (5) with respect to the parameter $\gamma \in (10.1, 15.2)$. The values for other parameters are chosen as $r = 1.5$, $\omega = 15$, $\alpha = 10$, $\xi = 0.10$, $e = 0.4$, $m_1 = 0.15$, $m_2 = 0.01$, $\sigma_1 = \sigma_2 = 0.2$, $\gamma_1 = \gamma_2 = 0.1$.

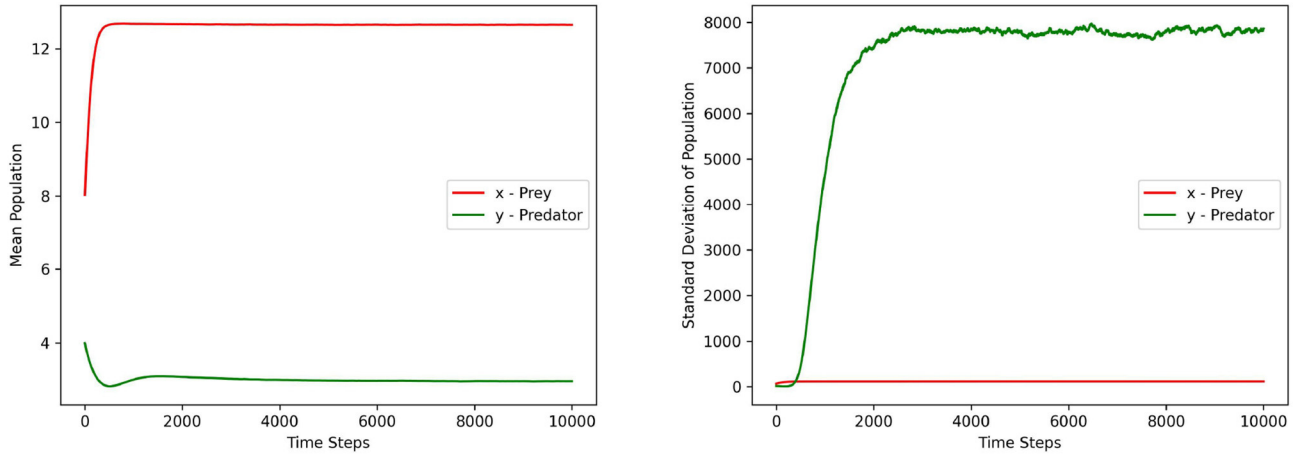

FIGURE 2
This figure depicts the mean and standard deviation of the predator, prey populations for the system (5) with respect to the parameter $\omega \in (8.1, 15.2)$. The values for other parameters are chosen as $r = 1.5$, $\gamma = 12$, $\alpha = 10$, $\xi = 0.10$, $e = 0.4$, $m_1 = 0.15$, $m_2 = 0.01$, $\sigma_1 = \sigma_2 = 0.2$, $\gamma_1 = \gamma_2 = 0.1$.

2.3. Stochastic sensitivity analysis

In this subsection we briefly depict the sensitivity analysis for the remaining parameters that are not perturbed by noise. This can in turn help in understanding the sensitivity of the model with respect to these unperturbed parameters.

Figures 1–3 depict the local sensitivity of the stochastic model (5) w.r.t. the unperturbed parameters γ, ω, and e in the model.

In this local sensitivity analysis, we simulated the system (5) 1,000 times for each value in the chosen parameter range.

Each figure contains two sub plots where the first and second plot depict the mean and standard deviation of prey, predator populations for the range of chosen parameter values respectively.

From the plots in Figures 1–3, it can be seen that the prey population in the system (5) is more sensitive with respect to these parameters than the predator population.

3. Stochastic time-optimal control problems

In this section, we formulate and study the stochastic time-optimal control problem for the prey-predator system (5) with quality (α) and quantity (ξ) of additional food as control variables.

3.1. Quality of additional food as stochastic time optimal control

In this subsection, we characterize the optimal quality of additional food for driving the system (5) to a desired equilibrium state in minimum time using the stochastic maximum principle. We fix the quantity of additional food $\xi > 0$ to be a constant and choose the objective functional to be minimized for this stochastic time optimal control problem as follows.

$$J(\alpha) = E\left[\int_0^T 1dt\right]. \tag{7}$$

From the Sufficient Stochastic Maximum Principle [33] for the optimal control problems of jump diffusion, we characterize the optimal solution of the stochastic time optimal control problem with state space as the solutions of (5) and the objective functional (7).

Let (p^*, q^*, r^*) be a solution of the adjoint equation in the unknown processes $p(t) \in \mathbb{R}^2$, $q(t) \in \mathbb{R}^{2\times 2}$, $r(t,z) \in \mathbb{R}^2$ satisfying the backward differential equations

$$\begin{aligned}
dp_1(t) = &\Bigg[\left(-r + \frac{2rx}{\gamma} - \frac{2\omega(1+\alpha\xi)x+1}{((1+\alpha\xi)(\omega x^2+1)+x)^2}\right)p_1(t) \\
&- \frac{(1-\omega x^2)(1+(\alpha-1)\xi)}{((1+\alpha\xi)(\omega x^2+1)+x)^2} eyp_2(t) - \sigma_1 q_1 \\
&- \int \gamma_1(v) r_1 \nu_1(dz_1)\Bigg]dt \\
&+ q_1(t)dW_1(t) + q_2(t)dW_2(t) + \int_{\mathbb{R}^n} r_1 \widetilde{N}(dt, dz) \\
dp_2(t) = -&\Bigg[\frac{-x}{(1+\alpha\xi)(\omega x^2+1)+x} p_1(t) \\
&+ \left(\frac{e(x+\xi(\omega x^2+1))}{(1+\alpha\xi)(\omega x^2+1)+x} - m_1 - 2m_2 y\right)p_2(t) \\
&+ \sigma_2 q_4 + \int \gamma_2(v) r_2 \nu_2(dz_2)\Bigg]dt \\
&+ q_3(t)dW_1(t) + q_4(t)dW_2(t) + \int_{\mathbb{R}^n} r_2 \widetilde{N}(dt, dz) \\
p_1(T) = 0,\ &p_2(T) = 0
\end{aligned} \tag{8}$$

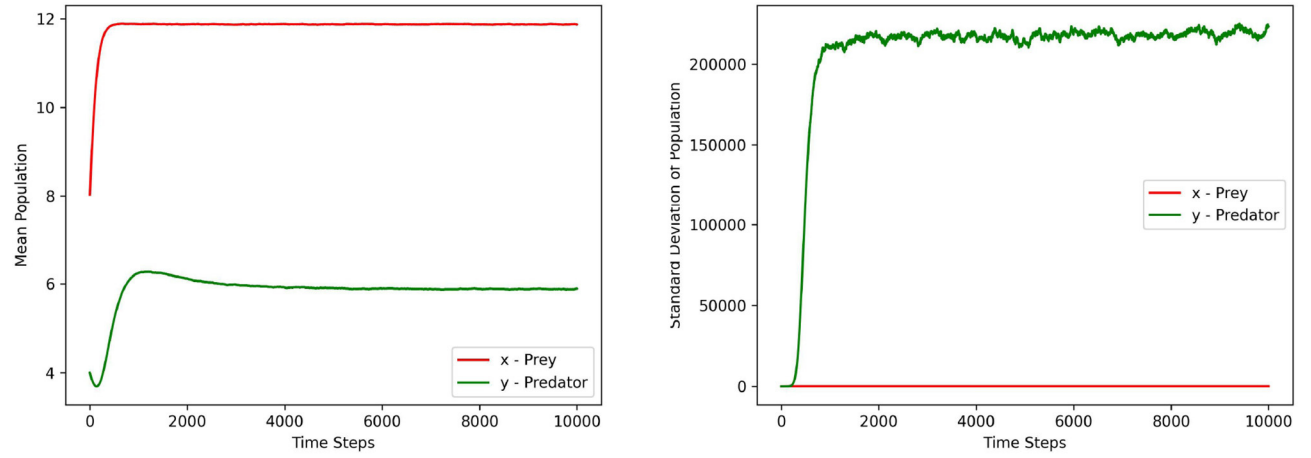

FIGURE 3
This figure depicts the mean and standard deviation of the predator, prey populations for the system (5) with respect to the parameter $e \in (0.1, 0.9)$. The values for other parameters are chosen as $r = 1.5,\ \gamma = 12,\ \omega = 15,\ \alpha = 10,\ \xi = 0.10,\ m_1 = 0.15,\ m_2 = 0.01,\ \sigma_1 = \sigma_2 = 0.2,\ \gamma_1 = \gamma_2 = 0.1$.

The Hamiltonian associated with this control problem is defined as follows.

$$\begin{aligned} &H(t,x,y,\alpha,p,q,r) \\ &= 1 + \left[r(1-\frac{x}{\gamma}) - \frac{y}{(1+\alpha\xi)(1+\omega x^2)+x} \right] xp_1 \\ &\quad + \left[\frac{e(x+\xi(\omega x^2+1))}{(1+\alpha\xi)(1+\omega x^2)+x} - m_1 - m_2 y \right] yp_2 \\ &\quad + \sigma_1 x q_1 + \sigma_2 y q_4 + x\int \gamma_1 r_1 \nu_1(dz_1) + y\int \gamma_2(\nu) r_2 \nu_2(dz_2) \end{aligned} \tag{9}$$

Let $U = \{\alpha(t) | 0 \leq \alpha(t) \leq \alpha_{max} \forall t \in (0, t_f]\}$ where $\alpha_{max} \in \mathbb{R}^+$. Let $\alpha^* \in U$ with the corresponding solution $(x^*, y^*) = [x(u^*), y(u^*)]$.

From the Arrow condition in the sufficient stochastic maximum Principle [33], we have

$$\begin{aligned} &\frac{\partial H}{\partial \alpha}\Big|_{\alpha^*} = 0 \\ &\quad \Longrightarrow \left[-yxp_1 \frac{-\xi(\omega x^2+1}{((1+\alpha\xi)(\omega x^2+1)+x)^2} \right. \\ &\qquad \left. - \frac{eyp_2(x+\xi(\omega x^2+1))(\xi(\omega x^2+1))}{((1+\alpha\xi)(\omega x^2+1)+x)^2} \right]\Big|_* = 0 \\ &\quad \Longrightarrow \left[yxp_1 - eyp_2(x+\xi(\omega x^2+1)) \right]\Big|_* = 0 \\ &\quad \Longrightarrow x^* p_1^* = ep_2^*(x^* + \xi(\omega x^{*^2}+1)) \end{aligned}$$

Hence the optimal control α^* should satisfy the following condition.

$$x^* p_1^* = ep_2^*(x^* + \xi(\omega x^{*^2}+1)) \tag{10}$$

Since the analytical solution of (8) is complex to solve, we numerically simulate these results in Subsection 3.4.

3.2. Quantity of additional food as stochastic time optimal control

In this subsection, we characterize the optimal quantity of additional food for driving the system (5) to a desired equilibrium state in minimum time using the stochastic maximum principle. We fix the quality of additional food $\alpha > 0$ to be a constant and choose the objective functional to be minimized for this stochastic time optimal control problem as follows.

$$J(\xi) = E\left[\int_0^T 1 dt \right]. \tag{11}$$

From the Sufficient Stochastic Maximum Principle [33] for the optimal control problems of jump diffusion, we characterize the optimal solution of the stochastic time optimal control problem with state space as the solutions of (5) and the objective functional (11).

Let (p^*, q^*, r^*) be a solution of the adjoint equation in the unknown processes $p(t) \in \mathbb{R}^2$, $q(t) \in \mathbb{R}^{2\times 2}$, $r(t,z) \in \mathbb{R}^2$ satisfying the backward differential equations

$$\begin{aligned} dp_1(t) = &\left[\left(-r + \frac{2rx}{\gamma} - \frac{2\omega(1+\alpha\xi)x+1}{((1+\alpha\xi)(\omega x^2+1)+x)^2} \right) p_1(t) \right. \\ &- \frac{(1-\omega x^2)(1+(\alpha-1)\xi)}{((1+\alpha\xi)(\omega x^2+1)+x)^2} eyp_2(t) \\ &\left. - \sigma_1 q_1 - \int \gamma_1(\nu) r_1 \nu_1(dz_1) \right] dt \\ &+ q_1(t) dW_1(t) + q_2(t) dW_2(t) + \int_{\mathbb{R}^n} r_1 \widetilde{N}(dt, dz) \end{aligned} \tag{12}$$

$$dp_2(t) = -\Bigg[\frac{-x}{(1+\alpha\xi)(\omega x^2+1)+x}p_1(t) + \Big(\frac{e(x+\xi(\omega x^2+1))}{(1+\alpha\xi)(\omega x^2+1)+x} - m_1 - 2m_2 y\Big)p_2(t) + \sigma_2 q_4 + \int \gamma_2(v) r_2 \nu_2(dz_2)\Bigg]dt + q_3(t)dW_1(t) + q_4(t)dW_2(t) + \int_{\mathbb{R}^n} r_2 \widetilde{N}(dt,dz)$$

$$p_1(T) = 0,\ p_2(T) = 0$$

The Hamiltonian associated with this control problem is defined as follows.

$$\begin{aligned} &H(t,x,y,\xi,p,q,r) \\ &= 1 + \left[r(1-\frac{x}{\gamma}) - \frac{y}{(1+\alpha\xi)(1+\omega x^2)+x}\right]xp_1 \\ &+ \left[\frac{e(x+\xi(\omega x^2+1))}{(1+\alpha\xi)(1+\omega x^2)+x} - m_1 - m_2 y\right]yp_2 \\ &+ \sigma_1 x q_1 + \sigma_2 y q_4 + x\int \gamma_1 r_1 \nu_1(dz_1) + y\int \gamma_2(v) r_2 \nu_2(dz_2) \end{aligned} \tag{13}$$

Let $U = \{\xi(t) | 0 \le \xi(t) \le \xi_{max} \forall t \in (0, t_f]\}$ where $\xi_{max} \in \mathbb{R}^+$. Let $\xi^* \in U$ with the corresponding solution $(x^*, y^*) = (x(\xi^*), y(\xi^*))$.

From the Arrow condition in the sufficient stochastic maximum Principle [33], we have

$$\begin{aligned} &\frac{\partial H}{\partial \xi}\Big|_{\xi^*} = 0 \\ &\Longrightarrow \Bigg[-yxp_1\frac{-\alpha(\omega x^2+1}{((1+\alpha\xi)(\omega x^2+1)+x)^2} + eyp_2\left(\frac{((1+\alpha\xi)(\omega x^2+1)+x)(\omega x^2+1) - \alpha(\omega x^2+1)(x+\xi(\omega x^2+1))}{((1+\alpha\xi)(\omega x^2+1)+x)^2}\right)\Bigg]\Bigg|_* = 0 \\ &\Longrightarrow \Big[\alpha xy(\omega x^2+1)p_1 + eyp_2(\omega x^2+1)(x(1-\alpha)(\omega x^2+1))\Big]\Big|_* = 0 \\ &\Longrightarrow \Big[\alpha x p_1 + ep_2(1+\omega x^2 + x(1-\alpha))\Big]\Big|_* = 0 \\ &\Longrightarrow \alpha x^* p_1^* + ep_2^*(1+\omega x^{*^2} + x^*(1-\alpha)) = 0 \end{aligned}$$

Hence the optimal control ξ^* should satisfy the following condition.

$$\alpha x^* p_1^* + ep_2^*(1+\omega x^{*^2} + x^*(1-\alpha)) = 0 \tag{14}$$

Since the analytical solution of (8) is complex to solve, we numerically simulate these results in Subsection 3.4.

3.3. Existence and uniqueness of solutions for the Forward Backward Stochastic Differential Equations with Jumps (FBSDEJ)

We so far obtained the adjoint Equations 8, 12 for the state Equation 5 and the objective functional (7), (11) using the sufficient stochastic maximum principle respectively. Upon simplifying the results obtained from the arrow condition (10), (14) from earlier two subsections, we see that the optimal controls are given by

$$\alpha^* = \frac{ep_2^*(1+x^*+\omega x^{*^2})}{ep_2^* x^* - p_1^* x^*},\ \xi^* = \frac{x^* p_1^* - ex^* p_2^*}{ep_2^*(1+\omega x^{*^2})} \tag{15}$$

In this section, we now prove the existence of optimal controls by proving the existence of the solutions for the FBSDEJ [(5), (8), (12)] which establishes the existence of (x^*, y^*, p_1^*, p_2^*) for all simulation purposes. Using the theorem in Al-Hussein and Gherbal [34], we now prove the existence of the optimal controls (15) in the following theorem.

Theorem 2. For any $(x_0, y_0) \in \mathbb{R}^{+^2}$, the FBSDEJ [(5), (8), (12)] admits an optimal stochastic control.

Proof. Let $(X_t)_{t\ge 0}$ be the solution of the Stochastic Differential Equation with Jumps (SDEJ)

$$\mathrm{d}X_t = b(X_t)\mathrm{d}t + \sigma(X_t)\mathrm{d}W(t) + \int_{\mathbb{R}} \Gamma(v)\widetilde{N}(\mathrm{d}t, \mathrm{d}v)$$

Here the term $b(X_t)$ denotes the drift coefficient, the term $\sigma(X_t)$ denotes the diffusion coefficient and the term $\Gamma(v)$ denotes the poisson term coefficient.

The theorem 1 in Section 3 guaranties the monotonicity and Lipschitz continuity of the drift coefficient, the diffusion coefficient and the poisson term coefficient of the state Equation 5.

Following the the existence and uniqueness theorem of FBDSDEJ in Al-Hussein and Gherbal [34], we are only left to prove the monotonicity and Lipschitz continuity of the drift and diffusion terms of the adjoint system of Equation 8.

From (8), due to the positivity of state variables guaranteed by theorem 1, the drift term and the diffusion terms are given

as follows.

$$b(X_t) \leq \begin{pmatrix} \left(\frac{2rx}{\gamma}\right) p_1(t) + \left(\omega e x^2 y\right) p_2(t) \\ (x) p_1(t) + (m_1 + 2m_2 y) p_2(t) \end{pmatrix}, \ \sigma(X_t) = \begin{pmatrix} q_1(t) & q_2(t) \\ q_3(t) & q_4(t) \end{pmatrix}$$

Since the drift coefficient is a linear combination of adjoint terms (p_1, p_2), the monotonicity and Lipschitz continuity are guaranteed.

In addition to this, the diffusion coefficient is independent of the adjoint terms (p_1, p_2). Therefore, the monotonicity and Lipschitz continuity are guaranteed for the diffusion coefficients.

Hence the existence of unique stochastic optimal controls are proved for FBSDEJ [(5), (8), (12)]. □

3.4. Numerical simulations

In this section, we perform the extensive numerical simulations using python by choosing the following parameters [24] for the model (5). $r = 1.5$, $\gamma = 12, \omega = 15$, $e = 0.4, m_1 = 0.15$, $m_2 = 0.01$, $\sigma_1 = \sigma_2 = 0.02$, $\gamma_1 = 1, \gamma_2 = 1$. In these simulations, white noise is simulated using the Box-Normal transformations and the poisson noise is simulated using the poisson point processes [35]. The state Equation 5 and the adjoint Equations 8, 12 are simulated using the Forward Backward Doubly Stochastic Differential Equations with Jumps (FBDSDEJ) method. The subplots in Figures 4, 5 depict the optimal state trajectories, optimal co-state trajectories, phase diagram, optimal quality of additional food and the optimal quantity of additional food respectively.

3.4.1. Applications to biological conservation

The subplots (4a) and (4b) depicts the optimal state trajectory of the system (5) from the initial state $(2, 8)$ that stabilizes over time around the state $(16, 90)$. The subplot (4d) gives the phase diagram which shows the trajectories are stabilized over high values of prey and predator. The subplots (4e) and (4f) depicts the optimal quality and quantity of additional food respectively. These plots show that the high quality of additional food is required to achieve biological conservation. Even if the quantity of additional food is lower, still we will be able to achieve biological conservation with higher quality of additional food.

3.4.2. Applications to pest management

The subplots (5a) and (5b) depicts the optimal state trajectory of the system (5) from the initial state $(7, 5)$. It can be seen that the system can be driven to a low prey dominated state. The subplot (5d) depicts this property more clearly through the phase diagram where it reaches the lowest prey value over the time. The subplots (5e) and (5f) depicts that a lesser quality of additional food and a lower quantity of additional food is good enough to achieve pest management where pest is viewed as prey.

3.5. Sensitivity of time optimal controls

In this subsection we perform the sensitivity analysis for the optimal control variables $\alpha(t)$ and $\xi(t)$ with respect to the different values for the model parameters

In Figure 6, frames (6a) and (6b) depict the sensitivity of the control variables with respect to the parameters r and γ respectively. Frames (6c) and (6d) depict the sensitivity of the control variables with respect to the parameters ω and e respectively. In Figure 6, frames (6a) and (6b) depict the sensitivity of the control variables with respect to the parameters m_1 and m_2, respectively.

From the sensitivity analysis depicted in Figures 6, 7 we see that the optimal quality control seems to be more sensitive with respect to the parameter r in comparison to the other parameters.

4. Effect of noise on the optimal control problem

In this section, we briefly study the effects of discrete and continuous noise on the system (3). We compared the dynamics of the state trajectories and control variables with and without these noises.

In Figure 8, frames (8a) and (8b) depict the optimal prey and optimal predator populations respectively with no noise, white noise and with both white noise and Lévy noise. Frame (8c) depicts the corresponding trajectories of co-state variables. Frame (8d) depicts the phase space of the state variables. Frames (8e) and (8f) depict the optimal quality and quantity control trajectories respectively.

From the plots in Figure 8 we see that both the discrete and continuous noise can lead to fluctuations in prey dynamics compared to that of predator. From the phase plots it can be seen that the converging pattern to the final state more or less follow a similar trend. Overall we find that the prey seems to be more influenced by the noise than that of predator.

5. Discussions and conclusions

This paper studies a stochastic prey-predator system exhibiting Holling type-IV functional response along with the combined influence of white noise and Lévy noise. We do the time-optimal control studies for this system, with the quality and the quantity of additional food as control variables. To begin with, we formulated a stochastic model by considering multiplicative noise to both prey and predator. In theorem 1, we proved the existence of a unique positive global solution of (5). Further, we formulated the time-optimal control problem with the objective to minimize the final time in which the system reaches the pre-defined state. Using the sufficient stochastic maximum principle, we characterized the optimal control values. In theorem 2, we proved that the existence and uniqueness of Forward Backward Doubly Stochastic Differential Equations with Jumps (FBDSDEJ). We also numerically simulated the theoretical findings and applied them in the context of biological conservation and pest management.

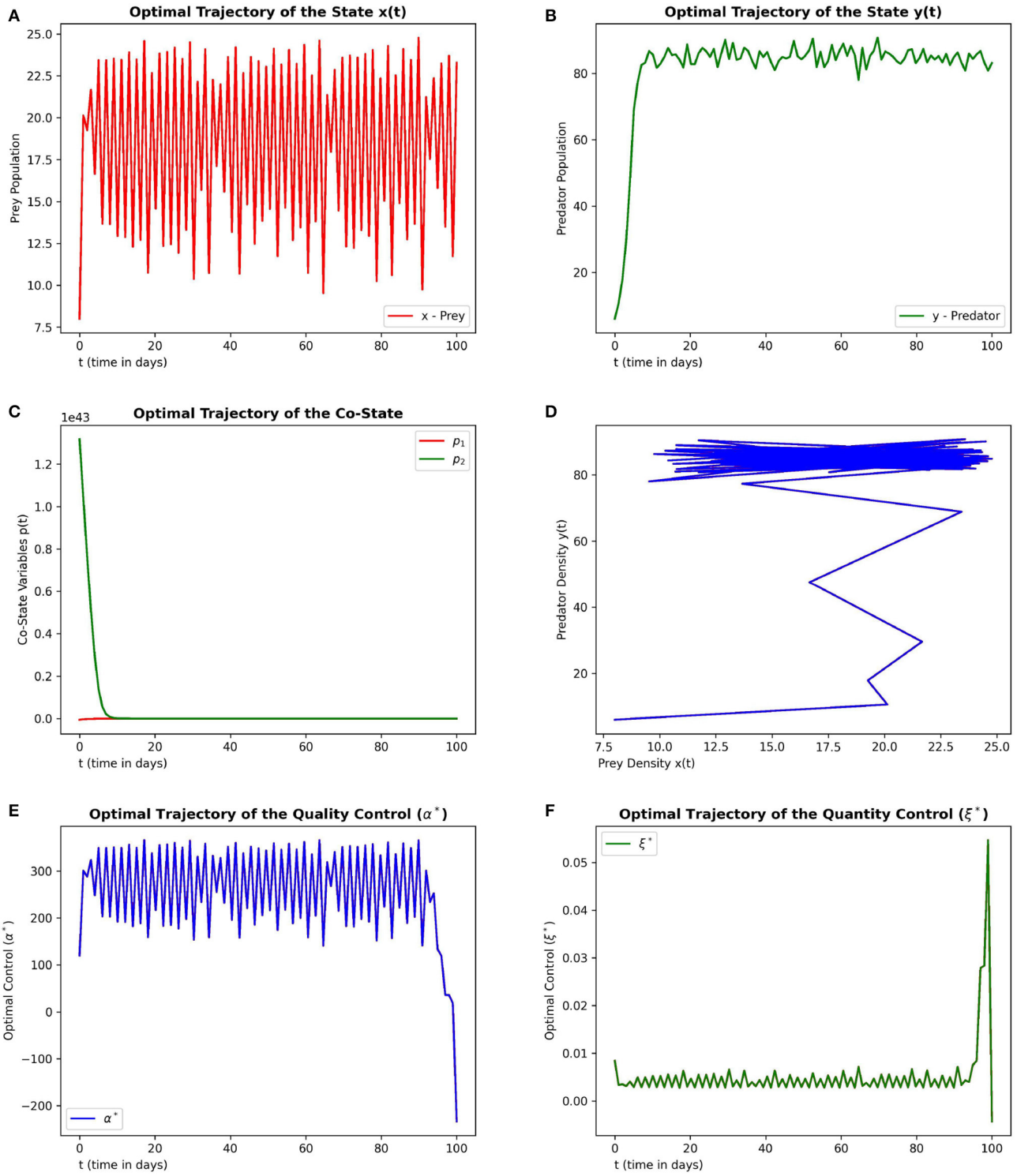

FIGURE 4
This figure depicts the simulations of time-optimal control problem with respect to the control variables in the context of biological conservation. The subfigures **(A–C)** depict the optimal prey, predator and co-state vectors respectively. The subfigure **(D)** depicts the phase diagram between prey and predator densities. The subfigures **(E, F)** depict the optimal quality and quantity control variables. The parameter values are chosen as $r = 1.5,\ \gamma = 12,\ \omega = 15,\ e = 0.4,\ m_1 = 0.15,\ m_2 = 0.01$.

To understand the sensitivity of this stochastic system, we firstly performed the sensitivity analysis with respect to the individual parameters and later did the sensitivity analysis for the optimal control variables with respect to the parameters of the system. The findings revealed that the stochastic system as such is minimally sensitive with respect to the system parameters and the optimal

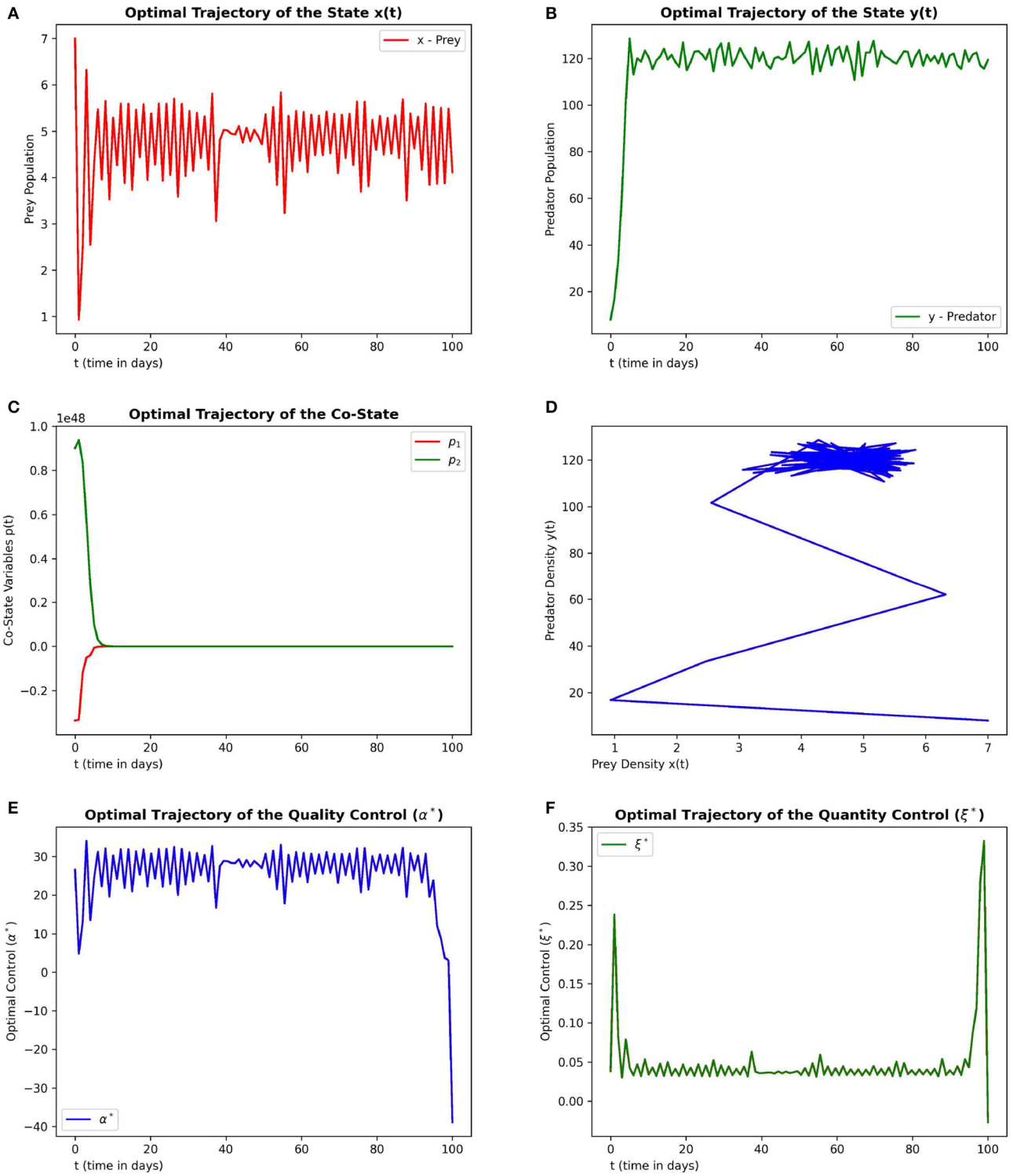

FIGURE 5
This figure depicts the simulations of time-optimal control problem with respect to the control variables in the context of pest management. The subfigures **(A–C)** depict the optimal prey, predator and co-state vectors respectively. The subfigure **(D)** depicts the phase diagram between prey and predator densities. The subfigures **(E, F)** depict the optimal quality and quantity control variables. The parameter values are chosen as $r = 1.5,\ \gamma = 4,\ \omega = 6,\ e = 0.6,\ m_1 = 0.1,\ m_2 = 0.01$.

quality control variable seems to be more sensitive with respect to the parameter, growth rate r relative to the other parameters.

Finally a brief study on the influence of different noises on this stochastic system revealed that both the discrete and continuous noise induced fluctuations in the prey dynamics and seem to have minimal effect on the predator dynamics.

Some of the salient features of this work include the following. Unlike the most traditional papers, here we

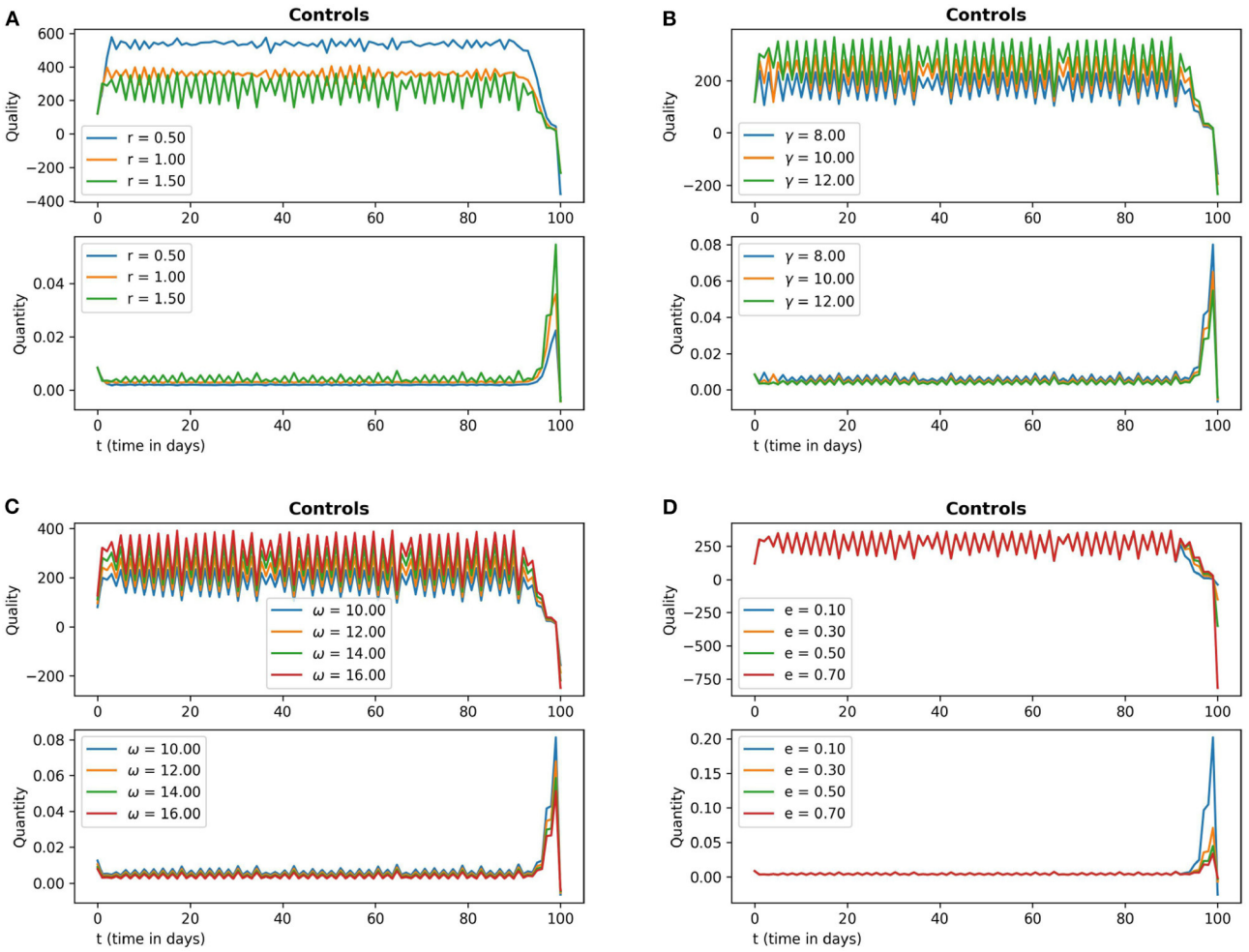

FIGURE 6
The subfigures **(A–D)** in this figure depict the optimal quality and optimal quantity of additional food (15) with respect to the parameter values r, γ, ω and e respectively. The other parameter values are chosen as $r = 1.5,\ \gamma = 12,\ \omega = 15,\ e = 0.4,\ m_1 = 0.15,\ m_2 = 0.01$.

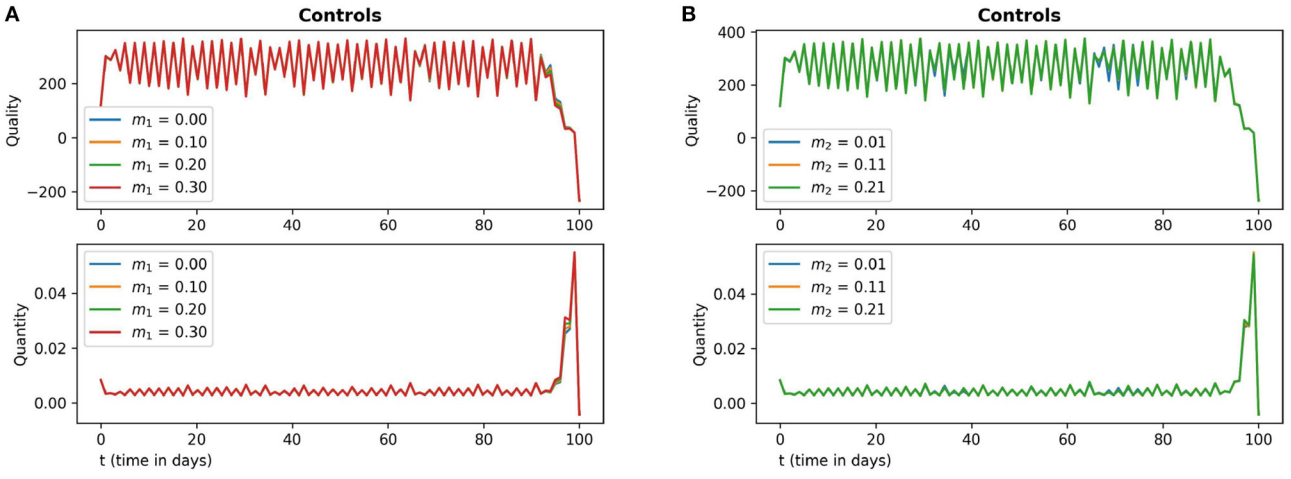

FIGURE 7
The subfigures **(A, B)** in this figure depict the optimal quality and optimal quantity of additional food (15) with respect to the parameter values m_1 and m_2 respectively. The other parameter values are chosen as $r = 1.5,\ \gamma = 12,\ \omega = 15,\ e = 0.4$.

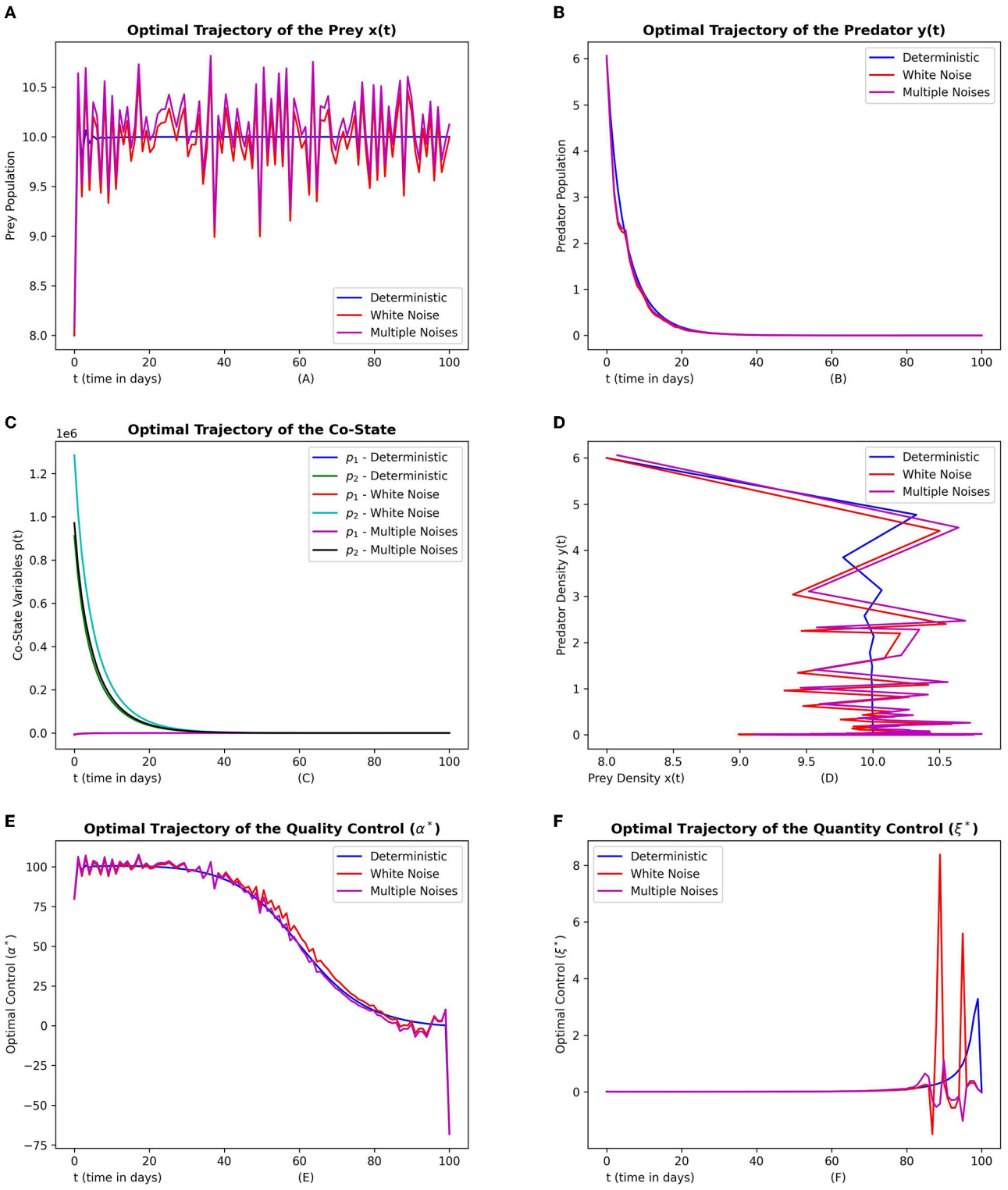

FIGURE 8
This figure depicts the simulations of time-optimal control problem with respect to the control variables. The subfigures **(A–C)** depict the optimal prey, predator and co-state vectors respectively. The subfigure **(D)** depicts the phase diagram between prey and predator densities. The subfigures **(E, F)** depict the optimal quality and quantity control variables. The three graphs in each subfigure corresponds to the dynamics of the system with no noise, white noise and multiple noises. The parameter values are chosen as $r = 1.5$, $\gamma = 12$, $\omega = 15$, $e = 0.4$, $m_1 = 0.15$, $m_2 = 0.01$.

considered a stochastic time-optimal control problem. As Intra-specific competition among predators is ineluctable, we also explicitly incorporated the intra-specific competition into our model. This paper mainly deals with the novel study of the time-optimal control problems where the state equations involve both the discrete and continuous noise which is challenging. We also performed the stochastic sensitivity analysis.

To sum up this work has been an initial attempt and a first of its kind dealing with the Stochastic Time Optimal Control studies for prey-predator systems involving group defense of the prey. Since this is an initial exploratory research we didn't include finer specificalities such as mutual interference of the predators and also did not elaborate much on the stochastic bifurcation aspect. In future we wish to incorporate and study these aspects. We also intend to extend these studies in the setting of Markov Chain and Partial Differential Equations.

Data availability statement

The original contributions presented in the study are included in the article/supplementary material, further inquiries can be directed to the corresponding author.

Author contributions

DP conceived the idea, worked and executed all the theoretical and numerical findings, and framed the manuscript. DV conceived and designed the paper, helped in structuring, and finalizing the manuscript. All authors contributed to the article and approved the submitted version.

Funding

This research was supported by National Board of Higher Mathematics (NBHM), Department of Atomic Energy (DAE), Government of India under project grant-Time Optimal Control Studies and Bifurcation Analysis of Coupled Nonlinear Dynamical Systems with Applications to Pest Management, Sanction number: [02011/11/2021NBHM(R.P)/R&D II/10074].

Acknowledgments

The authors dedicate this paper to the founder chancellor of SSSIHL, Bhagawan Sri Sathya Sai Baba. DV also dedicates this paper to his loving elder brother D. A. C. Prakash who still lives in his heart.

Conflict of interest

The authors declare that the research was conducted in the absence of any commercial or financial relationships that could be construed as a potential conflict of interest.

Publisher's note

References

1. Lotka AJ. *Elements of Physical Biology*. Philadelphia, PA: Williams & Wilkins (1925).

2. Volterra V. Variazioni e fluttuazioni del numero d'individui in specie animali conviventi. *Memoria della Reale Accademia Nazionale dei Lincei*. (1927) 2:31–113.

3. Kot M. *Elements of Mathematical Ecology*. Cambridge: Cambridge University Press (2001).

4. Metz JA, Diekmann O. *The Dynamics of Physiologically Structured Populations*. Cham: Springer (2014). vol. 68.

5. Geritz S, Gyllenberg M. A mechanistic derivation of the DeAngelis–Beddington functional response. *J Theoret Biol*. (2012) 314:106–8. doi: 10.1016/j.jtbi.2012.08.030

6. Arditi R, Ginzburg LR. Coupling in predator-prey dynamics: ratio-dependence. *J Theoret Biol*. (1989) 139:311–26.

7. Hassell M, Varley G. New inductive population model for insect parasites and its bearing on biological control. *Nature*. (1969) 223:1133–7.

8. Crowley PH, Martin EK. Functional responses and interference within and between year classes of a dragonfly population. *J North Am Benthol Soc*. (1989) 8:211–21.

9. Freedman HI, Wolkowicz GS. Predator-prey systems with group defence: the paradox of enrichment revisited. *Bullet Math Biol*. (1986) 48:493–508.

10. Yano S. Cooperative web sharing against predators promotes group living in spider mites. *Behav Ecol Sociobiol*. (2012) 66:845–53. doi: 10.1007/s00265-012-1332-5

11. McClure M, Despland E. Defensive responses by a social caterpillar are tailored to different predators and change with larval instar and group size. *Naturwissenschaften*. (2011) 98:425–34. doi: 10.1007/s00114-011-0788-x

12. Srinivasu PDN, Prasad BSRV, Venkatesulu M. Biological control through provision of additional food to predators: a theoretical study. *Theoret Popul Biol*. (2007) 72:111–20. doi: 10.1016/j.tpb.2007.03.011

13. Srinivasu PDN, Prasad BSRV. Time optimal control of an additional food provided predator–prey system with applications to pest management and biological conservation. *J Math Biol*. (2010) 60:591–613. doi: 10.1007/s00285-009-0279-2

14. Srinivasu PDN, Vamsi DKK, Aditya I. Biological conservation of living systems by providing additional food supplements in the presence of inhibitory effect: a theoretical study using predator–prey models. *Diff Eq Dyn Syst*. (2018) 26:213–46. doi: 10.1007/s12591-016-0344-4

15. Srinivasu PDN, Vamsi DKK, Ananth VS. Additional food supplements as a tool for biological conservation of predator-prey systems involving type III functional response: a qualitative and quantitative investigation. *J Theoret Biol*. (2018) 455:303–18. doi: 10.1016/j.jtbi.2018.07.019

16. Vamsi DKK, Kanumoori DSSM, Chhetri B. Additional food supplements as a tool for biological conservation of biosystems in the presence of inhibitory effect of the prey. *Acta Biotheoret*. (2020) 68:321–55. doi: 10.1007/s10441-019-09371-x

17. Ananth VS, Vamsi DKK. An optimal control study with quantity of additional food as control in prey-predator systems involving inhibitory effect. *Comput Math Biophys*. (2021) 9:114–45. doi: 10.1515/cmb-2020-0121

18. Sabelis MW, Van Rijn PC. When does alternative food promote biological pest control? *IOBC WPRS Bulletin*. (2006) 29:195. Available online at: https://bugwoodcloud.org/bugwood/anthropod/2005/vol2/8e.pdf

19. Ananth VS, Vamsi DKK. Achieving minimum-time biological conservation and pest management for additional food provided predator–Prey systems involving inhibitory effect: a qualitative investigation. *Acta Biotheoret*. (2022) 70:1–51. doi: 10.1007/s10441-021-09430-2

20. May RM. Stability and complexity in model ecosystems. In: *Stability and Complexity in Model Ecosystems*. Princeton, NJ: Princeton University Press (2019) 109–138.

21. Elton CS. *The Ecology of Invasions by Animals and Plants*. Berlin: Springer Nature (2020).

22. Li L, Zhao W. Deterministic and stochastic dynamics of a modified Leslie-Gower prey-predator system with simplified Holling-type IV scheme. *Math Biosci Eng*. (2021) 18:2813–31. doi: 10.3934/mbe.2021143

23. Xu D, Liu M, Xu X. Analysis of a stochastic predator–prey system with modified Leslie–Gower and Holling-type IV schemes. *Phys A Stat Mech Appl*. (2020) 537:122761. doi: 10.1016/j.physa.2019.122761

24. Ma T, Meng X, Chang Z. Dynamics and optimal harvesting control for a stochastic one-predator-two-prey time delay system with jumps. *Complexity*. (2019) 2019. doi: 10.1155/2019

25. Jia W, Xu Y, Li D, Hu R. Stochastic analysis of predator–prey models under combined gaussian and poisson white noise via stochastic averaging method. *Entropy*. (2021) 23:1208. doi: 10.3390/e23091208

26. Prakash DB, Vamsi DKK. Stochastic optimal and time-optimal control studies for additional food provided prey–predator systems involving Holling type III functional response. *Comput Math Biophys*. (2023) 11:20220144. doi: 10.48550/arXiv.2207.06668

27. Sengupta S, Das P, Mukherjee D. Stochastic non-autonomous Holling type-III prey-predator model with predator's intra-specific competition. *Discr Contin Dyn Syst B*. (2018) 23:3275. doi: 10.3934/dcdsb.2018244

28. Bodine EN, Yust AE. Predator-prey dynamics with intraspecific competition and an allee effect in the predator population. *Lett Biomathemat*. (2017) 4:23–38. doi: 10.1080/23737867.2017.1282843

29. Bera SP, Maiti A, Samanta G. Stochastic analysis of a prey–predator model with herd behaviour of prey. *Nonlin Anal*. (2016) 21:345–61. doi: 10.15388/NA.2016.3.4

30. Belabbas M, Ouahab A, Souna F. Rich dynamics in a stochastic predator-prey model with protection zone for the prey and multiplicative noise applied on both species. *Nonlin Dyn*. (2021) 106:2761–80. doi: 10.1007/s11071-021-06903-4

31. La Cognata A, Valenti D, Dubkov A, Spagnolo B. Dynamics of two competing species in the presence of Lévy noise sources. *Phys Rev E*. (2010) 82:e011121. doi: 10.1103/PhysRevE.82.011121

32. Øksendal B, Sulem A. *Stochastic Control of Jump Diffusions*. Cham: Springer (2005).

33. Framstad NC, Øksendal B, Sulem A. Sufficient stochastic maximum principle for the optimal control of jump diffusions and applications to finance. *J Opt Theory Appl*. (2004) 121:77–98. doi: 10.1023/B:JOTA.0000026132.62934.96

34. Al-Hussein A, Gherbal B. Existence and uniqueness of the solutions of forward-backward doubly stochastic differential equations with Poisson jumps. *Random Operat Stochast Eq*. (2020)28:253–68. doi: 10.1515/rose-2020-2044

35. Zou X, Wang K. Numerical simulations and modeling for stochastic biological systems with jumps. *Commun Nonlin Sci Numer Simulat*. (2014) 19:1557–68. doi: 10.1016/j.cnsns.2013.09.010

frontiers | Frontiers in Applied Mathematics and Statistics

TYPE Original Research
PUBLISHED 16 August 2023
DOI 10.3389/fams.2023.1225137

OPEN ACCESS

EDITED BY
Alain Miranville,
University of Poitiers, France

REVIEWED BY
María Fabiana Laguna,
Bariloche Atomic Centre (CNEA), Argentina
Pankaj Tiwari,
University of Kalyani, India
Eric Okyere,
University of Energy and Natural Resources, Ghana

*CORRESPONDENCE
Daniel J. Coffield Jr.
✉ dcoffiel@umich.edu

RECEIVED 18 May 2023
ACCEPTED 27 July 2023
PUBLISHED 16 August 2023

CITATION
Coffield DJ Jr, Spagnuolo AM, Capouellez R and Stryker GA (2023) A mathematical model for Chagas disease transmission with neighboring villages.
Front. Appl. Math. Stat. 9:1225137.
doi: 10.3389/fams.2023.1225137

A mathematical model for Chagas disease transmission with neighboring villages

Daniel J. Coffield Jr.[1]*, Anna Maria Spagnuolo[2], Ryan Capouellez[3] and Gabrielle A. Stryker[4]

[1]Department of Mathematics, University of Michigan-Flint, Flint, MI, United States, [2]Department of Mathematics and Statistics, Oakland University, Rochester, MI, United States, [3]Computer Science Department, Courant Institute of Mathematical Sciences, New York University, New York, NY, United States, [4]Department of Biological Sciences, Central Washington University, Ellensburg, WA, United States

Chagas disease has been the target of widespread control programs, primarily through residual insecticide treatments. However, in some regions like the Gran Chaco, these efforts have failed to sufficiently curb the disease. Vector reinfestation into homes and vector resistance to insecticides are possible causes of the control failure. This work proposes a mathematical model for the dynamics of Chagas disease in neighboring rural villages of the Gran Chaco region, incorporating human travel between the villages, passive vector migration, and insecticide resistance. Computational simulations across a wide variety of scenarios are presented. The simulations reveal that the effects of human travel and passive vector migration are secondary and unlikely to play a significant role in the overall dynamics, including the number of human infections. The numerical results also show that insecticide resistance causes a notable increase in infections and is an especially important source of reinfestation when spraying stops. The results suggest that control strategies related to migration and travel between the villages are unlikely to yield meaningful benefit and should instead focus on other reinfestation sources like domestic foci that survive insecticide spraying or sylvatic foci.

KEYWORDS

Chagas disease, delay differential equations, mathematical model, insecticide resistance, vector migration

1. Introduction

Trypanosoma cruzi is a parasitic hemoflagellate that infects mammals, including humans, wherever the Triatominae vectors are found, between approximately 40° N and S of the equator in the Americas [1]. Chagas disease (American trypanosomiasis), caused by *T. cruzi* infection in humans, is responsible for disability and early death in approximately one-third of those infected [2]. The WHO reports that approximately 8 million individuals are currently infected with Chagas disease, an estimated 25 million people are potentially at risk of infection, and more than 10,000 people die annually from the disease [3]. Chagas disease is increasingly being detected in the US, Canada, and many European and Asian countries due to human migration between Latin America and the rest of the world [4]. Therefore, it is becoming a global threat to public health.

Chagas disease has been the target of widespread and largely successful control programs over the past few decades [5]. Such efforts–prominently including the Southern Cone Initiative, which was begun in 1991–have had a tremendous impact, more than halving the number of infected individuals. However, the disease remains a baleful threat due to large

number of sylvatic reservoir hosts found throughout Latin America and the possibility of resurgence in places where incidence has been reduced. In particular, the Gran Chaco, a region over 600,000 km^2 in size located in southcentral South America, is of notable concern. There, the major disease control strategies have failed, and Chagas disease remains endemic, threatening the approximately five million inhabitants [6–8]. For example, one rural village in the region was recently surveyed, and over 80% of the adults were found to be infected [9].

Chagas disease has historically been a problem associated with rural regions of Latin America, largely due to the tendency of its insect vectors to live in the crevices of homes made from inexpensive and easily accessible materials such as mud, adobe, straw, and palm thatch. The disease has spread in recent years as people have moved from rural areas to urban locations within Latin America and throughout the world [3, 10]. The estimated burden of Chagas disease in the United States is greater than 300,000 individuals, with 30,000–45,000 cardiomyopathy cases and 63–315 congenital infections annually [11]. Los Angeles blood banks have an estimated seroprevalence among all blood donors as high as 1 in 3,800 [12]. The enduring presence and recent diffusion of Chagas disease is quite concerning as it is a chronic and potentially life-threatening infection [13]. At present, there is no vaccine for Chagas disease, and treatments with drugs such as benznidazole and nifurtimox are long, have serious potential side effects, and diminish in effectiveness with time since infection. As a result, the primary method of disease control is prevention [3].

Trypanosoma cruzi infection can be due to exposure to infected Triatominae feces, blood transfusion, organ donation, or congenital transmission [10]. The subfamily Triatominae or kissing bugs are large bloodsucking insects that predominately hide in the homes of their host during the day and feed on blood at night [3]. Should the Triatominae bite a mammal infected with *T. cruzi*, it may become infected and spread the disease. The parasites are present in the feces of the vectors and infection only occurs if the parasites come in contact with the mucosa through the eyes, the mouth, or enter through the nearby bite site [3, 10]. For this reason the most important reservoirs for *T. cruzi* are insectivorous mammals which can serve as hosts for *T. cruzi* [14]. Many methods of inhibiting transmission to humans, such as blood screening, home improvements, and bednets, are currently in use, with the primary means of vector control being residual insecticide spraying [3].

Residual insecticide treatment of endemic areas has shown tremendous success in most regions, but in some like the Gran Chaco, they have failed to sufficiently curb the disease, and the uneven success of current prevention methods in these regions warrants further study. Of particular interest are vector reinfestation into homes and vector resistance to insecticides, both of which are important possible causes of control failure. Reinfestation of vectors into homes is a major concern, because even a small lingering population of vectors in a village that has been treated with insecticides can quickly return to pre-spraying levels of infestation; therefore, migration could contribute to rapid population recovery and thus account for control failure in regions like the Gran Chaco [6, 7]. Reinfestation is a particularly prominent concern in the Gran Chaco due to a combination of political instability causing unpredictable changes in control strategies and economic instability causing widespread human migration [6, 7]. Along with these concerns, field work supports the idea that vector movement is playing an important role in control failure; recent research suggests that *Triatoma infestans*, the primary vector in the Grand Chaco, from sylvatic populations and neighboring townships are re-infesting villages in the Gran Chaco and that prevention tactics are needed for effective vector control [15–18].

In addition, despite an initial assumption of the Southern Cone Initiative that the vectors do not have sufficient genetic variability to develop resistance, various sources have shown that populations of *T. infestans* in the Gran Chaco and other areas are resistant to the insecticides currently in use [6, 7, 19]. For example, in 2002, vectors in four separate villages in Argentina were found to have high resistance to the pyrethroid insecticides deltamethrin and, β-cypermethrin [20]. Additionally, insecticide resistance has been observed within the Gran Chaco region, which suggests that it may be playing a role in the failure of control efforts there [19]. The possibility of insecticide resistance is especially problematic because vector control plays such a key role in current disease prevention efforts.

The purpose of this study is to analyze these potential sources of reinfestation using a differential equations model. This work is the latest in a series of works that have used Chagas disease models to analyze the effectiveness of various control strategies [21–26]. The previous works have assumed that reinfestation occurs due to a small population of vectors that avoid insecticide spraying. In this study, we compare this cause of control failure with vector reinfestation through migration by expanding the model to simulate the spread of Chagas disease in a system of villages rather than a single town. We then use this updated model to analyze the impact of different control strategies with a focus on how they interact with vector migration. We also consider the impact of larger populations of residual vectors that survive insecticide use due to resistance.

2. Materials and methods

The model in this work expands upon the one used in "A Mathematical Model of Chagas Disease Dynamics in the Gran Chaco Region" [26], which we update to more accurately reflect the available research on *T. infestans* and *T. cruzi*. As in [26], the model is specifically designed to analyze villages in the Gran Chaco, and these villages are assumed to have sufficiently large populations so that differential equations are appropriate for modeling them. This assumption is consistent with field data, see [9], where the average village size is 462 people. For each village, we model the total domestic vectors, infected domestic vectors, total peridomestic vectors, infected peridomestic vectors, infected humans, susceptible humans, infected domestic animals that we will refer to as dogs, and infected peridomestic mammals (goats and pigs). We also consider chickens as a potential blood meal source, but do not model their population since they are not susceptible to *T. cruzi* infection. Furthermore, as this model considers a system of villages, multiple sets of these eight equations coupled by migration terms are used rather than a single set. Throughout, parameters that may vary between villages are denoted with a j

subscript, and those that are assumed to be uniform across villages are not.

Let $V_j = V_j(t)$ represent the total number of domestic vectors in village j at time t, $V_{i_j} = V_{i_j}(t)$ the number of infected domestic vectors, $W_j = W_j(t)$ the total number of peridomestic vectors, $W_{i_j} = W_{i_j}(t)$ the number of infected peridomestic vectors, $N_{i_j} = N_{i_j}(t)$ the number of infected humans, $N_{s_j} = N_{s_j}(t)$ the number of susceptible humans, $D_{i_j} = D_{i_j}(t)$ the number of infected dogs, $M_{i_j} = M_{i_j}(t)$ the number of infected peridomestic mammals, $N_j(t) = N_{s_j}(t) + N_{i_j}(t)$ the total number of humans, $D_j(t)$ the total number of dogs, $M_j(t)$ the total number of mammals, and $C_j(t)$ the number of chickens. In this work, the total dog, mammal, and chicken populations are not modeled, but rather obtained from [27] and [28] and defined explicitly. However, infected dogs and mammals are modeled as sub-populations of the known total populations. We use the notation $f_+ = \max(f, 0)$ and $f_- = \min(f, 0)$ throughout.

2.1. Total domestic vectors

First, we model the growth of domestic vectors by the using a delayed logistic term:

$$d_{h_j}(t-\tau)V_j(t-\tau)\left(1-\frac{V_j(t-\tau)}{K_{V_j}}\right)_+, \tag{1}$$

where the delay τ is the gestation time of the vectors, K_{V_j} is the carrying capacity of the vectors in village j, and $d_{h_j}(t-\tau)$ is the egg hatching rate in village j at time $t-\tau$. Since adult female vectors lay eggs after having a complete blood-meal, the egg hatching rate is dependent on the biting rate $B_j(t-\tau)$, which is the average number of bites each vector makes per day. In addition to the biting rate, the egg hatching rate is naturally assumed to be dependent on the number of eggs a female vector lays after a blood-meal ϕ_l, the proportion of adult females in the population ν, and the proportion of eggs that hatch ϕ_h. Thus, the egg hatching rate is given by

$$d_{h_j}(t-\tau) = \nu\phi_l\phi_h B_j(t-\tau). \tag{2}$$

Since a larger blood supply results in more biting (up to a maximum per day), the biting rate $B_j(t)$ is dependent on the domestic blood supply $b_{sup_j}(t)$ of village j at the time when the female lays eggs, and it is also dependent on the season [29]. In order to accurately capture the seasonal dependence, we construct a seasonal biting rate $b(t)$ (defined in Table 3) based on data from [28]. However, this function $b(t)$ is obtained from data in a setting with a particular known blood supply $b_{sup_{known}}(t)$ [defined in equation (43)] and does not capture the blood meal dependence, so we also use a Holling Type II response to obtain the final biting rate

$$B_j(t) = b(t)\left(\frac{\beta}{b_{max}}\right)\left(\frac{b_{sup_j}(t)}{b_{sup_j}(t)+A_b(t)}\right), \tag{3}$$

where $b_{sup_j}(t)$ is the domestic blood supply in village j, β is the maximum possible daily feedings of a vector, and b_{max} is the maximum value of $b(t)$. A_b is chosen such that

$$\left(\frac{\beta}{b_{max}}\right)\left(\frac{b_{sup_{known}}(t)}{b_{sup_{known}}(t)+A_b(t)}\right) = 1. \tag{4}$$

This is done so that if the blood supply in village j matches the conditions in [28] (that is, $b_{sup_j} = b_{sup_{known}}$), then $B(t) = b(t)$ and the biting rate agrees with the empirical results.

We now consider the domestic blood supply $b_{sup_j}(t)$, which is composed of total humans, dogs, and chickens. Since the vectors prefer certain blood sources over others, each one is translated into a number of humans, so that the unit of measurement is human factors [28, 30]. More specifically, the human factors for a dog and a chicken are represented by d_f and c_f, respectively. Also, the blood supply is dependent on the availability of humans, dogs, and chickens in the domestic region in village j at time t, given by $a_{N_j}(t)$, $a_{Dh_j}(t)$, and $a_{Ch_j}(t)$, respectively. These time-dependent values represent the proportion of the respective populations available for biting in the domestic region, which may vary due to various factors, such as dogs sleeping outside or people being unavailable for biting because of their protection (at night) when they are using bednets [28]. Therefore, the total blood supply is given by

$$b_{sup_j}(t) = a_{N_j}(t)N_j(t) + d_f a_{Dh_j}(t)D_j(t) + c_f a_{Ch_j}(t)C_j(t), \tag{5}$$

which can be thought of as the equivalent number of human factors available for biting.

We now consider the deaths of vectors. Natural death is modeled by

$$-d_m V_j(t), \tag{6}$$

where d_m is the natural death rate. We also assume that the vectors die due to overpopulation, which is modeled by

$$d_k\left(1-\frac{V_j(t)}{K_{V_j}}\right)_-, \tag{7}$$

where d_k is the death rate due to the population being over the carrying capacity. In addition, death can be caused by insecticide spraying. We assume there is a sub-population of vectors V_{res_j} that does not die from spraying, being protected in cracks in the walls or by insecticide resistance. Recent field surveys confirm that domestic vectors that survive spraying continue to be a source of reinfestation [18]. For simplicity, we assume that V_{res_j} is constant for a given village. Therefore, the term that models death due to spraying is given by

$$-r_j(t)\left(V_j(t)-V_{res_j}\right)_+, \tag{8}$$

where $r_j(t)$ is the mortality rate due to spraying of non-resistant vectors.

As was done in [26], we assume the net movement into (or out of) the domestic region from (or to) the peridomestic region of a village is given by

$$\rho\left(\frac{W_j(t)}{K_{W_j}}-\frac{V_j(t)}{K_{V_j}}\right). \tag{9}$$

Here, ρ is a constant parameter with units vectors per day, and the term inside the parentheses captures the density dependence by comparing the ratios of the vector population to the carrying capacity in the respective regions. We note that the movement of vectors between the domestic and peridomestic region is still poorly understood, and a more thorough analysis of this term can be found in [26].

A novel aspect of our model is the migration of vectors between villages. Vectors move between villages primarily in two ways: passively via human movement and actively via flight [15]. However, even with villages within approximately 500 m of each other there is sometimes no flight of vectors between them [15], so we consider active transport negligible in our village system. For passive migration, which occurs when vectors and their eggs are carried by traveling individuals, we assume that the rate is dependent on the number of vectors and humans present in the domestic region of each village in the following way. We let $\alpha_{N_{j,k}}$ be the daily rate of people traveling from village j to village k, and use η to denote the average ratio of vectors that live in the luggage or other travel items in the domicile. Then the number of people traveling daily from village j to village k is given by $\alpha_{N_{j,k}} N_j(t)$, and on average, each person is carrying $\eta V_j(t)/N_j(t)$ vectors. Thus, the number of vectors per day passively transporting into (and out of) village j, and from (and into) village k, is

$$p_{V_{k,j}} V_k(t) - p_{V_{j,k}} V_j(t), \tag{10}$$

where, $p_{V_{j,k}} = \eta \alpha_{N_{j,k}}$.

Finally, the complete equation used to model domestic vectors is

$$\begin{aligned}\frac{dV_j}{dt} &= d_{h_j}(t-\tau)V_j(t-\tau)\left(1-\frac{V_j(t-\tau)}{K_{V_j}}\right)_+ \\ &\quad -d_k V_j(t)\left(1-\frac{V_j(t)}{K_{V_j}}\right)_- \\ &\quad -d_m V_j(t) - r_j(t)\left(V_j(t)-V_{res_j}\right)_+ + \rho\left(\frac{W_j(t)}{K_{W_j}} - \frac{V_j(t)}{K_{V_j}}\right) \\ &\quad + \sum_{k\neq j}\left(p_{V_{k,j}} V_k(t) - p_{V_{j,k}} V_j(t)\right).\end{aligned} \tag{11}$$

2.2. Infected domestic vectors

A domestic vector becomes infected by biting infected humans and infected dogs [31]. Thus, the term that models the growth of the infected domestic vector population is

$$B_j(t)\left(V_j(t)-V_{i_j}(t)\right)\left(\frac{P_{NV}a_{N_j}(t)N_{i_j}(t) + P_{MV}d_f a_{Dh_j}(t)D_{i_j}(t)}{b_{sup_j}(t)}\right), \tag{12}$$

where P_{NV} and P_{MV} are the proportion of vectors that become infected after taking a blood meal from infected humans and mammals (including dogs). Note that $B_j(t)\left(V_j(t)-V_{i_j}(t)\right)$ is the daily number of bites by non-infected vectors and that the latter half of (12) is the fraction of bites that cause infection. The vectors do not pass *T. cruzi* to their young, so this is the only term for the growth of the infected vector population [32].

The death rates for infected vectors are assumed to be the same as those for all vectors with no preference for the infected or susceptible populations, so the terms accounting for mortality are the same as those for total domestic vectors but multiplied appropriately by V_{i_j}/V_j. The transport rates between populations of vectors are subject to the same assumption, and they are correspondingly multiplied by the appropriate ratios of infected vectors.

Thus, the complete equation is

$$\begin{aligned}\frac{dV_{i_j}}{dt} &= B_j(t)\left(V_j(t)-V_{i_j}(t)\right)\left(\frac{P_{NV}a_{N_j}(t)N_{i_j}(t) + P_{MV}d_f a_{Dh_j}(t)D_{i_j}(t)}{b_{sup_j}(t)}\right) \\ &\quad -d_k V_{i_j}(t)\left(1-\frac{V_j(t)}{K_{V_j}}\right)_- - d_m V_{i_j}(t) \\ &\quad -r_j(t)\left(1-\frac{V_{res_j}}{V_j(t)}\right)_+ V_{i_j}(t) + \rho\left(\frac{W_{i_j}(t)}{K_{W_j}} - \frac{V_{i_j}(t)}{K_{V_j}}\right) \\ &\quad + \sum_{k\neq j}\left(p_{V_{k,j}} V_{i_k}(t) - p_{V_{j,k}} V_{i_j}(t)\right).\end{aligned} \tag{13}$$

2.3. Total peridomestic vectors

Naturally, the dynamics of the peridomestic vectors are similar to those of the domestic vectors; however, there are some minor differences due to the different setting. First, the egg hatching rate is updated to depend on the peridomestic blood supply, $\tilde{b}_{sup_j}(t)$, which is given by

$$\tilde{b}_{sup_j}(t) = d_f a_{Dp_j}(t)D_j(t) + m_f a_{M_j}(t)M_j(t) + c_f a_{Cp_j}(t)C_j(t). \tag{14}$$

Here, $a_{Dp_j}(t)$ is the peridomestic availability of dogs, $a_{Cp_j}(t)$ is the peridomestic availability of chickens, $a_{M_j}(t)$ is the availability of mammals, and m_f is the mammal factor analagous to d_f and c_f [28]. Thus, the peridomestic biting rate $\tilde{B}_j(t)$ is given by

$$\tilde{B}_j(t) = b(t)\left(\frac{\beta}{b_{max}}\right)\left(\frac{\tilde{b}_{sup_j}(t)}{\tilde{b}_{sup_j}(t) + A_b(t)}\right), \tag{15}$$

and the peridomestic egg hatching rate is given by

$$\tilde{d}_{h_j}(t-\tau) = \nu\phi_l\phi_h\tilde{B}_j(t-\tau). \tag{16}$$

Second, we assume that luggage containing items such as clothing is what harbors vectors for passive transport [15], so as there is no luggage in the peridomestic region there is correspondingly no term for passive transport (We relax this assumption in Simulation 4 and consider a case with transport of peridomestic vectors). Therefore, we have

$$\begin{aligned}\frac{dW_j}{dt} &= \tilde{d}_{h_j}(t-\tau)W_j(t-\tau)\left(1-\frac{W_j(t-\tau)}{K_{W_j}}\right)_+ \\ &\quad -d_k W_j(t)\left(1-\frac{W_j(t)}{K_{W_j}}\right)_-\end{aligned}$$

$$-d_m W_j(t) - r_j(t)\left(W_j(t) - W_{res_j}\right)_+ - \rho\left(\frac{W_j(t)}{K_{W_j}} - \frac{V_j(t)}{K_{V_j}}\right). \quad (17)$$

2.4. Infected peridomestic vectors

The dynamics of infected peridomestic vectors are derived from those of the total peridomestic vectors just as for the domestic vectors, so the equation is given by

$$\begin{aligned}\frac{dW_{i_j}}{dt} &= \tilde{B}_j(t)\left(W_j(t) - W_{i_j}(t)\right) \quad (18)\\ &\times\left(\frac{P_{MV}a_{M_j}(t)m_f M_{i_j}(t) + P_{MV}d_f a_{Dp_j}(t)D_{i_j}(t)}{\tilde{b}_{sup_j}(t)}\right)\\ &-d_k W_{i_j}(t)\left(1 - \frac{W_j(t)}{K_{W_j}}\right)_- - d_m W_{i_j}(t)\\ &-r_j(t)\left(1 - \frac{W_{res_j}}{W_j(t)}\right)_+ W_{i_j}(t) - \rho\left(\frac{W_{i_j}(t)}{K_{W_j}} - \frac{V_{i_j}(t)}{K_{V_j}}\right).\end{aligned}$$

2.5. Susceptible humans

We now consider susceptible humans. We note that all children of susceptible humans are born susceptible, and a certain fraction P_{NN} of children born to infected mothers are also born infected due to congenital transmission with the rest being born susceptible [33–35]. Also, due to the relatively long time it takes for Chagas disease to cause death, the birth rate of infected mothers is assumed to be the same as that of susceptible ones. Thus, using a logistic model, the growth term is given by

$$G_N\left(N_{s_j}(t) + (1 - P_{NN})N_{i_j}(t)\right)\left(1 - \frac{N_j(t)}{K_{N_j}}\right)_+, \quad (19)$$

where G_N is the daily growth rate of humans with unlimited resources. For the death term, we use

$$-\gamma_{N_s}N_{s_j}(t), \quad (20)$$

where γ_{N_s} is the per day death rate of susceptible humans.

Along with death, we consider the loss of susceptible humans due to infection. The rate of infection is taken to be the product of the number of bites per day by infected vectors and the fraction of those bites that cause human infection, which yields the following term:

$$-B_j(t)\left(\frac{P_{VN}a_{N_j}(t)N_{s_j}(t)}{b_{sup_j}(t)}\right)V_{i_j}(t). \quad (21)$$

Finally, as we consider multiple villages, we include terms for the movement of people between them. We assume this movement depends on a per-person travel rate, so that the rate of people entering and leaving village j (from and to village k) is given by

$$\alpha_{N_{k,j}}N_{s_k} - \alpha_{N_{j,k}}N_{s_j}, \quad (22)$$

where $\alpha_{N_{j,k}}$ is the daily rate of movement of people from village j to k.

Thus, the complete equation is

$$\begin{aligned}\frac{dN_{s_j}}{dt} &= G_N\left(N_{s_j}(t) + (1 - P_{NN})N_{i_j}(t)\right)\left(1 - \frac{N_j(t)}{K_{N_j}}\right)_+ \quad (23)\\ &-B_j(t)\left(\frac{P_{VN}a_{N_j}(t)N_{s_j}(t)}{b_{sup_j}(t)}\right)V_{i_j}(t) - \gamma_{N_s}N_{s_j}(t)\\ &+\sum_{k\neq j}\left(\alpha_{N_{k,j}}N_{s_k} - \alpha_{N_{j,k}}N_{s_j}\right).\end{aligned}$$

2.6. Infected humans

The model for infected humans is similar to that of susceptible ones. However, the birth term reflects that only infected mothers can give birth to infected children and that only a certain percentage of their children are born infected. Also, the susceptible humans that become infected join the infected population, and the death rate of infected humans is assumed to be higher. However, the travel rates are assumed to be the same. Thus, the equation is

$$\begin{aligned}\frac{dN_{i_j}}{dt} &= G_N P_{NN}N_{i_j}(t)\left(1 - \frac{N_j(t)}{K_{N_j}}\right)_+\\ &+B_j(t)\left(\frac{P_{VN}a_{N_j}(t)N_{s_j}(t)}{b_{sup_j}(t)}\right)V_{i_j}(t)\\ &-\gamma_{N_i}N_{i_j}(t) + \sum_{k\neq j}\left(\alpha_{N_{k,j}}N_{i_k} - \alpha_{N_{j,k}}N_{i_j}\right). \quad (24)\end{aligned}$$

2.7. Infected dogs

We first consider the birth rate of infected dogs. To do this, we consider the total population of dogs in village j, $D_j(t)$, which we assume is known. Then, assuming a growth rate of $\alpha_j(t)$ for the total dogs and that susceptible and infected dogs die at the same rate of γ_D, we have $D_j'(t) = \alpha_j(t)D_j(t) - \gamma_D D_j(t)$. Finally, since $D_j(t)$ is known, and hence, $D_j'(t)$ is also known, we also have $\alpha_j(t)$ in terms of known quantities:

$$\alpha_j(t) = \frac{D_j'(t)}{D_j(t)} + \gamma_D. \quad (25)$$

Therefore, as infected dogs are only born to infected mothers, the birth term for infected dogs is given by

$$P_{MM}\left(\frac{D_j'(t)}{D_j(t)} + \gamma_D\right)D_{i_j}(t), \quad (26)$$

where P_{MM} is the proportion of dogs infected by vertical transmission.

In addition, the infected dog population could grow due to infected vector bites on susceptible dogs. Therefore, the term we use is similar to that used to model infection of humans. However, since dogs inhabit both domestic and peridomestic regions, there are two separate terms to model infection using appropriate respective

biting terms, blood supplies, populations, and availability values. Thus, the terms used are

$$B_j(t)\frac{P_{VM}d_f a_{Dh_j}(t)\left(D_j(t)-D_{i_j}(t)\right)}{b_{sup_j}(t)}V_{i_j}(t) \tag{27}$$

and

$$\tilde{B}_j(t)\frac{P_{VM}d_f a_{Dp_j}(t)\left(D_j(t)-D_{i_j}(t)\right)}{\tilde{b}_{sup_j}(t)}W_{i_j}(t) \tag{28}$$

for the domestic and peridomestic regions, respectively.

Then, including the death term, the complete equation is given by

$$\begin{aligned}\frac{dD_{i_j}}{dt} &= B_j(t)\frac{P_{VM}d_f a_{Dh_j}(t)\left(D_j(t)-D_{i_j}(t)\right)}{b_{sup_j}(t)}V_{i_j}(t) \\ &+\tilde{B}_j(t)\frac{P_{VM}d_f a_{Dp_j}(t)\left(D_j(t)-D_{i_j}(t)\right)}{\tilde{b}_{sup_j}(t)}W_{i_j}(t) \\ &+P_{MM}\left(\frac{D_j'(t)}{D_j(t)}+\gamma_D\right)D_{i_j}(t)-\gamma_D D_{i_j}(t).\end{aligned} \tag{29}$$

2.8. Infected mammals

Finally, we consider infected mammals. This equation is similar to that for dogs, but it differs slightly in that mammals do not enter the domestic region and thus there are no terms for infection from domestic vectors. Therefore, we have

$$\begin{aligned}\frac{dM_{i_j}}{dt} &= \tilde{B}_j(t)\frac{P_{VM}m_f a_{M_j}(t)\left(M_j(t)-M_{i_j}(t)\right)}{\tilde{b}_{sup_j}(t)}W_{i_j}(t) \\ &+P_{MM}\left(\frac{M_j'(t)}{M_j(t)}+\gamma_M\right)M_{i_j}(t)-\gamma_M M_{i_j}(t).\end{aligned} \tag{30}$$

2.9. The full model

Thus, the full model for village j is given by the following eight differential equations and the initial conditions found in Table 2:

$$\begin{aligned}\frac{dV_j}{dt} &= d_{h_j}(t-\tau)V_j(t-\tau)\left(1-\frac{V_j(t-\tau)}{K_{V_j}}\right)_+ \\ &-d_k V_j(t)\left(1-\frac{V_j(t)}{K_{V_j}}\right)_- \\ &-d_m V_j(t)-r_j(t)\left(V_j(t)-V_{res_j}\right)_+ \\ &+\rho\left(\frac{W_j(t)}{K_{W_j}}-\frac{V_j(t)}{K_{V_j}}\right) \\ &+\sum_{k\neq j}\left(p_{V_{k,j}}V_k(t)-p_{V_{j,k}}V_j(t)\right)\end{aligned} \tag{31}$$

$$\begin{aligned}\frac{dV_{i_j}}{dt} &= B_j(t)\left(V_j(t)-V_{i_j}(t)\right)\left(\frac{P_{NV}a_{N_j}(t)N_{i_j}(t)+P_{MV}d_f a_{Dh_j}(t)D_{i_j}(t)}{b_{sup_j}(t)}\right) \\ &-d_k V_{i_j}(t)\left(1-\frac{V_j(t)}{K_{V_j}}\right)_- - d_m V_{i_j}(t) \\ &-r_j(t)\left(1-\frac{V_{res_j}}{V_j(t)}\right)_+ V_{i_j}(t)+\rho\left(\frac{W_{i_j}(t)}{K_{W_j}}-\frac{V_{i_j}(t)}{K_{V_j}}\right) \\ &+\sum_{k\neq j}\left(p_{V_{k,j}}V_{i_k}(t)-p_{V_{j,k}}V_{i_j}(t)\right)\end{aligned} \tag{32}$$

$$\begin{aligned}\frac{dW_j}{dt} &= \tilde{d}_{h_j}(t-\tau)W_j(t-\tau)\left(1-\frac{W_j(t-\tau)}{K_{W_j}}\right)_+ \\ &-d_k W_j(t)\left(1-\frac{W_j(t)}{K_{W_j}}\right)_- \\ &-d_m W_j(t)-r_j(t)\left(W_j(t)-W_{res_j}\right)_+ \\ &-\rho\left(\frac{W_j(t)}{K_{W_j}}-\frac{V_j(t)}{K_{V_j}}\right)\end{aligned} \tag{33}$$

$$\begin{aligned}\frac{dW_{i_j}}{dt} &= \tilde{B}_j(t)\left(W_j(t)-W_{i_j}(t)\right) \\ &\times\left(\frac{P_{MV}a_{M_j}(t)m_f M_{i_j}(t)+P_{MV}d_f a_{Dp_j}(t)D_{i_j}(t)}{\tilde{b}_{sup_j}(t)}\right) \\ &-d_k W_{i_j}(t)\left(1-\frac{W_j(t)}{K_{W_j}}\right)_- - d_m W_{i_j}(t) \\ &-r_j(t)\left(1-\frac{W_{res_j}}{W_j(t)}\right)_+ W_{i_j}(t)-\rho\left(\frac{W_{i_j}(t)}{K_{W_j}}-\frac{V_{i_j}(t)}{K_{V_j}}\right)\end{aligned} \tag{34}$$

$$\begin{aligned}\frac{dN_{s_j}}{dt} &= G_N\left(N_{s_j}(t)+(1-P_{NN})N_{i_j}(t)\right)\left(1-\frac{N_j(t)}{K_{N_j}}\right)_+ \\ &-B_j(t)\left(\frac{P_{VN}a_{N_j}(t)N_{s_j}(t)}{b_{sup_j}(t)}\right)V_{i_j}(t)-\gamma_{N_s}N_{s_j}(t) \\ &+\sum_{k\neq j}\left(\alpha_{N_{k,j}}N_{s_k}-\alpha_{N_{j,k}}N_{s_j}\right)\end{aligned} \tag{35}$$

$$\begin{aligned}\frac{dN_{i_j}}{dt} &= G_N P_{NN}N_{i_j}(t)\left(1-\frac{N_j(t)}{K_{N_j}}\right)_+ \\ &+B_j(t)\left(\frac{P_{VN}a_{N_j}(t)N_{s_j}(t)}{b_{sup_j}(t)}\right)V_{i_j}(t) \\ &-\gamma_{N_i}N_{i_j}(t)+\sum_{k\neq j}\left(\alpha_{N_{k,j}}N_{i_k}-\alpha_{N_{j,k}}N_{i_j}\right)\end{aligned} \tag{36}$$

$$\begin{aligned}\frac{dD_{i_j}}{dt} &= B_j(t)\frac{P_{VM}d_f a_{Dh_j}(t)\left(D_j(t)-D_{i_j}(t)\right)}{b_{sup_j}(t)}V_{i_j}(t) \\ &+\tilde{B}_j(t)\frac{P_{VM}d_f a_{Dp_j}(t)\left(D_j(t)-D_{i_j}(t)\right)}{\tilde{b}_{sup_j}(t)}W_{i_j}(t) \\ &+P_{MM}\left(\frac{D_j'(t)}{D_j(t)}+\gamma_D\right)D_{i_j}(t)-\gamma_D D_{i_j}(t)\end{aligned} \tag{37}$$

$$\frac{dM_{i_j}}{dt} = \tilde{B}_j(t)\frac{P_{VM}m_f a_{M_j}(t)\left(M_j(t) - M_{i_j}(t)\right)}{\tilde{b}_{sup_j}(t)}W_{i_j}(t) + P_{MM}\left(\frac{M_j'(t)}{M_j(t)} + \gamma_M\right)M_{i_j}(t) - \gamma_M M_{i_j}(t). \quad (38)$$

We now establish the baseline parameter values. We separate these values into two categories: those considered to be biological in nature and generally consistent in all villages and those that depend on the structure of the particular collection of villages being modeled. For example, we consider the vector gestation time and the proportion of vector bites that result in a human being affected to be the same in any village, whereas values such as the number of houses in a village and the availability of dogs in the domestic region clearly depend on the particular village in question. The parameter values used are based upon existing data of Chagas disease and the Gran Chaco region when available, but we note that these values have a high degree of aleatory variability and epistemic uncertainty. The constant biological parameters are found in Table 1. We note that the human growth rate G_N was chosen so that the total human population grows at an approximate annual rate of 1.0% over the 30 years of simulation. This is consistent with recent population data for Bolivia, Paraguay, and Argentina, the three countries that contain the vast majority of the Gran Chaco region [46–48]. In addition, the infection proportion P_{VN} is unknown, so we choose a value that agrees with the *T. cruzi* seroprevalence in humans of 51.7% found in surveys in the Bolivian Chaco [9]. The village dependent values are found in Table 2 with citations where the value was chosen based on empirical data.

We now consider the time-dependent parameters. Based on data from [28], the number of goats in village j is given by

$$G_j(t) = H_j\left(17.5 - 2.5\cos\left(\frac{2\pi}{365/2}(t - 45.75)\right)\right), \quad (39)$$

where H_j is the number of houses in village j, which yields a (smooth) function with a period of half a year. This function is extended periodically. Similarly, the number of pigs is also derived from [28] and it is taken to be yearly periodic. The (smooth) function for the first year is given by

$$P_j(t) = \begin{cases} H_j, & 0 \le t \le 181.5 \\ H_j\left(1.75 - 0.75\cos\left((t - 181.5)\pi\right)\right), & 181.5 < t \le 182.5 \\ 2.5H_j, & 182.5 < t < 272.75 \\ H_j\left(1.75 + 0.75\cos\left((t - 272.75)\pi\right)\right), & 272.75 \le t < 273.75 \\ H_j, & 273.75 \le t \le 365. \end{cases} \quad (40)$$

Combining these two functions, we have that

$$M_j(t) = P_j(t) + G_j(t) \quad (41)$$

TABLE 1 Constant parameter values used in the baseline simulation.

Parameter	Definition	Baseline value	Units	Source
ν	Fraction of vectors that are adult females	1073/60000	$\frac{\text{adult female vector}}{\text{vector}}$	[36]
ϕ_l	Eggs laid per bite per fed adult female vector	20	$\frac{\text{egg/bite}}{\text{adult female vector}}$	[28, 29]
ϕ_h	Fraction of eggs that successfully hatch	0.831	vector/egg	[28, 29]
τ	Vector gestation time	20	days	[37]
β	Max possible bites per vector per day	0.47	bites/vector/day	[27, 29, 38]
P_{NV}	Per bite human to vector infection prop.	0.03	no units	[39]
P_{VN}	Per bite vector to human infection prop.	0.00515	no units	Est. [39]
P_{VM}	Per bite vector to mammal/dog infection prop.	0.02	no units	Est. [39]
P_{MV}	Per bite mammal/dog to vector infection prop.	0.49	no units	Est. [39]
P_{NN}	Per birth human to human infection prop.	0.073	no units	Est. [35]
P_{MM}	Per birth mammal/dog to mammal/dog infection prop.	0.1	no units	Est. [33, 40, 41]
d_f	Human factor of one dog	2.45	humans/dog	[27]
c_f	Human factor of one chicken	0.35	humans/chicken	[27, 30]
m_f	Human factor of one mammal	2.45	humans/mammal	Est. [27]
b_{max}	Max value of $b(t)$	0.34	bites/day/vector	Est. [28]
γ_{N_i}	Per day mortality rate of infected humans	0.00004163	1/day	Est. [42, 43]
γ_D	Per day mortality rate of dogs	1/1788.5	1/day	This study
γ_M	Per day mortality rate of mammals	1/1095	1/day	This study
γ_{N_s}	Per day mortality rate of susceptible humans	1/27783.8	1/day	Est. [42, 43]
G_N	Per day human growth rate	0.00019	1/day	This study
d_m	Death rate (per day) of vectors	0.023677446	1/day	Est. [29]
d_k	Death rate (per day) of vectors due to overpopulation	$10 * d_m$	1/day	This study

TABLE 2 Village parameter values used in the baseline simulation.

Parameter	Definition	Baseline value	Units	Source
K_{V_j}	Domestic vector carrying capacity in village j	$1.301 * H_j$	vectors	[44, 45]
K_{W_j}	Peridomestic vector capacity in village j	$36.26 * H_j$	vectors	[44, 45]
K_{N_j}	Per village human carrying capacity in village j	$10 * H_j$	humans	This study
ρ	Factor for per day vector migration between the peridomestic and domestic regions	1	vectors/day	This study
H_j	Total number of houses in village j	74	houses	[28]
C_j	Total number of chickens in village j	$15 * H_j$	chickens	[28]
D_j	Total number of dogs in village j	$2.9 * H_j$	dogs	[27]
a_{Dh_j}	Domestic dog availability in village j	0.59	no units	[30]
a_{Dp_j}	Peridomestic dog availability in village j	0.13	no units	[30]
a_{N_j}	Human availability in village j	1	no units	This study
V_{res_j}	Min number of domestic vectors due to cracks and resistance	$0.05 * H_j$	vectors	This study
W_{res_j}	Min number of peridomestic vectors due to cracks and resistance	$0.05 * H_j$	vectors	This study
η	Proportion of vectors in luggage of one person	0.1	1/person	This study
$\alpha_{N_{j,k}}$	Rate of human travel from village j to k	1/7	1/day	This study
$V_{0_j}(t), t \in [-\tau, 0]$	Initial number of total domestic vectors in village j	50	vectors	This study
V_{i0_j}	Initial number of infected domestic vectors in village j	30	vectors	This study
$W_{0_j}(t), t \in [-\tau, 0]$	Initial number of total peridomestic vectors in village j	1800	vectors	This study
W_{i0_j}	Initial number of total infected peridomestic vectors in village j	1400	vectors	This study
N_{s0_j}	Initial number of susceptible humans in village j	193	humans	Est. [39]
N_{i0_j}	Initial number of infected humans in village j	207	humans	Est. [39]
D_{i0_j}	Initial number of infected dogs in village j	165	dogs	This study
M_{i0_j}	Initial number of infected peridomestic mammals in village j	1150	mammals	This study

TABLE 3 Defining points of the piecewise-linear time dependent parameters.

Function	$t = 45.625$ (Fall)	$t = 136.875$ (Winter)	$t = 228.125$ (Spring)	$t = 319.375$ (Summer)
$a_{C_j}(t)$	0.38		0.83	
$a_{G_j}(t)$		1	0	
$a_{P_j}(t)$		0	1	
$b(t)$	0.14	0.18	0.34	0.23

For availability, we first define the total chicken availability $a_{C_j}(t)$, goat availability $a_{G_j}(t)$, and pig availability $a_{P_j}(t)$, all of which are obtained from data in [28]. We use continuous, yearly-periodic, piecewise-linear functions defined by the values listed in Table 3 and shown in Figure 1. We assume that there are an equal number of chickens in the peridomestic region and the domestic region, so we take $a_{Cp_j}(t) = 0.5 * a_{C_j}(t)$ for the peridomestic chicken availability and $a_{Ch_j}(t) = 0.5 * a_{C_j}(t)$ for the domestic availability. We then take $a_{M_j}(t)$ to be the weighted average of $a_{P_j}(t)$ and $a_{G_j}(t)$, yielding

$$a_{M_j}(t) = \frac{a_{P_j}(t)P_j(t) + a_{G_j}(t)G_j(t)}{M_j(t)}. \tag{42}$$

For the biting term, we again use a yearly-periodic piecewise-linear function as defined in Table 3. For the known blood supply, we use

$$b_{sup_{known}}(t) = c_f a_C(t) C_{known}(t) + m_f a_M(t) M_{known}(t), \tag{43}$$

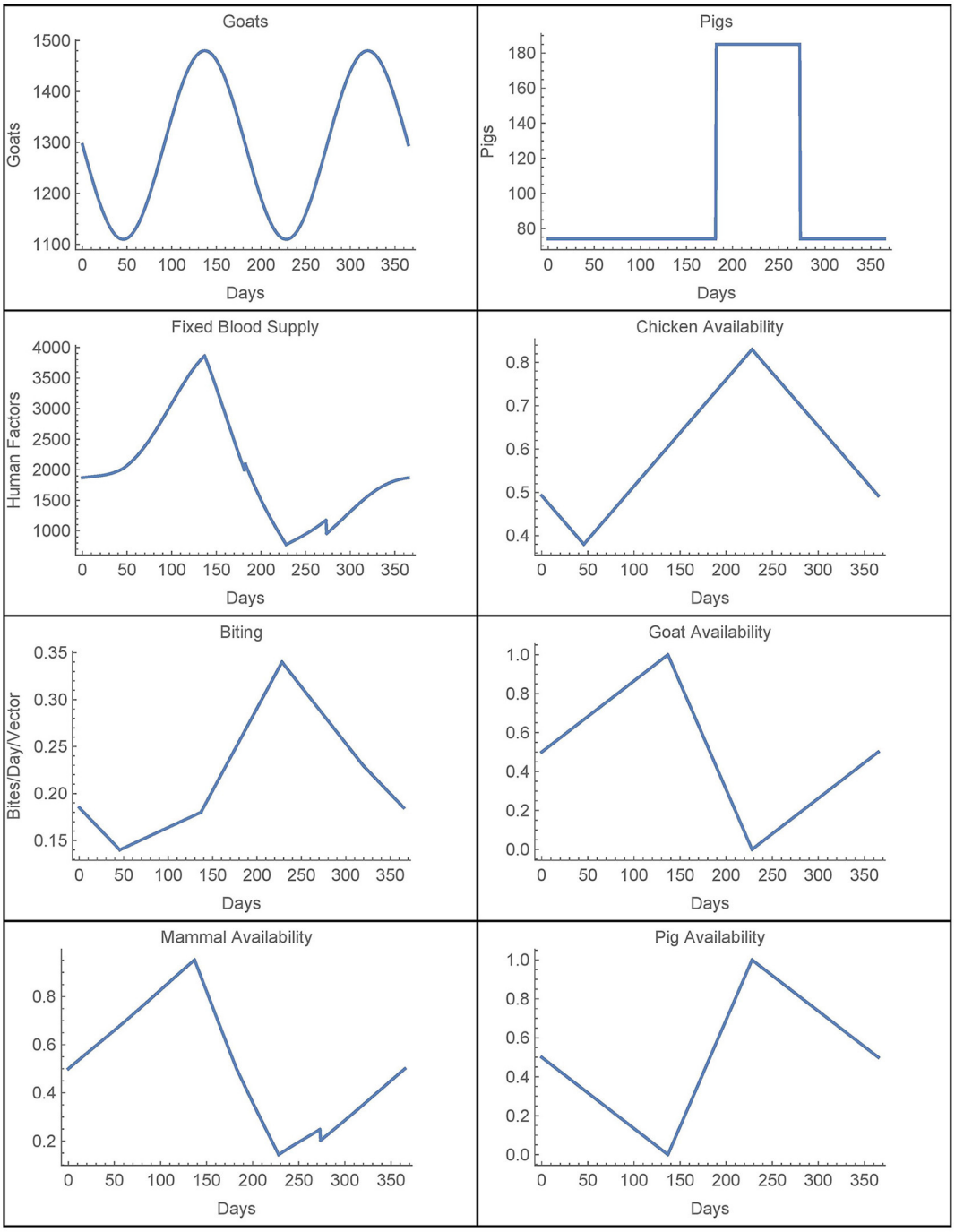

FIGURE 1
Time-dependent parameters.

where $a_C(t)$ and a_M are defined the same as $a_{C_j}(t)$ and a_{M_j}, and $C_{known}(t)$ and $M_{known}(t)$ are given by $H_{known} = 74$. Both of these functions are also derived from [28]. Finally, we define a yearly periodic active spraying mortality function, $r(t)$, with the first year given by

$$r(t) = \begin{cases} 0, & 0 \le t < t_1 \\ \left(e^{-\lambda(t-t_1)^2} - e^{-1/2}\right)\bar{r}_{max}, & t_1 \le t \le t_2 \\ 0, & t_2 < t \le 365 \end{cases} \tag{44}$$

with $t_1 = 212.5$, $t_2 = 303.75$, and

$$\lambda = \frac{1}{2(91.25)^2}, \qquad \bar{r}_{max} = \frac{1}{1 - e^{-1/2}}$$

as defined in [25]. This corresponds to spraying at t_1 with residual effects that diminish until disappearing at t_2. We take $r_j(t) = r(t)$ in spraying years for village j and $r_j(t) = 0$ otherwise. The time-dependent parameters, with the exception of the active spraying mortality function, are shown over the course of 1 year in Figure 1.

10.3389/fams.2023.1225137

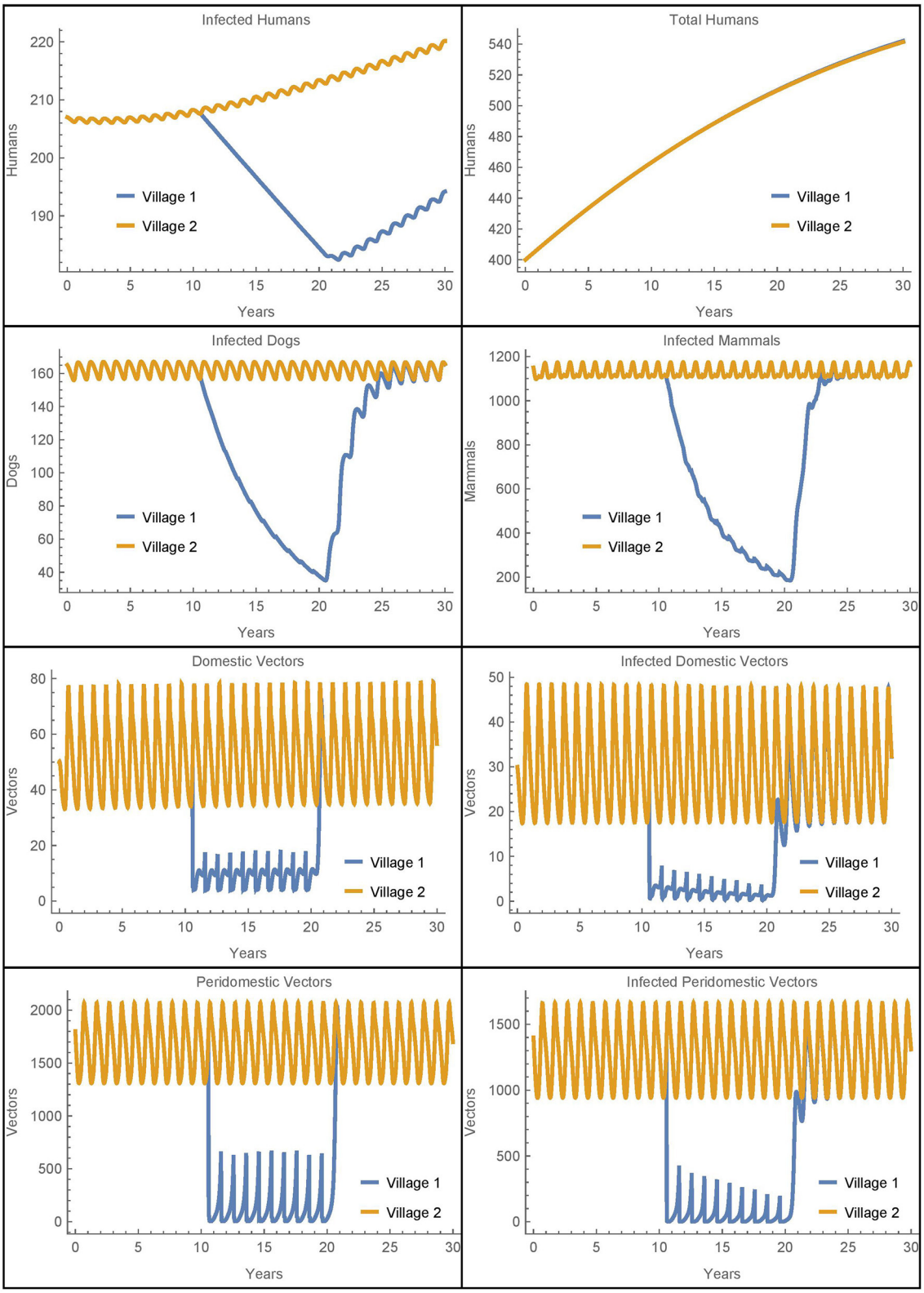

FIGURE 2
Baseline simulation: the populations of two identical villages with baseline parameters, insecticide spraying only in village 1, and no travel between them.

10.3389/fams.2023.1225137

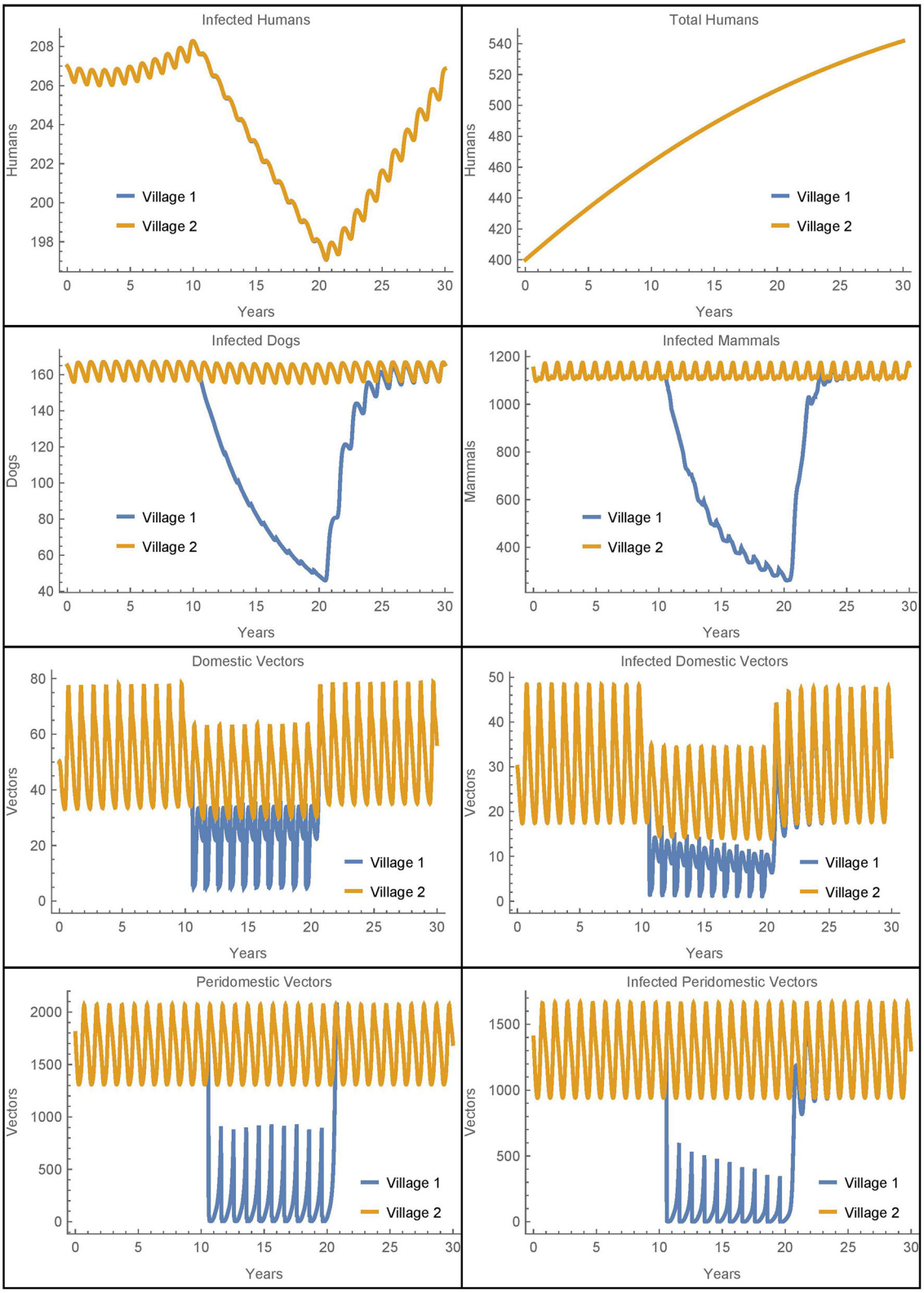

FIGURE 3
Neighboring villages with human travel and vector migration: the populations of two neighboring villages with human travel and vector transport between them and insecticide spraying only in village 1.

10.3389/fams.2023.1225137

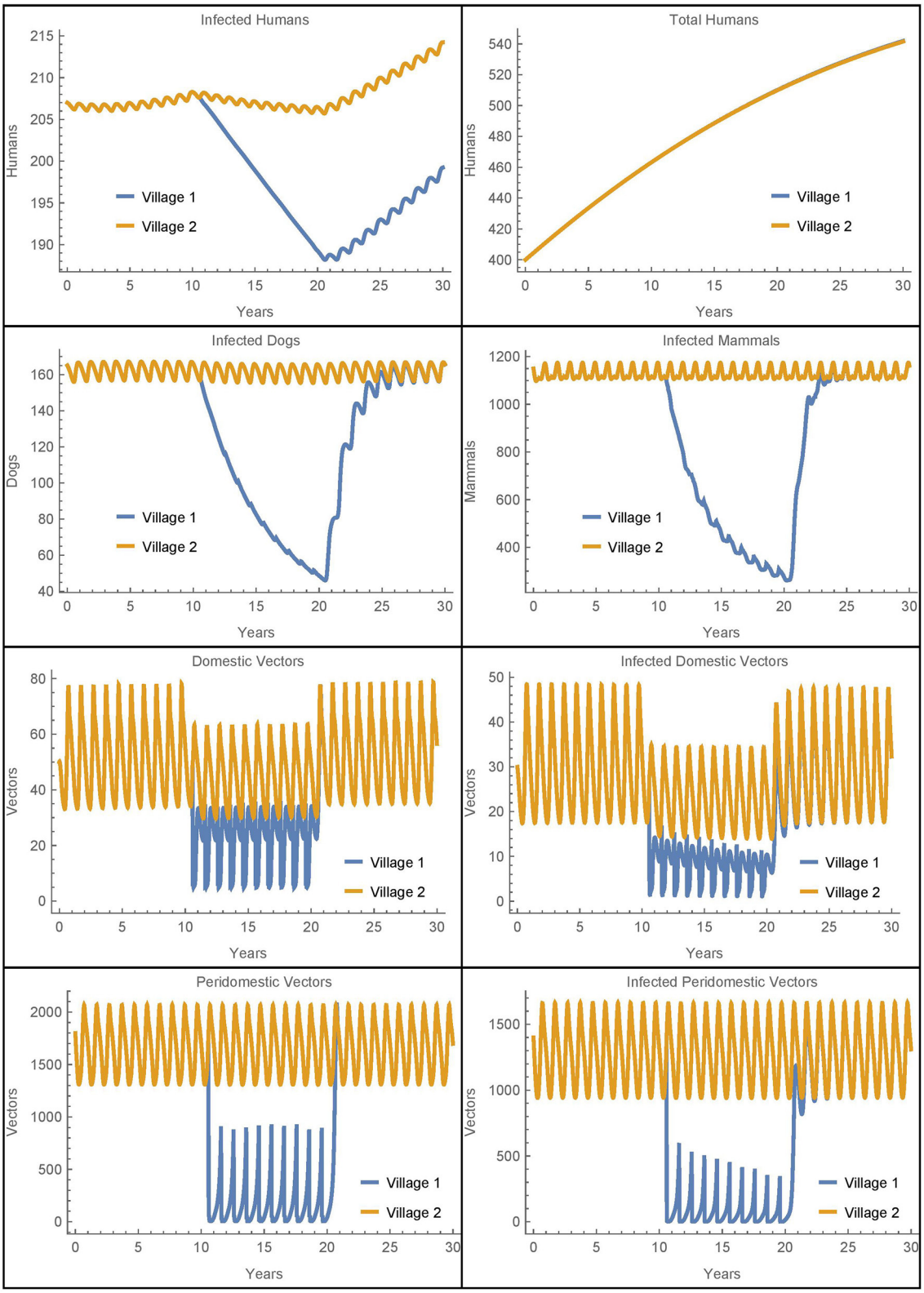

FIGURE 4
Neighboring villages with passive vector migration: the populations of two neighboring villages with vector transport between them and insecticide spraying only in village 1.

3. Results

We first establish a baseline simulation of two identical villages with the default parameter values. Insecticide spraying occurs in village 1 once per year for 10 consecutive years, there is no insecticide spraying in village 2, and there is no travel or interaction between the two villages. We then compare this simulation to several studies where village 1 is connected through travel with village 2, which can serve as a source of reinfestation. All numerical solutions were obtained using the NDSOLVE numerical differential equations solver in `Wolfram Mathematica`. Graphs were also produced in `Wolfram Mathematica`.

3.1. Simulation 0: baseline

For the baseline case with resistant vectors, the simulation is run for 30 years, during which insecticide spraying in village 1 occurs from year 11 to year 20. This is done so that the populations can reach steady oscillations before spraying begins and so that the behavior of the populations before, during, and after insecticide use can be analyzed. The results of this baseline simulation may be seen in Figure 2.

Before spraying begins, all the non-human populations demonstrate almost steady oscillations. These oscillations continue for the full 30 years in village 2. In village 1, after spraying starts, the vector populations quickly reach new smaller steady oscillations while the infected populations decrease. Once insecticide use stops, the non-human populations rapidly return to the same oscillating patterns that they demonstrated before it began, and the number of infected humans begins to increase again. This is largely in line with the qualitative results found in the baseline simulations in [26], although there is a more noticeable decrease in the infected populations in the current work as a result of the updated parameters.

3.2. Simulation 1: two neighboring villages with travel and vector migration

In this section, we simulate the populations of two villages that are connected by human travel, including the passive transport of vectors. We use the baseline parameters in both villages and include insecticide spraying from year 11 to year 20 only in village 1. This scenario investigates how isolated rural villages with different control measures might affect each other, and in particular, the role village 2 might play as a reinfestation source for village 1. Here we simulate the case where travel between the villages is common, with the average person traveling to the other village once per week ($\alpha_{N_{1,2}} = \alpha_{N_{2,1}} = 1/7$). Additionally, we specify that 10% of the vectors live in luggage or other travel items in the homes. The results are shown in Figure 3.

We see that during the spraying years, the domestic vector populations in village 1 and village 2 are higher and lower, respectively, as compared to the baseline case. These changes reflect the mixing of the vector populations in the two villages due to the passive transport of vectors. More strikingly, there is a complete

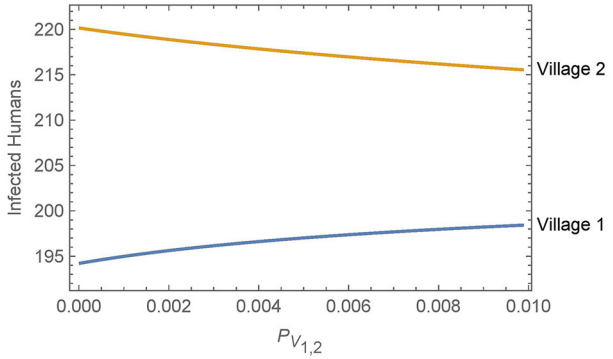

FIGURE 5
Neighboring villages with variable levels of vector migration: the numbers of infected humans after 30 years in two neighboring villages as a function of the travel parameters. The value of $P_{V_{1,2}} = P_{V_{2,1}} = \eta\alpha_{N_{1,2}}$ varies from $\eta = 1\%$ and $\alpha_{N_{1,2}} = 1$/year on the low end to $\eta = 10\%$ and $\alpha_{N_{1,2}} = 1/(10$ days) on the high end.

mixing of the human populations between the villages so that they have the same number of infected humans despite the difference in control measures. While the travel between the villages does increase the number of human infections in village 1, it is important to note that the total number of human infections in the two villages after 30 years is identical to the baseline case. That is, the additional infections in village 1 are offset by fewer infections in village 2. Thus, the movement of infected humans and vectors from village 2 to village 1 spreads the disease burden between the villages but does not increase the total number of infected humans.

It is not clear from this simulation to what extent the change in the infected human populations is a result of the humans traveling vs. the vectors being transported. To isolate the effects, we ran a similar simulation with the same level of human travel but with no vector transport. The results for the human populations were identical to those seen in Figure 3 while the rest of the populations had dynamics similar to the baseline case. We see that the transport of vectors has little effect on the number of infected humans when the human populations are mixing at such a high rate. These results were further confirmed in scenarios with much lower rates of human travel. For example, when humans travel once per year between the villages, it takes about 22 years for the two human populations to fully mix, but the overall number of infections remains the same. And, removing vector transport in this case also has no effect on the total number of human infections in either village.

Overall, we see that vector migration is not a significant source of reinfestation in this scenario and that travel redistributes the number of human infections, but does not increase them. The human travel in this scenario is similar to migration as people travel to and stay in the other village. As such, the eventual complete mixing of the populations is likely unrealistic, potentially obscures the differences between the two villages, and does not increase the total number of human infections. Thus, to further investigate the potential effects of vector migration, we will consider in Simulations 2–7 human travel that passively transports the vectors while the humans themselves do not move to the new village. These

10.3389/fams.2023.1225137

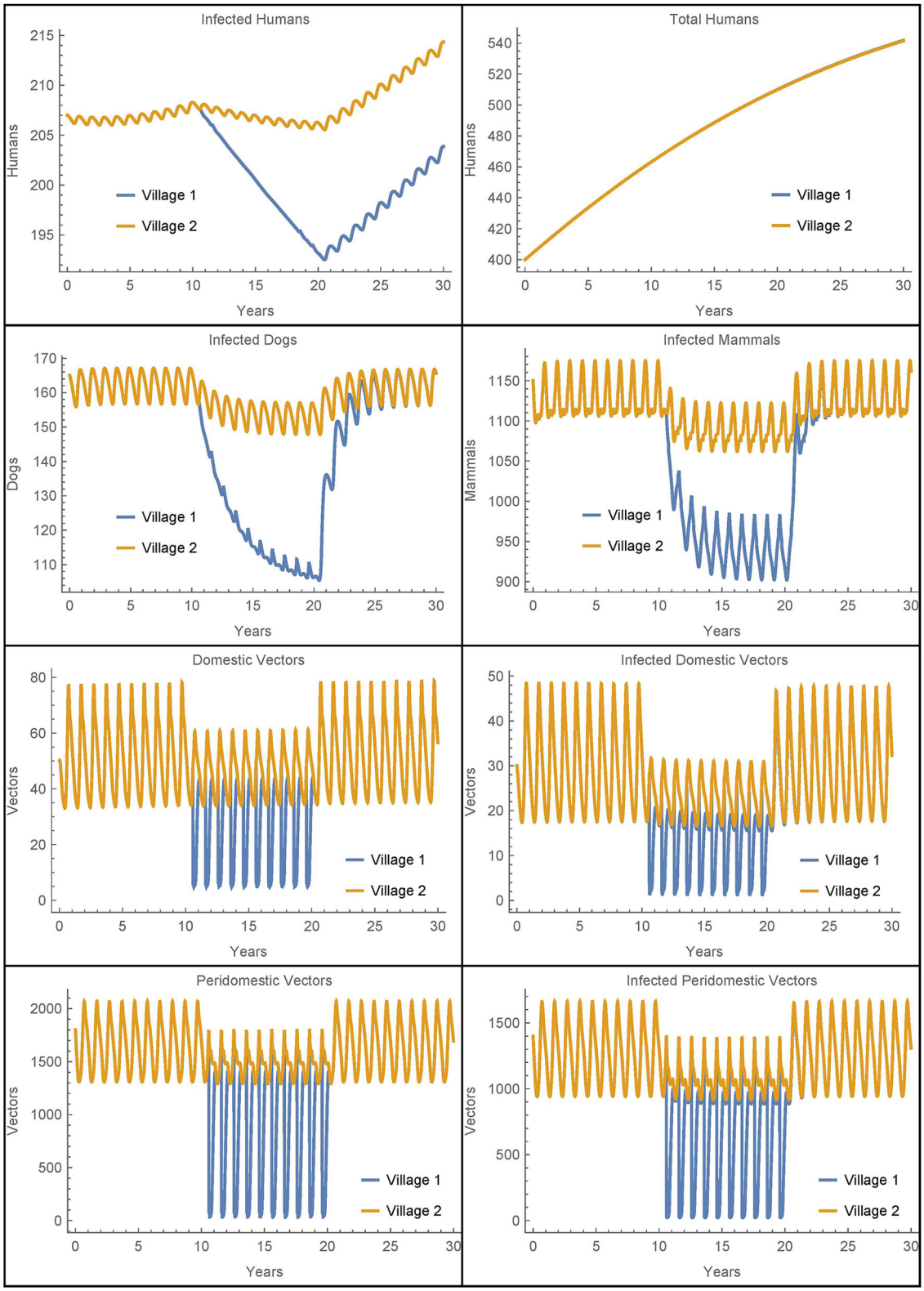

FIGURE 6
Neighboring villages with domestic and peridomestic vector migration: the populations of two neighboring villages with domestic and peridomestic vector transport between them and insecticide spraying only in village 1.

simulations represent scenarios where humans transport objects containing vectors but do not stay in the other village.

3.3. Simulation 2: two neighboring villages with vector migration

In this section, we simulate the populations of two villages with the same parameters and insecticide spraying as in Simulation 1, but with the travel terms removed from the human equations. That is, we consider the baseline simulation with the addition of passive vector migration but not human travel. The results are shown in Figure 4 where we see that, except for infected humans, all the population dynamics are similar to those in Simulation 1 (Figure 3).

Because we have removed human population mixing, the differences in the number of human infections are attributable solely to the passive transport of vectors. As in Simulation 1, we see more vectors in village 1 during spraying years as compared to the baseline case. These additional vectors in village 1 that come from village 2 do result in five more infected humans in village 1 after 30 years as compared to the baseline. However, there are six fewer infected humans in village 2 in this scenario. So while the disease burden has slightly shifted from village 2 to village 1, the overall effect is small and the number of human infections across both villages remains nearly constant. We see that the transport of vectors does not have a significant impact on human infections in this scenario.

3.4. Simulation 3: two neighboring villages with variable travel parameters

We further investigate the effect of the travel parameters in this section by considering the number of infected humans in both villages after 30 years as a function of $P_{V_{1,2}} = P_{V_{2,1}} = \eta\alpha_{N_{1,2}}$. We recall that $\alpha_{N_{j,k}}$ is the daily travel rate of humans from village j to village k and η is the average ratio of vectors that live in the luggage or other travel items. As in Simulation 2, to isolate the effect of vector migration, the humans transport the vectors between villages but do not stay in the other village. All other parameters are held at the baseline values in both villages, with insecticide spraying in village 1, but not in village 2. The results are shown in Figure 5.

Overall, we see that vector migration has a relatively small effect on the infected human populations across a broad range of travel scenarios. Small changes in the travel parameters have negligible effects on the infected human populations and even a change from no travel to high levels of travel and vector transport results in only a handful of additional infections in village 1 after 30 years. Furthermore, any increase in human infections in village 1 is offset by a similar decrease in infections in village 2.

3.5. Simulations 4–5: peridomestic vector migration and other travel scenarios

Next we consider a simulation where vectors may be passively transported from the peridomestic regions of a village in addition to being transported from the homes. In this scenario, vectors may be hiding in materials (e.g., straw, hay, or animal feed) that are transported from the peridomestic region in one village to the peridomestic region in another during agricultural activities. To accomplish this in the model, we modify the equations for the peridomestic vector equations to include transport terms that are analogous to the transport terms in the domestic vector equations. The travel parameters are set to the same level as those in Simulation 2, while all other parameters are at their baseline values and insecticide spraying occurs only in village 1. As in Simulations 2–3, the humans transfer terms are removed from the equations, though the humans still transport the vectors. The results are shown in Figure 6.

As expected, we now see a mixing of the peridomestic vectors, just as we saw with the domestic vectors in Figures 3, 4. Additionally, we see differences in the infected dog and infected mammals populations as compared to those in Figures 3, 4, where there was no peridomestic vector transport. The decline and rebound of the infected human population is qualitatively similar to those in Figure 4, though the rebound after spraying ceases is more pronounced. After 30 years, the number of people infected in village 1 is about nine higher than the baseline case and four higher than Simulation 2, the case with only domestic vector transport. Notably, the number of infected humans in village 2 does not decline to offset the increase in village 1, but rather stays about the same as in Simulation 2. Nevertheless, the total infected humans across both villages is only four higher than the baseline case.

We ran additional simulations to see if other differences between the villages might affect the role that vector migration plays. We first considered the size of village 2, allowing village 1 to be connected to a smaller or larger village by varying the number of houses in village 2 from 40 to 145. We then considered the number of infected humans after 30 years using different rates of domestic vector migration. We did not include peridomestic vector migration or the transfer of humans between the populations. All other parameters are held at the baseline values in both villages, with insecticide spraying only in village 1.

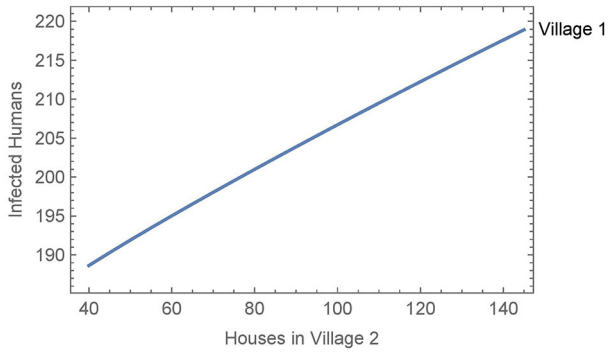

FIGURE 7
Neighboring villages with variable number of houses in village 2: the number of infected humans after 30 years in village 1 as a function of the number of houses in village 2 with vector migration between them.

10.3389/fams.2023.1225137

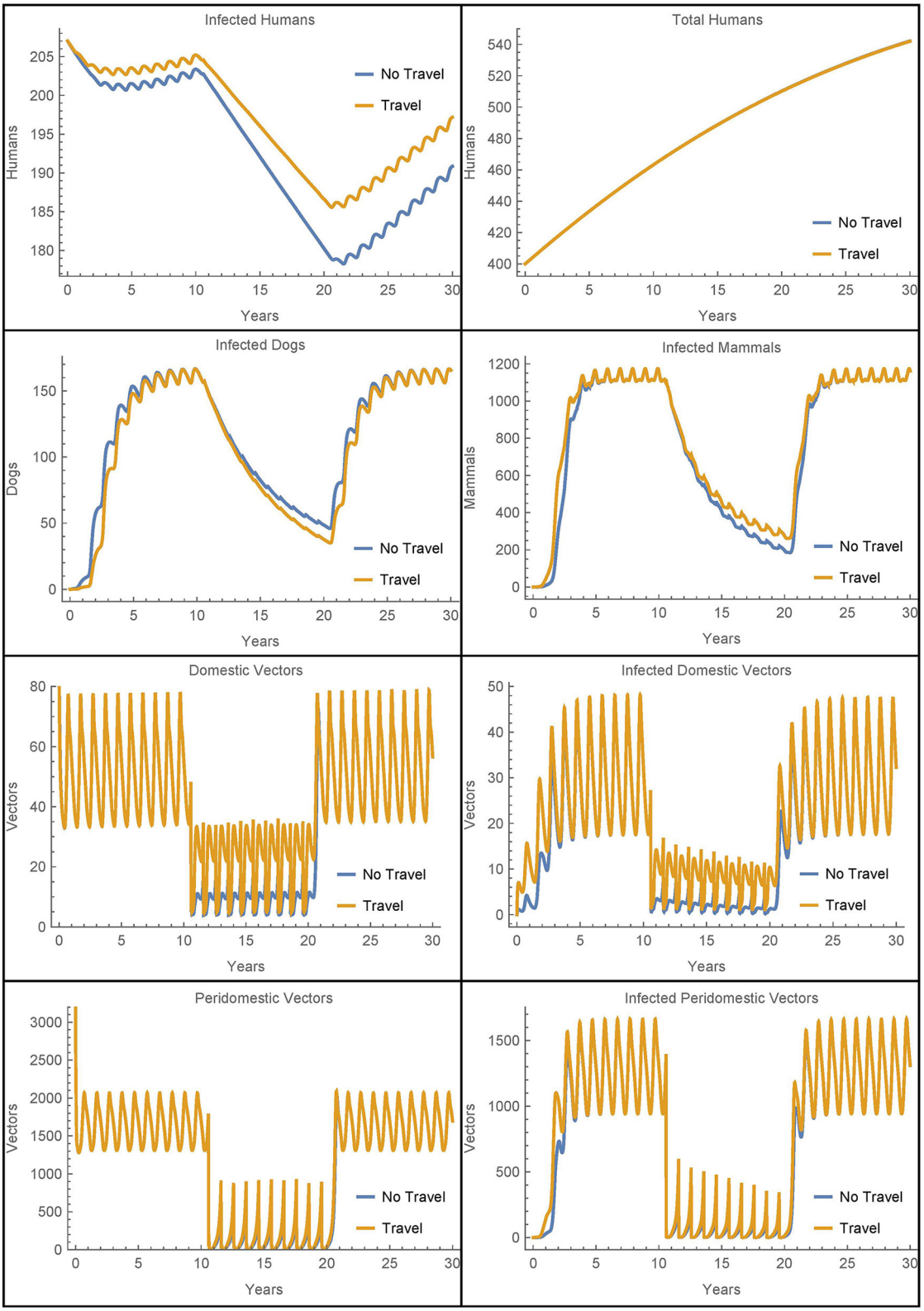

FIGURE 8
Village 1 with no infected animals or vectors: the populations of village 1, with and without travel to village 2, when only humans are initially infected.

10.3389/fams.2023.1225137

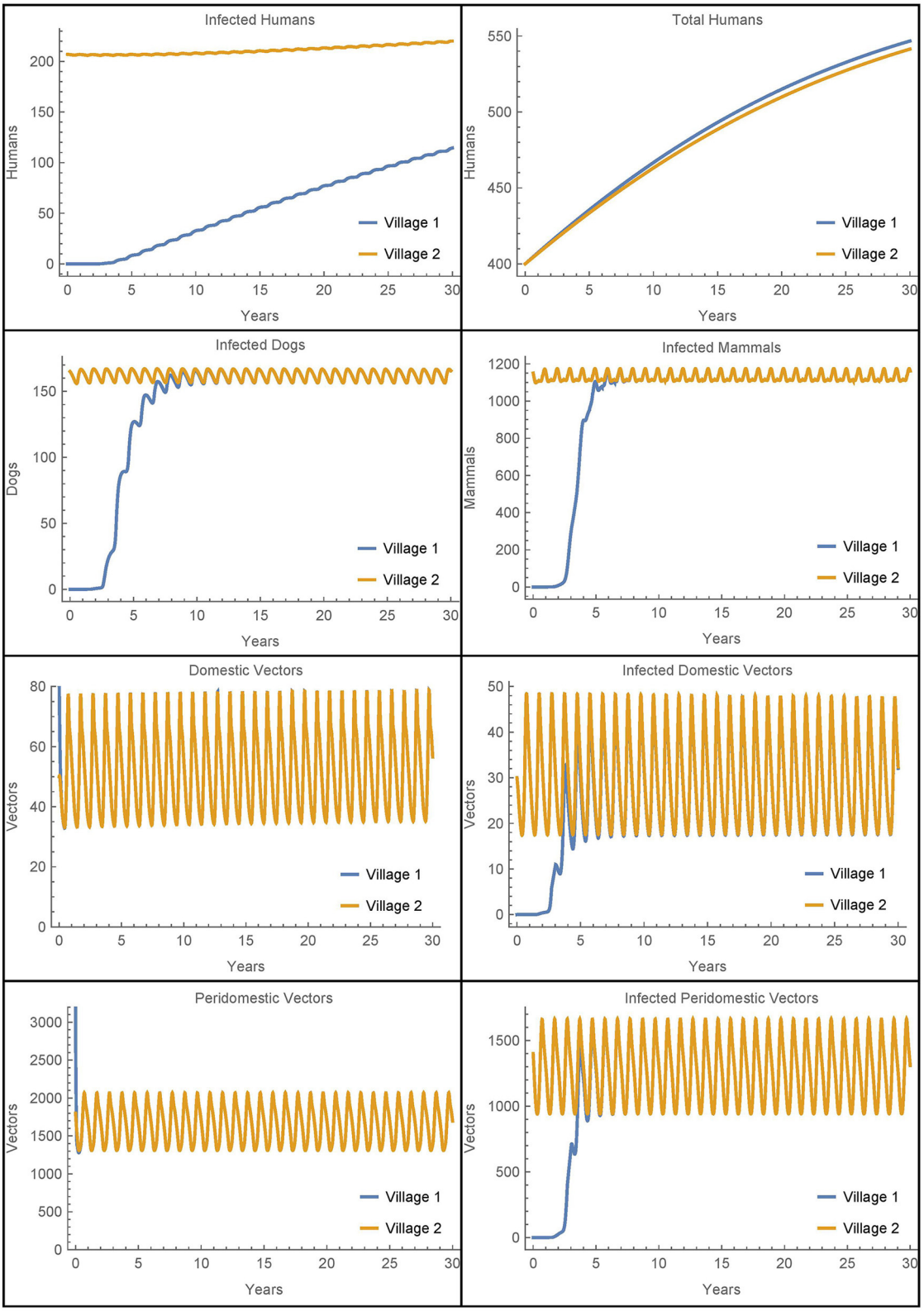

FIGURE 9
Vector migration to a disease-free village: the populations of two neighboring villages, one which is initially infection-free, with low levels of vector migration between them and no insecticide spraying.

When vector migration is low ($\alpha_{N_{1,2}} = \alpha_{N_{2,1}} = 1/365$ and $\eta = 0.01$), the number of infected humans in village 1 is essentially independent of the number of houses in village 2, varying by less than a single person over the whole range of house values in village 2. We then increased the travel parameters to their values from Simulation 2, see Figure 7. In this case, the number of humans infected after 30 years increases by about thirty people over the whole range of house values in village 2. This suggests that the size of the neighboring village with no insecticide spraying may be a significant factor in determining the effects of vector migration in spreading the disease.

Finally, we ran a similar simulation where we allowed the use of bed nets in village 2 to vary from 0% to 100% effectiveness. In both high and low vector migration scenarios, the use of bed nets in village 2 had no meaningful effect on the number of infected people in village 1. Overall, we see under a variety of circumstances that vector migration plays only a minor role in the spread of infection, except when there is substantial travel to a nearby larger village.

3.6. Simulations 6–7: low infection scenarios

In the preceding scenarios where infected populations are already established, travel and vector migration has had only a secondary or marginal effect on the dynamics. Accordingly, in this section we consider scenarios where infections in village 1 are very low so that travel can play a potentially larger role in reintroducing infected vectors.

First, we modify Simulation 2 so that initially in village 1, there are no infected animals or vectors, only infected humans. We modify the corresponding susceptible populations so that the total populations are initially the same and leave the initial human populations, infected and susceptible, as in the baseline case. All other parameters are set to their baseline values, the travel parameters are as in Simulation 2, and insecticide spraying occurs only village 1. The results are shown in Figure 8 where they are contrasted with an otherwise identical scenario that involves no travel between the two villages.

We see that in this extreme scenario, the reinfestation of village 1 caused by the transport of vectors from village 2 does increase the number of infected humans above the level of infection that would occur without the travel between the villages. However, we see that in both cases the other infected populations rebound within a few years and the vector migration from village 2 results in fewer than seven additional human infections at the 30 year mark.

Next, we modify the above scenario so that there are no infected animals or humans initially in village 1 and adjust the susceptible populations accordingly to maintain the same total values at time 0. The travel parameters are set much lower to $\alpha_{N_{1,2}} = \alpha_{N_{2,1}} = 1/365$ and $\eta = 0.01$. Also, notably we do not include insecticide spraying in either village. The results are shown in Figure 9.

As expected, the introduction of infected vectors from village 2 leads to an eventual explosion of infection throughout all populations in village 1. The infected vector populations reach steady levels within about 5 years and the dogs and mammals reach steady levels soon thereafter. Even though the travel between the villages is very low, within 30 years, around 20% of the humans in village 1 are infected. However, we note that if travel with village 2 is entirely removed from this last scenario and instead we introduce a single infected vector in the domicile at time 0, we get nearly identical dynamics and a slightly higher number of infected humans after 30 years. It is clear that once the infection is introduced from any source, it is the local dynamics in the village that drive the further infection in the village and not the ongoing reinfestation of vectors through transport.

3.7. Simulations 8–9: resistance

Finally, we look at the sensitivity of the baseline simulation to the number of resistant vectors in the village. Figure 10 depicts the number of infected humans after 30 years in a single, unconnected village as a function of the number of resistant vectors $V_{res} = W_{res}$. All other parameters are set to their baseline values and insecticide spraying occurs from year 11 to year 20, as in the baseline simulation.

We see that the first resistant vector has a substantial impact on human infections, leading to 16 more infections after 30 years. And, as expected, more resistant vectors leads to more infected humans, though at a decreasing rate. Figure 11 shows all the populations in the village in the extreme cases of 0, 1, and 40 resistant vectors. When there are no resistant vectors, the total number of vectors approaches zero during spraying years and does not recover for at least 5 years after spraying. However, with only a single resistant vector, the vector populations are able to rebound quickly to pre-spraying levels with 1–2 years. Additional resistant vectors lead to a quicker rebound of vector populations, but not significantly. Indeed, the presence of any resistant vectors allows the vector populations to rebound quickly.

Figure 11 also shows increased human infections with $V_{res} = 40$ as compared to $V_{res} = 1$, but this is due almost entirely to the

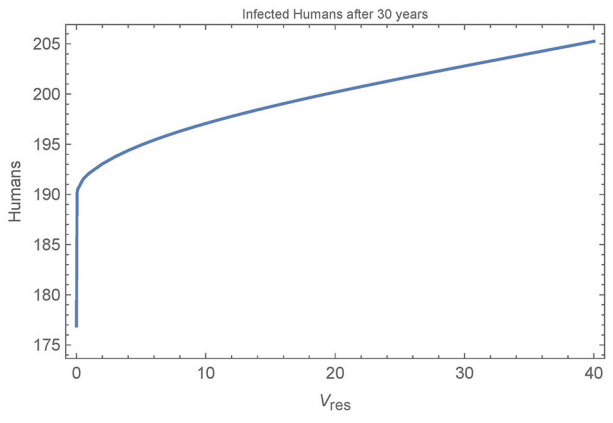

FIGURE 10
Resistant vectors in a single village: the number of infected humans in a single village after 30 years as a function of the number of resistant vectors $V_{res} = W_{res}$. All other parameters are set to their baseline values.

10.3389/fams.2023.1225137

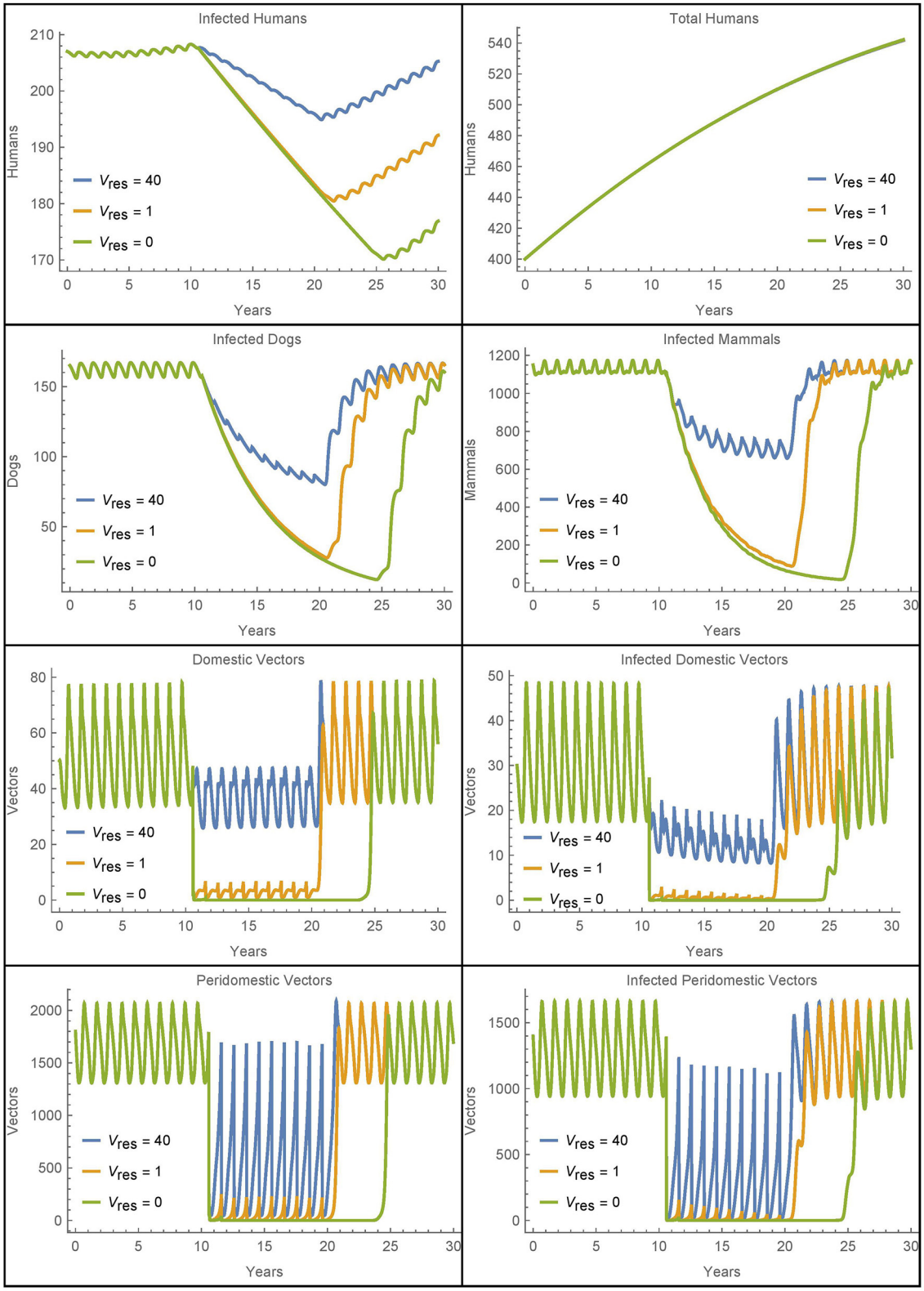

FIGURE 11
Resistant vectors in a single village: the populations in a village in different cases for the number of resistant vectors $V_{res} = W_{res}$.

sustained higher level of vectors during the spraying years, and not due to a quicker rebound of vector populations.

4. Discussion

In this work, we expand existing Chagas disease models by including novel travel and transport terms, allowing for the investigation of potentially significant infection dynamics due to travel and the exploration of relevant control strategies. In particular, the simulations seek to analyze the effects of travel and vector migration between two rural villages, one with insecticide spraying and the other with lax control methods and corresponding higher infection levels. However, these simulations suggest that human travel and the passive transport of vectors is unlikely to play a significant role in Chagas disease dynamics in rural villages.

Simulations 1 and 2 demonstrate that travel has only marginal effects on the total number of infected humans even when there is weekly travel between the villages. Simulation 3 further shows that the total number of human infections changes very little over a wide range of travel and vector migration parameters. Additionally, allowing for peridomestic vector migration does further increase the number of infected humans after 30 years in the village with spraying, but the increase remains below 3% and the net increase in both villages is under 2%. If, however, the village with no insecticide spraying is much larger than the one with spraying, and there is substantial travel between the two, then the village with spraying can see a marked increase in humans infections after 30 years as compared to the case with no travel. Otherwise, we see that the effects on human infections of travel and vector migration between villages are likely secondary across a wide range of scenarios.

Simulation 6 shows that travel and vector transport could play a role in reintroducing infected vectors into a village with no infected animals or vectors, though this scenario is unlikely. Nevertheless, and most importantly, it is not the ongoing travel that causes an eventual spike in infections. Rather, it is the introduction of any infection, in a vector or otherwise, that eventually leads to elevated infection levels in all populations, as seen in Simulation 7. Ultimately, the most significant role of travel is in introducing *T. cruzi* into an infection-free village. But once introduced, travel becomes relatively insignificant and local dynamics dominate. Given the nature of travel between villages and the endemic nature of Chagas disease, it is unlikely that control strategies related to travel will yield meaningful benefit.

We also considered the effects of insecticide resistance on the disease dynamics. Simulations 8 and 9 show that any insecticide resistance, even a single vector, can notably increase the number of human infections over 30 years by allowing the vector population to quickly rebound to pre-spraying levels once insecticide spraying ceases. Additionally, a large number of resistant vectors can further increase human infections by keeping vector numbers relatively high even during times of insecticide spraying.

Overall, these simulations suggest that human travel and passive vector migration between rural villages are not significant sources of reinfestation in the Gran Chaco. Control measures should instead focus on other reinfestation sources like sylvatic foci or domestic foci that survive insecticide spraying. A possible, unlikely exception would be the case when travel or migration is from areas where Chagas disease is endemic to areas where it is not, for example, from rural communities to urban ones [49]. Such a scenario could be considered in future work but would require significant modeling changes as the model here specifically considers travel between rural villages, which have quite different transmission dynamics than urban settings.

Data availability statement

The original contributions presented in the study are included in the article/supplementary material, further inquiries can be directed to the corresponding author.

Author contributions

DC, AS, RC, and GS contributed to the conception and design of the study. RC performed preliminary simulations and wrote the first draft of the manuscript. DC performed the final simulations and substantially revised the draft to incorporate changes in the model and results. All authors contributed to the article and approved the submitted version.

Conflict of interest

The authors declare that the research was conducted in the absence of any commercial or financial relationships that could be construed as a potential conflict of interest.

Publisher's note

References

1. Clayton J. Chagas disease 101. *Nature* (2010) 465 (Suppl 7301):S4–S5. doi: 10.1038/nature09222

2. Bilate AM, Cunha-Neto E. Chagas disease cardiomyopathy: current concepts of an old disease. *Rev Inst Med Trop São Paulo.* (2008) 50:67–74. doi: 10.1590/S0036-46652008000200001

3. WHO. *Chagas Disease (American trypanosomiasis)*. WHO. Available online at: https://www.who.int/news-room/questions-and-answers/item/chagas-disease

4. Bonney KM. Chagas disease in the 21st century: a public health success or an emerging threat? *Parasite.* (2014) 21:11. doi: 10.1051/parasite/20 14012

5. Dias JC, Silveira AC, Schofield CJ. The impact of Chagas disease control in Latin America: a review. *Mem Inst Oswaldo Cruz.* (2002) 97:603–12. doi: 10.1590/S0074-02762002000500002

6. Gurtler RE. Sustainability of vector control strategies in the Gran Chaco Region: current challenges and possible approaches. *Mem Inst Oswaldo Cruz.* (2009) 104(Suppl 1):52–9. doi: 10.1590/S0074-02762009000900009

7. Gurtler RE, Kitron U, Cecere MC, Segura EL, Cohen JE. Sustainable vector control and management of Chagas disease in the Gran Chaco, Argentina. *Proc Natl Acad Sci USA.* (2007) 104:16194–9. doi: 10.1073/pnas.0700863104

8. Lucero RH, Bruses BL, Cura CI, Formichelli LB, Juiz N, Fernandez GJ, et al. Chagas' disease in Aboriginal and Creole communities from the Gran Chaco Region of Argentina: Seroprevalence and molecular parasitological characterization. *Infect Genet Evol.* (2016) 41:84–92. doi: 10.1016/j.meegid.2016.03.028

9. Samuels AM, Clark EH, Galdos-Cardenas G, Wiegand RE, Ferrufino L, Menacho S, et al. Epidemiology of and impact of insecticide spraying on Chagas disease in communities in the Bolivian Chaco. *PLoS Negl Trop Dis.* (2013) 7:e2358. doi: 10.1371/journal.pntd.0002358

10. CDC. *Parasites - American Trypanosomiasis (also known as Chagas Disease)*. CDC. Available online at: https://www.cdc.gov/parasites/chagas/index.html

11. Bern C, Montgomery SP. An estimate of the burden of Chagas disease in the United States. *Clin Infect Dis.* (2009) 49:e52–4. doi: 10.1086/605091

12. Bern C, Montgomery SP, Katz L, Caglioti S, Stramer SL. Chagas disease and the US blood supply. *Curr Opin Infect Dis.* (2008) 21:476–82. doi: 10.1097/QCO.0b013e32830ef5b6

13. Cucunuba ZM, Okuwoga O, Basanez MG, Nouvellet P. Increased mortality attributed to Chagas disease: a systematic review and meta-analysis. *Parasit Vec.* (2016) 9:42. doi: 10.1186/s13071-016-1315-x

14. Roellig DM, Ellis AE, Yabsley MJ. Oral transmission of *Trypanosoma cruzi* with opposing evidence for the theory of carnivory. *J Parasitol.* (2009) 95:360–4. doi: 10.1645/GE-1740.1

15. Cecere MC, Vasquez-Prokopec GM, Gurtler RE, Kitron U. Reinfestation sources for Chagas disease vector, *Triatoma infestans*, Argentina. *Emerg Infect Dis.* (2006) 12:1096–102. doi: 10.3201/eid1207.051445

16. Ceballos LA, Piccinali RV, Marcet PL, Vazquez-Prokopec GM, Cardinal MV, Schachter-Broide J, et al. Hidden sylvatic foci of the main vector of Chagas disease *Triatoma infestans*: threats to the vector elimination campaign? *PLoS Negl Trop Dis.* (2011) 5:e1365. doi: 10.1371/journal.pntd.0001365

17. Cecere MC, Vazquez-Prokopec GM, Gurtler RE, Kitron U. Spatio-temporal analysis of reinfestation by *Triatoma infestans* (Hemiptera: Reduviidae) following insecticide spraying in a rural community in northwestern Argentina. *Am J Trop Med Hyg.* (2004) 71:803–10. doi: 10.4269/ajtmh.2004.71.803

18. Rojas de Arias A, Messenger LA, Rolon M, Vega MC, Acosta N, Villalba C, et al. (2022) Dynamics of Triatoma infestans populations in the Paraguayan Chaco: population genetic analysis of household reinfestation following vector control. *PLoS ONE* 17: e0263465. doi: 10.1371/journal.pone.0263465

19. Bustamante Gomez M, Goncalves Diotaiuti L, Gorla DE. Distribution of pyrethroid resistant populations of *Triatoma infestans* in the southern cone of South America. *PLoS Negl Trop Dis.* (2016) 10:e0004561. doi: 10.1371/journal.pntd.0004561

20. Picollo MI, Vassena C, Santo Orihuela P, Barrios S, Zaidemberg M, Zerba E. High resistance to pyrethroid insecticides associated with ineffective field treatments in *Triatoma infestans* (Hemiptera: Reduviidae) from Northern Argentina. *J Med Entomol.* (2005) 42:637–42. doi: 10.1093/jmedent/42.4.637

21. Coffield DJ, Kuttler K, Qu X, Rabinovich J, Shillor M, Spagnuolo A, et al. Model for the transmission of Chagas disease with random inputs. *Biomath.* (2014) 3:1–16. doi: 10.11145/j.biomath.2014.11.071

22. Coffield DJ, Spagnuolo A. Steady state stability analysis of a Chagas disease model. *Int J Math Models Biosci.* (2014) 3:1–13. doi: 10.11145/j.biomath.2014.05.261

23. Coffield DJ, Spagnuolo AM, Shillor M, Mema E, Pell B, Pruzinsky A, et al. A model for Chagas disease with oral and congenital transmission. *PLoS ONE.* (2013) 8:e67267. doi: 10.1371/journal.pone.0067267

24. Spagnuolo AM, Shillor M, Kingsland L, Thatcher A, Toeniskoetter M, Wood B. A logistic delay differential equation model for Chagas disease with interrupted spraying schedules. *J Biol Dyn.* (2012) 6:377–94. doi: 10.1080/17513758.2011.587896

25. Spagnuolo AM, Shillor M, GA S. A model for Chagas disease with controlled spraying. *J Biol Dyn.* (2011) 5:299–317. doi: 10.1080/17513758.2010.505985

26. Spagnuolo AM, Coffield DJ, Carigan A, Hee-Jin Corcoran A, Van Loo B, Shillor M, et al. Carignan AM, et al. A mathematical model of Chagas disease dynamics in the Gran Chaco Region. *J Coupled Syst Multiscale Dyn.* (2015) 3:177–99. doi: 10.1166/jcsmd.2015.1078

27. Gurtler RE, Cecere MC, Lauricella MA, Cardinal MV, Kitron U, Cohen JE. Domestic dogs and cats as sources of *Trypanosoma cruzi* infection in rural northwestern Argentina. *Parasitology.* (2007) 134(Pt 1):69–82. doi: 10.1017/S0031182006001259

28. Ceballos LA, Vazquez-Prokopec GM, Cecere MC, Marcet PL, Gurtler RE. Feeding rates, nutritional status and flight dispersal potential of peridomestic populations of *Triatoma infestans* in rural northwestern Argentina. *Acta Trop.* (2005) 95:149–59. doi: 10.1016/j.actatropica.2005.05.010

29. Castanera M, Gurtler RE. A stage-structured stochastic model of the population dynamics of *Triatoma infestans*, the main vector of Chagas disease. *Ecol Modell.* (2003) 162:33–53. doi: 10.1016/S0304-3800(02)00388-5

30. Gurtler RE, Ceballos LA, Ordonez-Krasnowski P, Lanati LA, Stariolo R, Kitron U. Strong host-feeding preferences of the vector *Triatoma infestans* modified by vector density: implications for the epidemiology of Chagas disease. *PLoS Negl Trop Dis.* (2009) 3:e447. doi: 10.1371/journal.pntd.0000447

31. Gurtler RE, Cohen JE, Cecere MC, Chuit R. Shifting host choices of the vector of Chagas disease, *Triatoma infestans*, in relation to the availability of host in houses in North-West Argentina. *J Appl Ecol.* (1997) 34:699–715.

32. Stevens L, Dorn PL, Schmidt JO, Klotz JH, Lucero D, Klotz SA. Kissing bugs. The vectors of Chagas. *Adv Parasitol.* (2011) 75:169–92. doi: 10.1016/B978-0-12-385863-4.00008-3

33. Gurtler RE, Segura EL, Cohen JE. Congenital transmission of *Trypanosoma cruzi* infection in Argentina. *Emerg Infect Dis.* (2003) 9:29–32. doi: 10.3201/eid0901.020274

34. Kirchhoff LV. Chagas disease (American Trypanosomiasis). *Infect Dis Clin North Am.* (1999) 7:487–502.

35. Munoz J, Coll O, Juncosa T, Verges M, del Pino M, Fumado V, et al. Prevalence and vertical transmission of *Trypanosoma cruzi* infection among pregnant Latin American women attending 2 maternity clinics in Barcelona, Spain. *Clin Infect Dis.* (2009) 48:1736–40. doi: 10.1086/599223

36. Gurtler RE, Cecere MC, Fernandez MdelP, Vazquez-Prokopec GM, Ceballos LA, Gurevitz JM, et al. Key source habitats and potential dispersal of *Triatoma infestans* populations in Northwestern Argentina: implications for vector control. *PLoS Negl Trop Dis.* (2014) 8:e3238. doi: 10.1371/journal.pntd.0003238

37. Dias JC. Southern Cone Initiative for the elimination of domestic populations of *Triatoma infestans* and the interruption of transfusional Chagas disease. Historical aspects, present situation, and perspectives. *Mem Inst Oswaldo Cruz.* (2007) 102(Suppl 1):11–8. doi: 10.1590/S0074-02762007005000092

38. Catala S. The biting rate of *Triatoma infestans* in Argentina. *Med Vet Entomol.* (1991) 5:325–33.

39. Cohen JE, Gurtler RE. Modeling household transmission of American trypanosomiasis. *Science.* (2001) 293:694–8. doi: 10.1126/science.1060638

40. Kribs-Zaleta C. Estimating contact process saturation in sylvatic transmission of *Trypanosoma cruzi* in the United States. *PLoS Negl Trop Dis.* (2010) 4:e656. doi: 10.1371/journal.pntd.0000656

41. Kribs-Zaleta CM. Alternative transmission modes for *Trypanosoma cruzi*. *Math Biosci Eng.* (2010) 7:657–73. doi: 10.3934/mbe.2010.7.657

42. Rassi A, Rassi A, Marin-Neto JA. Chagas heart disease: pathophysiologic mechanisms, prognostic factors and risk stratification. *Mem Inst Oswaldo Cruz.* (2009) 104(Suppl 1):152–8. doi: 10.1590/S0074-02762009000900021

43. Agency CIA. *CIA World Factbook*. (2009). Available online at: https://www.cia.gov/the-world-factbook/countries/argentina/

44. Cerece MC, Canale DM, Gurlter RE. Effects of refuge availability on the population dynamics of *Triatoma infestans* in central Argentina. *J Appl Ecol.* (2003) 40:742–56. doi: 10.1046/j.1365-2664.2003.00825.x

45. Cavallo MJ, Amelotti I, Abrahan L, Cueto G, Gorla DE. Rural houses infestation by Triatoma infestans in northwestern Argentina: vector control in a high spatial heterogeneous infestation area. *PLoS ONE.* (2018) 13:e0201391. doi: 10.1371/journal.pone.0201391

46. *Worldometers* (2022). Available online at: https://www.worldometers.info/world-population/bolivia-population/

47. *Worldometers* (2022). Available online at: https://www.worldometers.info/world-population/paraguay-population/

48. *Worldometers* (2022). Available online at: https://www.worldometers.info/world-population/argentina-population/

49. Colussi C, Stafuza M, Nepote M, Mendicino D. Seroprevalence of Chagas disease in urban and rural indigenous populations of the south of Gran Chaco. *Rev Soc Bras Med Trop.* (2022) 55:e04792021. doi: 10.1590/0037-8682-047 9-2021

frontiers | Frontiers in Applied Mathematics and Statistics

TYPE Original Research
PUBLISHED 31 August 2023
DOI 10.3389/fams.2023.1224891

OPEN ACCESS

EDITED BY
Asep K. Supriatna,
Padjadjaran University, Indonesia

REVIEWED BY
Arrival Rince Putri,
Andalas University, Indonesia
Sania Qureshi,
Mehran University of Engineering and Technology, Pakistan
Ummu Atiqah Mohd Roslan,
University of Malaysia Terengganu, Malaysia

*CORRESPONDENCE
Fekadu Mosisa Legesse
✉ fekadumosisa22@gmail.com

RECEIVED 18 May 2023
ACCEPTED 02 August 2023
PUBLISHED 31 August 2023

CITATION
Legesse FM, Rao KP and Keno TD (2023) Cost effectiveness and optimal control analysis for bimodal pneumonia dynamics with the effect of children's breastfeeding.
Front. Appl. Math. Stat. 9:1224891.
doi: 10.3389/fams.2023.1224891

Cost effectiveness and optimal control analysis for bimodal pneumonia dynamics with the effect of children's breastfeeding

Fekadu Mosisa Legesse*, Koya Purnachandra Rao and Temesgen Duressa Keno

Department of Mathematics, College of Natural and Computational Science, Wallaga University, Nekemte, Ethiopia

The global impact of exclusive versus inclusive nursing on particular baby mortalities and morbidities from conception to 6 months is examined in this study. Exclusive breastfeeding practices are more crucial and effective in preventing illness outbreaks when there is no access to appropriate medications or vaccinations. Additionally, this study takes optimal control theory into account, applying it to a system of differential equations that uses Pontryagin's Maximum Principle to describe a bimodal pneumonia transmission behavior in a vulnerable compartment. The proposed pneumonia transmission model was then updated to include two control variables. These include preventing illness exposure in susceptible children through various preventative measures and treating infected children through antibiotics, hospital care, and other treatments. If the threshold number ($\mathfrak{R}_0$) is less than one, then treatment and prevention rates are increased, and the disease will be wiped out of the population. However, when ($\mathfrak{R}_0$) is greater than one, then the disease persists in the population, which indicates that prevention and treatment rates are low. To evaluate the cost-effectiveness of all potential control techniques and their combinations, the incremental cost-effectiveness ratio (ICER) was determined. The simulation results of the identified model show that the interventions of prevention and treatment scenarios were the most successful in eradicating the dynamics of the pneumonia disease's propagation during the epidemic, but they were ineffective from a cost-saving perspective. Therefore, limiting pneumonia transmission to prevention alone during an outbreak is the most economical course of action.

KEYWORDS

inclusive and exclusive, cost-effectiveness, pneumonia, optimal control, S_1S_2EIR model, ICER, breastfeeding

1. Introduction

Infant (child) disability and death are the primary continuing public health issues worldwide. However, newborn (child) mortality and morbidity rates are greatly impacted by deaths caused by infectious illnesses. Infectious diseases can take 7 from 10 childhood deaths throughout the world. Pneumonia is one of the most common causes of death worldwide among acute respiratory infections, accounting for 30% of all child fatalities. Ninety-five percent of cases of pneumonia occur in developing countries. As a result, infectious illnesses are more likely to kill newborn babies in these countries [1, 2].

Among acute respiratory infection (ARI) diseases, pneumonia is the one that affects children's lungs. Approximately 740,180 children aged 05 years died because of pneumonia in 2019, which accounts for 14 and 22% of all deaths of children below 5 years and 1–5 year(s) old, respectively, and deaths are higher in Asia and Africa [3]. Hence, of infectious diseases, pneumonia causes the most children's deaths worldwide [4]. Pneumonia can be caused either by viruses, bacteria, or fungi; among these, bacterial pneumonia is the leading cause of death for children under 6 years of age. By immunizing against the disease, providing appropriate nutrition (EBF), and decreasing environmental variables, pneumonia can be avoided [5]. Additionally, using many control measures, such as prevention, treatment, and reducing indoor air pollution, can halt the spread of pneumonia. The following research has been carried out to address non-exclusive EBF or a lack of EBF, one of the main risk factors for infectious illnesses.

The first natural diet for infants is their mother's milk, which contains all the nutrients and energy required for a baby throughout the first 6 months of life [6]. According to WHO recommendations, newborns should receive only breast milk for the first 6 months of their lives. Thereafter, additional (complementary) foods are allowed for 18 months or more, followed by breastfeeding. Hence, infants (children) can achieve good growth and development [7]. Therefore, for children in the first months of life up to 6 months, any additional food or liquid (even water) is not permitted except vitamins, mineral supplements, and medicine[7, 8].

An intervention of double control has been offered to help eliminate the mortality and disability rates among children because of infectious diseases. Breastfeeding is one of the most popular and cost-effective strategies (interventions) for preventing pediatric pneumonia and all other causes of death [9–11]. Furthermore, the WHO, UNICEF, AAP, AAFP, and NNPE advocate starting breastfeeding promptly within the first hour after birth and continuing to exclusively breastfeed with human milk for the following 6 months to reduce the baby (child) death and disability rate. Continual breastfeeding with other appropriate foods will follow for the first 2 years of life to ensure that the children have healthy optimal growth and development [2].

Most of the studies assure that over two-thirds of the deaths occurring globally in the first year of life of children are often associated with a loss of exclusive breastfeeding or inappropriate feeding exercises [10]. Sub-optimal breastfeeding contributes to 18% of acute respiratory disease deaths among children under 5 years old in low-income countries [6].

Evidence suggests that if the EBF length is properly maintained, it can significantly increase immunity and lower the risk of death and disability from communicable and non-communicable diseases in both the early and advanced phases [12, 13]. EBF throughout the first 6 months of a baby's (or child's) life can typically lower the likelihood of developing any infectious diseases [14]. For the first 6 months of their lives, infants (children) who were nursed exclusively had a higher risk of contracting infectious diseases than those who were not [9, 15].

According to [10, 16], 1.24 million or 96% of child deaths occur during the first 6 months of life due to inappropriate EBF practices, and the mortality rate is higher in Africa and Asia. Additionally, poor breastfeeding results in more than 236,000 child deaths annually in a select few nations, including Nigeria, China, Mexico, Indonesia, and India [17]. Furthermore, in low- and middle-income nations, inadequate breastfeeding was found to be responsible for 18 and 30% of acute respiratory and diarrheal mortalities, respectively [18]. To reduce child mortality among children under the age of five, the WHO advises that an EBF of 90% is needed globally. Furthermore, the Sustainable Development Goals (SDGs) plan envisaged an increase in EBF of 50% by 2025 [19, 20]. According to the study by [12, 20], raising the EBF rate in middle-income and developing nations to an ideal level can reduce infant mortality among children under the age of five by 13 to 15%.

Mathematical models are frequently used to (i) analyse the dynamics of the spread of infectious diseases like cholera, bronchiolitis, pneumonia, and others; (ii) employ a variety of control methods to reduce or stop the spread of infectious diseases; and (iii) predict the effects of these diseases on people's lives, socio-economic systems, and national health programmes and policies. However, none of the aforementioned studies take into account a mathematical model method to illustrate the transmission behavior of infectious diseases, particularly pneumonia.

Several mathematical modeling studies have been conducted to estimate the potential burden of the endemic and the various control approaches for the endemic disease of pneumonia in children. Tilahun et al. [21] considered a non-linear deterministic model for the transmission of the pneumonia disease in a population of variable size, together with optimal control and cost-effectiveness measures. Agusto et al. [22] studied the advantage of isolation strategies and quarantine effectiveness measures against outbreaks of disease in the absence of appropriate medicines or vaccines.

Swai et al. [23] formulated an optimal control of pneumonia transmission in two strains by incorporating drug resistance. Additionally, how measures such as vaccination, public awareness campaigns, and therapy can reduce pneumonia transmission patterns should be considered. Tessema et al. [24] also developed a deterministic mathematical model of drug-resistant pneumonia with ideal preventive measures and cost-effectiveness evaluations. Based on the simulation values of optimal controls for the proposed model, they concluded that the combination of prevention, treatment, and screening of infectious persons is the most efficient and cost-effective way to remove pneumonia infections from the community. The diagnostic problem of distinguishing between bacterial and non-bacterial pneumonia is the main reason antibiotics are used to treat pneumonia in children. Consequently, Wu et al. [25] present causal Bayesian networks (BNs) in their model as useful tools for resolving this problem because they provide succinct maps of the probabilistic relationships between variables and produce results in a way that is understandable and justified by incorporating domain expert knowledge and numerical data.

Kotola and Mekonnen [26] created a deterministic model to demonstrate the efficacy of interventions for pneumonia and meningitis co-infection and provide a reasoned recommendation to public health officials, decision-makers in government policy, and programme implementers. Owing to their shared clinical

characteristics and significant effects on human morbidity and mortality, pneumonia and tuberculosis are two of the most frequent airborne infections. Therefore, in a community of populations with both diseases, co-infection of the two diseases becomes inevitable. Owing to a lack of resources, the significant illness burden that these endemics together impose necessitates an efficient intervention to mitigate the impact. Thus, the authors in Gweryina et al. [27] use a pragmatic approach to create an SEIR model for the co-dynamics of tuberculosis and pneumonia. Using a variety of parameters, Naveed et al. [28] investigated the dynamics of delayed pneumonia-like infectious illnesses. Kassa et al. [29] and Rafiq et al. [30] offer a mathematical model of COVID-19 that includes bimodal virus transmission in a susceptible compartment.

Until now, only Legesse et al. [31] formulated a S_1S_2CIR deterministic mathematical model by grouping susceptible children as inclusively and exclusively breastfeed children and verify that inclusive breastfeeding children are more exposed to pneumonia than those children breastfeed exclusively. However, they did not take into account optimal control analysis in their research. Furthermore, no research has been carried out so far to assess the impact of EBF practice on child mortality rates and the efficacy of EBF practice in lowering pediatric mortality due to infectious disease (pneumonia). With this as a backdrop, the study's objective is to apply mathematical models with optimal control and accessible methods to treat pneumonia in infants between the ages of 0 and 6 months who do not participate in EBF. By increasing the prevalence of EBF and stepping up efforts to reduce non-exclusive breastfeeding, the findings of this study will help in making decisions that will reduce child mortality and impairment from pneumonia.

The article is organized as follows. The proposed model is formulated in the Construction of a Bimodal Pneumonia Model section and its analysis is presented in the Analyzing the Model Qualitatively section. Stability analysis of the equilibria is then discussed in the Equilibrium Point Stability section. Extension of the proposed model into optimal control is presented in The Proposed Model Under Optimal Control section. Numerical simulations are performed to support the analytical results discussed in the Analyzing the Model Qualitatively section and are presented in the Results and Discussion. Cost-effective analysis is performed in the subsequent section followed, finally, by the Conclusion.

2. Construction of the bimodal pneumonia model

In this model, the overall population size N(t) is divided into five mutually exclusive compartments based on the disease condition of the population as a whole. Furthermore, the total population size N(t) at any given time t is given by:

$$N(t) = S_I(t) + S_E(t) + E(t) + I(t) + R(t) \tag{1}$$

At any time instant $t \in [0, \infty)$, the real valued differentiable state variables $S_I(t)$,$S_E(t)$,$E(t)$,$I(t)$, and $R(t)$ represent the number of susceptible children that are not exclusively breastfed, susceptible children that are exclusively breastfed, children exposed to the disease, children that are seriously infected, and children who have obtained temporary immunity from pneumonia, respectively. This research assumes that the two susceptible classes $S_I(t)$ and $S_E(t)$ are enlisted into the population at rates of Λ_1 and Λ_2, respectively. They acquire pneumonia infection through effective contact with the infected humans $I(t)$ or via inhalation of contaminated air droplets at a force of infection given by

$f_i = \frac{\beta_i I}{N}$, where $i = 1, 2$ and $\beta_j = kP_j$, where $j = 1, 2$.

Here $\beta_j = kP_j$ for $j = 1, 2$ denotes the transmission rates. However, k stands for the number of contacts, and P_j is the probability of close contact rates between two susceptible humans with the infected individuals causing infection.

Humans exposed to pneumonia advance at a γ rate to the infected compartment $I(t)$. The sub-populations are all reduced at the same time because a consistent natural mortality rate of μ is taken into account for each compartment. The parameters σ and α at the infected stage indicate the mortality rate from pneumonia disease, which only falls in the infected class, and the percentage of children who recover due to therapy or innate immunity, respectively. Those individuals that have recovered from pneumonia are assumed to have partial immunity and again become susceptible at a rate of δ. This study also assumes that a child who has obtained partial immunity does not again join exclusively breastfed children because as one individual is infected with infectious diseases they cannot regain their original immunity [31]. Using the parameter values, basic model assumptions, and state variables described above, we have generated a systematic diagram (Figure 1), and the corresponding model equation is given by Equation (2).

$$\begin{cases} \frac{dS_I}{dt} &= \Lambda_1 + \delta R - f_1 S_I - \mu S_I \\ \frac{dS_E}{dt} &= \Lambda_2 - f_2 S_E - \mu S_E \\ \frac{dE}{dt} &= f_1 S_I + f_2 S_E - (\gamma + \mu) E \\ \frac{dI}{dt} &= \gamma E - (\sigma + \alpha + \mu) I \\ \frac{dR}{dt} &= \sigma I - (\mu + \delta) R \end{cases} \tag{2}$$

With the following initial conditions:

$$S_I(0) \geq 0, S_E(0) \geq 0, E(0) \geq 0, I(0) \geq 0, R(0) \geq 0 \tag{3}$$

3. Analyzing the model qualitatively

This subsection explains the qualitative behavior of the model being considered for the long run.

3.1. Positivity and boundedness of solution

To ensure that the generated dynamical system's (2) positivity of solution is both epidemiologically meaningful and theoretically well-posed, we must show that all the state variables of the dynamical systems are non-negative.

Theorem 3.1. All the solutions of Equation (2) with the positive initial condition given on Equation (3) are non-negative.

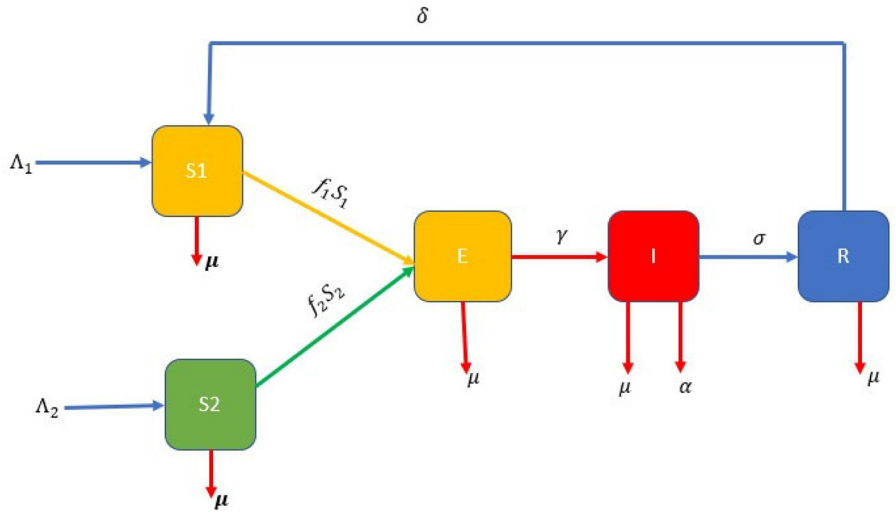

FIGURE 1
Model flow chart.

Proof. From Equation (3), all the state variables are positive or zero at the initial time, then $T > 0$. To show the positivity of all the state variables select any equation of Equation (2), randomly let it be

$$\frac{dS_I}{dt} = \Lambda_1 + \delta R - f_1 S_I - \mu S_I$$

$$\frac{dS_I}{dt} + (f_1 + \mu)S_I = \Lambda_1 + \delta R$$

$$\frac{d}{dt}[e^{\int_0^T (f_1+\mu)dt'} S_I] = (e^{\int_0^T (f_1+\mu)dt'})[\Lambda_1 + \delta R] \quad (4)$$

where $t' \in [0, T]$ and each state variable are non-negative at t'. Equation (4) is integrated with regard to time to produce

$$S_I(t) = k_1 S_I(0) + k_1 \left[\int_0^T (e^{\int_0^T (f_1+\mu)dt'})[\Lambda_1 + \delta R]dt \right] \geq 0 \quad (5)$$

where $k_1 = e^{-\int_0^T (f_1+\mu)dt'}$. From Equation (4), we observe that $S_I(t)$ is non-negative for all $t > 0$. In a similar fashion, one can show $S_E(t) \geq 0, E(t) \geq 0, I(t) \geq 0$ and $R(t) \geq 0$.

Theorem 3.2. The closed positive invariant set Ω is a biologically and mathematically well-posed region of the initial value problems defined on Equations (2), (3), where

$$\Omega = \{(S_I, S_E, C, E, R) \in R_+^5 : 0 < N(S_I, S_E, E, I, R) \leq \frac{\Lambda_1 + \Lambda_2}{\mu}\} \quad (6)$$

Proof. For convenience, we let $S_1 = S_I, S_2 = S_E, r_1 = \gamma + \mu, r_2 = \sigma + \alpha + \mu, r_3 = \mu + \delta$ throughout this study. Differentiating Equation (1) with respect to t gives

$$\frac{dN}{dt} = \frac{dS_I}{dt} + \frac{dS_E}{dt} + \frac{dE}{dt} + \frac{dI}{dt} + \frac{dR}{dt}$$

$$\frac{dN}{dt} = \Lambda_1 + \Lambda_2 - \mu(S_I + S_E + E + I + R) - \alpha I$$

$$\frac{dN}{dt} = \Lambda_1 + \Lambda_2 - \mu N - \alpha I \quad (7)$$

In the absence of infectious rate Equation (7) reduced to

$$\frac{dN}{dt} \leq \Lambda_1 + \Lambda_2 - \mu N. \quad (8)$$

Integrating both sides of Equation (8) with regard to t and taking the limit of Equation (8) as $t \longrightarrow \infty$, we obtain

$$N(t) \leq \frac{\Lambda_1 + \Lambda_2}{\mu} - \frac{\Lambda_1 + \Lambda_2 - \mu N_0}{\mu} e^{-\mu t} \quad (9)$$

$$N(t) \leq \frac{\Lambda_1 + \Lambda_2}{\mu}. \quad (10)$$

Therefore, each solution of the initial value problems on Equations (2) and (3) remains in Equation (6) for all $t > 0$. This result can be summarized as lemma below.

Lemma 3.1. Ω is a positively invariant region for the Equation (2) with initial condition Equation (3) in R_+^5.

3.2. Threshold parameter

Before calculating the expression for threshold quantity ($\Re_0$), determine pneumonia free of Equation (2). For this aim, equate the right hand side of Equation (2) to zero. After that, substitute in $S_1(t) = S_I(0) > 0, S_E(t) = S_E(0) > 0, E(t) = E_0 = I(t) = I_0$ and $R(t) = R_0 = 0$. Thus,

$$E_0 = \left(\frac{\Lambda_1}{\mu}, \frac{\Lambda_2}{\mu}, 0, 0, 0\right). \quad (11)$$

Hence, E_0 is the pneumonia free-equilibrium of Equation (2). By using DFE we can account the threshold number ($\mathfrak{R}_0$) following the work in Agusto [22], and we used the method of next generation matrix to obtain the required threshold number and from the transmission matrix

$$\mathcal{F} = DF(E_0) = \begin{bmatrix} \frac{\partial F_1(E_0)}{\partial E} & \frac{\partial F_1(E_0)}{\partial I} \\ \frac{\partial F_2(E_0)}{\partial E} & \frac{\partial F_2(E_0)}{\partial I} \end{bmatrix}.$$

Where $F_1(t) = f_1 S_I + f_2 S_E$ and $F_2(t) = \gamma E$

$$\mathcal{F} = \begin{bmatrix} 0 & \frac{\Lambda_1\beta_1+\Lambda_2\beta_2}{\Lambda_1+\Lambda_2} \\ \gamma & 0 \end{bmatrix} \tag{12}$$

and the transition matrix V is given by

$$\mathcal{V} = DF(E_0) = \begin{bmatrix} \frac{\partial V_1(E_0)}{\partial E} & \frac{\partial V_1(E_0)}{\partial I} \\ \frac{\partial V_2(E_0)}{\partial E} & \frac{\partial V_2(E_0)}{\partial I} \end{bmatrix}.$$

where $V_1 = r_1 E$ and $V_2 = r_2 I$.

$$\Rightarrow \mathcal{V} = \begin{bmatrix} r_1 & 0 \\ 0 & r_2 \end{bmatrix} \tag{13}$$

Hence, using the next generation matrix calculated from Equations (12), (13) we get

$$\mathcal{F}\mathcal{V}^{-1} = \frac{1}{r_1 r_2} \begin{bmatrix} 0 & r_1 \frac{\beta_1\Lambda_1+\beta_2\Lambda_2}{\Lambda_1+\Lambda_2} \\ \gamma r_2 & 0 \end{bmatrix} \tag{14}$$

Now, the governing eigenvalue of Equation (14) represents $\mathfrak{R}_0$ of Equation (2), which is given by

$$\mathfrak{R}_0 = \sqrt{\frac{\gamma(\beta_1\Lambda_1 + \beta_2\Lambda_2)}{r_1 r_2(\Lambda_1 + \Lambda_2)}} \tag{15}$$

The threshold number ($\mathfrak{R}_0$) is a quantity that determines how pneumonia spreads within the population or fades out of the society. If $\mathfrak{R}_0 < 1$ then the disease will fade out of the community. This shows that more exclusivity in breastfeeding children is added to the susceptible class. Because exclusively breastfed individuals have high natural immunity, they are less exposed to the diseases. $\mathfrak{R}_0 > 1$ shows that there is a continuation of disease spread within the population.

3.3. Existence of the model's endemic equilibrium point

In this part, we examine the condition known as EE of Equation (2). The fundamental motivation for this equilibrium is that it is utilized to estimate how long pneumonia will continue to affect the population. To identify the prerequisites for an equilibrium in which community pneumonia is endemic (that is, at least one of $E^* \neq 0$ or $I^* \neq 0$), denoted by $E_e = (S_I^*, S_E^*, E^*, I^*, R^*)$. To find E_e, equate each equation in Equation (2) to zero and express each state variable in terms of the force of infection at the steady state (f_i^* where i=1,2), given by

$$f_1^* = \frac{\beta_1 I}{N^*},\ f_2^* = \frac{\beta_2 I}{N^*}$$

$$\begin{aligned} S_I^* &= \tfrac{\Lambda_1 r_3 + \delta\sigma I^*}{r_3(f_1^* - \mu)}, \\ S_E^* &= \tfrac{\Lambda_2}{f_1^* - \mu} = \tfrac{\Lambda_2(\Lambda_1+\Lambda_2)}{\mu(\beta_2 I^* - (\Lambda_1+\Lambda_2))}, \\ E^* &= \tfrac{r_2 I^*}{\gamma}\mathfrak{R}_0^2, \\ I^* &= \tfrac{\gamma E^*}{r_2}, \\ R^* &= \tfrac{\sigma}{r_3}\mathfrak{R}_0^2 \end{aligned} \tag{16}$$

Therefore, the existence of E_e in Equation (16) depends on $\mathfrak{R}_0$, meaning that E_e from Equation (2) exists if $\mathfrak{R}_0 > 1$.

4. Equilibrium point stability analysis

The two equilibria of Equation (2) are shown in this subsection to have both local and global asymptotic stability. We employ the Jacobian matrices of system on Equation (2) at DFE and EE for local stability and the Lyapunov function for the global stability of both equilibria to confirm this stability.

4.1. Local stability analyses

Theorem 4.1. The disease free-equilibrium point (E_0), of Equation (2) corresponding to the considered model is locally asymptotically stable if $\mathfrak{R}_0 < 1$ and not stable otherwise.

Proof. To prove this, first determine the Jacobian matrix evaluated at E_0 becomes

$$J(E_o) = \begin{bmatrix} -\mu & 0 & 0 & -\frac{\beta_1\Lambda_1}{\Lambda_1+\Lambda_2} & \delta \\ 0 & -\mu & 0 & -\frac{\beta_2\Lambda_2}{\Lambda_1+\Lambda_2} & 0 \\ 0 & 0 & -r_1 & \frac{\beta_1\Lambda_1+\beta_2\Lambda_2}{\Lambda_1+\Lambda_2} & 0 \\ 0 & 0 & \gamma & -r_2 & 0 \\ 0 & 0 & 0 & \sigma & -r_3 \end{bmatrix} \tag{17}$$

The characteristic polynomial of Equation (17) becomes

$$\Psi(\lambda) = (\lambda + \mu)^2(\lambda + r_3)(\lambda^2 + D_1\lambda + D_2) \tag{18}$$

The first three eigenvalues of Equation (18) are $\lambda = -\mu$ a double root, $\lambda = -r_3$. All are negative, and we use the RouthHurwitz criterion to confirm the presence of the remaining eigenvalues in the manner described below:

$$D_1 = r_1 + r_2 > 0,$$

$$D_2 = r_1 r_2 - \gamma\frac{\beta_1\Lambda_2 + \beta_2\alpha}{\Lambda_1 + \Lambda_2} = r_1 r_2(1 - \mathfrak{R}_0^2) > 1$$

As a result, the RouthHurwitz criteria's required condition is confirmed whenever $\mathfrak{R}_0 < 1$. Therefore, the DFE (E_0) of Equation (2) is locally asymptotically stable (LAS) when $\mathfrak{R}_0 < 1$.

Theorem 4.2. The disease endemic equilibrium point (E_e), of Equation (2) is LAS in Ω if $\mathfrak{R}_0 > 1$ and unstable otherwise.

Proof. To prove the local stability of E_e, first determine the desired Jacobean matrix $J(E_e)$ of system (2) at the endemic equilibrium, which is given as Equation (19)

$$J(E_e) = \begin{bmatrix} -(f_1^* + \mu) & 0 & 0 & -\frac{\beta_1 S_I^*}{N^*} & \delta \\ 0 & -(f_2^* + \mu) & 0 & -\frac{\beta_2 S_E^*}{N^*} & 0 \\ f_1^* & f_2^* & -r_1 & \frac{\beta_1 S_I^* + \beta_2 S_E^*}{N^*} & 0 \\ 0 & 0 & \gamma & -r_2 & 0 \\ 0 & 0 & 0 & \sigma & -r_3 \end{bmatrix} \quad (19)$$

The characteristics polynomial corresponding to Equation (19) is

$$(\lambda + (f_1^* + \mu))(\lambda + (f_2^* + \mu))(\lambda + r_1)(\lambda + r_2)(\lambda + r_3) = 0 \quad (20)$$

The first three roots of Equation (20) are $\lambda = -r_1 < 0, \lambda = -r_2 < 0$, and $\lambda = -r_3 < 0$ and the remaining roots can be calculated from

$$\lambda^2 + a_1\lambda + a_2$$

where

$$a_1 = f_1^* + f_2^* + 2\mu \quad \text{and} \quad a_2 = f_1^* f_2^* + 2\mu(f_1^* + f_2^*) + \mu^2$$

and f_1^*, f_2^* are defined as the force of infection at the endemic equilibrium.

As $\lambda^2 + a_1\lambda + a_2$ has both roots with a negative real part (and the system with characteristic equation $P(\lambda) = \lambda^2 + a_1\lambda + a_2 = 0$ is stable) if and only if $a_1, a_2 > 0$, clearly $a_1, a_2 > 0$. Hence by RouthHurwitz criteria, for $\mathfrak{R}_0 > 1$, the endemic equilibrium (E_e) is LAS.

4.2. Global stability analysis

In this section, we use LaSalle's invariant principle to analyse the global stability of both equilibria of Equation (2) by creating suitable Lyapunov functions.

Theorem 4.3. If $\mathfrak{R}_0 < 1$, then the disease free-equilibrium (E_0) of Equation (2) is GAS in Ω and unstable otherwise.

Proof. We first create a suitable Lyapunov function of the type

$$L(t) = k_1 E(t) + k_2 I(t) \quad (21)$$

where $k_i, i = 1, 2$ are positive real numbers to be chosen later. Upon differentiating Equation (21) along its trajectories with respect to t and simplifying, the result yields

$$\frac{dL}{dt} = k_1 \frac{dE}{dt} + k_2 \frac{dI}{dt},$$

$$\frac{dL}{dt} = k_1(f_1 S_I + f_1 S_E - r_1 E) + k_2(\gamma E - r_2 I) \quad (22)$$

Now, we choose $k_1 = \gamma$ and $k_2 = r_1$, and simplification of Equation (22) yields

$$\frac{dL}{dt} = \gamma(f_1 S_I + f_1 S_E) - r_1 r_2 I,$$

$$\frac{dL}{dt} = \left[\gamma\left(\frac{\beta_1 \Lambda_1 + \beta_2 \Lambda_2}{\Lambda_1 + \Lambda_2}\right) - r_1 r_1\right] I \quad (23)$$

Simplification and some rearrangement of Equation (23) will give:

$$\frac{dL}{dt} = -r_1 r_2 \left(1 - \mathfrak{R}_0^2\right) I \quad (24)$$

Thus, $\frac{dL}{dt} < 0$ whenever $\mathfrak{R}_0 < 1$. Additionally, $\frac{dL}{dt} = 0$ if and only if $E(t) = 0$ and $I(t) = 0$. Hence, the largest compact invariant set $\{(S_I, S_E, E, I, R) \in \Omega : \frac{dL}{dt} = 0\}$ is the singleton E_0, which is the disease-free equilibrium. Therefore, using LaSalle's invariant principle [32], we conclude that the point E_0 is globally asymptotically stable in Ω if $\mathfrak{R}_0 < 1$.

Theorem 4.4. The disease endemic equilibrium point (E_e) of Equation (2) is GAS in the invariant region stated in Theorem 3.2 as Ω if $\mathfrak{R}_0 > 1$.

Proof. To prove the global behavior of E_e, we systematically construct a Lyapunov function V of the form as Legesse et al. [31]

$$V(x_i) = \sum_1^n \left(x_i - x_i^* - x_i^* ln\left(\frac{x_i}{x_i^*}\right)\right) \quad (25)$$

where x_i represents the compartments in the model and i = 1,...5 and x_i^* is the endemic equilibrium point. This is defined as

$$V(S_I^*, S_E^*, C^*, I^*, R^*) = \left(S_I - S_I^* - S_I^* ln\left(\frac{S_I}{S_I^*}\right)\right) + \left(S_E - S_E^* - S_E^* ln\left(\frac{S_E}{S_E^*}\right)\right) + + \left(E - E^* - E^* ln\left(\frac{E}{E^*}\right)\right) + \left(I - I^* - I^* ln\left(\frac{I}{I^*}\right)\right) + \left(R - R^* - R^* ln\left(\frac{R}{R^*}\right)\right)$$

Then, after differentiating V with regard to time t, the following is obtained.

$$\frac{dV}{dt} = \left(1 - \frac{S_I^*}{S_I}\right)\frac{dS_I}{dt} + \left(1 - \frac{S_E^*}{S_2}\right)\frac{dS_E}{dt} + \left(1 - \frac{E^*}{E}\right)\frac{dE}{dt} + \left(1 - \frac{I^*}{I}\right)\frac{dI}{dt} + \left(1 - \frac{R^*}{R}\right)\frac{dR}{dt} \quad (26)$$

Next, substituting $\frac{dS_I}{dt}, \frac{dS_E}{dt}, \frac{dE}{dt}, \frac{dI}{dt}, \frac{dR}{dt}$ in Equation (26) using Equation (2) gives

$$\frac{dV}{dt} = \left(1 - \frac{S_I^*}{S_I}\right)(\Lambda_1 + \delta R - f_1 S_I - \mu S_I) + \left(1 - \frac{S_E^*}{S_E}\right) (\Lambda_2 - f_2 S_E - \mu S_E) + \left(1 - \frac{E^*}{E}\right)(f_1 S_I + f_2 S_E - (\gamma + \mu)E) + \left(1 - \frac{I^*}{I}\right)(\gamma E - (\sigma + \alpha + \mu)I) + \left(1 - \frac{R^*}{R}\right)(\sigma I - (\mu + \delta)R) \quad (27)$$

10.3389/fams.2023.1224891

$$= \left(\frac{S_I - S_I^*}{S_I}\right)\left(\Lambda_1 + \delta R - (f_1+\mu)(S_I - S_I^*) - (f_1+\mu)S_I^*\right)$$
$$+ \left(\frac{S_E - S_E^*}{S_E}\right)\left(\Lambda_2 - (f_2+\mu)(S_E - S_E^*) - (f_2+\mu)S_E^*\right) +$$
$$\left(\frac{E - E^*}{E}\right)\left(f_1 S_I + f_2 S_E - (\gamma+\mu)(E - E^*) - (\gamma+\mu)E^*\right)$$
$$+ \left(\frac{I - I^*}{I}\right)\left(\gamma E - (\sigma+\alpha+\mu)(I - I^*) - (\sigma+\alpha+\mu)I^*\right)$$
$$+ \left(\frac{R - R^*}{R}\right)\left(\sigma I - (\mu+\delta)(R - R^*) - (\mu+\delta)R^*\right).$$

We can put $\frac{dV}{dt}$ as $\frac{dV}{dt} = \Psi_1 - \Psi_2$ where

$$\Psi_1 = \Lambda_1 + \Lambda_2 + \delta R + f_1 S_I + \gamma E + \sigma I + (f_1+\mu)\frac{S_I^{*2}}{S_I} +$$
$$(f_2+\mu)\frac{S_E^{*2}}{S_E} + (\gamma+\mu)\frac{E^{*2}}{E} + (\mu+\delta)\frac{R^{*2}}{R}.$$

$$\Psi_2 = \frac{(S_I - S_I^*)^2}{S_I}(f_1+\mu) + \Lambda_1\frac{S_I^*}{S_I} + \delta R\frac{S_I^*}{S_I} + (f_1+\mu)S_I^* +$$
$$\frac{(S_E - S_E^*)^2}{S_E}(f_2+\mu) + \frac{S_E^*}{S_E}\Lambda_2 - (f_1+\mu)S_E^* + \frac{f_1 S_I E^*}{E} + f_2 S_E +$$
$$\frac{(f_2 S_E E^*}{E} - (\gamma+\mu)\frac{(E - E^*)^2}{E} - (\gamma+\mu)E^* - \gamma E\frac{I^*}{I} -$$
$$(\sigma+\alpha+\mu)\frac{(I - I^*)^2}{I} + (\sigma+\alpha+\mu)I^* + (\sigma+\alpha+\mu)\frac{I^{*2}}{I} +$$
$$\sigma I + \sigma I\frac{R^*}{R} - (\mu+\delta)\frac{(R - R^*)^2}{R} + (\mu+\delta)R^*.$$

Thus, if $P < N$, then $\frac{dV}{dt} \leq 0$. Hence, $\frac{dV}{dt} \leq 0$ when $\Re_0 > 1$. Clearly, $\frac{dV}{dt} = 0$ if and only if $S_I = S_I^*, S_E = S_E^*, E = E^*, I = I^*$, and $R = R^*$. Therefore, the largest compact positive invariant in set $\{(S_I, S_E, E, I, R) \in \Omega : \frac{dV}{dt} = 0\}$ is the singleton E_e, which is a disease endemic equilibrium of Equation (2). Generally, by LaSalle's invariant principle, E_e is GAS in the biologically feasible region when $\Re_0 > 1$.

5. The proposed model under optimal control

This section focuses on using optimum control techniques with the model under consideration from Equation (2). In a short amount of time, we were able to manage or reduce the diseases in the community with the use of these strategies. The pneumonia model is expanded to include the following two control variables, each of which is defined as follows:

u_1: a campaign to prevent the spread of the disease among people who are vulnerable.

u_2: by treating infectious diseases, a treatment effort is made to minimize infection or maximize recovery.

After incorporating u_1 and u_2 in Equation (2), we obtain the following optimal control model Equation (28).

$$\begin{cases} \frac{dS_I}{dt} &= \Lambda_1 + \delta R - (1-u_1)f_1 S_I - \mu S_I \\ \frac{dS_E}{dt} &= \Lambda_2 - (1-u_1)f_2 S_E - \mu S_E \\ \frac{dE}{dt} &= (1-u_1)(f_1 S_I + f_2 S_E) - (\gamma+\mu)E \\ \frac{dI}{dt} &= \gamma E - (\sigma+u_2)I - (\alpha+\mu)I \\ \frac{dR}{dt} &= (\sigma+u_2)I - (\mu+\delta)R \end{cases} \tag{28}$$

The control set U is Lebesgue measurable and has the following definition in order to explore the optimal levels of the controls: $U = \{(u_1(t), u_2(t))\} : \{0 \leq u_1 < 1, 0 \leq u_2 < 1, 0 \leq t \leq T\}$ where $\{0 \leq u_1 < 1, 0 \leq u_2 < 1, 0 \leq t \leq T\}$ is the set of admissible controls. Our goal is to find a control u and S_I, S_E, E, I, and R that minimize the proposed objective function J given below, while maintaining the lowest cost of control implementation in Equation (2). The proposed objective functional J should follow the epidemic Equation (2), which is given by

$$J(u_1, u_2) = \min_{u_1, u_2} \int_0^{t_f} (b_1 E + b_2 I + \frac{1}{2}\sum_{i=1}^{2} w_i u_i^2)dt \tag{29}$$

subject to Equation (3), where b_1 and b_2 are the weight positive constants associated with the number of exposed children and infected children, respectively, while w_1 and w_2 are positive constants, present the relative cost weight, which is associated with control measures u_1 and u_2, respectively. We assume costs are non-linear in nature; hence, the control variables in J are in second degree polynomial form [21, 23]. The major thing that is required of us is to reduce the number of exposed and affected children while maintaining a low cost. Thus, we are going to find optimal controls (u_1^*, u_2^*), such that

$$J(u_1^*, u_2^*) = min\{J(u_1, u_2)/u_i \in U\},$$

where $U = (u_1, u_2)$: each u_i is measurable with $0 \leq u_i < 1, i = 1, 2$ for $t \in [0, t_f]$.

5.1. The Hamiltonian and optimality system

Here, applying the principle of Pontryagin [34], Maximum Principle, we can drive the necessary conditions that the optimal control solution must satisfy [35]. Therefore, this principle converts the model Equations (28), (29) into a problem of minimizing a Hamiltonian, H, point-wise with respect to u_1 and u_2, and we obtained a Hamiltonian (H) defined as:

$$H(t, x(t), u(t), \lambda(t)) = f(t, x(t), u(t)) + \lambda g(t, x(t), u(t))$$

where

$$f(t, x(t), u(t)) = b_l E + b_2 I + \frac{1}{2}w_1 u_1^2 + \frac{1}{2}w_2 u_2^2,$$

$$g(t, x(t), u(t)) = (g_1, g_2, g_3, g_4, g_5)^T,$$

where

$$\begin{aligned} g_1 &= \Lambda_1 + \delta R - (1-u_1)f_1 S_I - \mu S_I, \\ g_2 &= \Lambda_2 - (1-u_1)f_2 S_E - \mu S_E, \\ g_3 &= (1-u_1)(f_1 S_I + f_2 S_E) - (\gamma+\mu)E, . \\ g_4 &= \gamma E - (r_2+u_2)I, \\ g_5 &= (\sigma+u_2)I - (\mu+\delta)R. \end{aligned}$$

Hence the Hamiltonian becomes

$$H(S_I, S_E, E, I, R, t) = f(E, I, u_1, u_2, t) + \lambda_1 \frac{dS_I}{dt} + \lambda_2 \frac{dS_E}{dt} + \lambda_3 \frac{dE}{dt} + \lambda_4 \frac{dI}{dt} + \lambda_5 \frac{dR}{dt}$$

$$H(S_I, S_E, E, I, R, t) = f(E, I, u_1, u_2, t) + \lambda_1 g_1 + \lambda_2 g_2 + \lambda_3 g_3 + \lambda_4 g_4 + \lambda_5 g_5$$

$$H = b_l E + b_2 I + \frac{1}{2} w_1 u_1^2 + \frac{1}{2} w_2 u_2^2 + \lambda_1 g_1 + \lambda_2 g_2 + \lambda_3 g_3 + \lambda_4 g_4 + \lambda_5 g_5 \quad (30)$$

where $f(E, I, u_1, u_2, t) = b_1 E + b_2 I + \frac{1}{2}\sum_{i=1}^{2} w_i u_i^2, \lambda_i, i = 1, 2$ are the adjoint variable functions which are determined by using Pontryagin's maximal principle [34] and use Swai et al. [23] for verification of existence of the optimal control pairs.

Theorem 5.1. There exists adjoint variable λ_i, where $i = 1, ..., 5$ with transversality conditions $\lambda_i(t_f) = 0, i = 1, ..., 5$ for an optimal control (u_1^*, u_2^*) that minimizes $J(u_1, u_2)$ such that:

$$\frac{d\lambda}{dt} = -\frac{\partial H}{\partial X},$$

where $X = (S_I, S_E, E, I, R)^T$ and $\lambda = (\lambda_1, \lambda_2, \lambda_3, \lambda_4, \lambda_5)^T$ $\lambda(T) = 0$ transidentality condition.
Now,

$$\frac{d\lambda_1}{dt} = -\frac{\partial H}{\partial S_I} = -(\lambda_1(0 - (1-u_1)f_1 - \mu) + \lambda_2(0) + \lambda_3((1-u_1)(f_1) + \lambda_4(0) + \lambda_5(0))$$

$$= \lambda_1((1-u_1)f_1 + \mu) - \lambda_3(1-u_1)f_1$$

$$\frac{d\lambda_2}{dt} = -\frac{\partial H}{\partial S_E} = -(\lambda_2(\lambda_1(0) - (1-u_1)f_2 - \mu) + \lambda_3((1-u_1)(f_2) + \lambda_4(0) + \lambda_5(0))$$

$$= \lambda_2((1-u_1)f_2 + \mu) - \lambda_3(1-u)f_2$$

$$\frac{d\lambda_3}{dt} = -\frac{\partial H}{\partial E} = -(b_1 + \lambda_1(0) + \lambda_2(0) + \lambda_3(-(\gamma+\mu)) + \lambda_4(\gamma) + \lambda_5(0))$$

$$= -b_1 + \lambda_3(\gamma+\mu) - \lambda_4\gamma = -b_1 + \lambda_3\gamma_1 - \lambda_4\gamma$$

$$\frac{d\lambda_4}{dt} = -\frac{\partial H}{\partial I} = -(b_2 - \frac{\lambda_1\beta_1(1-u_1)S_I}{N} - \frac{\lambda_2\beta_2(1-u_1)S_E}{N} + \frac{\lambda_3(1-u_1)(\beta_1 S_I + \beta_2 S_E)}{N} - \lambda_4(\sigma + u_2 + \alpha + \mu) - \lambda_5(\sigma + u_2)$$

$$= -b_2 + \lambda_1\beta_1(1-u_1)\frac{\Lambda_1}{\Lambda_1+\Lambda_2} + \lambda_2\beta_2(1-u_1)\frac{\Lambda_2}{\Lambda_1+\Lambda_2} - \lambda_3(1-u_1)\left(\frac{\beta_1\Lambda_1 + \beta_2\Lambda_2}{\Lambda_1+\Lambda_2}\right) + \lambda_4(\gamma_2 + u_2) - \lambda_5(\sigma + u_2)$$

$$\frac{d\lambda_5}{dt} = -\frac{\partial H}{\partial R} = -(\lambda_1\sigma + \lambda_2(0) + \lambda_3(0) + \lambda_4(0) - \lambda_5(\mu+\delta))$$

$$= -(\lambda_1\delta - \lambda_5(\mu+\delta)) = -\lambda_1\delta + \lambda_5\gamma_3$$

In a similar manner, we obtained the controls by solving the equation $\frac{\partial H}{\partial u_i} = 0$ at u_i^*, for i = 1, 2 in accordance with Pontryagin [34]'s methodology and obtained:

$$w_1 u_1 + \lambda_1 f_1 S_I + \lambda_2 f_2 S_E - \lambda_3(f_1 S_I + f_2 S_E) = 0$$

$$u_1 = \frac{(\lambda_3 - \lambda_1)\beta_1\Lambda_1 + (\lambda_3 - \lambda_2)\beta_2\Lambda_2}{w_1(\Lambda_1 + \Lambda_2)} I$$

$$u_1^* = max\left\{0, min\left\{1, \frac{(\lambda_3 - \lambda_1)\beta_1 S_I + (\lambda_3 - \lambda_2)\beta_2 S_E}{w_1 N} I\right\}\right\}$$

Similarly $\frac{\partial H}{\partial u_2} = 0$

$$w_2 u_2 - \lambda_4 I + \lambda_5 I = 0$$

From this

$$u_2 = \frac{(\lambda_4 - \lambda_5)I}{w_2}$$

This implies that

$$u_2^* = \begin{cases} u_2, \ if \ 0 < u_2 < 1 \\ 0, if \ u_2 < 0 \\ 1, if \ u_2 > 1 \end{cases}$$

The above equation in compact notation is

$$u_2^* = max\left\{0, min\left\{1, \frac{(\lambda_4 - \lambda_5)I}{w_2}\right\}\right\}$$

TABLE 1 Pneumonia model parameter values with their source.

Parameter	Value	References
α	0.33	[21]
Λ_1	0.02	Assumed
Λ_2	0.5	Assumed
μ	0.01	[21]
σ	0.0238	[33]
k	0 – 10	[23]
δ	0.	[21]
p_j $j = 1, 2$	0.89-0.99	[23]
γ	0.1096	Assumed

Considering the bounds of the control quintuple, we have

$$\begin{aligned} u_1^* &= max\left\{0, min\left\{1, \frac{(\lambda_3-\lambda_1)\beta_1\Lambda_1+(\lambda_3-\lambda_2)\beta_2\Lambda_2}{w_1(\Lambda_1+\Lambda_2)}I\right\}\right\} \\ u_2^* &= max\left\{0, min\left\{1, \frac{(\lambda_4-\lambda_5)I}{w_2}\right\}\right\} \end{aligned} \tag{31}$$

The optimality system is obtained from the state Equation (29) together with adjoint variables and the transversality condition in Theorem 5.1 by including the characterized control set and initial condition.

$$\begin{aligned} \frac{dS_I}{dt} &= \Lambda_1 + \delta R - (1-u_1)f_1 S_I - \mu S_I \\ \frac{dS_E}{dt} &= \Lambda_2 - (1-u_1)f_2 S_E - \mu S_E \\ \frac{dE}{dt} &= (1-u_1)(f_1 S_I + f_2 S_E) - (\gamma+\mu)E \\ \frac{dI}{dt} &= \gamma E - (\sigma+u_2)I - (\alpha+\mu)I \\ \frac{dR}{dt} &= (\sigma+u_2)I - (\mu+\delta)R \\ \frac{d\lambda_1}{dt} &= (1-u_1)f_1(\lambda_1-\lambda_3) + \lambda_1\mu \\ \frac{d\lambda_2}{dt} &= (1-u_1)f_2(\lambda_2-\lambda_3) + \lambda_2\mu \\ \frac{d\lambda_3}{dt} &= -b_1 + \lambda_3\gamma_1 - \lambda_4\gamma \\ \frac{d\lambda_4}{dt} &= -b_2 + (1-u_1)(\lambda_1-\lambda_3)\frac{\beta_1 S_I}{N} + (1-u_1) \\ &(\lambda_2-\lambda_3)\frac{\beta_2 S_E}{N} + \lambda_4(r_2+u_2) - \lambda_5(\sigma+u_2) \\ \frac{d\lambda_5}{dt} &= -\lambda_1\delta + \lambda_5(\mu+\delta) \end{aligned} \tag{32}$$

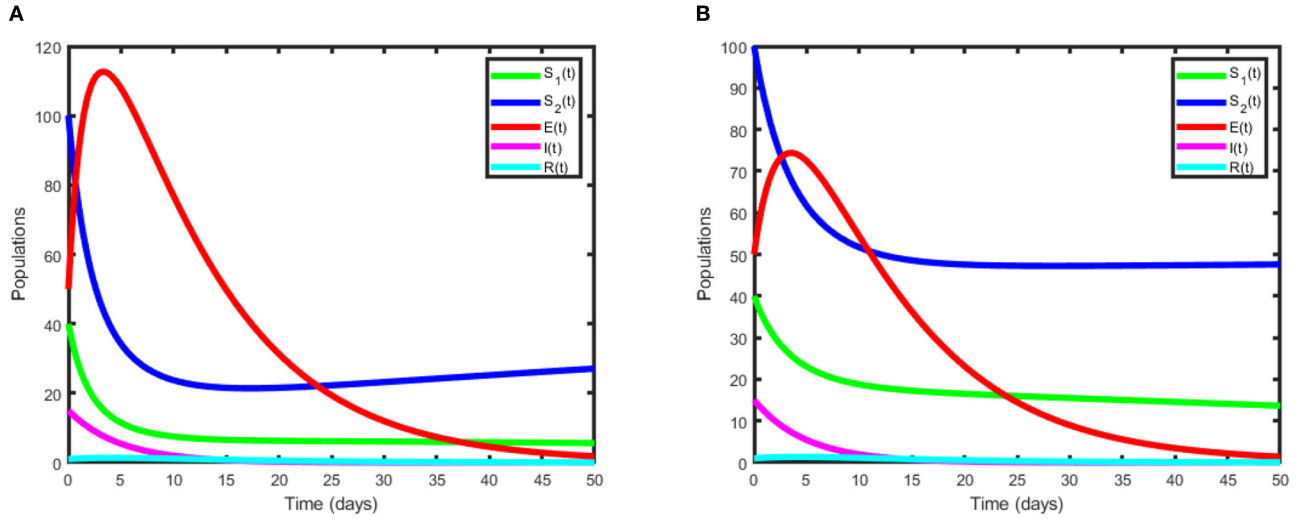

FIGURE 2
The pneumonia model's trajectory of solutions converges to **(A)** DFEP and **(B)** EEP.

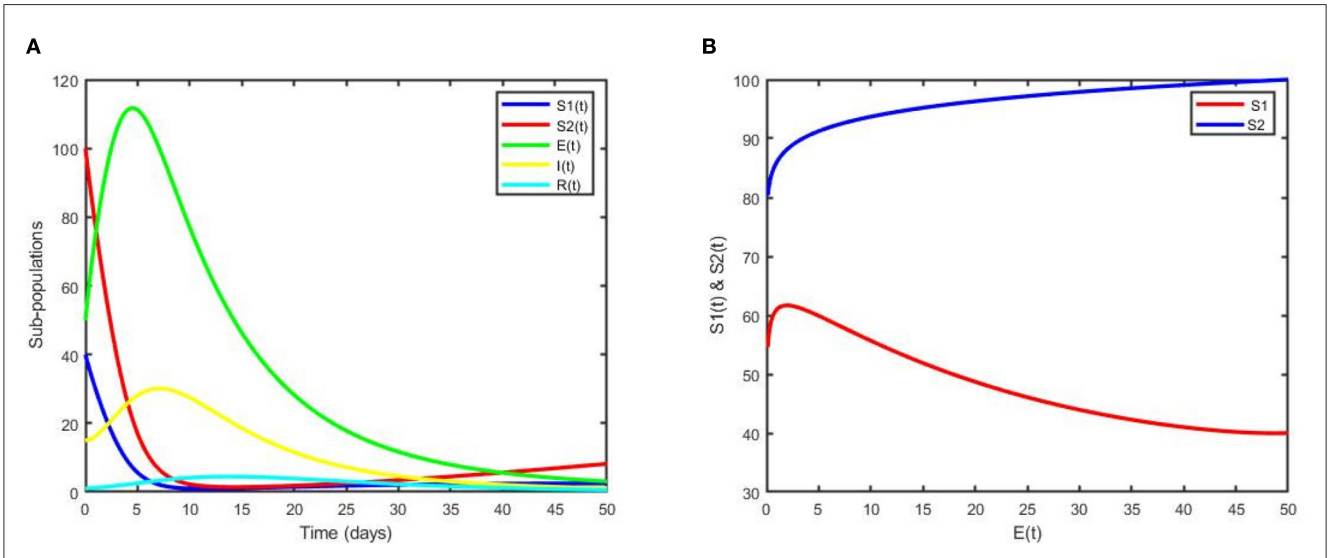

FIGURE 3
(A) Dynamics of sub-populations for the DFE point. **(B)** The phase portrait for $S_I(t)$ and $S_E(t)$ vs. E(t).

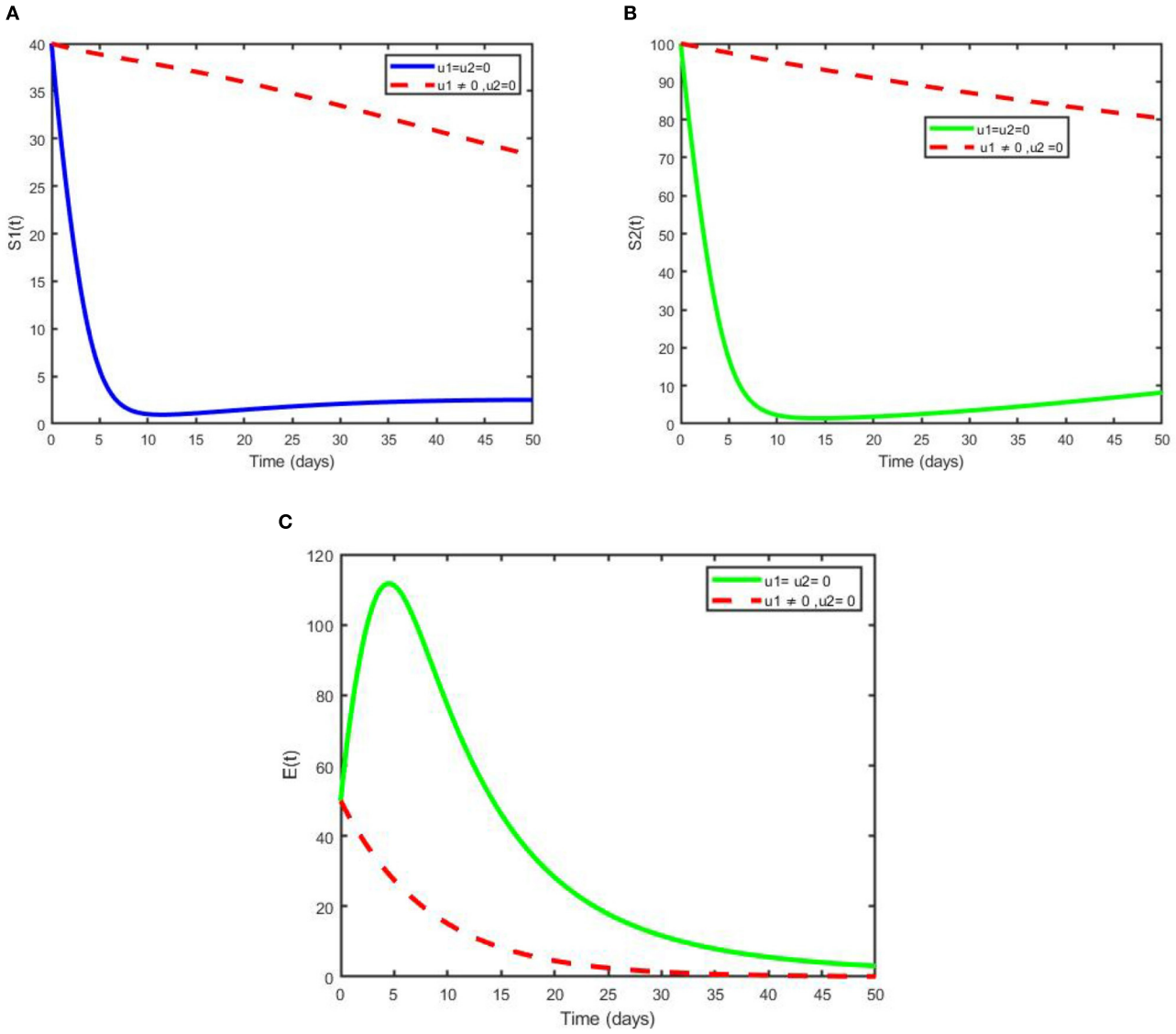

FIGURE 4
Simulation of the optimal model showing the effect of prevention on **(A)** not exclusively breastfeed individuals, **(B)** exclusively breastfeed individuals, and **(C)** exposed individuals.

$$\lambda_i(t_f) = 0, i = 1, ..., 5$$

$$S_I(0) = S_{I0}, S_E(0) = S_{E0}, E(0) = E_0, I(0) = I_0, R(0) = R_0$$

Therefore, using the optimality system 32, it is possible to calculate the optimal control. Consequently, the optimal problem is minimal at control u_1^* and u_2^*, as shown by the fact that the second derivatives of the Lagrangian with regard to u_1 and u_2, respectively, are positive.

6. Results and discussion

To analyse the dynamics of pneumonia disease with or without control measures, numerical simulations are performed on the suggested model and optimality system using the parameter values indicated in Table 1. In addition, we assumed the initial population size to be $S_I(0) = 40; S_E(0) = 100; E(0) = 50; I(0) = 15;$ and R(0) = 1 for the purpose of numerical simulation. The weight constant values are chosen as $b_1 = 3; b_2 = 3; w_1 = 0.05$ and $w_2 = 0.03$. First, we simulate the pneumonia model for the case $R_0 = 0.8513 < 1$, which indicates that the pneumonia disease dies out from the society. As a result, the pneumonia model's solution trajectory moves toward a disease-free equilibrium point. The disease-free equilibrium point is demonstrated to be locally asymptotically stable as all the trajectories of the model converge to DFE, see Figure 2A. Next, we plotted the graphics for the case $R_0 = 1.4232 > 1$, which implies that the disease is endemic. In this case, the solution curves are converging to the endemic equilibrium point, which verifies the linear stability of the EE point (see Figure 2B).

Now, to extend the proposed model to optimal control, we focus on the parameter values and initial population, which give

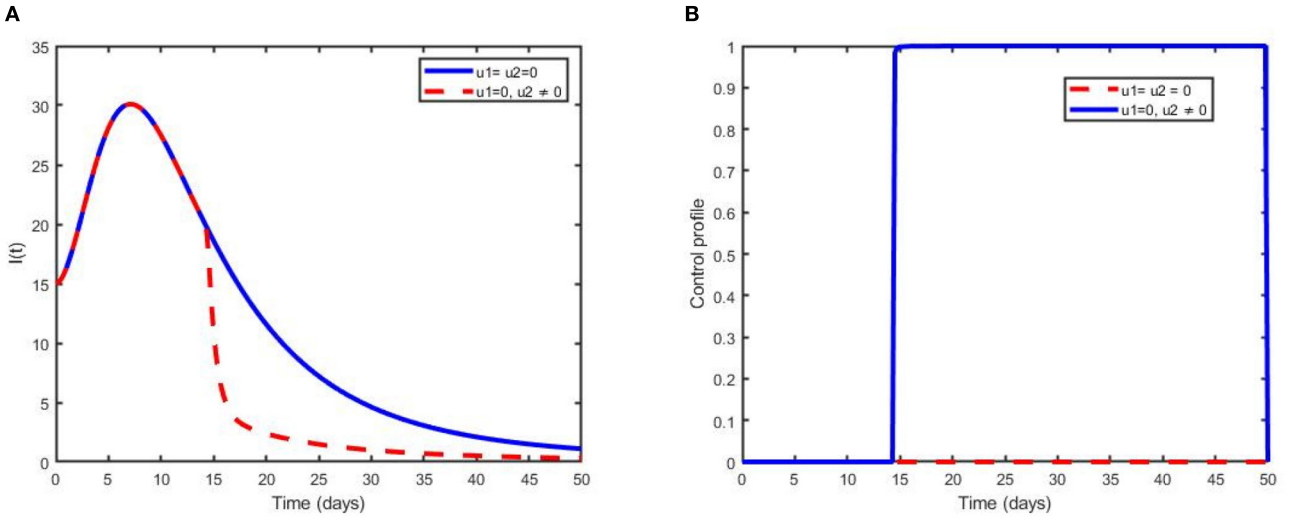

FIGURE 5
Simulations showing **(A)** the optimal use of treatment only ($u2$) and **(B)** its control profile.

$R_0 = 1.4232 > 1$ to analyze the model. In light of the fact that diseases are still prevalent in society, adding control factors to the mode is appropriate. Figures 3–6 demonstrate the impact of prevention and treatment on the dynamics of pneumonia.

The plot in Figure 3A illustrates that subpopulations converge to the DFE point, which indicates that pneumonia has been eliminated from the community. Moreover, it can be observed that the two susceptible populations decrease while the exposed and infected children increase for a few years and decrease rapidly afterward to the DFE point. Figure 3B reveals that even if controls are applied, non-exclusively breastfed children are more exposed to pneumonia than exclusively breastfed children. In general, from Figures 2A, 3A, we can easily see the impact of control variables on the transmission dynamics of pneumonia.

6.1. Contingency plans

We utilized the following scenarios to assess how each regulation would affect the dynamics of pneumonia spread:
(i) Optimal use of prevention (u_1 only).
(ii) Optimal use of treatment (u_2 only).
(iii) Optimal use of prevention (u_1) and treatment (u_2) intervention.

6.1.1. Scenario A: control of pneumonia with prevention only

This scenario shows the use of only one control measure, prevention (u_1), and the other controls were set to zero. As clearly observed from Figures 4A, B, with the optimal use of a prevention strategy, the two susceptible individuals increase due to the prevention strategy, and when we compare it with the case free of prevention, the number of susceptibilities of individuals to the diseases is less. Moreover, the number of total exposed humans decreases more with control than when there is no control, as depicted in Figure 4C. Since the number of infection averted human from pneumonia disease due to this strategy is less in number, hence additional intervention is required.

6.1.2. Scenario B: control of pneumonia with treatment only

Scenario B is shown in Figures 5A, B, which illustrate that treatment has a significant impact in reducing the number of children infected with pneumonia after 14 years. It can be noted that the number of infected individuals slightly decreases and becomes effective after some time; hence, more interventions are needed to eliminate the disease from the community.

6.1.3. Scenario C: optimal use of the two controls

This strategy demonstrates the effect of the optimal use of prevention for the exposed humans and treatment for the infectious humans to decrease the number of exposed and infected individuals in the society. Additionally, this intervention reduces the spread of pneumonia dynamics governed by model (2) in the population. The numbers of exposed individuals and infectious individuals decrease more rapidly when the two control scenarios are in use compared with when controls are not used or one control is used, as depicted in Figures 6A, B. Figure 6F reveals that the optimal use of prevention. $u_1(t)$ is maximum at 100% throughout the proposed days until reaching the final time that maximum prevention is applied to control pneumonia. Optimal use of treatment $u_2(t)$ is kept at the maximum

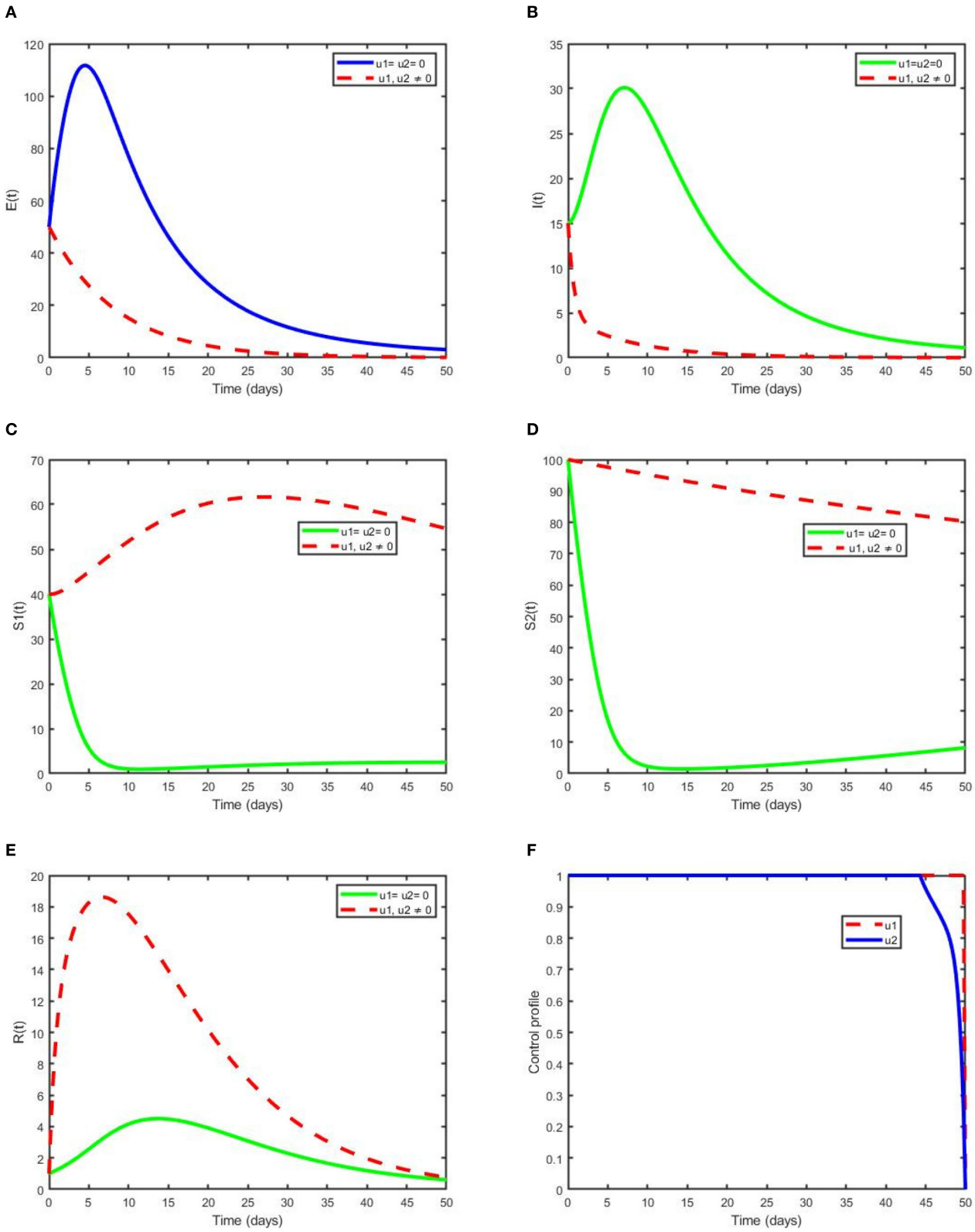

FIGURE 6
Simulations demonstrating optimal use of prevention (u_1) and treatment (u_2) on **(A)** E **(B)** I **(C)** S_E **(D)** S_I **(E)** R and **(F)** its control profile.

level for 48 days before arriving at the minimum at the final intervention time. Figures 6C–E reveal, respectively, the size of S_I, S_E, and R increases compared with non-control and one control intervention. This confirms that a maximum number of children's pneumonia diseases are averted due to the intervention of the two controls.

7. Cost-effectiveness analysis

In this section, we present cost-effectiveness analysis, which is used to evaluate the benefits related to a health intervention(s) or strategy (strategies) (for instance treatment and prevention), to elaborate the strategy's costs [22]. The number of infections averted is given as the difference between total infectious individuals without control and total infectious individuals with control. Using the parameter values in Table 1 and initial conditions of state variables with the weight constant values chosen, the ICER is determined for each intervention labeled as prevention, treatment, and a combination of both. The prevention strategy includes vaccination (immunization), personal hygiene, avoiding exposure to people who are ill, covering a cough, and adequate nutrition (scenario A), while the treatment intervention involves antibiotics that stop the infection from progressing (these medicines are used to treat bacterial pneumonia), hospital treatment (allowed for more severe cases), rest, etc. (scenario B). The combination of prevention and treatment scenario C. This is obtained by balancing the change between the costs and health outcomes of these intervention strategies; usually obtained by using the incremental cost-effectiveness ratio (ICER), which is described as:

$$ICER = \frac{\text{change in total costs between strategies}}{\text{change in health benefits between strategies}} \tag{33}$$

where the numerator of the ICER represents the difference in cost-benefit and the denominator measures the change in health benefit.

According to the simulation outcomes of the optimality system, the control scenarios are then ranked in ascending order of total number of infections averted, i.e., prevention of infections in susceptible children using vaccines, personal hygiene and others (strategy A), treatment of infected individuals with antibiotics (strategy B), and a combination of prevention and treatment (strategy C), as shown in Table 2.

The ICER is obtained through the following computation:

$$ICER(B) = \frac{1102.5}{701.9053} = 1.5707$$
$$ICER(A) = \frac{346.4642 - 1102.5}{1665.791 - 701.9053} = -0.7827$$
$$ICER(C) = \frac{1753.1540 - 346.4642}{2178.746 - 1665.791} = 2.741$$

Now, comparing strategy A and B incrementally, the ICER for the two competing strategies is calculated as above and it shows that $ICER\ (B) > ICER\ (A)$. From this, we can see that strategy A saves 0.7827 more than strategy B, and strategy B is a bit more expensive. Hence, we excluded strategy B from the set of competing strategies, and finally, we compared strategies A and C as depicted in Table 3. From *ICER (A)* and *ICER (C)* in Table 3 we can see that strategy C saves 2.741 than strategy A. Hence, we exclude strategy C, because it is a bit expensive. Therefore, we conclude that strategy A the cheapest of all compared strategies, that meant it is the most cost-effective for pneumonia disease control intervention strategies.

TABLE 2 Incremental cost-effectiveness ratio in increasing order of total infections averted.

Strategies	Total infections averted	Total cost	ICER
StrategyB	701.9053	1102.5	1.5707
StrategyA	1665.791	346.4642	−0.7827
StrategyC	2178.746	1753.1540	2.741

TABLE 3 Comparison between intervention strategies A and C.

Strategies	Total infections averted	Total cost	ICER
StrategyA	1665.791	346.4642	0.2080
StrategyC	2178.746	1753.1540	2.7423

8. Conclusion

This study is concerned with the mathematical analysis of a pneumonia transmission model with naturally acquired immunity in the presence of effective exclusively breastfed infants and a lack of naturally acquired immunity due to the loss of exclusively breastfed infants. This work also shows that if the threshold number is smaller than unity, then the pneumonia-free equilibrium point is both locally and globally asymptotically stable, which means pneumonia is wiped out of the community. If the threshold number is greater than unity, then an endemic equilibrium of the model occurs, which shows the persistence of the diseases in the population.

To control pneumonia spread dynamics in a population, multiple time-dependent control variables, including prevention using vaccines, personal hygiene, etc., treatment of infectious humans using antibiotics, hospital treatment, and rest are considered. An analysis of the optimal control model is carried out theoretically, and the model is simulated to determine the effects of combining the two control intervention strategies on the spread dynamics of pneumonia in the community. It is shown that the number of infected children is minimized through prevention and treatment intervention strategies. Throughout this work, based on the results in Table 3, we recommend the prevention of susceptible children from being exposed to the diseases using vaccination, public health education, etc., to reduce new exposed cases and the number of infected children due to pneumonia in our society with the least cost.

In general, we considered cleanliness as a method of preventing pneumonia in children under the age of five in the earlier studies on the dynamics of bimodal pneumonia [31]. However, in the present study, we considered the extension of the bimodal pneumonia model to optimal control using two time-dependent control measures, namely prevention and treatment. In addition, we analyzed the cost-effectiveness of intervention strategies. The result of the analysis reveals that prevention strategies are the most cost-effective way of eradicating pneumonia. Therefore, the present study is more effective and cost-effective in preventing pneumonia transmission than the previous study.

Data availability statement

The original contributions presented in the study are included in the article/supplementary material, further inquiries can be directed to the corresponding author.

Author contributions

FL conceptualized, planned, and prepared the article as well as the figures. The final manuscript's review, modification, and literature search were all aided by the efforts of all writers. The article's submission was reviewed and approved by all authors.

Conflict of interest

The authors declare that the research was conducted in the absence of any commercial or financial relationships that could be construed as a potential conflict of interest.

Publisher's note

All claims expressed in this article are solely those of the authors and do not necessarily represent those of their affiliated organizations, or those of the publisher, the editors and the reviewers. Any product that may be evaluated in this article, or claim that may be made by its manufacturer, is not guaranteed or endorsed by the publisher.

References

1. Elyas L, Mekasha A, Admasie A, Assefa E. Exclusive breastfeeding practice and associated factors among mothers attending private pediatric and child clinics, Addis Ababa, Ethiopia: a cross-sectional study. *Int J Pediatr*. (2017) 2017:8546192. doi: 10.1155/2017/8546192

2. Abdulla F, Hossain MM, Karimuzzaman M, Ali M, Rahman A. Likelihood of infectious diseases due to lack of exclusive breastfeeding among infants in Bangladesh. *PLoS ONE*. (2022) 17:e0263890. doi: 10.1371/journal.pone.0263890

3. Morty RE. World health day observances in November 2021: advocating for adult and pediatric pneumonia, preterm birth, and chronic obstructive pulmonary disease. *Am J Physiol Lung Cell Mol Physiol*. (2021) 321:L954L957. doi: 10.1152/ajplung.00423.2021

4. Otoo D, Opoku P, Charles S, Kingsley AP. Deterministic epidemic model for (SVCSyCAsyIR) pneumonia dynamics, with vaccination and temporal immunity. *Infect Dis Model*. (2020) 5:42–60. doi: 10.1016/j.idm.2019.11.001

5. Kizito M, Tumwiine J, A. mathematical model of treatment and vaccination interventions of pneumococcal pneumonia infection dynamics. *J Appl Mathem*. (2018) 2018:2539465. doi: 10.1155/2018/2539465

6. Alebel A, Tesma C, Temesgen B, Ferede A, Kibret GD. Exclusive breastfeeding practice in Ethiopia and its association with antenatal care and institutional delivery: a systematic review and meta-analysis. *Int Breastfeed J*. (2018) 13:1–12. doi: 10.1186/s13006-018-0173-x

7. Rajeshwari K, Bang A, Chaturvedi P, Kumar V, Yadav B, Bharadva K, et al. Infant and young child feeding guidelines: 2010. *Indian Pediatr*. (2010) 47:995–1004.

8. Arage G, Gedamu H. Exclusive breastfeeding practice and its associated factors among mothers of infants less than six months of age in Debre Tabor town, Northwest Ethiopia: a cross-sectional study. *Adv Public Health*. (2016) 2016:3426249. doi: 10.1155/2016/3426249

9. Turin CG, Ochoa TJ. The role of maternal breast milk in preventing infantile diarrhea in the developing world. *Curr Trop Med Rep*. (2014) 1:97–105. doi: 10.1007/s40475-014-0015-x

10. Tewabe T, Mandesh A, Gualu T, Alem G, Mekuria G, Zeleke H. Exclusive breastfeeding practice and associated factors among mothers in Motta town, East Gojjam zone, Amhara Regional State, Ethiopia, 2015: a cross-sectional study. *Int Breastfeed J*. (2016) 12:1–7. doi: 10.1186/s13006-017-0103-3

11. Mgongo M, Mosha MV, Uriyo JG, Msuya SE, Stray-Pedersen B. Prevalence and predictors of exclusive breastfeeding among women in Kilimanjaro region, Northern Tanzania: a population based cross-sectional study. *Int Breastfeed J*. (2013) 8:1–8. doi: 10.1186/1746-4358-8-12

12. Mogre V, Dery M, Gaa PK. Knowledge, attitudes and determinants of exclusive breastfeeding practice among Ghanaian rural lactating mothers. *Int Breastfeed J*. (2016) 11:1–8. doi: 10.1186/s13006-016-0071-z

13. Ajetunmobi OM, Whyte B, Chalmers J, Tappin DM, Wolfson L, Fleming M, et al. Breastfeeding is associated with reduced childhood hospitalization: evidence from a Scottish Birth Cohort (1997-2009). *J Pediatr*. (2015) 166:620–5. doi: 10.1016/j.jpeds.2014.11.013

14. Martin CR, Ling PR, Blackburn GL. Review of infant feeding: key features of breast milk and infant formula. *Nutrients*. (2016) 8:279. doi: 10.3390/nu8050279

15. Arifeen S, Black RE, Antelman G, Baqui A, Caulfield L, Becker S. Exclusive breastfeeding reduces acute respiratory infection and diarrhea deaths among infants in Dhaka slums. *Pediatrics*. (2001) 108:e67–e67. doi: 10.1542/peds.108.4.e67

16. Sefene A, Birhanu D, Awoke W, Taye T. Determinants of exclusive breastfeeding practice among mothers of children age less than 6 month in Bahir Dar city administration, Northwest Ethiopia; a community based cross-sectional survey. *Sci J Clin Med*. (2013) 2:153–9. doi: 10.11648/j.sjcm.20130206.12

17. Collective GB UNICEF. *Nurturing the health and wealth of nations: the investment case for breastfeeding*. Technical Report, World Health Organization. (2017).

18. Bhandari N, Chowdhury R. Infant and young child feeding. *Proc Indian Nat Sci Acad*. (2016) 82:1507–17. doi: 10.16943/ptinsa/2016/48883

19. Organization WH. *Tracking universal health coverage: first global monitoring report*. World Health Organization. (2015).

20. Sajjad S, Roshan R, Tanvir S. Impact of maternal education and source of knowledge on breast feeding practices in Rawalpindi city. *MOJCRR*. (2018) 1:212–42. doi: 10.15406/mojcrr.2018.01.00035

21. Tilahun GT, Makinde OD, Malonza D. Modelling and optimal control of pneumonia disease with cost-effective strategies. *J Biol Dyn*. (2017) 11:400–26. doi: 10.1080/17513758.2017.1337245

22. Agusto FB. Optimal isolation control strategies and cost-effectiveness analysis of a two-strain avian influenza model. *Biosystems*. (2013) 113:155–64. doi: 10.1016/j.biosystems.2013.06.004

23. Swai MC, Shaban N, Marijani T. Optimal control in two strain pneumonia transmission dynamics. *J Appl Mathem*. (2021) 2021:8835918. doi: 10.1155/2021/8835918

24. Tessema FS, Bole BK, Rao PK. Optimal control strategies and cost effectiveness analysis of Pneumonia disease with drug resistance. *Int J Nonl Analy Appl*. (2023) 14:903–17. doi: 10.22075/ijnaa.2022.26746.3402

25. Wu Y, Mascaro S, Bhuiyan M, Fathima P, Mace AO, Nicol MP, et al. Predicting the causative pathogen among children with pneumonia using a causal Bayesian network. *PLoS Comput Biol*. (2023) 19:e1010967. doi: 10.1371/journal.pcbi.1010967

26. Kotola BS, Mekonnen TT. Mathematical model analysis and numerical simulation for codynamics of meningitis and pneumonia infection with intervention. *Sci Rep*. (2022) 12:1–22. doi: 10.1038/s41598-022-06253-0

27. Gweryina RI, Madubueze CE, Bajiya VP, Esla FE. Modeling and analysis of tuberculosis and pneumonia co-infection dynamics with cost-effective strategies. *Results Control Optimiz*. (2023) 10:100210. doi: 10.1016/j.rico.2023.100210

28. Naveed M, Baleanu D, Raza A, Rafiq M, Soori AH, Mohsin M. Modeling the transmission dynamics of delayed pneumonia-like diseases with a sensitivity of parameters. *Adv Differ Equat*. (2021) 2021:1–19. doi: 10.1186/s13662-021-03618-z

29. Kassa SM, Njagarah JB, Terefe YA. Analysis of the mitigation strategies for COVID-19: from mathematical modelling perspective. *Chaos, Solitons Fractals*. (2020) 138:109968. doi: 10.1016/j.chaos.2020.109968

30. Rafiq M, Ali J, Riaz MB, Awrejcewicz J. Numerical analysis of a bi-modal COVID-19 sitr model. *Alexandria Eng J*. (2022) 61:227–35. doi: 10.1016/j.aej.2021.04.102

31. Legesse FM, Rao KP, Keno TD. Mathematical Modeling of a Bimodal Pneumonia Epidemic with Non-breastfeeding Class. *Appl Math*. (2023) 17:95–107. doi: 10.18576/amis/170111

32. Dano LB, Rao KP, Keno TD. Modeling the combined effect of hepatitis b infection and heavy alcohol consumption on the progression dynamics of liver cirrhosis. *J Mathematics*. (2022) 2022:6936396. doi: 10.1155/2022/6936396

33. Otieno O, Joseph M, John O. "Mathematical Model for Pneumonia Dynamics among Children," in *The 2012 southern Africa mathematical sciences association conference (SAMSA 2012)*. (2012).

34. Pontryagin LS. *Mathematical Theory of Optimal Processes*. London: CRC press. (1987).

35. Lenhart S, Workman JT. *Optimal Control Applied to Biological Models*. New York: Chapman and Hall/CRC. (2007). doi: 10.1201/9781420011418

Frontiers in
Applied Mathematics and Statistics

Investigates both applied and applicable mathematics and statistical techniques

Explores how the application of mathematics and statistics can drive scientific developments across data science, engineering, finance, physics, biology, ecology, business, medicine, and beyond

---

Discover the latest Research Topics

See more →

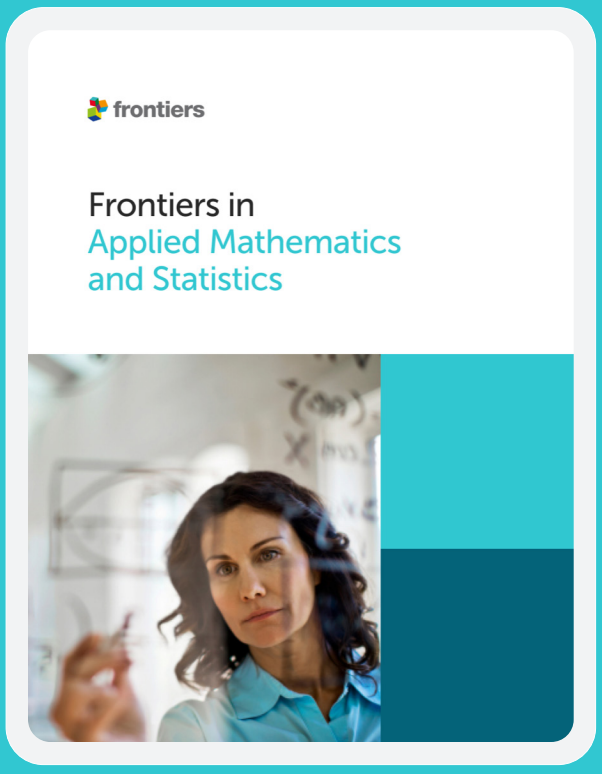

Frontiers

Avenue du Tribunal-Fédéral 34
1005 Lausanne, Switzerland
frontiersin.org

Contact us

+41 (0)21 510 17 00
frontiersin.org/about/contact